

INDUCTIVE MEASUREMENTS OF HEAVY FERMION SUPERCONDUCTORS

By

PHILIPPE J.-C. SIGNORE

**A DISSERTATION PRESENTED TO THE GRADUATE SCHOOL
OF THE UNIVERSITY OF FLORIDA IN PARTIAL FULFILLMENT
OF THE REQUIREMENTS FOR THE DEGREE OF
DOCTOR OF PHILOSOPHY**

UNIVERSITY OF FLORIDA

1994

ACKNOWLEDGMENTS

The author wishes to express his sincere gratitude and appreciation to his advisor, Professor Mark W. Meisel, for his patient guidance and encouragement throughout the entire course of this work. In addition, the author gratefully acknowledges Professors G. Bosman, L. E. Seiberling, C. J. Stanton, G. R. Stewart, and N. W. Sullivan for serving on his supervisory committee, and Professors S. E. Brown and F. Sharifi for their active contributions to this work.

The faculty, postdoctoral fellows, administrative and technical support of the entire low temperature group have contributed a great deal to this work, and their efforts are duly appreciated. Special thanks are expressed to the graduate students of the low temperature group for their help and for maintaining a camaraderie that contributed to a pleasant and positive working atmosphere. The author feels proud to belong to such a group and wishes his colleagues the best of luck for the future.

The author gratefully acknowledges his family for their constant support and their inspiration throughout the years. The author would like to thank Caroline Cox for her assistance in the editing and proofreading of the manuscript, as well as for her patience and faithful encouragements.

TABLE OF CONTENTS

	<u>Page</u>
ACKNOWLEDGMENTS	ii
LIST OF TABLES	vi
LIST OF FIGURES.....	vii
ABSTRACT.....	xiv
CHAPTERS	
1 INTRODUCTION	1
1.1 Heavy Fermion Systems	2
1.1.1 Heavy Fermion Compounds.....	2
1.1.2 Heavy Fermion Superconductors.....	3
1.2 Unconventional Superconductivity	6
1.2.1 Definition	6
1.2.2 Experimental Evidences for Unconventional Superconductivity.....	8
1.2.3 Unconventional Superconductivity in UPt ₃	11
2 OVERVIEW OF EXPERIMENTAL WORK -- UPt ₃ AND UBe ₁₃	14
2.1 Experimental Work -- UPt ₃	14
2.1.1 Crystal Structure	15
2.1.2 Specific Heat Measurements.....	15
2.1.3 Ultrasonic Studies.....	21
2.1.4 Phase Diagrams	22
2.1.5 Antiferromagnetism and Superconductivity.....	26
2.1.6 Structure Modifications and Superconductivity.....	28
2.1.7 Nuclear Magnetic Resonance and Muon Spin Relaxation Knight Shifts.....	29
2.1.8 Point Contact Spectroscopy.....	30
2.1.9 Concluding Remarks.....	31
2.2 Experimental Work -- UBe ₁₃	32
2.2.1 Crystal Structure	33
2.2.2 Specific Heat Measurements.....	33

2.2.3	Penetration Depth, Mean Free Path, and Coherence Length	36
2.2.4	Phase Diagrams	38
2.2.5	Nuclear Magnetic Resonance and Muon Spin Relaxation Knight Shifts.....	39
2.2.6	Anomaly Around 8 K.....	41
2.2.7	Thorium Doped UBe ₁₃ Experiments	42
2.2.8	Concluding Remarks.....	45
3	APPARATUS AND EXPERIMENTAL TECHNIQUES.....	46
3.1	Low Temperatures	46
3.1.1	Dilution Refrigerator	46
3.1.2	Thermometry.....	49
3.1.3	Temperature Control	57
3.2	ac Susceptibility	60
3.2.1	Hardware Used for the Mutual Inductance Technique.....	61
3.2.2	Principles of the Mutual Inductance Technique	64
3.2.3	Peak in $\chi''(T)$ in the Vicinity of T_c and in Zero dc Magnetic Field	72
3.3	Tunnel Diode Oscillators	77
3.3.1	Hardware Used for the Tunnel Diode Oscillator Technique	77
3.3.2	Tunnel Diode Oscillators and Penetration Depth.....	80
4	INDUCTIVE MEASUREMENTS -- UPt₃.....	85
4.1	Penetration Depth in Superconductors.....	85
4.1.1	Conventional Superconductors	85
4.1.2	Unconventional Superconductors.....	92
4.1.3	Motivation for Studying the Penetration Depth in Superconductors	95
4.2	Previous Work on the Penetration Depth of UPt ₃	95
4.2.1	dc Measurements.....	95
4.2.2	Radio Frequency Measurements	96
4.2.3	Muon Spin Relaxation Measurements	97
4.2.4	Motivation for Studying the Penetration Depth in UPt ₃	97
4.3	Sample Histories	98
4.3.1	Sample No. 1.....	98
4.3.2	Sample No. 2.....	100
4.3.3	Sample No. 3.....	104
4.3.4	Sample No. 4.....	104
4.3.5	Sample No. 5.....	108
4.3.6	Sample No. 6.....	108
4.4.7	Sample No. 7.....	108
4.4.8	Sample No. 8.....	108
4.4	Results	109
4.4.1	Mutual Inductance Results.....	109

4.4.2 Resonant Technique Results	132
4.5 Discussion.....	145
4.5.1 Linear Temperature Dependence of $\lambda(T)$	145
4.5.2 Quadratic Temperature Dependence of $\lambda(T)$	146
4.5.3 Double Feature Near T_c	147
4.5.4 High Frequency Effects.....	148
4.5.5 Upturn in $\chi'(T)$ for $B_{dc} \geq 1.2$ T	154
4.6 Conclusions.....	159
 5 INDUCTIVE MEASUREMENTS -- UBe ₁₃	160
5.1 Upper Critical Magnetic Fields in Superconductors	160
5.1.1 Type I, Type II, $B_{c1}(T)$ and $B_{c2}(T)$	160
5.1.2 $B_{c2}(T)$ for Type II Superconductors.....	161
5.2 Previous Work on the Upper Critical Field of UBe ₁₃	165
5.2.1 $B_{c2}(T)$ of Single Crystal UBe ₁₃	165
5.2.2 Anisotropy of $B_{c2}(T)$ for $T/T_c \rightarrow 1$	167
5.2.3 Our Motivation for Studying $B_{c2}(T)$ in UBe ₁₃	169
5.3 Sample Histories	169
5.4 Results	175
5.4.1 Normal State Susceptibility.....	175
5.4.2 Phase Diagrams	180
5.4.3 Temperature Dependence of the Penetration Depth.....	204
5.5 Discussion.....	222
5.5.1 Isotropic $B_{c2}(T)$ in the limit $T/T_c \rightarrow 1$	223
5.5.2 Anomaly in Sample No. 3	228
5.5.3 Temperature Dependence of the Penetration Depth.....	230
5.6 Conclusions.....	230
 6 CONCLUSIONS	233
6.1 UPt ₃	233
6.1.1 Conclusions.....	233
6.1.2 Future Work.....	234
6.2 UBe ₁₃	236
6.2.1 Conclusions.....	236
6.2.2 Future Work.....	237
 APPENDIX.....	238
 REFERENCES.....	242
 BIOGRAPHICAL SKETCH.....	256

LIST OF TABLES

<u>Tables</u>	<u>page</u>
1-1 Ground state of various heavy fermions systems.....	4
2-1 Summary of lattice parameters of UPt ₃	15
2-2 Summary of lattice parameters of UBe ₁₃	33
3-1 Diagnostic thermometers.....	51
3-2 Coefficients for LS-Burns, 350 mK ≤ T ≤ 2 K	55
3-3 Coefficients for LS-Burns, 2 K ≤ T ≤ 4.2 K.....	55
4-1 Predicted λ(T) for the axial state and the polar state	93
4-2 Characteristics of the eight UPt ₃ samples investigated in this work	99
4-3 Summary of λ(T) obtained from this work.....	144
5-1 Characteristics of the three UBe ₁₃ samples investigated in this work.....	170

LIST OF FIGURES

<u>Figure</u>	<u>page</u>
1-1 Definition of unconventional superconductivity	7
2-1 Atomic configuration in the hexagonal unit cell of UPt ₃	16
2-2 Specific heat of UPt ₃ in the vicinity of T _C	20
2-3 B-T phase diagram of UPt ₃ for the magnetic field parallel to the c-axis.....	24
2-4 B-T phase diagram of UPt ₃ for the magnetic field perpendicular to the c-axis	25
2-5 P-T phase diagram of UPt ₃	27
2-6 Crystal structure of UBe ₁₃	34
2-7 Upper critical field in UBe ₁₃ for a single crystal and a polycrystal	40
2-8 Superconducting T _C -x phase diagram for U _{1-x} Th _x Be ₁₃	43
3-1 Determination of the circulation rate of the dilution refrigerator.....	50
3-2 Calibration curve for thermometer No. 26	53
3-3 Calibration curve for thermometer LS-Burns.....	54
3-4 Magnetoresistance of RuO ₂ thick chip thermometer	56
3-5 Resistance of RuO ₂ thick chip thermometer mounted on the mixing chamber and on the cold finger.....	58

3-6	Circuit used for temperature control.....	59
3-7	Circuit used for the mutual inductance technique	62
3-8	Geometry and dimensions of coils used for the mutual inductance technique.....	63
3-9	χ' and χ'' as a function of r_s/δ for a normal metal	68
3-10	$\chi'(T)$ and $\chi''(T)$ for aluminum at 317 Hz	71
3-11	$\chi'(T)$ and $\chi''(T)$ for zinc at 317 Hz	72
3-12	$\chi'(T)$ and $\chi''(T)$ calculated for a normal metal exhibiting a sharp drop in resistivity.....	75
3-13	Circuit used for the tunnel diode oscillator technique.....	78
3-14	Typical I-V characteristic of tunnel diodes.....	79
3-15	TDO results on aluminum at 10 MHz.....	82
3-16	TDO results on zinc at 2 MHz.....	84
4-1	Temperature dependence from BCS in the local limit.....	90
4-2	SEM pictures of UPt ₃ sample No. 1	101
4-3	Resistivity as a function of T ² for UPt ₃ sample No. 1.....	102
4-4	Specific heat in the vicinity of T _c for UPt ₃ sample No. 1.....	103
4-5	SEM pictures of UPt ₃ sample No. 2	105
4-6	SEM pictures of UPt ₃ sample No. 3	106
4-7	SEM pictures of UPt ₃ sample No. 7	107

4-8	$\chi'(T)$ for unannealed and annealed UPt ₃ sample No. 1	111
4-9	$\chi'(T)$ in the vicinity of T _C for UPt ₃ sample No. 1.....	112
4-10	$\chi'(T)$ and $\chi''(T)$ for UPt ₃ sample No. 1, as grown.....	113
4-11	$\chi'(T)$ and $\chi''(T)$ for UPt ₃ sample No. 1, annealed, etched, unpolished.....	114
4-12	$\chi''(T)$ in the vicinity of T _C for UPt ₃ sample No. 1, before and after polishing	115
4-13	$\chi'(T)$ and $\chi''(T)$ for UPt ₃ sample No. 1, annealed, etched, polished.....	117
4-14	$\chi'(T)$ in the vicinity of T _C for UPt ₃ sample No. 1 for 48 Hz < f < 32 kHz.....	118
4-15	$\chi'(T=80\text{ mK}, 600\text{ mK})$ as a function of frequency for UPt ₃ sample No. 1 polished.....	119
4-16	B-T phase diagram for UPt ₃ sample No. 1, polished	121
4-17	$\chi'(T)$ for UPt ₃ sample No. 1, polished and with B < 0.5 T.....	122
4-18	$\chi'(T)$ for UPt ₃ sample No. 1, polished and with 1 T < B < 1.6 T	123
4-19	$\chi'(T)$ and $\chi''(T)$ for UPt ₃ sample No. 2.....	124
4-20	$\chi'(T)$ and $\chi''(T)$ for UPt ₃ sample No. 3.....	125
4-21	$\chi'(T)$ and $\chi''(T)$ for UPt ₃ sample No. 4.....	127
4-22	$\chi'(T)$ and $\chi''(T)$ for UPt ₃ sample No. 5.....	128
4-23	$\chi'(T)$ and $\chi''(T)$ for UPt ₃ sample No. 6.....	130
4-24	$\chi'(T)$ and $\chi''(T)$ for UPt ₃ sample No. 7.....	131
4-25	$\chi'(T)$ and $\chi''(T)$ for UPt ₃ sample No. 8.....	133

4-26	$[f(T_{\min}) - f(T)] / f(T_{\min})$ for UPt ₃ sample No. 1, annealed, etched, unpolished	134
4-27	$[f(T_{\min}) - f(T)] / f(T_{\min})$ for UPt ₃ sample No. 1, annealed, etched, polished	136
4-28	$[f(T_{\min}) - f(T)] / f(T_{\min})$ for UPt ₃ sample No. 2	137
4-29	$[f(T_{\min}) - f(T)] / f(T_{\min})$ for UPt ₃ sample No. 3	138
4-30	$[f(T_{\min}) - f(T)] / f(T_{\min})$ for UPt ₃ sample No. 4	140
4-31	$[f(T_{\min}) - f(T)] / f(T_{\min})$ for UPt ₃ sample No. 5	141
4-32	$[f(T_{\min}) - f(T)] / f(T_{\min})$ for UPt ₃ sample No. 6	142
4-33	$[f(T_{\min}) - f(T)] / f(T_{\min})$ for UPt ₃ sample No. 7	143
4-34	Inductive response in the vicinity of T _c for UPt ₃ sample No. 2 and for low and high frequencies.....	150
4-35	$[f(T_{\min}) - f(T)] / f(T_{\min})$ for UPt ₃ sample No. 1, annealed, etched, polished at 6 MHz and 33 MHz	153
4-36	Upturn in $\chi'(T)$ for UPt ₃ sample No. 1 and B _{dc} = 1.4 T	155
4-37	Upturn in $\chi'(T)$ sample No. 1 and B _{dc} = 1.2 T and B _{dc} = 1.4 T.....	158
5-1	Upper critical field of niobium	163
5-2	Upper critical field of a UBe ₁₃ single crystal	166
5-3	Anisotropy of B _{C2} (T) in UBe ₁₃	168
5-4	SEM pictures of UBe ₁₃ sample No. 1	171
5-5	SEM pictures of UBe ₁₃ sample No. 2	172

5-6	SEM pictures of UBe ₁₃ sample No. 3	173
5-7	SEM pictures of UBe ₁₃ sample No. 3, after polishing	174
5-8	$\chi'(T)$ for UBe ₁₃ sample No. 1, in the normal state.....	176
5-9	$\chi'(T)$ for UBe ₁₃ sample No. 2, in the normal state.....	177
5-10	$\chi'(T)$ for UBe ₁₃ sample No. 3, in the normal state.....	178
5-11	$\chi'(T)$ in the vicinity of T_C , for UBe ₁₃ sample No. 1, $\mathbf{B}_{dc} \parallel [100]$, with $B_{dc} \leq 0.5$ T.....	181
5-12	$\chi'(T)$ in the vicinity of T_C , for UBe ₁₃ sample No. 1, $\mathbf{B}_{dc} \parallel [110]$, with $B_{dc} \leq 0.5$ T.....	182
5-13	$\chi'(T)$ in the vicinity of T_C , for UBe ₁₃ sample No. 2, $\mathbf{B}_{dc} \parallel [100]$, with $B_{dc} \leq 0.5$ T.....	183
5-14	$\chi'(T)$ in the vicinity of T_C , for UBe ₁₃ sample No. 2, $\mathbf{B}_{dc} \parallel [110]$, with $B_{dc} \leq 0.5$ T.....	184
5-15	$\chi'(T)$ in the vicinity of T_C , for UBe ₁₃ sample No. 3, $\mathbf{B}_{dc} \parallel [100]$, with $B_{dc} \leq 0.5$ T.....	185
5-16	$\chi'(T)$ in the vicinity of T_C , for UBe ₁₃ sample No. 3, $\mathbf{B}_{dc} \parallel [110]$, with $B_{dc} \leq 0.5$ T.....	186
5-17	$\chi'(T)$ in the vicinity of T_C , for UBe ₁₃ sample No. 1, $\mathbf{B}_{dc} \parallel [100]$, with $1\text{ T} \leq B_{dc} \leq 8\text{ T}$	187
5-18	$\chi'(T)$ in the vicinity of T_C , for UBe ₁₃ sample No. 1, $\mathbf{B}_{dc} \parallel [110]$, with $1\text{ T} \leq B_{dc} \leq 8\text{ T}$	188
5-19	$\chi'(T)$ in the vicinity of T_C , for UBe ₁₃ sample No. 2, $\mathbf{B}_{dc} \parallel [100]$, with $1\text{ T} \leq B_{dc} \leq 8\text{ T}$	189
5-20	$\chi'(T)$ in the vicinity of T_C , for UBe ₁₃ sample No. 2, $\mathbf{B}_{dc} \parallel [110]$, with $1\text{ T} \leq B_{dc} \leq 8\text{ T}$	190
5-21	$\chi'(T)$ in the vicinity of T_C , for UBe ₁₃ sample No. 3, $\mathbf{B}_{dc} \parallel [100]$, with $1\text{ T} \leq B_{dc} \leq 7.5\text{ T}$	191

5-22	$\chi'(T)$ in the vicinity of T_C , for UBe ₁₃ sample No. 3, $\mathbf{B}_{dc} \parallel [110]$, with $1 \text{ T} \leq B_{dc} \leq 7.5 \text{ T}$	192
5-23	$\chi'(T)$ in the vicinity of T_C , for UBe ₁₃ sample No. 1, $\mathbf{B}_{ac} \parallel [100]$, for two different runs.....	194
5-24	Complete B-T phase diagram for UBe ₁₃ sample No. 1.....	195
5-25	Complete B-T phase diagram for UBe ₁₃ sample No. 2.....	196
5-26	B-T phase diagram for UBe ₁₃ sample No. 3	197
5-27	$\chi'(B)$ and $\chi''(B)$ for UBe ₁₃ sample No. 1, for $T = 200 \text{ mK}$ and $T = 600 \text{ mK}$	199
5-28	$\chi'(B)$ and $\chi''(B)$ for UBe ₁₃ sample No. 2, for $T = 500 \text{ mK}$	200
5-29	$\chi'(B)$ and $\chi''(B)$ for UBe ₁₃ sample No. 3, $\mathbf{B}_{dc} \parallel [100]$, for $T = 100 \text{ mK}$	201
5-30	$\chi'(B)$ and $\chi''(B)$ for UBe ₁₃ sample No. 3, $\mathbf{B}_{dc} \parallel [100]$, for $T = 175 \text{ mK}$	202
5-31	$\chi'(B)$ and $\chi''(B)$ for UBe ₁₃ sample No. 3, $\mathbf{B}_{dc} \parallel [100]$, for $T = 250 \text{ mK}$	203
5-32	$\chi'(B)$ and $\chi''(B)$ for UBe ₁₃ sample No. 3, $\mathbf{B}_{dc} \parallel [100]$, for $T = 400 \text{ mK}$	205
5-33	$\chi'(T)$ for UBe ₁₃ sample No. 3, $\mathbf{B}_{dc} \parallel [100]$, for $B_{dc} = 3 \text{ T}$	206
5-34	$\chi'(B)$ and $\chi''(B)$ for UBe ₁₃ sample No. 3, $\mathbf{B}_{dc} \parallel [110]$, for $T = 100 \text{ mK}$	207
5-35	$\chi'(B)$ and $\chi''(B)$ for UBe ₁₃ sample No. 3, $\mathbf{B}_{dc} \parallel [110]$, for $T = 250 \text{ mK}$	208
5-36	$\chi'(B)$ and $\chi''(B)$ for UBe ₁₃ sample No. 3, $\mathbf{B}_{dc} \parallel [110]$, for $T = 400 \text{ mK}$	209
5-37	$\chi'(T)$ for UBe ₁₃ sample No. 3, $\mathbf{B}_{dc} \parallel [110]$, for $B_{dc} = 3 \text{ T}$	210
5-38	$\chi'(T)$ for UBe ₁₃ sample No. 3, $\mathbf{B}_{dc} \parallel [110]$, for $B_{dc} = 2 \text{ T}$	211

5-39	$\chi'(T)$ for UBe ₁₃ sample No. 3, $\mathbf{B}_{dc} \parallel [110]$, for $B_{dc} = 1$ T	212
5-40	$\chi'(T)$ for UBe ₁₃ sample No. 3, $\mathbf{B}_{dc} \parallel [110]$, for $B_{dc} = 0.5$ T	213
5-41	$\chi'(T)$ for UBe ₁₃ sample No. 3, $\mathbf{B}_{ac} \parallel [110]$, for $B_{dc} = 0$ T.....	214
5-42	Complete B-T phase diagram for UBe ₁₃ sample No. 3.....	215
5-43	$\chi'(T)$ for UBe ₁₃ sample No. 1, $\mathbf{B}_{ac} \parallel [100]$, in the superconducting state	216
5-44	$\chi'(T)$ for UBe ₁₃ sample No. 1, $\mathbf{B}_{ac} \parallel [100]$, $T/T_c \leq 0.5$	217
5-45	$\chi'(T)$ for UBe ₁₃ sample No. 1, $\mathbf{B}_{ac} \parallel [110]$, in the superconducting state	218
5-46	$\chi'(T)$ for UBe ₁₃ sample No. 1, $\mathbf{B}_{ac} \parallel [110]$, $T/T_c \leq 0.5$	219
5-47	$\chi'(T)$ for UBe ₁₃ sample No. 3, $\mathbf{B}_{ac} \parallel [100]$, in the superconducting state	220
5-48	$\chi'(T)$ for UBe ₁₃ sample No. 3, $\mathbf{B}_{ac} \parallel [100]$, $T/T_c \leq 0.5$	221
5-49	Effect of demagnetization factor on $B_{c2}(T)$	227
5-50	Phase diagram of UBe ₁₃ propoed by Ellman <i>et al.</i> (1991).....	231

Abstract of Dissertation Presented to the Graduate School
of the University of Florida in Partial Fulfillment of the
Requirements for the Degree of Doctor of Philosophy

INDUCTIVE MEASUREMENTS OF HEAVY FERMION SUPERCONDUCTORS

By

PHILIPPE J.-C. SIGNORE

December, 1994

Chairman: Mark W. Meisel
Major Department: Physics

Experimental results are presented on the temperature dependence of the penetration depth, $\lambda(T)$, in UPt_3 , and on the upper critical field, $B_{c2}(T)$, of UBe_{13} . The objective of this work was to obtain a better understanding of the unusual superconductivity in these materials.

The inductive response of eight UPt_3 samples obtained from seven different materials fabrication groups was measured from 50 to 700 mK at frequencies varying between 32 Hz and 33 MHz. The low frequency (≤ 4.7 kHz) data suggest a linear temperature dependence of $\lambda(T/T_c \leq 0.5)$ for the samples possessing a double feature near the superconducting transition temperature, T_c . We have verified that this double feature present in $\lambda(T)$ for some of the samples corresponds to the double jump observed in the specific heat. On the other hand, $\lambda(T/T_c \leq 0.5)$ was found to have a quadratic temperature dependence for unannealed specimens which exhibit only a single transition at T_c . The linear temperature dependence in $\lambda(T)$ is consistent with the presence of line nodes in the basal plane, while the quadratic dependence found for other samples indicate

that impurity scattering dominates in these specimens. The double transition in $\lambda(T)$ has been studied in magnetic fields up to 1.6 T for one of the specimens, and the resulting phase diagram is consistent with the one constructed from thermodynamical measurements. The high frequency (≥ 3 MHz) data suggest $\lambda(T/T_C \leq 0.5) \propto T^\eta$, where $2 \leq \eta \leq 4$. The possible origins of the frequency dependence of $\lambda(T)$ are discussed, as well as the effect of the surface quality on η .

Using sensitive mutual induction techniques, we have systematically measured $B_{c2}(T)$ for three UBe₁₃ single crystals in fields up to 8 T oriented along the [100] and [110] directions, with particular emphasis on the region near the zero field critical temperature. In that low field regime and within our experimental uncertainties of 0.5 mK and 0.5 mT, no anisotropy in $B_{c2}(T)$ was observable for any of the samples. For one of these specimens, an anomaly in $\chi'(B,T)$ was observed below the superconducting transition. The complete $B_{c2}(T)$ phase diagrams are presented and compared to the results of other workers. The temperature dependence of the penetration depth down to 50 mK and in zero field is measured on two of the crystals.

CHAPTER 1

INTRODUCTION

One of the exciting challenges in condensed matter physics is the search for evidence of superconducting phases whose theoretical descriptions deviate from the conventional Bardeen-Cooper-Schrieffer (BCS) model. Due to the great number of unusual properties they exhibit, heavy fermion (and high temperature) superconductors are considered good candidates for being non-BCS-like superconductors, and are often referred to as "unconventional superconductors." In section 1.2, the meaning of "unconventional superconductivity" will be more precisely defined. Prior to this discussion, the seven heavy fermion superconductors known to date, along with several other heavy fermion systems, are overviewed in section 1.1. The rest of the dissertation is outlined as follows. Chapter 2 reviews the experimental work already published on UPt_3 and UBe_{13} . These two materials are the focus of this dissertation. Because of their rather low critical temperatures, T_c , ($T_c \approx 0.5$ K for UPt_3 and $T_c \approx 0.9$ K for UBe_{13}), our experiments utilized several standard low temperature physics tools, which are described in Chapter 3, along with the details of our measuring techniques. Our results on UPt_3 are presented and discussed in Chapter 4. Our study of UPt_3 centered around measuring the temperature dependence of the penetration depth, $\lambda(T)$, which is a measure of the superconducting electron density. The motivation behind these measurements is established in section 4.1. Chapter 5 treats the UBe_{13} experiments, which were concentrated around measuring the upper critical field, $B_{c2}(T)$, in the low field region ($B \leq 0.5$ T), in an effort to search for crystalline anisotropy of $B_{c2}(T)$ that would suggest the existence of an anisotropic order parameter. The motivation behind these

measurements is given in section 5.1. Finally, the conclusions of this work are summarized in Chapter 6, where future directions are also suggested.

1.1 Heavy Fermion Systems

Heavy fermion compounds are characterized by a large specific heat electronic coefficient, γ , compared to ordinary metals, such as lead ($\gamma \approx 10 \text{ mJ/(K}^2\text{ mole)}$). As will be shown in subsection 2.1.2.a, within the Fermi liquid theory, γ is directly proportional to the density of states per unit volume at the Fermi surface, which, in turn, is proportional to the effective mass, m^* , of the quasiparticles. Therefore, a large γ is indicative of a large m^* , justifying the designation of the materials as heavy fermion (or electron) systems. Although the absolute definition of a "heavy" fermion compound is not clear cut, a material with $m^* \geq 100 m_e$, where m_e is the mass of the bare electron, is usually considered a heavy fermion system. In subsection 1.1.1, a brief description of the heavy fermion state is given, in addition to examples of heavy fermion compounds. For a more comprehensive discussion of the heavy fermion state, see, for example, Stewart (1984), Lee *et al.* (1986), Ott (1987), Sigrist and Ueda (1991), Grewe and Steglich (1991), Steglich *et al.* (1992), and Proceedings of the International Conference on Magnetism (1992).

1.1.1 Heavy Fermion Compounds

Heavy fermion compounds contain lanthanide (predominantly Ce) or actinide (predominantly U) ions, that possess an unfilled electronic f -shell, which gives rise to a magnetic moment at the ion site. Above a characteristic temperature, referred to as T^* (typically of the order of tens of kelvin), the systems can be described best by conduction electrons with conventional masses moving through a lattice of well localized magnetic moments. This picture is supported, for example, by a Curie-Weiss type susceptibility, which is consistent with a set of noninteracting local moments. Below T^* , by a

mechanism that is not yet fully understood, but most likely related to the interaction between the "light" conduction electrons and the localized f -electrons, the system loses its local moments and the f -electrons become part of the Fermi surface. The system is then described best as a Fermi liquid with an enhanced effective mass, *i.e.* linear specific heat with a large γ and a temperature independent Pauli spin susceptibility. One of the experimental results that has motivated a great deal of research on these materials is the puzzling fact that heavy fermion systems possess a wide variety of possible ground states, some of which are listed in Table 1-1. In the next subsection, we take a closer look at the heavy fermion systems possessing a superconducting ground state.

1.1.2 Heavy Fermion Superconductors

The first report of superconductivity in a heavy fermion compound was published by Steglich *et al.* (1979), who reported resistivity, ac susceptibility, dc Meissner effect and specific heat measurements in CeCu_2Si_2 consistent with a superconducting transition around 0.65 K. This result was somewhat of a surprise since rare earth ions (Ce), through their $4f$ electron magnetic moments, were known to break the superconducting paired electrons. For example, the transition temperature of LaAl_2 is suppressed when doped with Ce ions. Another unexpected result was that, while CeCu_2Si_2 was superconducting, LaCu_2Si_2 was not. Since the only difference between the two compounds is the $4f$ electrons at each Ce site for CeCu_2Si_2 , it became evident that these electrons played a key role in generating the superconductivity. This evidence is further supported by the large jump in the specific heat at the transition temperature.

The second heavy fermion superconductor to be discovered was UBe_{13} (Ott *et al.*, 1983). A review of the experimental results reported for this material is given in section 2.2. One aspect that sets this material apart from the other heavy fermion superconductors (except for Th doped UBe_{13}) is its cubic crystal structure. Because of this higher symmetry, anisotropies in the normal state properties are minimized, and this

Table 1-1 Ground state of various heavy fermion systems, as determined experimentally. Values for γ are given in (mJ/K² mole).

Compounds	Ground State	Ordering Temperature	γ	References
CeCu ₆	Paramagnet	no spontaneous ordering $T > 3$ mK	1300	Satoh <i>et al.</i> (1988) Jin <i>et al.</i> (1991)
CeRu ₂ Si ₂	Paramagnet	no spontaneous ordering $T > 40$ mK	600	Gupta <i>et al.</i> (1983) Steglich (1985)
UCd ₁₁	Antiferromagnet	$T_N \approx 5.0$ K	840	Fisk <i>et al.</i> (1984)
NpBe ₁₃	Antiferromagnet	$T_N \approx 3.4$ K	900	Stewart <i>et al.</i> (1984a)
U ₂ Zn ₁₇	Antiferromagnet	$T_N \approx 9.7$ K	550	Ott <i>et al.</i> (1984a)
CeCu ₂ Si ₂	Superconductor	$T_c \approx 0.65$ K	1000	Steglich <i>et al.</i> (1979)
UBe ₁₃	Superconductor	$T_c = 0.9$ K	1100	See section 2.2
U _{1-x} Th _x Be ₁₃	Antiferromagnet & Superconductor	$T_c \approx 0.6$ K $T_N \approx 0.4$ K	2300 (x = 3%)	See section 2.2.7
UPt ₃	Antiferromagnet & Superconductor	$T_N \approx 5.0$ K $T_c \approx 0.5$ K	430	See section 2.1
URu ₂ Si ₂	Antiferromagnet & Superconductor	$T_N \approx 17.0$ K $T_c \approx 1.5$ K	180	Palstra <i>et al.</i> (1985)
UNi ₂ Al ₃	Antiferromagnet & Superconductor	$T_N \approx 4.6$ K $T_c \approx 1.0$ K	120	Geibel <i>et al.</i> (1991b)
UPd ₂ Al ₃	Antiferromagnet & Superconductor	$T_N \approx 14.0$ K $T_c \approx 2.0$ K	150	Geibel <i>et al.</i> (1991a)
Ce ₃ Bi ₄ Pt ₃	Semiconductor	Gap ≈ 35.0 K	75	Hundley <i>et al.</i> (1990)
CeNiSn	Semiconductor	Gap ≈ 6.0 K	210	Takabatake <i>et al.</i> (1990)

fact facilitates the study of the anisotropies of the superconducting properties. As will be discussed in section 1.2, measurements of the anisotropy of the superconducting properties can lead to the determination of the symmetry of the superconducting order parameter, which establishes whether or not a superconductor is conventional or unconventional. In fact, measurements of the anisotropy in the upper critical field are central to our experiments on UBe₁₃, which are presented and discussed in Chapter 5.

Another interesting compound is U_{1-x}Th_xBe₁₃. For $0.019 < x < 0.045$, this material exhibits a superconducting transition around 0.6 K, followed by a second transition (Ott *et al.*, 1984b). The nature of this second transition is controversial, although muon spin relaxation data suggest magnetic ordering (Heffner *et al.*, 1990). A brief discussion of this heavy fermion system is given in subsection 2.2.7.

The next heavy fermion superconductor to be discovered was UPt₃ (Stewart *et al.*, 1984b). For the past decade, this system seems to have become the most studied heavy fermion compound. Its unusual superconducting phase diagram, and the occurrence of power law dependences for various thermodynamic properties at low temperatures have made this material the best candidate for unconventional superconductivity. In fact, one of the main results from our experiments on UPt₃, namely the linear temperature dependence of the penetration depth (see Chapter 4), offers a strong piece of evidence for non-BCS-like superconductivity. A review of the experimental results reported on UPt₃ is given in section 2.1, and two (of the many) theoretical descriptions proposed for UPt₃ are discussed in subsection 1.2.3.

The three other heavy fermion superconductors listed in Table 1-1, namely URu₂Si₂, UNi₂Al₃, and UPd₂Al₃, have a common feature of possessing a relatively low specific heat electronic coefficient, $\gamma < 200 \text{ mJ} / (\text{K}^2 \text{ mole})$, and are sometimes referred to as semi-heavy fermion materials. In addition, all three exhibit, above the superconducting transition, an unambiguous antiferromagnetic ordering, identified via neutron experiments (Broholm *et al.*, 1987; Schröder *et al.*, 1994; Kita *et al.*, 1994) and

also observed in specific heat and susceptibility data (Palstra *et al.*, 1985; Geibel *et al.* 1991a, 1991b). This relative ease in observing the signature of the antiferromagnetic transition is not shared with UPt₃, where the antiferromagnetic transition around 5 K has only been observed through neutron scattering and muon spin relaxation experiments (see section 2.1.5).

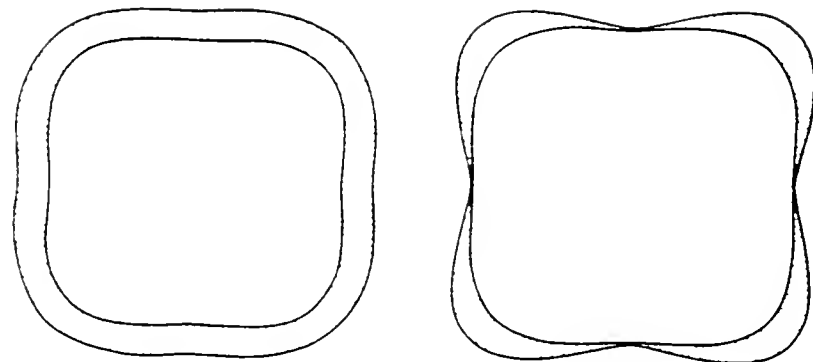
1.2 Unconventional Superconductivity

In this section, the definition of the term "unconventional superconductivity" is given (subsection 1.2.1), followed by a discussion of various experimental signatures expected from unconventional superconductors (subsection 1.2.2). In subsection 1.2.3, two of the theoretical "unconventional" models, proposed to describe superconductivity in UPt₃, are discussed.

1.2.1 Definition

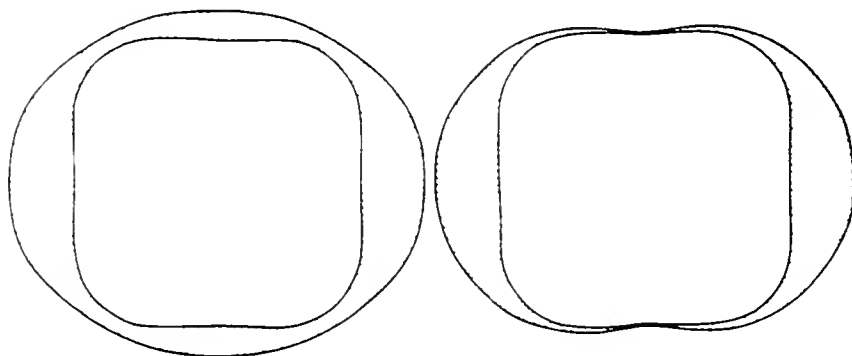
The term "unconventional superconductivity" is often associated with the presence of an anisotropy in the energy gap and/or the presence of nodes in the energy gap structure. As will be shown below, these two conditions are not appropriate criteria for unconventionality.

The definition that we adopt has been given, among others, by Rainer (1988) and Fulde, Keller, and Zwicknagl (1988), who stated that the symmetry of the energy gap (or order parameter) of an *unconventional* superconductor is lower than the symmetry of the Fermi surface (or underlying crystal). This definition has been widely adopted by many in the field, for example Choi and Sauls (1991), and Sauls (1994a). The concept is illustrated in Fig. 1-1. In this figure, a cubic crystal structure is assumed. Clearly, the Fermi surfaces in drawings (a) and (b) have the same symmetry as the energy gap, *i.e.* a $\pi/2$ rotation gives the same picture. However, the energy gaps in drawings (c) and (d)



(a)

(b)



(c)

(d)

Fig. 1-1. Examples of conventional superconductors (a) and (b) : the Fermi surfaces (inner lines) have the same symmetries as the energy gaps (outer lines). Examples of unconventional superconductors (c) and (d) : the Fermi surfaces (inner lines) have higher symmetries than the energy gaps (outer lines). Drawings are from Fulde, Keller, and Zwicknagl (1988).

have lower symmetries than the Fermi surfaces, so that a $\pi/2$ rotation gives the same Fermi surface, but not the same gap.

A different definition of unconventional superconductivity that is sometimes put forward is related to the nature of the pairing interaction. In this case, phonon mediated pairing is considered as conventional, while any other pairing mechanisms are unconventional.

A third definition sometimes found is the statement that superconductors exhibiting anisotropic properties are unconventional. A caveat associated with this assertion is the fact that conventional superconductors also possess anisotropic properties, for example Nb and V have upper critical fields with orientation dependences, which are non-negligible at higher fields (Williamson, 1970; Butler, 1980). These anisotropies are caused by Fermi surfaces of cubic symmetry (non-spherical).

For the purposes of this dissertation, we chose to use the definition given by Rainer (1988) and Fulde, Keller, and Zwicknagl (1988). Given this definition, the type of experimental results that can be taken as evidence for unconventional superconductivity need to be discussed.

1.2.2 Experimental Evidence for Unconventional Superconductivity

1.2.2.a Multiple phase diagrams

It is well known that the magnetic field - temperature, B-T, phase diagram of a conventional type I superconductor exhibits one phase (the Meissner state), while the B-T phase diagram of a conventional type II superconductor features a Meissner state plus a vortex lattice state (Tinkham, 1975). One of the most convincing experimental results, that can be put forward as a signature of unconventionality, is a superconducting state possessing additional phases. For example, superfluid ^3He , the only unambiguous unconventional superfluid known to date, exhibits an A-phase and a B-phase in zero field and an additional A_1 phase in a magnetic field (see, for example, Tilley and Tilley, 1990).

The existence of these multiple phases is related to the fact that the Cooper pairs in ${}^3\text{He}$ are in a triplet ($S = 1$, where S is the spin angular momentum of the Cooper pair) and a p-wave ($L = 1$, where L is the orbital angular momentum of the Cooper pair) state, which implies several possible superfluid phases (Vollhardt and Wölfle, 1990). As can be expected, the two phases with lowest energy are observed in zero field. In comparison, a superconductor, whose Cooper pairs are in a singlet ($S = 0$) and an s-wave ($L = 0$) state, has only one zero field phase. On the other hand, a superconductor in a singlet and d-wave ($L = 2$) state possesses several zero field superconducting phases. When ${}^3\text{He}$ goes from one phase to the other, the transition can be observed, for example, with specific heat measurements. For instance, at constant pressure, specific heat data show two transitions, one between the normal fluid and the A-phase, and one between the A-phase and the B-phase (Halperin *et al.*, 1976). Similar double transitions in the specific heat have also been observed in UPt_3 . In fact, various techniques (such as specific heat, ultrasonic attenuation, thermal expansion) probing the magnetic field-temperature-pressure phase diagram of UPt_3 have revealed the existence of at least four different superconducting phases (see section 2.1.4). Of all undoped heavy fermion superconductors, such a multiple superconducting phase diagram has only been reported for UPt_3 .

1.2.2.b Power law temperature dependences

A second hint for unconventionality is the non-exponential temperature dependence of various properties, such as specific heat, ultrasonic attenuation, and penetration depth. A conventional superconductor possesses a finite energy gap surrounding its entire Fermi surface, so that the thermally activated quasiparticles lead to an exponential temperature dependence of various properties such as specific heat, penetration depth, and ultrasonic attenuation. On the other hand, if the energy gap goes to zero somewhere on the Fermi surface, then the properties related to the excitation spectrum will follow power laws. At sufficiently low temperatures, the exponent of the power laws depends on the types of nodes (lines or points) and on the manner in which the

gap goes to zero (linearly or quadratically). Several of the heavy fermion superconductors exhibit such power law dependences. For example, as discussed in subsection 2.2.2, the specific heat of UBe₁₃ follows a $T^{-2.75 \pm 0.25}$ dependence, and the penetration depth of UPt₃, discussed in detail in Chapter 4, is linear in temperature. The observation of non-exponential temperature dependences is therefore often taken as evidence for unconventional superconductivity. As an aside, we note that in Fig. 1.1, a conventional superconductor with nodes in its energy gap structure is shown schematically. This condition is theoretically possible, but in reality, no such material has been identified. Although for some superconductors the gap is reduced along a particular direction, it never actually goes to zero, with the exception of a few two-dimensional systems (e.g. some organic and high temperature superconductors).

1.2.2.c Anisotropic properties

A third experimental clue for unconventional superconductivity is a strong anisotropy in the superconducting properties. For example, measuring the angular dependence of the slope of the upper critical field, $B_{c2}(T)$, as $T/T_c \rightarrow 1$ has been considered a "crucial" test for unconventional superconductivity (Gor'kov, 1987; Rainer, 1988). Of course, all solids have a crystal structure and therefore a non-spherical Fermi surface, so that an energy gap of the same symmetry as the Fermi surface (conventional) is never isotropic. However, in numerous metals, the anisotropy of the Fermi surface is rather small, so that conventional superconducting properties are usually isotropic. For that reason, large anisotropies, not accounted for by the anisotropy in the normal state properties, are usually taken as evidence for unconventional superconductivity. A typical example is the ultrasonic attenuation in UPt₃ discussed in subsection 2.1.3. However, it should be emphasized, that when suggesting unconventionality on the basis of anisotropic properties, one has to check first that the orientation dependence is not simply related to Fermi surface effects. This test is not always feasible if the Fermi surface is not well characterized.

A special case is the upper critical field as $T/T_c \rightarrow 1$ which is always isotropic for conventional superconductors with a cubic crystallographic symmetry. Therefore, observing an angular dependence in $B_{c2}(T/T_c \rightarrow 1)$ for UBe₁₃ (cubic) would provide strong evidence for unconventional superconductivity in this material, while an isotropic behavior would be an inconclusive result. Our measurements of $B_{c2}(T)$ in UBe₁₃ are discussed in detail in Chapter 5.

1.2.2.d Concluding remarks

Very few experimental measurements offer unambiguous proof for unconventional superconductivity. The three tests just discussed only give suggestive evidence. However, if an overwhelming majority of experimental results are consistent with unconventionality, then one can legitimately believe in unconventional superconductivity for a particular material, such is the case for UPt₃. Other experimental measurements, such as photo-emission spectroscopy, Josephson junction tunneling (Tsuei *et al.* 1994), or non-linear Meissner effect (see section 6.1.2), have been proposed to directly test the conventionality of superconductors. On the other hand, these experiments are usually technically difficult, and can still lead to ambiguous results (Rainer 1988).

1.2.3 Unconventional Superconductivity in UPt₃

Several theoretical models have been proposed for UPt₃ (see, for example, Blount *et al.*, 1990; Joynt *et al.*, 1990; Machida and Ozaki, 1991; and Chen and Garg, 1993), and in this section, we treat two of them (Sauls, 1994a and 1994b; Putikka and Joynt, 1989). The states that are briefly reviewed here, and that lead to unconventional superconductivity as defined in subsection 1.2.1, are two of the most successful in accounting for the various experimental results found in UPt₃, and for this reason, they have become two of the most popular.

The two states reviewed here, named E_{2u} and E_{1g}, represent two of the basis functions of the irreducible representations of the symmetry group for hexagonal crystals.

These basis functions, which were established for various symmetry groups by Volovik and Gor'kov (1985), correspond to the superconducting phases that can form at the transition temperature (Yip and Garg, 1993). This approach is only valid if spin-orbit coupling is strong, so that the electron spins are "frozen in the lattice," *i.e.* the rotations of the crystal also rotate the order parameter (Volovik and Gor'kov, 1985). It turns out that for the hexagonal symmetry, the basis functions can be divided into two categories. The first includes the wavefunctions that transform into themselves under all symmetry operations and are nondegenerate. These functions are called one-dimensional and are labeled by A (even), and B (odd). The second includes wavefunctions that require a linear combination of two basis functions in order to transform under symmetry operations. These functions, which have a degeneracy of two, are called two-dimensional, 2D, and are denoted by E_u (even) and E_g (odd). The E_{2u} wavefunction refers to a triplet state, while E_{1g} refers to a singlet state.

Both of these 2D models exhibit only one phase transition in zero field. In order to be consistent with the double transition observed experimentally in UPt_3 , they require a symmetry breaking field to lift the degeneracy. Such a symmetry breaking perturbation may originate from the antiferromagnetic ordering at higher temperature (Aeppli *et al.*, 1988), or possibly from another mechanism such as the structure modulation reported by Midgley *et al.* (1993).

Another similarity shared by these two states is that they both lead to gap structures with line nodes in the basal plane. This feature is important since a number of experimental works, including the data presented in Chapter 4, suggest the presence of such nodes for UPt_3 .

The two models differ on two important points. First, the E_{2u} can account for a tetracritical point in the magnetic field-temperature diagram, while the E_{1g} cannot (Sauls, 1994a, 1994b). Although the presence of a tetracritical point has not been established experimentally with certitude, at least for all orientations of the field (Adenwalla *et al.*,

1990), the inability of the E_{1g} wavefunction to account for this possibility has been considered a major obstacle for this state in describing UPt₃. The second difference between the two states is that while the E_{2u} wavefunction can explain the observed anisotropy of the upper critical field in terms of anisotropic Pauli limiting, the singlet E_{1g} state cannot. Although more experiments are needed to determine with confidence the nature of the superconducting state in UPt₃, the E_{2u} state seems to be a good candidate. In Chapter 6, several future experimental tests are proposed to answer this issue.

CHAPTER 2

OVERVIEW OF EXPERIMENTAL WORK -- UPt₃ AND UBe₁₃

In this chapter, the major experimental results involving UPt₃ and UBe₁₃ are reviewed. Emphasis is placed on the measurements directly related to the superconducting state, although some normal state results are discussed as well. One can consult the numerous reviews available in the literature for a more exhaustive summary (Stewart, 1984; de Visser *et al.*, 1987a, 1987b; Fisk *et al.*, 1986, 1988, 1993; Ott, 1987; Taillefer *et al.*, 1990; von Löhneysen, 1994).

2.1 Experimental work-- UPt₃

Superconductivity in UPt₃ was discovered by Stewart *et al.* (1984b) who reported resistivity, specific heat, and susceptibility measurements consistent with a superconducting transition around 0.5 K. This discovery sparked great excitement for the experimental and theoretical study of this material. For the past decade, several experimental findings have established various unusual phenomena related to the superconducting state of UPt₃, suggesting that this material is a non-BCS-like superconductor.

In the next subsections, the aforementioned results are presented and compared to the behavior expected for a BCS superconductor. Measurements of the penetration depth are reviewed in detail in Chapter 4 and are not discussed here. After a review of the crystal structure in UPt₃, normal and superconducting state specific heat measurements are presented and followed by a brief summary of ultrasonic studies. The all important phase diagrams are then reviewed prior to a discussion of two possible symmetry breaking fields, namely antiferromagnetism and structure modulations. Two short status reports on

the Knight shift measurements and point contact spectroscopy results are then given. Brief conclusions mark the end of the section.

2.1.1 Crystal Structure

UPt₃ has a hexagonal closed-packed (hcp) structure, with two formula units in the primary cell (Heal and Williams, 1955). Figure 2-1 shows a schematic representation of the atomic configuration in the hexagonal unit cell. Many measurements on UPt₃ are taken with respect to two principal symmetries which are defined by the c-axis and the basal plane, respectively. The lattice constant and other crystallographic parameters are summarized in Table 2-1.

Table 2-1. Summary of lattice parameters of UPt₃. Values for a and b are from Chen *et al.* (1984).

a (Å)	c (Å)	c/a	Volume of unit cell Ω_m (m ³)	Mol. weight M (kg)	Density ρ (kg/m ³)	T _{melt} (C)
5.764	4.899	0.850	1.41×10^{-28}	0.8233	1.94×10^4	1700

2.1.2 Specific Heat Measurements

Historically, normal state specific heat measurements played an important role in the understanding of UPt₃. In this subsection, these measurements are considered first and are followed by a survey of results obtained in the superconducting state.

2.1.2.a Normal state

Between 1 K and 20 K, the specific heat as a function of temperature, c(T), can be fitted to the expression (Stewart *et al.* 1984b; de Visser *et al.*, 1984; Frings *et al.* 1985; Brodale *et al.* 1986)

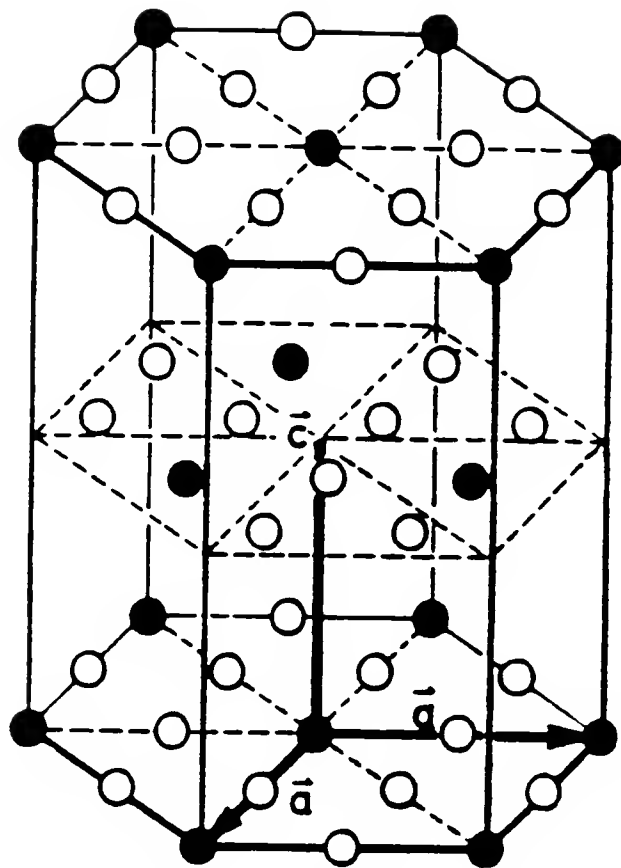


Fig. 2-1. Atomic configuration in the hexagonal unit cell of UPt₃. The a , b , and c vectors define the primary cell, and their values are given in Table 2-1. This figure was taken from de Visser *et al.* (1987b).

$$c(T) = \gamma T + \beta T^3 + \delta T^3 \ln(T / T_{SF}). \quad (2.1)$$

The first term, γT , corresponds to the electronic contribution. The linear coefficient, γ , is related to the density of states per unit volume at the Fermi surface, $N(\varepsilon_F)$, by

$$\gamma = \frac{\pi^2}{3} k_B^2 N(\varepsilon_F), \quad (2.2)$$

where k_B is the Boltzmann constant (Ashcroft and Mermin, 1976). For a Fermi liquid, $N(\varepsilon_F)$ is given by

$$N(\varepsilon_F) = \frac{4 m^* k_F}{\hbar^2}, \quad (2.3)$$

where k_F is the Fermi wave vector, m^* is the effective mass of the electrons (quasiparticles), and \hbar is Plank's constant. The Fermi wave vector can be estimated for UPt₃ by assuming three *f*-electrons per U-atom, or six per unit cell ($Z = 6$), contribute to the itinerant band and by using the following expression for a spherical Fermi surface,

$$k_F = \left[\frac{3 \pi^2 Z}{\Omega_m} \right]^{1/3}. \quad (2.4)$$

From the value of Ω_m given in Table 2-1, one finds $k_F \approx 1.08 \times 10^{10} \text{ m}^{-1}$. Substituting Eqs. (2.3) and (2.4) into Eq. (2.2) and using the value $\gamma = 0.430 \text{ J} / (\text{K}^2 \text{ mol UPt}_3)$ reported by Fisher *et al.* (1989), one may estimate the effective mass of the quasiparticles in UPt₃ to be $m^* \approx 180 m_e$, where m_e is the mass of the bare electron. Compared to the effective mass in ordinary metals ($1 - 3 m_e$), m^* in UPt₃ is very large, justifying the

designation of this material as a heavy fermion (electron) system. In addition, this large effective mass gives a relatively low Fermi temperature, $T_F \approx 300$ K for UPt₃, compared to ordinary metals for which $T_F \approx 10^5$ K. Different values for γ in UPt₃ have been reported and vary between 0.413 (de Visser *et al.*, 1984) and 0.450 J/(K² mol UPt₃) (Stewart *et al.* 1984).

The second term in Eq. (2.1) corresponds to the phonon contribution to the specific heat. The phonon coefficient, β , can be used to estimate the Debye temperature, Θ_D , since these two parameters are related by the expression

$$\beta = 234 n k_B \Theta_D^3, \quad (2.5)$$

where n is the number of atoms per unit volume (in UPt₃, $n = 8 / \Omega_m$) (Ashcroft and Mermin, 1976). De Visser *et al.* (1987a) reported a value of β near 8.5×10^{-4} J/(K⁴ mol UPt₃) giving $\Theta_D \approx 420$ K. This value is of the same order as the Debye temperatures found for ordinary metals (Al : $\Theta_D \approx 400$ K; Cu : $\Theta_D \approx 315$ K). One might expect that below 1 K ($\ll \Theta_D$), all real phonon excitations are minimal, so that the properties measured below this temperature, particularly in the superconducting state, are electronic in nature.

The third term in Eq. (2.1) is generally attributed to the presence of spin fluctuations (SF) in analogy to ³He, where a $T^3 \ln T$ term is also observed and considered to be a general property of an interacting Fermi liquid (Stewart *et al.*, 1984; de Visser *et al.*, 1984; Frings *et al.*, 1985). It is precisely the coexistence between magnetic spin fluctuations and superconductivity that motivated a great deal of experimental and theoretical work on UPt₃.

2.1.2.b Superconducting state

Specific heat measurements in the superconducting state have revealed a number of interesting results. For example, Fisher *et al.* (1989) reported two jumps separated by

60 mK in the vicinity of the critical temperature, T_c , as an intrinsic feature of UPt₃. This result is shown in Fig. 2-2. Critics have argued that the double jump could come from the presence of a second crystallographic phase with a different critical temperature. This argument was later weakened by the fact that, in some cases, "as grown" samples, initially showing a single broad transition, exhibited two sharp jumps near T_c after annealing (Vorenkamp *et al.*, 1990; Midgley *et al.*, 1993). The double feature was eventually reported in results for many different samples (single crystal and polycrystalline specimens) and was observable in other physical properties, such as ultrasonic attenuation (as discussed below), thermal expansion (Hasselbach *et al.*, 1990), and susceptibility (this work). It is important to note that one of the original samples studied by Fisher *et al.* (1989) is sample No. 4 described in this work, for which the results are presented and discussed in Chapter 4.

Magnetic field studies of the specific heat showed that the separation between the two peaks became smaller with field, ultimately vanishing near $B = 0.5$ T for fields perpendicular to the c-axis (Hasselbach *et al.* 1989; Bogenberger *et al.* 1993). The multiple phase diagram in the B-T plane drawn from such measurements and others (see section 2.1.4.b on the upper critical field below) contributes the strongest piece of evidence for unconventional superconductivity in UPt₃ as defined in Chapter 1.

Another interesting finding is the temperature dependence of the specific heat below T_c , $c_s(T)$, which varies as $c_s(T) = \gamma_s T + \delta_s T^2$ between 100 mK and 400 mK (Hasselbach *et al.*, 1989). This result is in contrast with the exponentially decaying $c_s(T)$ predicted by the BCS theory in the limit $T \rightarrow 0$. The non-exponential decay of $c_s(T)$ in UPt₃ is taken as evidence for the presence of nodes in the energy gap structure. More specifically, a quadratic temperature dependence is consistent with lines of nodes, while a T^3 dependence, as observed in UBe₁₃ (see section 2.2.2.b), indicates the presence of point nodes. In addition, the residual linear specific heat, $\gamma_s T$, of UPt₃ is evidence that the

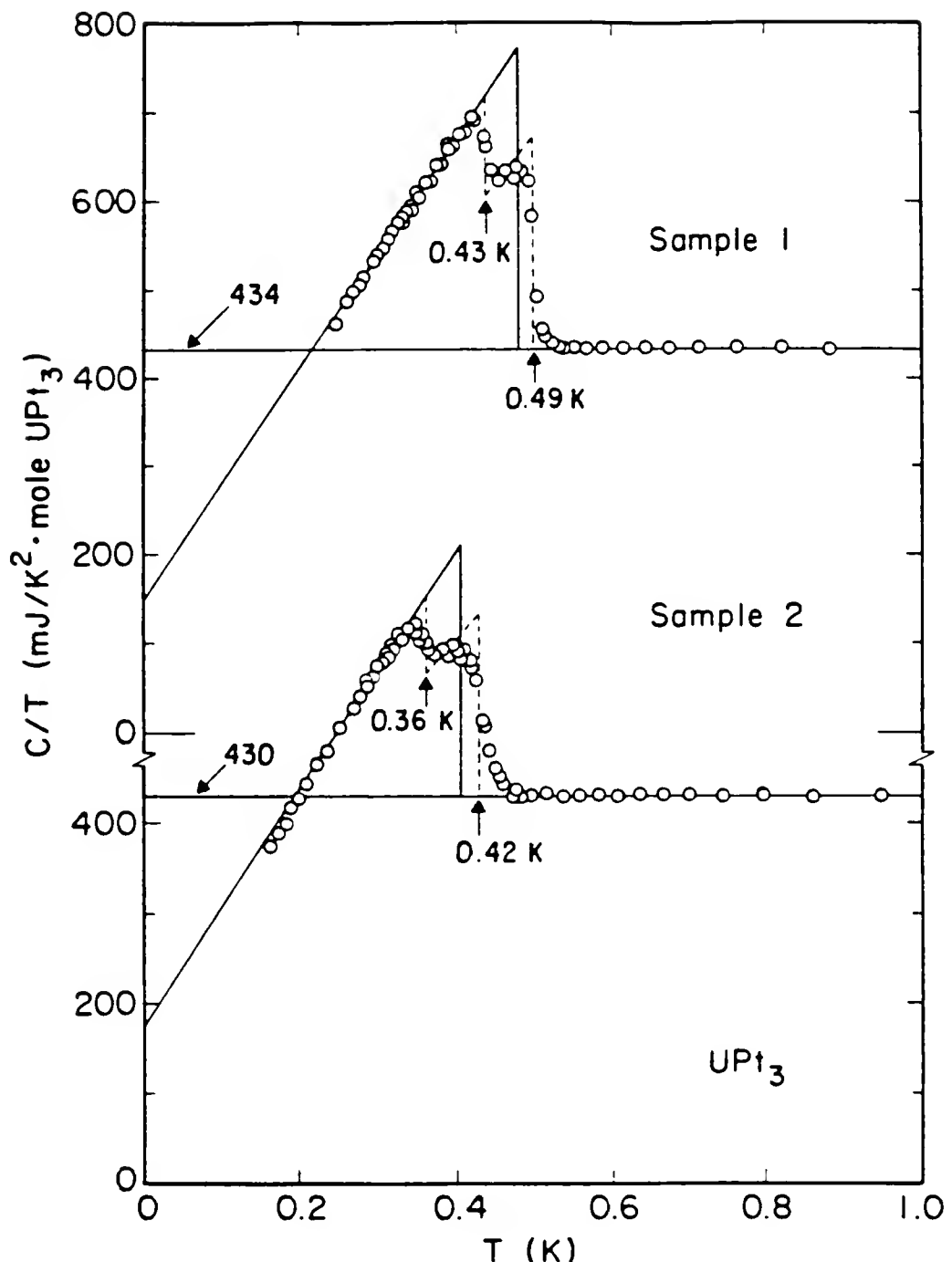


Fig. 2-2. Specific heat of UPt₃ in the vicinity of the superconducting transition indicating the double transitions at zero field. Measurements were performed by Fisher *et al.* (1989) on two polycrystalline specimens. Sample labeled No. 2 on the figure is sample No. 4 used in this work (see Chapter 4). For that specimen, the lower transition is $T_{c1} \approx 0.36$ K, while the higher transition is $T_{c2} \approx 0.42$ K, so that the splitting $\Delta T_c \approx 60$ mK.

superconductivity does not cover the entire Fermi surface and that nodes in the energy gap are present. However, one should keep in mind that, first, these power laws are extracted for very limited ranges of temperature, *i.e.* at most one decade (50 mK to 500 mK), and second, the exponential dependence predicted from the BCS theory is expected only for $T \ll T_c$. Typically, for UPt_3 , the lowest temperature achieved by specific heat measurements corresponds to about $T/T_c \approx 0.1$.

Using a nuclear demagnetization cryostat, Schuberth *et al.* (1990 and 1992) were able to measure specific heat down to 10 mK. The extraction of the power law temperature dependence of $c_s(T)$ was difficult because their data showed a large anomaly around 18 mK. The experiments were conducted on two different samples, one of which is sample No. 2 of this work (see Chapter 4). These authors suggested that this result was the signature of a new phase transition taking place in the superconducting electronic system. To clarify this issue, Jin *et al.* (1992) measured sound velocity and attenuation of a third sample down to 5 mK and reported no sign of an anomaly near 18 mK. The specific heat anomaly near 18 mK is, therefore, sample dependent and could be related to the presence of impurities.

2.1.3 Ultrasonic Studies

Measurements of sound velocity and sound attenuation are powerful techniques because they probe the properties of the crystal along specific axes. This feature, shared also with penetration depth and thermal conductivity measurements, is especially useful for studying the energy gap structure. A very important result, establishing the anisotropic nature of superconductivity in UPt_3 , came from transverse sound attenuation measured by Shivaram *et al.* (1986a) for sound propagation within the basal plane and polarization, ε , parallel and perpendicular to the plane. The attenuation in the superconducting state increased linearly with temperature for ε parallel to the basal plane, while the increase was quadratic for ε perpendicular to the plane. These results are very different from the

attenuation expected for a BCS-like superconductor which exhibits an isotropic attenuation, α_{BCS} , with a temperature dependence given by the expression

$$\alpha_{\text{BCS}} = \frac{2 \alpha_n}{e^{\Delta(T)/k_B T}}, \quad (2.6)$$

where α_n is the normal state sound attenuation and $\Delta(T)$ is the energy gap (Tinkham, 1975). Attenuation of longitudinal sound along the c-axis has been measured by Bishop *et al.* (1984) who reported a quadratic temperature dependence.

The results from these two groups are consistent with an energy gap possessing line nodes in the basal plane and point nodes where the z-axis intersects the Fermi surface. As discussed in Chapter 4, the penetration depth measurements presented in this dissertation are consistent with this picture.

2.1.4 Phase Diagrams

2.1.4.a Lower critical magnetic field

Early measurements of the lower critical magnetic field, $B_{\text{c1}}(T)$, in UPt_3 were reported by Shivaram *et al.* (1989) who used a tunnel diode oscillator technique similar to the one used in this work (see Chapter 3). Keeping the temperature constant and sweeping a dc magnetic field, they extracted the lower critical field and reported a kink in $B_{\text{c1}}(T)$ around $0.7 \text{ T}/T_c$ for fields perpendicular to the c-axis. This kink is thought to correspond to the lower transition observed in the specific heat. The scatter in the data for the fields parallel to the c-axis did not allow one to unambiguously establish the existence of a kink for this orientation. Later measurements of $B_{\text{c1}}(T)$ by Vincent *et al.* (1991) showed a kink in both directions. From these measurements, one can estimate the lower critical field as $T \rightarrow 0$ to be around 10 mT for both directions, although Wüchner *et al.* (1993) reported a lower value of 6.5 mT.

2.1.4.b Upper critical magnetic field

The upper critical field, $B_{c2}(T)$, in UPt_3 has been extensively studied with various techniques which include specific heat (Hasselbach *et al.*, 1989; Bogenberger *et al.*, 1993), ultrasound velocity (Bruls *et al.*, 1990), resistivity (Chen *et al.*, 1984; Hasselbach *et al.*, 1990), thermal expansion (Hasselbach *et al.* 1990; de Visser *et al.* 1993), magnetostriction (de Visser *et al.*, 1993), and susceptibility (this work). The most comprehensive study on $B_{c2}(T)$ was performed by Adenwalla *et al.* (1990) and Lin (1993), who measured sound attenuation and velocity in fields parallel, perpendicular and at 45° with respect to the c-axis. The two samples investigated in their study are samples No. 5 and No. 6 of this work (see Chapter 4). Two of the phase diagrams (parallel and perpendicular to the c-axis) constructed from these sound measurements are shown in Figs. 2-3 and 2-4 (Lin, 1993). It is clear that there exist three distinct phases (A, B, and C) in the mixed state of UPt_3 . As mentioned previously, these multiple superconducting phases set UPt_3 apart from any other superconductor and represent the most convincing argument for unconventional superconductivity in this material.

The field at which the transition lines cross or merge (see Figs. 2-3 and 2-4) is sometimes referred to as B^* . An important point to notice from these phase diagrams is their anisotropy. The value of $B_{c2}(T)$ as $T \rightarrow 0$ is $B_{c2}(0) \approx 2.0$ T for the field parallel to the c-axes, while $B_{c2}(0) \approx 2.5$ T for the field oriented perpendicular. In addition, $B^* \approx 0.9$ T for B parallel to the c-axis, while $B^* \approx 0.4$ T for B perpendicular to the c-axis. Furthermore, $B_{c2}(T)$ has a clear kink at B^* for fields perpendicular, while the kink may not be present for fields parallel to the c-axis. Finally, the four transition lines seem to come to a tetracritical point at B^* for B perpendicular to the c-axis, while the resolution for the other orientation does not allow a distinction between a single tetracritical point and two tricritical points (Lin, 1993).

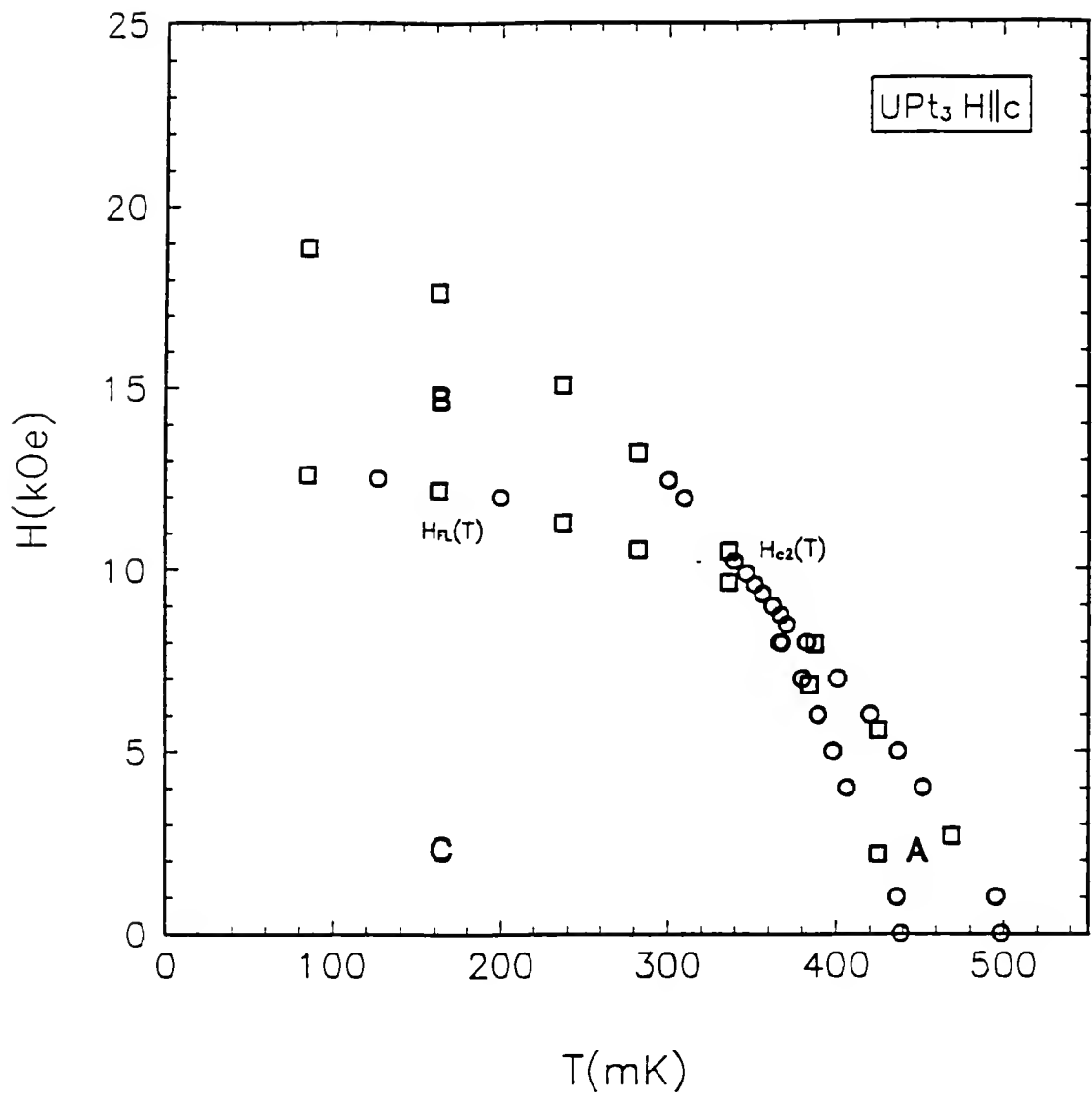


Fig. 2-3. The complete superconducting B-T phase diagram of UPt_3 for the magnetic field parallel to the c -axis. The open circles are determined from temperature sweeps and open squares are determined from field sweeps. Data taken from Lin (1993) (sample No. 1). This specimen is sample No. 5 of this work.

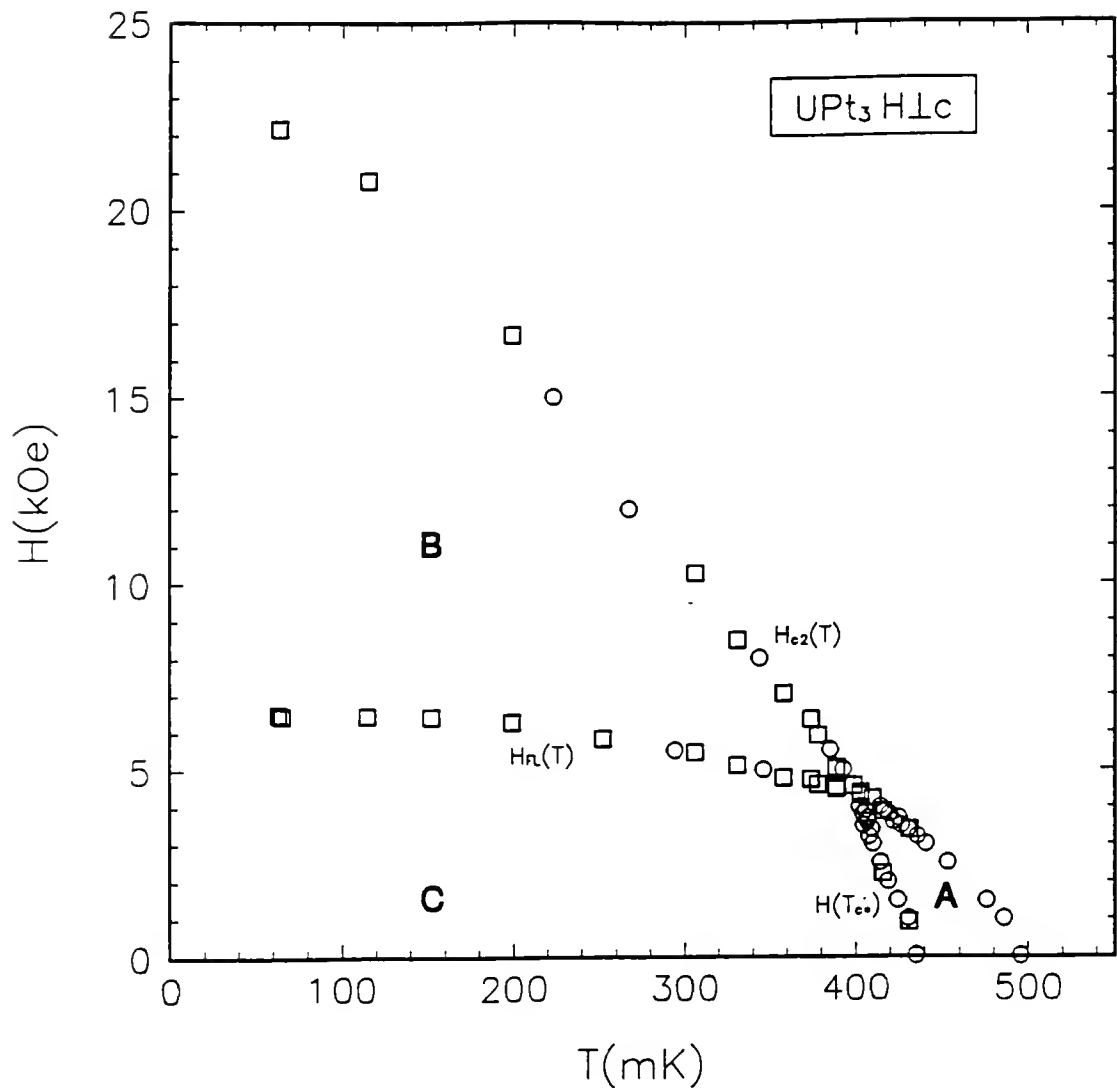


Fig. 2-4. The complete superconducting B-T phase diagram of UPt_3 for the magnetic field perpendicular to the c-axis. The open circles are determined from temperature sweeps and open squares are determined from field sweeps. Data taken from Lin (1993) (sample No. 1). This specimen is sample No. 5 of this work.

2.1.4.c Critical pressure

Behnia *et al.* (1990) reported upper critical magnetic fields measured by resistivity as a function of temperature and pressure. Their results showed that $B_{C2}(T)$ behaves very differently below and above B^* , in a manner suggesting that the high temperature, low field phase is rapidly suppressed by pressure.

The double jump in specific heat has been studied as a function of hydrostatic pressure, P , by Trappman *et al.* (1991) who reported that the two transitions observed for $P = 0$ merged at a critical pressure $P^* = 3.7$ kbar. The phase diagram that they constructed is shown in Fig. 2-5.

Recently the complete B-T-P phase diagrams for fields parallel and perpendicular to the c-axis were reported by Bouklby, Bullock and Shivaram (1994) from ultrasonic studies.

2.1.5 Antiferromagnetism and Superconductivity

One of the most difficult challenges facing the various superconductivity models for UPt_3 is to account for the unusually rich phase diagram presented in the previous subsection. Most models call for a combination of a nonzero angular momentum pairing and a symmetry breaking field responsible for lifting the degeneracy, thereby splitting the transition in $B = 0$ and creating a multiple phase diagram. To date, there exist two strong candidates for this symmetry breaking field. One of them, discussed in this subsection, is an antiferromagnetic transition with a Néel temperature, T_N , near 5 K, while the other, discussed in the next subsection, is related to a structure modulation.

Aeppli *et al.* (1988, 1989) performed neutron diffraction measurements which suggested that UPt_3 was an antiferromagnet with ordered moments of $(0.02 \pm 0.01)\mu_B$ lying in the basal plane and a Néel temperature of 5 K. The first evidence for the coupling between the antiferromagnetic moments and superconductivity was given by the temperature dependence of the magnetic Bragg intensity in zero field, which increases

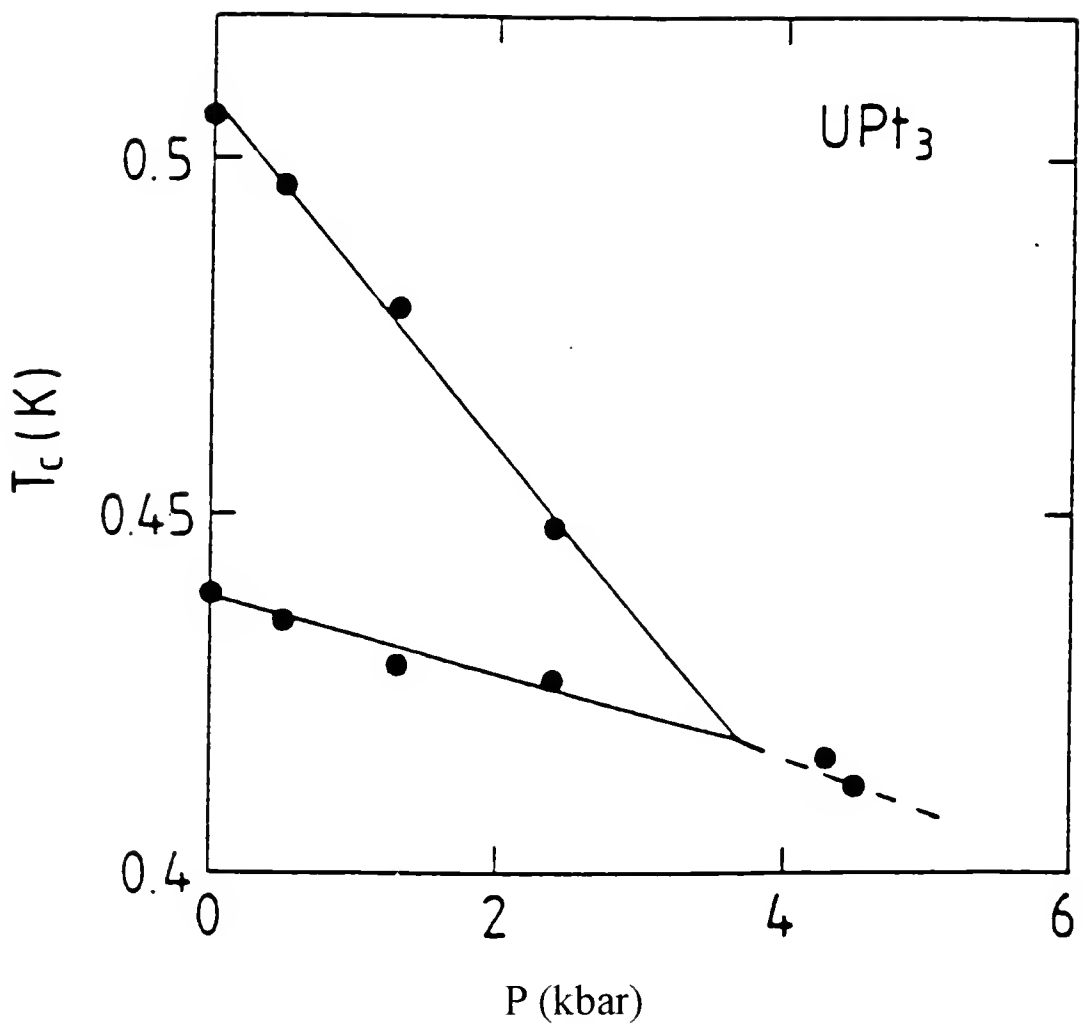


Fig. 2-5. The temperature-pressure phase diagram derived from specific heat measurements by Trappman *et al.* (1991).

linearly with decreasing temperature from 5 K down to T_C , but then decreases from T_C down to the lowest measured temperature (≈ 0.1 K).

Further evidence for the strong correlation between the order parameter of antiferromagnetism and superconductivity in UPt₃ came from neutron diffraction studies under hydrostatic pressure (Hayden *et al.*, 1992). These experiments showed that antiferromagnetism is suppressed at roughly the same pressures at which the two specific heat jumps merge (Fig. 2-5).

One of the problems associated with considering antiferromagnetism as the symmetry breaking field is the short magnetic coherence length of approximately 200 Å (Aeppli *et al.*, 1988, 1989; Hayden *et al.*, 1992), which is of the same order of magnitude as the superconducting coherence length (Shivaram *et al.*, 1986b). It is unclear how such a small magnetic coherence length, in addition to the tiny antiferromagnetic moment, can produce a sizable splitting of the superconducting transition (von Löhneysen *et al.*, 1994). Furthermore, specific heat, sound velocity, and magnetization measurements have failed to unambiguously identify this antiferromagnetic transition around 5 K (Fisher *et al.*, 1991; Adenwalla *et al.*, 1990). In view of these unanswered questions, alternative possibilities for the symmetry breaking field have been put forward, one of which is discussed in subsection 2.1.6.

2.1.6 Structure Modifications and Superconductivity

Recently, transmission electron microscopy was performed by Midgley *et al.* (1993) to investigate the structure of annealed and "as grown" single crystals of UPt₃ cut from the same rod. In the annealed sample, they found a well-defined incommensurate lattice distortion extending over domains of approximately 10⁴ Å (two orders of magnitude longer than the zero temperature superconducting coherence length). On the other hand, the "as grown" sample exhibited some superstructure which lacked the long range coherence of the annealed specimen. Moreover, the annealed sample showed a well

defined double transition in the specific heat ($T_{C2} \approx 0.52$ K and $T_{C1} \approx 0.47$ K), while the "as grown" crystal exhibited a single broad transition with a much lower onset temperature, $T_c \approx 0.41$ K. These observations suggest that the splitting of the transition in UPt_3 may be related to these structural domains which clearly break the hexagonal symmetry over long distances. However, the microscopic details of this structure perturbation on the superconducting state have not yet been described.

2.1.7 Nuclear Magnetic Resonance and Muon Spin Relaxation Knight Shifts

Information about the type of pairing present in a superconductor can be obtained by measuring the electron spin susceptibility, χ_{sc} , in the superconducting state. In an s-wave superconductor, the electrons are paired in states with opposite spins. Thus, the spin susceptibility falls from its normal state value to zero at $T = 0$. In the BCS theory, the temperature dependence of χ_{sc} is given in terms of the Yosida function, $Y(T)$, as

$\chi_{sc} = \chi_n Y(T)$, where χ_n is the normal state susceptibility. On the other hand, an odd parity pairing, with finite angular momentum, will give a different functional form for χ_{sc} . The spin susceptibility can be studied by measuring the Knight shift, $K_s(T)$, in nuclear magnetic resonance (NMR) (Slichter, 1978) and muon spin relaxation (μSR) experiments (Knetsch, 1992).

The Knight shift in UPt_3 has been measured by Kohori *et al.* (1987) who performed NMR on ^{195}Pt . The results showed a temperature independent Knight shift above and below the transition temperature indicating that the spin susceptibility did not change. The authors suggested that these results were consistent with an odd parity pairing (p-wave) or a singlet superconductor with significant spin-orbit scattering from impurities. It is important to note that, because of the Meissner effect (the expulsion of the magnetic field from the sample except within a distance given by the penetration depth), NMR must be performed on powdered samples or on a great number of small whiskers. After obtaining a powder of their sample, Kohori *et al.* (1987) remeasured the ac

susceptibility and found a very broad transition with a lower T_c compared to the original bulk specimen, indicating the presence of impurities or defects in the powdered sample. The Knight shift in UPt_3 was also measured using μSR by Luke *et al.* (1991) who reported results consistent with the findings of the NMR study.

Lee *et al.* (1993) measured the Knight shift on small, single crystal whiskers. The whiskers (approximately one thousand of them) were aligned together using a magnetic field method at room temperature. The normal state measurements, performed between 4 K and 50 K, were consistent with the results obtained by Kohori *et al.*

2.1.8 Point Contact Spectroscopy

A point contact (PC) can be obtained by pressing a normal metal needle or wire against the surface of a superconductor. A simplified view of a point contact is a tunnel junction in parallel with a shunt resistance, R_0 . The current consists of two components: a small tunneling current and a direct part (through the shunt). As the temperature drops below the critical temperature of the superconductor, the magnitude of the tunneling current changes due to the gap structure. An I-V characteristic of a PC can, therefore, give information about the value of the energy gap. The details of point contact spectroscopy analysis are discussed by Blonder *et al.* (1982). In practice, since the majority of the total current flows through the shunt, the relative changes in the I-V curves, as the bias voltage is increased above the gap, are very small, so that only rough estimates of the gap values are possible (usually after plotting dV/dI vs. V).

Results of point contact spectroscopy on single crystals, reported by Goll *et al.* (1993), indicated some anisotropy in the energy gap structure. They found that the magnitude of the minimum in the dV/dI curves for current flowing parallel to the c-axis was 2% greater than that for currents in the basal plane. Furthermore, they reported the presence of a double minimum in the dV/dI curves for currents flowing parallel to the c-axis and only in the low field, low temperature superconducting phase, suggesting

different superconducting order parameters for the different phases. Recently, de Wilde *et al.* (1994) have also reported point contact results inconsistent with an isotropic energy gap.

It is important to keep in mind that point contact spectroscopy does not allow the clear identification of the direction of current flow, since the exact geometry of the contact between the electrode and the sample is not known. A much more powerful technique is to measure tunnel junction spectroscopy, but to date, these types of experiments have not lead to conclusive results for UPt₃.

2.1.9 Concluding Remarks

The results discussed above represent only a fraction of the overall pool of data available on UPt₃. For instance, thermal conduction (Benhia *et al.*, 1991, 1992) and expansion (de Visser *et al.* 1990, 1993; Hasselbach *et al.*, 1990) measurements were not presented in this section, although they contain useful information. For instance, thermal conduction measurements can be performed to study the B-T phase diagram and its anisotropy. Experiments probing the Fermi surface, such as the de Haas-van Alphen effect (Taillefer *et al.*, 1988a) and quantum oscillatory magnetoresistance (Julian *et al.*, 1992, 1994), are also available in the literature. The effects of doping UPt₃ with various elements such as B, Y, and Pd have been studied extensively (de Visser *et al.*, 1987, 1993; Aronson *et al.*, 1991; Knetsch *et al.*, 1992; Bakker *et al.*, 1992; Vorenkamp *et al.*, 1993a, 1993b). Measurements of resistivity, including magnetoresistance (Remenyi *et al.*, 1987; Taillefer *et al.*, 1988b) and surface resistance (Grimes *et al.*, 1991) (discussed in Chapter 4), have also been reported. As mentioned above, a number of experiments measuring the penetration depth have been performed and will be discussed in great detail in Chapter 4.

Although this section treated only a limited portion of the total experimental work on UPt₃, several important points can clearly be made from the observations described above. First, UPt₃ is not a conventional BCS-like superconductor. This assertion is

especially supported by the unusual phase diagrams (Figs. 2-3 and 2-4). Second, the energy gap is anisotropic and possesses nodes on the Fermi surface where it goes to zero. The exact structure (points or lines) and location of the nodes remains uncertain, although there is strong evidence (including the results of this work) that lines of nodes lie in the basal plane. Third, some of the experimental results are sample dependent, which means that specimen quality and characterization become very important. This sample dependence justifies the need for systematic studies of the same type of measurements on many different samples. For this reason, one of the original goals of the work described in this dissertation was to provide a comprehensive and systematic study of penetration depth measurements in UPt₃.

2.2 Experimental work -- UBe₁₃

Superconductivity in UBe₁₃ was first observed in 1975 by Bucher *et al.* (1975), who reported a superconducting transition at 0.97 K. This transition was argued to be extrinsic to UBe₁₃ and to be due to precipitated U filaments. Superconductivity, as an intrinsic property of UBe₁₃, was first reported in 1983 by Ott *et al.* (1983), who reported resistivity, specific heat, and susceptibility results consistent with a superconducting transition below 0.85 K. Since then, a number of experimental results have suggested that superconductivity in UBe₁₃ is unconventional (as defined in Chapter 1), although none of them offer definite proof.

In the next subsections, after describing the crystal structure of UBe₁₃, a number of the measurements supporting the unconventional superconductivity in this material are reviewed. First, a brief summary of the specific heat results and a discussion on the various length scales of the superconducting state are given. The phase diagrams are then presented, before a short status report on NMR and μ SR measurements. A subsection on the possible magnetic transition near 8 K is then included. Finally, experiments on

thoriated UBe₁₃ are presented before giving some concluding remarks. The anisotropy of the upper critical field is discussed in detail in Chapter 5 and is not presented here.

2.2.1 Crystal Structure

The crystal structure of UBe₁₃ (shown in Fig. 2-6) is the cubic NaZn₁₃ configuration (Benzinger and Rundle, 1949) with eight formula units in the primary cell. The lattice constant and other parameters are summarized in Table 2-2. Eight of the Be atoms (referred as Be_I) and the eight U atoms form a sublattice of cubic CsCl structure with lattice constant equal to $a/2$, while the remaining 96 Be atoms (Be_{II}) surround the U in an icosahedral formation, and the Be_I atoms in a polyhedron (snub cube) arrangement. The NaZn₁₃ structure is described in detail by Shoemaker *et al.* (1952).

For the purpose of this work, it is important to define two particular orientations with respect to the crystal structure. In Chapter 5, where the anisotropy in the upper critical field is discussed, measurements are presented for which a magnetic field has been applied parallel to the [100] and the [110] directions. The [100] direction refers to the direction parallel to the side of the cube defining the unit cell, while the [110] direction refers to the plane diagonal of the cube. Finally, the [111] direction refers to the body diagonal of the cube.

Table 2-2. Summary of lattice parameters of UBe₁₃.

a (Å)	Volume of unit cell Ω_m (m ³)	Mol. weight M (kg)	Density ρ (kg/m ³)	T_{melt} (C)
10.257	1.08×10^{-27}	0.355	4.368×10^3	~ 2000

2.2.2 Specific Heat Measurements

2.2.2.a Effective mass

Ott *et al.* (1983) reported a value for the electronic coefficient of the specific heat, γ , of $1.1 \text{ J}/(\text{K}^2 \text{ mol of UBe}_{13})$. Using Eqs. (2.2) and (2.3), one can estimate the effective

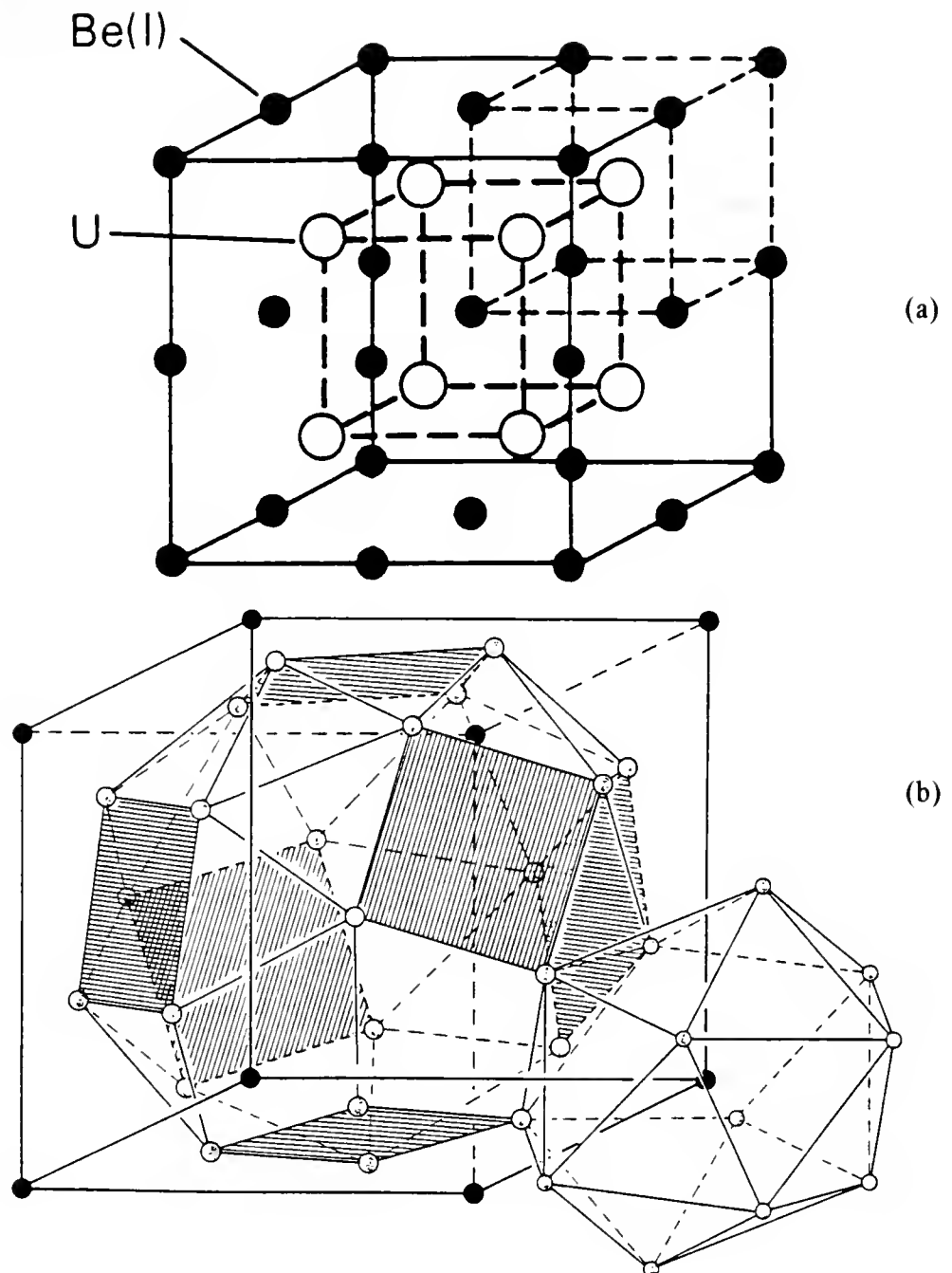


Fig. 2-6. Crystal structure of UBe_{13} . (a) Unit Cell showing the Cs-Cl sublattice. The Be_{II} are not shown for clarity. (b) Section of the unit cell showing the Be_{II} (open circles) in an icosahedral formation, and surrounding the U atom (not shown) located at the center of the cube . Also shown is the Be_{II} polyhedron (snub cube) arrangement surrounding the Be_{I} atoms (closed circles). This figure was taken from Knetsch (1992).

mass of the quasiparticles, m^* . The Fermi wave vector, k_F , can be calculated using Eq. (2.4) with $Z = 24$ (3 electrons per U atom and 8 U atoms per unit cell) and $\Omega_m = a^3 = 1.08 \times 10^{-27} \text{ m}^3$, giving $k_F = 8.68 \times 10^9 \text{ m}^{-1}$. These values give $m^* \approx 300 m_e$ which is greater than $m^* \approx 200 m_e$ reported by Ott *et al.* (1983) who used a slightly different value for Z .

2.2.2.b Superconducting state

Early specific heat measurements in the superconducting state by Ott *et al.* (1984b) and Mayer *et al.* (1986) showed a strong deviation from the BCS theory and suggested a temperature dependence of $c_s(T)$ close to T^3 . This result was interpreted as evidence for the presence of point nodes on the Fermi surface. It is important to stress that these T^3 power laws were extracted from a limited temperature range : $0.08 \leq T/T_c \leq 0.9$ for Ott *et al.*, and $0.22 \leq T/T_c \leq 0.98$ for Mayer *et al.*. Since the BCS theory predicts an exponential dependence only for the limit $T/T_c \rightarrow 0$, the statement that the T^3 power law is a signature of point nodes on the Fermi surface is not conclusive. Furthermore, as the results discussed below will show, this power law dependence of the specific heat might be sample dependent.

Measurements by Brison *et al.* (1988a) indicated that an upturn in $c_s(T) / T$ arises at low temperatures with a minimum around 90 mK and that the T^3 dependence was hardly achieved even at intermediate temperatures (150 mK - 500 mK). The authors suggested that these results could be explained by the presence of a small amount of impurities whose influence is amplified by the high sensitivity of anisotropic superconductors to them.

Later measurements of the specific heat in magnetic fields (1.89 T to 7.88 T) on the same sample used for the measurements just mentioned, indicated that, first, the power law dependence of $c_s(T)$ in fields was close to $c_s(T) = \gamma_s T + \beta T^2$; second, the upturn in $c_s(T) / T$ became greater with field; and third, the minimum rose in temperature with increasing fields (Brison *et al.*, 1988b). On the basis of entropy balance arguments, they

concluded that the upturn was intrinsic to UBe₁₃, and furthermore, that it corresponded to a magnetic transition.

The motivation for searching for a second transition below the superconducting one is partially based on the results obtained on Th-doped UBe₁₃ as will be discussed in greater detail in section 2.2.7. Briefly, for U_{1-x}Th_xBe₁₃, with 0.017 < x < 0.04, a second transition below T_C has been observed, the nature of which has not been clearly identified. One of the models attempting to explain these results predicts a second superconducting transition below T_C in the pure system as well. Other measurements, in addition to the specific heat data from Brison *et al.* (1988a, 1988b) have hinted at the existence of such a transition in pure UBe₁₃ (Rauchschwalbe *et al.*, 1987; Ellman *et al.*, 1991).

2.2.3 Penetration Depth, Mean Free Path, and Coherence Length

2.2.3.a $\lambda(0)$, ℓ , and ξ

An important property of a superconductor is the zero temperature value of the penetration depth, $\lambda(0)$. Several groups have reported values for $\lambda(0)$, which range from $\approx 2000 \text{ \AA}$ as determined by NMR results (MacLaughlin *et al.*, 1984) to $\approx 4000\text{-}5000 \text{ \AA}$ (Gross *et al.* 1986; Alekseevskii *et al.*, 1986) and $\approx 11000 \text{ \AA}$ (Gross *et al.*, 1988; Groß-Altag *et al.*, 1991) as extracted from magnetization measurements.

The electronic mean free path, ℓ , can be estimated using the expression

$$\ell = v_F \tau = \left(\frac{\hbar k_F}{2\pi m^*} \right) \left(\frac{m^*}{n e^2 \rho(T)} \right) \quad (2.7)$$

where v_F is the Fermi velocity, τ is the average time between scattering events, $n = Z / \Omega_m$ is the number of electrons per unit cell contributing to the conduction band, and $\rho(T)$ is the resistivity (Ashcroft and Mermin, 1976). From the resistivity data of Maple *et al.* (1985), one can estimate $\rho(T_C) \approx 125 \mu\Omega\text{cm}$ which gives $\ell \approx 13 \text{ \AA}$. It is important to

note that near T_c , the resistivity is still changing with temperature, so that $\rho(T_c)$ is not the residual resistivity, and the calculated ℓ may not reflect the residual mean free path. Furthermore, Eq. (2.7) is based on the free electron model, which may not be reliable for UBe₁₃. Taking these points into consideration, Brison *et al.* (1989) suggested that the mean free path may reach several hundred angstroms.

From the slope of the upper critical field near T_c , Maple *et al.* (1985) have estimated the superconducting coherence length, ξ , in UBe₁₃ to be $\approx 140 \text{ \AA}$. However, by using the BCS formula $\xi \equiv h v_f / 2\pi\Delta(0)$, they find $\xi \approx 50 \text{ \AA}$. From the above discussion of the mean free path, it is not clear whether UBe₁₃ is a superconductor in the clean limit ($\ell > \xi$) or in the dirty limit ($\ell < \xi$). Assuming $\lambda(0) = 5000 \text{ \AA}$, we can estimate the Ginzburg-Landau parameter $\kappa = 0.96 \lambda(0)/\xi \approx 100$ for the clean limit and $\kappa = 0.715 \lambda(0)/\ell \approx 300$ for the dirty limit, so UBe₁₃ may be considered a strong type II superconductor.

2.2.3.b $\lambda(T)$

The motivations for measuring the temperature dependence of the penetration depth, $\lambda(T)$, are discussed in detail in Chapter 4. Briefly, $\lambda(T)$ is related to the temperature dependence of the density of superconducting electrons, $n_s(T)$, which depends upon the energy gap structure. The fact that $\lambda(T)$ can be measured along different crystallographic directions, makes the study of the penetration depth a very powerful tool for investigating the gap structure.

The temperature dependence of the penetration depth on UBe₁₃ single crystals has been reported by Groß-Alltag *et al.* (1991). These authors reported a quadratic dependence for the excitation field parallel to the [100] and [110] directions. The results on our single crystals are described and discussed in Chapter 5, and are in conflict with the results of Groß-Alltag *et al.*

Measurements on polycrystalline specimens performed by other groups also indicated a quadratic temperature dependence of $\lambda(T)$ (Gross *et al.*, 1986; Einzel *et al.*, 1986). Gross *et al.* argued that these results were consistent with the existence of a gap

with linearly vanishing point nodes located on the Fermi surface. However, the same authors acknowledged the fact that any dirty superconductor could give a quadratic temperature dependence. The lack of conclusive evidence from penetration depth measurements motivated our studies of $\lambda(T)$ for our high purity single crystals described in Chapter 5.

2.2.4 Phase Diagrams

2.2.4.a Lower critical magnetic field

Rauchschwalbe (1987) measured $B_{c1}(T)$ from magnetization studies and reported $B_{c1}(0) \approx 4.6$ mT and $d(B_{c1})/dT$ near $T_c \approx 10$ mT/K. Although the author plotted the data against T^2 , $B_{c1}(T)$ did not quite follow the empirical quadratic dependence. This result cannot be taken as a signature for unconventional superconductivity since the BCS prediction and several conventional superconductors (such as aluminum, tin, indium, lead and mercury) deviate from this quadratic temperature dependence. In that regard, it would be interesting to fit Rauchschwalbe's data to the BCS prediction.

2.2.4.b Upper critical magnetic field

The upper critical field of polycrystalline UBe_{13} has been measured by several groups (Chen *et al.*, 1985; Rauchschwalbe *et al.*, 1985, 1987; Remenyi *et al.*, 1986; Schmiedeshoff *et al.*, 1988, 1992; Brison *et al.*, 1989). The results indicated an unusually large slope of $B_{c2}(T)$ in the limit $T/T_c \rightarrow 1$. For instance, Rauchschwalbe (1987) reported values near 200 T/K for $0.25 T < B < 2$ T, although values near 35 T/K are more common (Chen *et al.*, 1985). Above 2 T, $B_{c2}(T)$ changes slope to a lesser value (≈ 11.5 T/K) until about 6 T where it becomes steeper again (≈ 15 T/K) (Brison *et al.*, 1989). The reported values for the upper critical field in the $T/T_c \rightarrow 0$ limit range from ≈ 10 T (Remenyi *et al.*, 1986) to ≈ 13.5 T (Brison *et al.*, 1989). Various models have been used to explain the temperature dependence of $B_{c2}(T)$, but the data has not been

fitted successfully over the entire temperature range for any of them (Rauchschwalbe *et al.*, 1987; Brison *et al.*, 1989).

Results of $B_{C2}(T)$ on single crystals will be discussed in detail in Chapter 5, with an emphasis on the earlier work performed on the anisotropy in $B_{C2}(T)$ in the limit $T/T_C \rightarrow 1$. Briefly, the behavior of $B_{C2}(T)$ is similar in single and polycrystalline samples for $B < 6$ T, with a large initial slope (≈ 40 T/K for $B < 0.5$ T) and a change around 2 T to a smaller value (≈ 9 T/K) (Maple *et al.*, 1985). Above 6 T, the slope stays constant (as opposed to increasing as in the polycrystalline samples) and eventually levels off to $B_{C2}(0) \approx 9$ T. Figure 2-7 gives an example of $B_{C2}(T)$ for single and polycrystalline samples, the data is from Schmiedeshoff *et al.* (1992).

Finally, specific heat measurements as a function of magnetic field by Ellman *et al.* (1991), have suggested the presence of a second transition line below $B_{C2}(T)$. The existence of a second transition, below the superconducting one, has been postulated by Rauchschwalbe (1987) from his analysis of the thorium doped UBe_{13} results, which are discussed below.

2.2.5 Nuclear Magnetic Resonance and Muon Spin Relaxation Knight Shifts

2.2.5.a NMR

Early measurements of the temperature dependence of the spin-lattice relaxation time, T_1 , by MacLaughlin *et al.* (1984) indicated a T^3 dependence for $0.2 \text{ K} < T < T_C$, in contrast to the exponential behavior expected for a BCS superconductor at low temperatures. The authors suggested that their results were consistent with an energy gap possessing lines of nodes. However, they reported a strong deviation from the T^3 power law for $0.06 \text{ K} < T < 0.2 \text{ K}$, and this observation was unexplained. Clearly, this T^3 dependence of T_1 , extracted for such limited temperature range, cannot be considered as strong evidence for unconventional superconductivity.

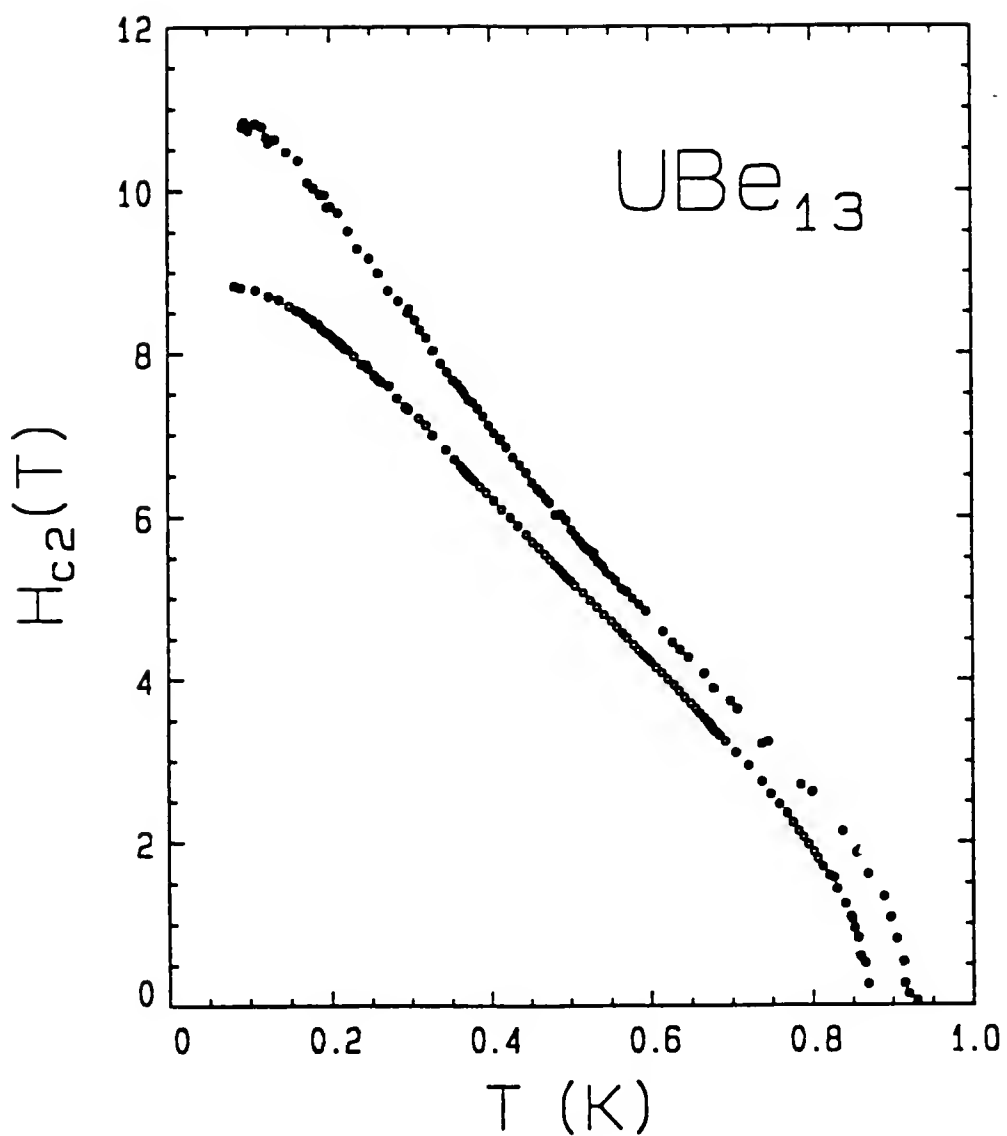


Fig. 2-7. Upper critical field in UBe₁₃ for single crystal (lower curve) and polycrystal (upper curve). Data from Schmiedeshoff *et al.* (1992).

The NMR Knight shift was reported as changing by less than 0.01% below T_c for an applied field of $B = 1.5$ T, consistent with an odd parity pairing (Heffner *et al.*, 1986). However, as shown in subsection 2.2.5.b, these results were not always reproducible.

2.2.5.b Muons

Heffner *et al.* (1986) reported a muon Knight shift change of 40% below T_c (in contrast to the NMR results just mentioned), and suggested that this result was most likely consistent with an even-parity pairing state. The same authors suggested that the difference between the NMR and the muon experiments was related to differences in sample qualities.

Luke *et al.* (1990) confirmed a very large muon Knight shift and reported a temperature dependence similar to that given by the Yosida function for a spin susceptibility of a conventional superconductor below T_c . However, the situation was further complicated when Luke *et al.* (1991) reported a temperature independent Knight shift in UBe_{13} , consistent with an odd parity pairing. As the above review showed, the inconsistency among the various experimental results makes it difficult to conclude on the nature of the superconductivity in UBe_{13} based on the NMR and μSR data.

2.2.6 Anomaly Around 8K

In the previous section on UPt_3 , it was stated that a candidate for the symmetry breaking field, responsible for the unusual phase diagram in this material, is the presence of antiferromagnetic ordering around 5 K. Another heavy fermion superconductor with non-BCS-like properties is URu_2Si_2 . In this material, an unambiguous magnetic ordering is observed at 17.5 K (Palstra *et al.*, 1985). The coexistence of magnetism and superconductivity in UPt_3 and URu_2Si_2 motivated numerous studies of the normal state of UBe_{13} in search of a magnetic transition. Magnetostriiction measurements by Kleiman *et al.* (1990) showed evidence of magnetic ordering around 8 K. It later appeared that this transition might be sample dependent. Several groups conducting similar experiments

did not observe the magnetic transition (de Visser *et al.*, 1992a, 1992b; Clayhold *et al.*, 1993). The discrepancy between these results motivated measurements of the normal state susceptibility of our three UBe₁₃ single crystals.

2.2.7 Thorium Doped UBe₁₃ Experiments

Many different elements have been used to dope UBe₁₃. A comprehensive study of doping experiments was performed by Kim (1992). This section treats only the work performed on U_{1-x}Th_xBe₁₃ for which a great deal of experimental results have been published since Ott *et al.* (1984a) reported a non-monotonic T_c-x curve. A complete T_c-x phase diagram, shown in Fig. 2-8, was established using a variety of measurement techniques (Ott, 1989; Heffner *et al.*, 1990). In particular, specific heat measurements indicated the existence of a second transition for 0.019 < x < 0.045 (Ott *et al.*, 1984a, 1985). The nature of this second transition has been the focus of numerous experimental and theoretical work, for it might hold the key to understanding superconductivity in pure UBe₁₃. An excellent guide to the literature on this subject has been given by Knetsch (1992).

There are several possible explanations for the second phase transition in thorianated UBe₁₃, three of which are briefly presented here. The first was proposed by Batlogg *et al.* (1985), who, from their ultrasound experiments, suggested an antiferromagnetic transition. Their hypothesis was supported by a well defined ultrasound attenuation peak near T_{C2}, 200 times larger than the expected total ultrasonic attenuation due to scattering from conduction electrons. Since s-wave superconductivity is known to be weakened by the presence of magnetism, the coexistence of superconductivity and antiferromagnetism suggests that superconductivity in U_{1-x}Th_xBe₁₃ is unconventional.

An alternative interpretation was later proposed by Joyst *et al.* (1986) who attempted to explain the ultrasound result in terms of a transition in which one

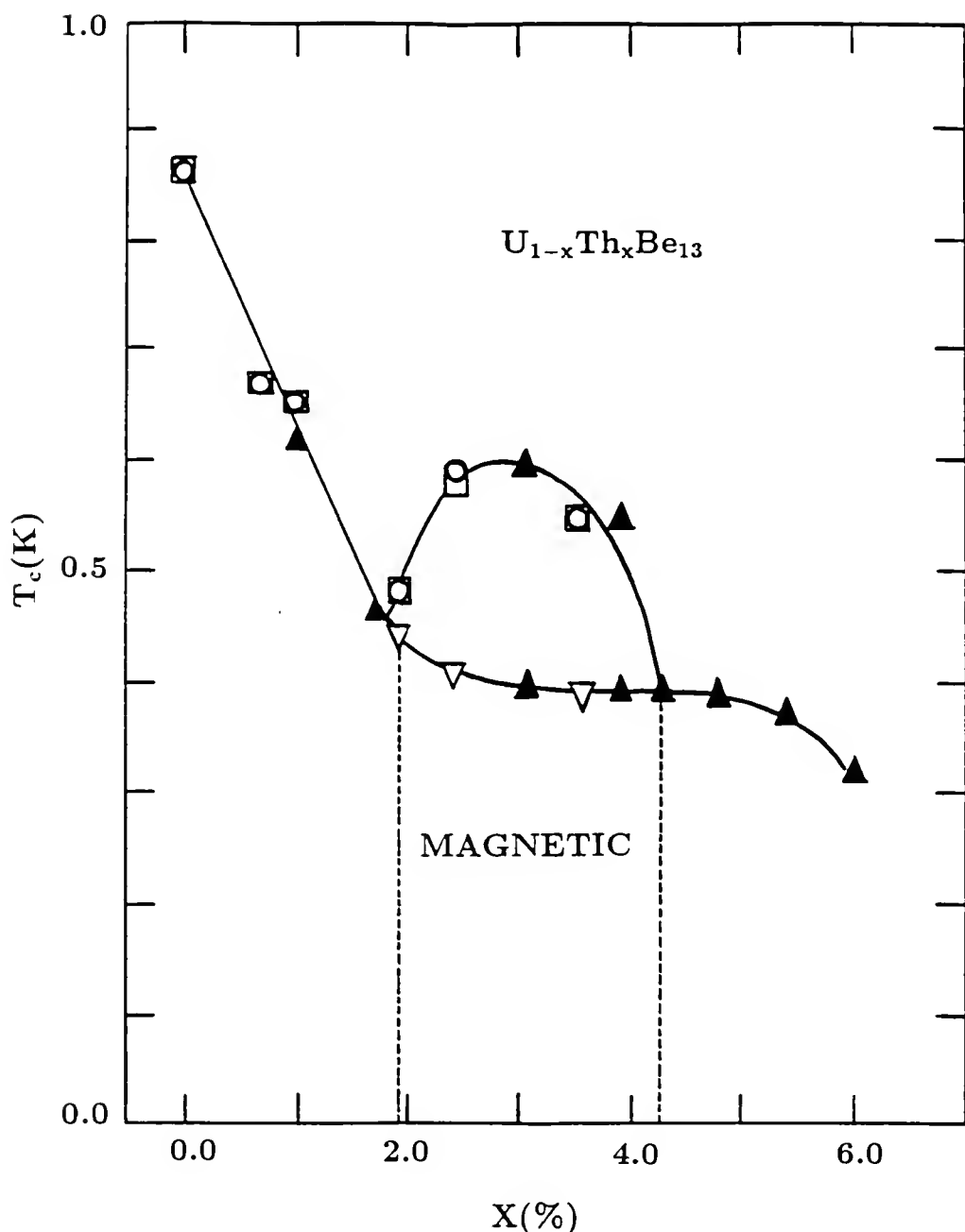


Fig. 2-8. Superconducting T_c -x phase diagram of $\mathbf{U}_{1-x}\mathbf{T}\mathbf{h}_x\mathbf{B}\mathbf{e}_{13}$ taken from Heffner *et al.* (1990). The symbols represent transition temperatures determined by different measurement techniques. \square : T_{c1} from susceptibility, \circ : T_{c1} from $B_{c1}(T)$, Δ : T_{c1}, T_{c2} from specific heat, ∇ : T_{c2} from $B_{c1}(T)$.

superconducting order parameter is replaced by another. Such a first order transition occurs in ^3He between the A- and the B-phases (Vollhardt and Wölfle, 1990).

A third explanation for the second transition in $\text{U}_{1-x}\text{Th}_x\text{Be}_{13}$ has been put forward by Rauchschwalbe *et al.* (1987) who suggested the existence of two different superconducting phases originating from two distinct parts of the Fermi surface. The authors took their analysis a step further and claimed that these two phases also coexisted in pure UBe_{13} , so a second superconducting transition near $T_{c2} \approx 0.6$ K should be observed below the first one at $T_{c1} \approx 0.9$ K. Rauchschwalbe *et al.* suggested that this second transition in UBe_{13} , less pronounced than in the thoriated system, was supported by specific heat data which showed an enhancement below T_{c1} compared to the predictions obtained from two different models (a strong coupling BCS and a strong coupling triplet state). The existence of a second phase transition below the first superconducting one will be further discussed in Chapter 5 where the phase diagram for one of our single crystals of UBe_{13} (No. 3), exhibiting signs of an anomaly below $B_{c2}(T)$, is presented. This discussion is also relevant to the specific heat results on pure UBe_{13} by Brison *et al.* (1988b), presented earlier, which suggested the existence of a transition below T_c , and to the phase diagram proposed by Ellman *et al.* (1991) with the second transition line below B_{c2} (see section 2.2.4). It is important to note that the picture presented by Rauchschwalbe *et al.* is independent of the type of pairing existing in the superconducting states.

Several other models have been proposed for the second transition in thoriated UBe_{13} (Kumar and Wölfle, 1987; Sigrist and Rice, 1989; Langner *et al.*, 1988). A scenario for the complete T_c -x diagram in $\text{U}_{1-x}\text{Th}_x\text{Be}_{13}$ has been given by Knetsch (1992). The model assumes a magnetic transition at T_{c2} and spin fluctuation mediated superconductivity.

2.2.8 Concluding Remarks

While some of the results presented here suggest that UBe₁₃ is an unconventional superconductor, there exists no strong, unambiguous evidence supporting this assertion. Several of the experimental measurements such as specific heat, Knight shift, observation of second transitions, values of $B_{c2}(0)$, the slope of $B_{c2}(T/T_c \rightarrow 1)$, and 8 K anomalies give sample dependent results. Therefore, it seems important to perform measurements on several different samples and to characterize the specimens as much as possible. This approach has been adopted for the work presented in Chapter 5.

This sample dependence has made the overall interpretation of the data on UBe₁₃ (and UPt₃) very difficult and may be related to the fact that unconventional superconductors are very sensitive to impurities, more so than their BCS counterparts (assuming that UBe₁₃ is indeed unconventional). Sample fabrication is, therefore, an extremely important aspect in this field. As different samples are grown using various techniques and starting materials, their impurity concentrations may vary, resulting in some inconsistencies in the experimental results. Sample histories, such as annealing, etching, polishing, and cutting also become relevant issues. In fact these sample fabrication problems are common to most superconductors possessing short coherence length and small energy gaps (*e.g.* organic, high temperature, Chevrel phase, and A15).

CHAPTER 3

APPARATUS AND EXPERIMENTAL TECHNIQUES

This chapter is divided into three parts. First, the dilution refrigerator, and its auxiliary equipment, used to achieve the low temperatures (from about 40 mK to 4 K), are described. In the second section, our technique to measure ac susceptibility, namely mutual inductance, is presented. In the third section, the tunnel diode oscillator technique, used to measure the inductive response of samples at radio frequencies (rf), is described.

3.1 Low Temperatures

This section deals with the cryogenic aspects of the experiments conducted for this dissertation. The topics include the dilution refrigerator, the thermometry, and the temperature control.

3.1.1 Dilution Refrigerator

Because the history and the principles of the dilution refrigerator are well covered in the literature (Lounasmaa, 1974; Betts, 1976; Pobell, 1992), this subsection covers only the aspects which are specific to our refrigerator. We perform our low temperature work using a homemade, continuous flow dilution refrigerator built in 1975 by R. M. Mueller under the supervision of Professor Dwight Adams. The entire refrigerator, with the exception of the gas handling system, fits inside an rf shielded cage made of copper screen. This cage protects the experiments and the electronics from potential noise and heating effects of external radio frequency radiation. The dilution unit is suspended from a one inch thick, triangular aluminum plate which is supported at its three corners by pneumatic isolation mounts from Newport Research Corporation. This setup provides isolation from mechanical vibrations. The gas mixture (about 20 liters at STP) has a $^3\text{He}/^4\text{He}$ ratio of

about 1/3 by volume. A rotary vacuum pump (model Ed330 from Edwards) and a diffusion pump (NRC model VHS-4, from Varian) make up our pumping system. It takes about 10 hours to cool from room temperature (RT) to the lowest temperature, T_{\min} , and, if necessary, the entire system can be turned around ($T_{\min} \rightarrow RT \rightarrow T_{\min}$) in 24 hours. Our 5 feet long dewar is a custom-built Cryogenic Associates "superinsulated" model with a 6-inch diameter fiberglass neck, a 12-inch diameter aluminum "belly", and a 6-inch diameter aluminum "tail". Due to the fact that fiberglass is permeable to helium at room temperature, exposure to concentrated helium gas (> 30 min) could compromise the vacuum inside the dewar. A 120 W bath heater, located at the bottom of the helium bath, facilitates rapid warming of the cryostat. The heater is equipped with a thermistor that shuts the heater off when it is just above room temperature (Mueller *et al.*, 1982).

In addition to the inner vacuum chamber (IVC), the dilution unit is surrounded by two copper radiation shields anchored at 0.6 K and 40 mK. The six step heat exchangers are made of copper and hold copper sinter. The mixing chamber is a 12 cm^3 copper cylinder holding approximately 6 m^2 of copper sinter, and is equipped with a $21.7 \text{ k}\Omega$ resistor that is used as a heater. The various experiments are mounted on two copper plates screwed into the mixing chamber. These two plates and the three copper legs connecting them have been electroplated with gold. In the next subsection, the electroplating procedure is presented. The cooling power of the dilution refrigerator is $130 \mu\text{W}$ at 100 mK with a ${}^3\text{He}$ circulation rate of $100 \mu\text{mol/sec}$ (see subsection 3.1.1.b). The minimum temperature measured outside the mixing chamber is $T_{\min} \approx 40 \text{ mK}$.

3.1.1.a Gold electro-plating

The following procedure was performed on several parts attached to the mixing chamber of our dilution refrigerator. The plating prevents the copper from oxidizing, which decreases its thermal conductivity. This procedure, which is standard in the micro-electronics industry, has been available at the University of Florida's Department of Physics through the help of Larry Phelps. Mr. Phelps supervised the plating of our parts

and assisted in the compilation of these notes. This method works exclusively for gold plating on copper.

Parts must be clean if plating is to be successful. If the parts have been machined, grease must be removed. A first wash in hydrochloric acid is followed by a dip into a Loncoterge solution made by the London Chemical Company (sold by Kepro). The parts are then washed in deionized water and finally rinsed with distilled water. The second step of the process involves estimating the surface area to be plated. This area determines the current to be used in the electro-plating. The current is calculated using the formula $I = 12.5 \text{ mA/in}^2 \times (\text{surface area})$. Once the power supply is set for the right current, the part is immersed into an Orosene 999 Gold Plating solution made by Technic, Inc. (sold by Kepro). The object to be plated is the cathode and the stainless steel bucket holding the solution is the anode. As the plating occurs, cyanide bubbles emerge from the solution. It is therefore best to perform the plating under a hood, but a well ventilated room is acceptable. The current density mentioned above was empirically found to give fairly slow outgassing. During plating of parts with complex geometries, the bubbles released may be trapped temporarily on the surface of the pieces. This effect may result in uneven plating. For this reason, it is important to keep the current low to minimize the degassing rate, giving the bubbles a chance to escape. Of course, lower currents mean slower plating rates. The above current density gives approximately 50 millionth of an inch every 40 minutes. For very flat parts, which would not trap bubbles, higher current densities can be applied. While the reaction takes place, one should occasionally agitate the parts gently to release any bubbles from the surface. After the plating has been stopped, the parts are washed with deionized water. The main plating solution can be recycled -- its cost, which follows the market price of gold, can be quite high.

3.1.1.b Measuring the ${}^3\text{He}$ circulation rate

In this subsection, the method used to estimate the ${}^3\text{He}$ circulation rate of our refrigerator is discussed. After cooling to 46 mK, the refrigerator was placed into a "one

"shot" mode, *i.e.* the gas recovered from the still was not recondensed, but stored into the cold trap ($T = 77$ K). The still was maintained at a constant temperature of about 650 mK. This still temperature was previously determined by maximizing the cooling power of the refrigerator. The pressure, P , of the cold trap was monitored as a function of time. From the volume of the trap ($V = 2.64 \times 10^{-3}$ m 3), the number of recovered moles was estimated from the ideal gas relation

$$N \text{ (moles)} = \frac{P V}{R T} , \quad (3.1)$$

where R is the universal gas constant (8.314 J mole $^{-1}$ K $^{-1}$). This method does not account for the amount of gas absorbed onto the surface of the charcoal present in the trap. Since the vapor pressure of ${}^4\text{He}$ at 650 mK (constant temperature of the still monitored through the experiment) is negligible compared to that of ${}^3\text{He}$, one can assume that the gas recovered from the still is mostly ${}^3\text{He}$. The two assumptions just mentioned, namely the ideal gas law and a 100% ${}^3\text{He}$ circulation, constitute the main source of errors for this estimation of the ${}^3\text{He}$ circulation rate, and it is important to keep in mind that the result is only a coarse estimate. Figure 3-1 shows N vs. time obtained from the above procedure. The line is the result of a linear fit, and indicates that the data fall on a straight line of slope $95 \mu\text{mol} / \text{sec}$, which corresponds to the circulation rate of ${}^3\text{He}$ for our refrigerator.

3.1.2 Thermometry

In this section, the different thermometers used on our cryostat are discussed. First, the "diagnostic" thermometers are described. These carbon resistors may be used to locate a problem, in the event that the refrigerator is malfunctioning. In the second subsection, the data acquisition thermometers are characterized. Finally, work on the

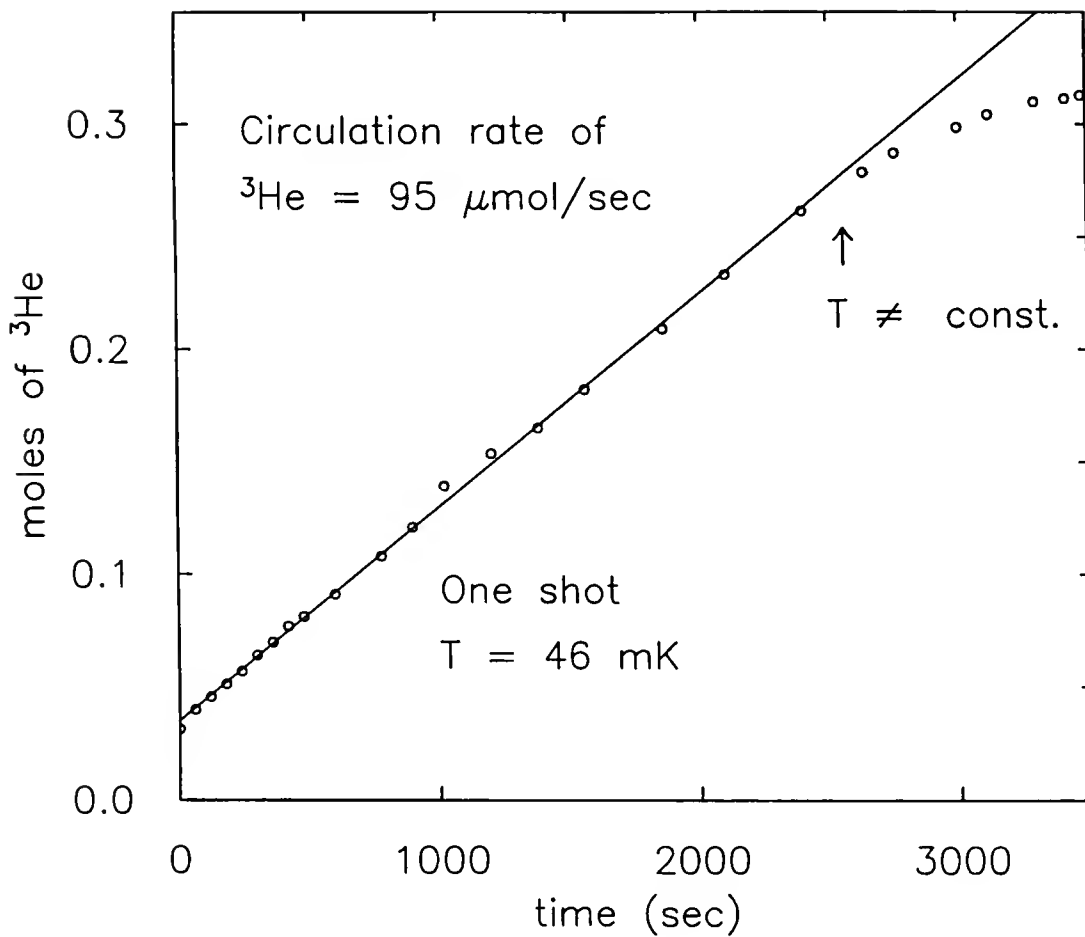


Fig. 3-1. Number of ${}^3\text{He}$ atoms (moles) as a function of time (sec) for our dilution refrigerator operated in a "one shot" mode at 46 mK. The line is the result of a linear fit. The slope of the line is $94 \mu\text{mol/sec}$, and corresponds to the ${}^3\text{He}$ circulation rate. After 2500 sec, the temperature started increasing.

magnetoresistance of thermometers and measurements of heating effects due to eddy currents are reported in the third subsection.

3.1.2.a Diagnostic thermometers

We use a total of eight diagnostic thermometers. Their labeling, location and resistance values at different temperatures are given in Table 3-1. Except for thermometer #8, all diagnostic thermometers are carbon resistors purchased from Speer. They were ground flat on two sides to expose the carbon core, and to increase the thermal contact area. The two surfaces were glued with stycast 2850 epoxy to a copper heat sink. Thermometer #8 is a RuO₂ thin film resistor. The resistances of the diagnostic thermometers are read with a Linear Research picowatt ac resistance bridge (LR110) operated in a two wire measurement mode.

Table 3-1. Labeling, location and resistance values of the eight diagnostic thermometers. All resistances are given in ohms. H. Ex. stands for heat exchanger, and M. C. stands for mixing chamber.

Labels	#1	#2	#3	#4	#5	#6	#7	#8
Location→ Temperature ↓	1K pot	Still	1 st H. Ex.	3 rd H. Ex.	5 th H. Ex.	6 th H. Ex.	M. C.	M. C.
300 K	913	771	348	336	356	346	345	1124
77 K	890	890	371	361	387	372	367	1127
4.2 K	1510	1280	410	410	420	420	410	1300
T _{min} ≈ 40 mK	2860	4990	3280	6850	7850	14000	18800	10250

3.1.2.b Data acquisition thermometers

We measure the temperature of our samples with two germanium resistive thermometers. The names "No. 26" and "LS-Burns" were adopted for them. We use

No. 26 between T_{\min} and 400 mK, while LS-Burns is used between 350 mK and 4.2 K. We measure the resistance of these two thermometers with an Linear Research ac resistance bridge (LR-400) in a four wire measurement configuration.

Other researchers, who have used thermometer No. 26, have calibrated it extensively against a ^3He vapor pressure thermometer, Cd, Zn, Al superconducting fixed points, and a ^3He melting curve thermometer. Figure 3-2 shows some of the calibration points, and the solid line represents the result of a fit to Eq. (3.2). This expression is used to determine temperatures from No. 26 resistance values, for temperatures between 40 mK and 400 mK, namely

$$T(\text{mK}) = \exp(22.188 - 6.243 \times LR + 0.7558 \times LR^2 - 0.03333 \times LR^3), \quad (3.2)$$

where $LR = \ln(R)$, and R is in ohms.

Thermometer LS-Burns (used for temperatures above 350 mK) was purchased by Professor M. Burns in 1987 from LakeShore Cryotronics, who calibrated it against a cerium magnesium nitrate magnetic thermometer as well as the National Bureau of Standards superconducting fixed points. Our laboratory inherited the use of the device after Dr. Burns joined Conductus Inc. in 1989. Figure 3-3 shows the calibration curve for LS-Burns, for which two different fits were performed. First, the calibration data were fitted to Eq. (3.3) for temperatures between 350 mK and 2 K:

$$T(\text{K}) = \sum A_i \times \cos(i \times \arccos(X)), \quad i = 0 \text{ to } 6 \quad (3.3)$$

where $X = ((Z - ZL) - (ZU - Z)) / (ZU - ZL)$, $Z = \log_{10}(R(\Omega))$, $ZL = 2.27231411327$, $ZU = 4.78304279264$, and the coefficients A_i 's are given in Table 3-2. The result of the fit is shown in Fig. 3-3.

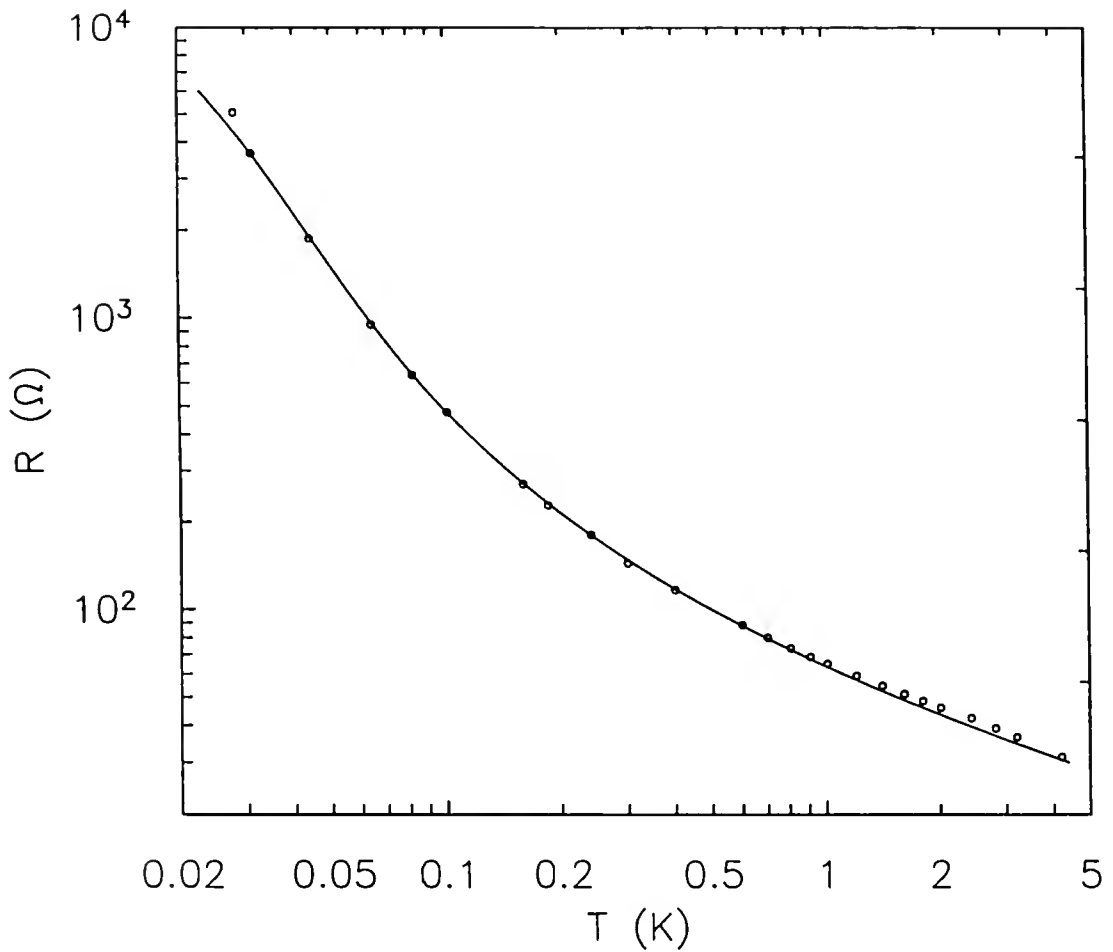


Fig. 3-2. Calibration curve for thermometer No. 26. The points, (o), were obtained from various primary thermometers (see text). The solid line represents the result of a fit to Eq. (3.1), which is used to determine temperatures from No. 26 resistance values, for temperatures between T_{\min} and 400 mK.

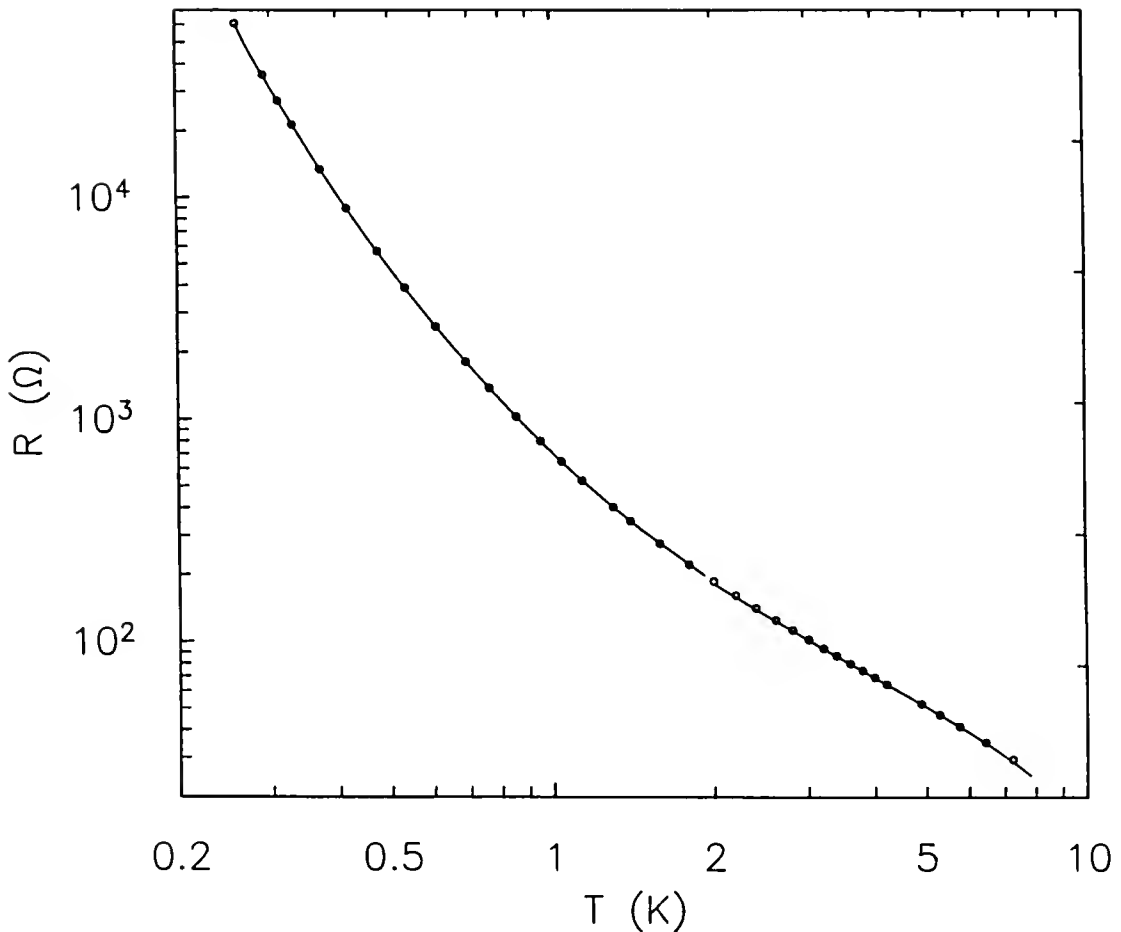


Fig. 3-3. Calibration curve for thermometer LS-Burns. The points, (o), were obtained from a cerium magnesium nitrate magnetic thermometer (LakeShore Cryotronics). The solid lines represent the results of fits which are used to determine temperatures from LS-Burns resistance values. For temperatures between 350 mK and 2 K, the data are fitted to Eq. (3.2); for temperatures above 2 K, the data are fitted to Eq. (3.3).

Table 3-2. Coefficients A_i's for Eq. (3.3), which is used to fit the calibration data for LS-Burns between 350 mK and 2 K.

A0	A1	A2	A3	A4	A5	A6
0.812184	-0.764916	0.282624	-0.095017	0.030477	-0.009407	0.002965

The second fit for the calibration data of LS-Burns was performed to Eq. (3.4) for temperatures between 2 K and 4.2 K:

$$T(K) = B_i \times R^i, \quad i = 0 \text{ to } 8 \quad (3.4)$$

where R is in ohms, and the coefficients B_i's are given in Table 3-3. The result of the fit is shown in Fig. 3-3.

Table 3-3. Coefficients B_i's for Eq. (3.4), which is used to fit the calibration data for LS-Burns between 2 K and 4.2 K.

B0	B1	B2	B3	B4
14.42179	-0.398553	7.02877×10^{-3}	-7.9265×10^{-5}	5.7991×10^{-7}
B5	B6	B7	B8	
-2.7254×10^{-9}	7.9050×10^{-12}	-1.284×10^{-14}	8.9113×10^{-18}	

3.1.2.c Thermometry in magnetic fields

We have measured the resistance as a function of temperature of a RuO₂ thick chip resistor in zero field and in fields up to 8 T. Some of the results of this work are shown in Fig. 3-4. This thermometer (named D-1k3) was manufactured by Dale Electronics, and is the RC-550 type with a nominal room temperature value of 1 kΩ. The magnetoresistance, R(B), of this unit was first studied by Meisel, Stewart, and Adams (1989), who reported $\{\{R(8T) - R(0)\}/R(0)\} = 8.8\%$ at 80 mK. Using this value, and our

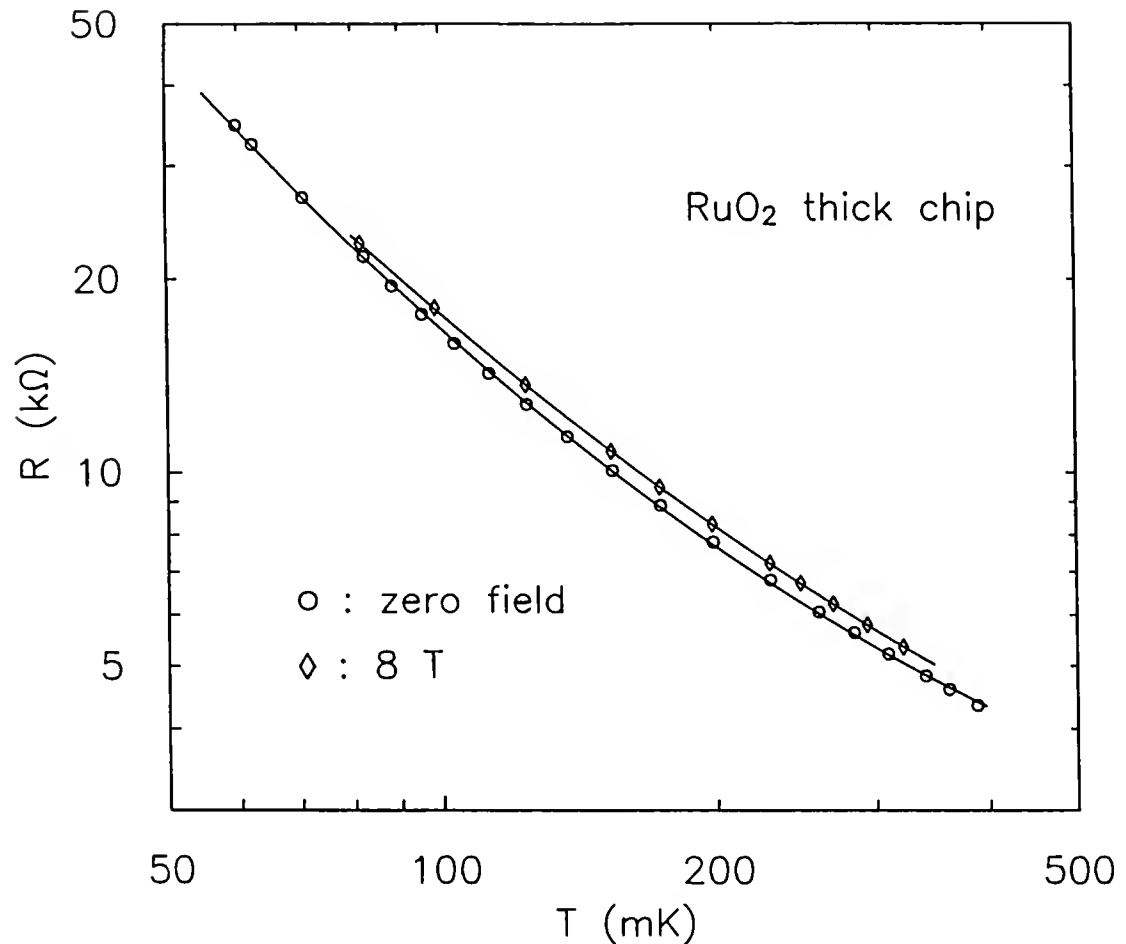


Fig. 3-4. Resistance of a RuO₂ thick chip thermometer (D-1k3) at zero field (○), and 8 T (◊). The lines are the results of fits : $\log_{10}(R) = 5.77 - 3.266 \log_{10}(T) + 0.497 [\log_{10}(T)]^2$ for zero field, and $\log_{10}(R) = 5.25 - 2.785 \log_{10}(T) + 0.391 [\log_{10}(T)]^2$ for 8 T.

observed value [$\{R(8T) - R(0)\}/R(0)$] = 3.3 %, we estimate the heating generated by our experiments (mutual inductance, see Chapters 4 and 5) to be about 3 mK at 8 T and 80 mK. Similar calculations give a temperature rise of about 1 mK at 8 T and 100 mK. These results indicate that heating does not play an important role in our field experiments, which do not extend above 8 T, or below 150 mK.

For the aforementioned magnetic field experiments, the sample was mounted on the end of a copper finger located at the center of the superconducting solenoid providing the field. The temperature was regulated with thermometers No. 26 and LS-Burns, which were mounted on the mixing chamber. To determine if a thermal gradient existed between the mixing chamber (thermometer) and the end of the copper finger (sample), we measured the resistance of another Dale thick chip when mounted on the mixing chamber (first run), and on the end of the finger (second run). The results are shown in Fig. 3-5, and indicate that there was a negligible temperature difference present between the two locations, and that the temperature read by the thermometers was that of the sample.

3.1.3 Temperature Control

The circuit used to control the temperature is shown in Fig. 3-6. A Quick Basic routine, which includes the thermometer calibration fits (Eqs. 3.2, 3.3, and 3.3), sends a command to the digital-analog converter (DAC, model 59501B from Hewlett Packard), which sends a constant voltage to the ac resistance bridge (LR400 from Linear Research). This voltage corresponds to a resistance value, which corresponds to a temperature. The relation between the voltage and the resistance is given in the manual of the LR400, and is entered in the computer routine, in addition to the relation between the resistance and the temperature (calibration fits). The LR400 compares the resistance set by the computer, via the DAC, and the resistance read from the thermometer (No. 26 or LS-Burns). A constant voltage, corresponding to the difference between the two resistances, is then sent by the LR400 to the temperature controller (LR130 from Linear Research). If the

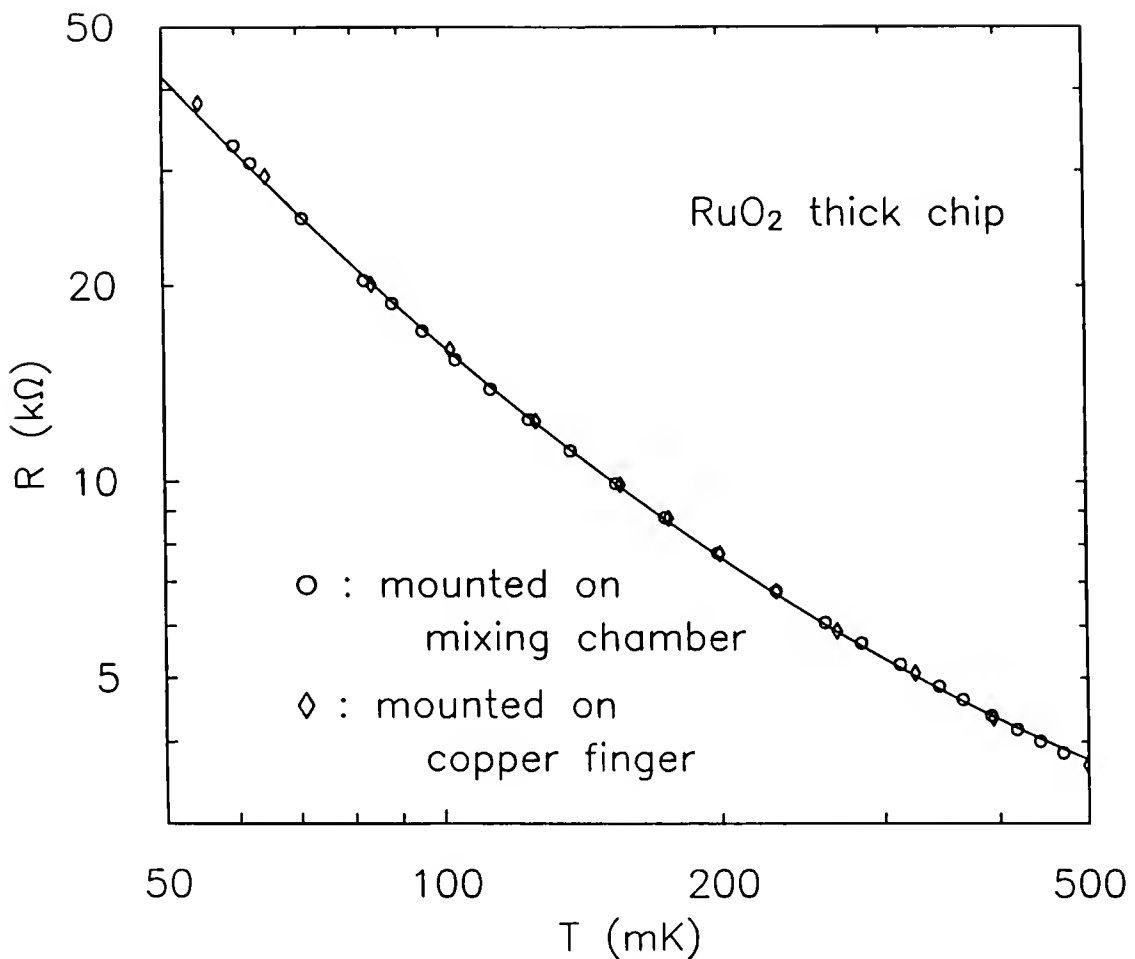


Fig. 3-5. Resistance of a RuO_2 thick chip thermometer (D-1k "B7p21") mounted on the mixing chamber (\circ), and on the end of the copper finger used for the magnetic field experiments (\diamond). The line is the result of a fit : $\log_{10}(R) = 5.50 - 3.06 \log_{10}(T) + 0.46 [\log_{10}(T)]^2$.

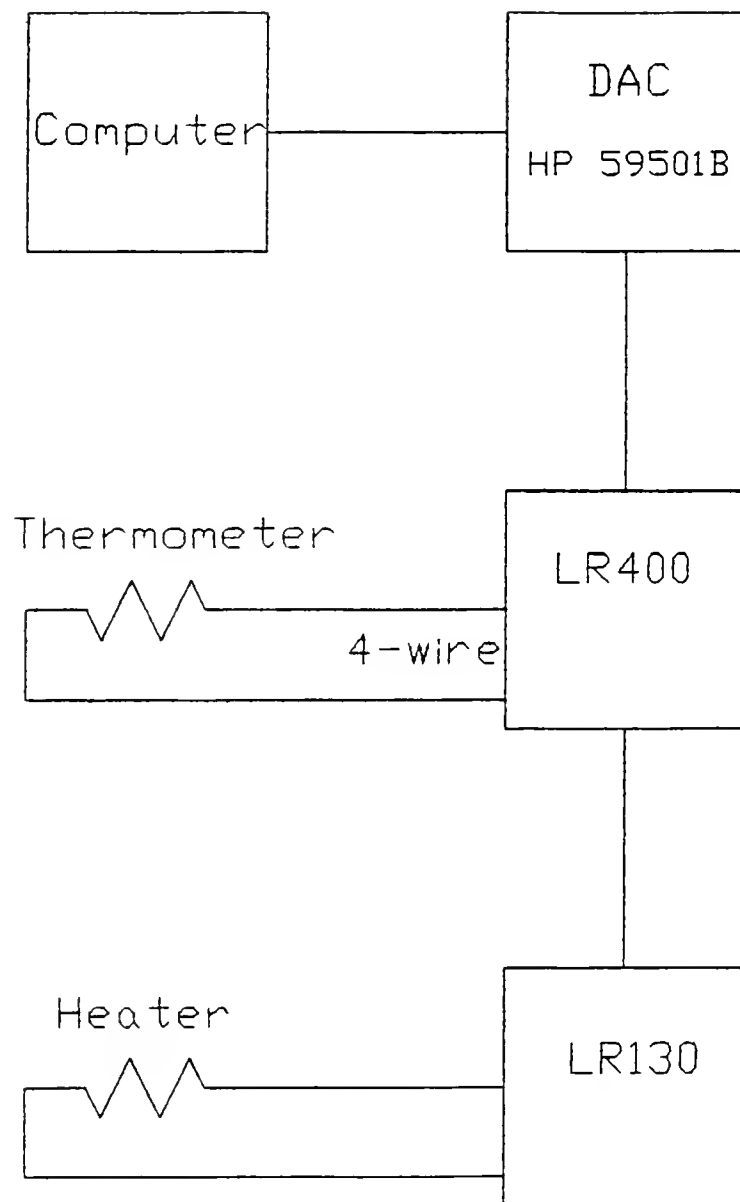


Fig. 3-6. Circuit used for temperature control.

temperature of the refrigerator is too low compared to the set temperature, the LR130 sends a voltage to a heater ($21.7\text{ k}\Omega$ resistor). If the temperature is too high, the LR130 reduces the voltage sent to the heater, and lets the refrigerator decrease the temperature. For 5 mK steps, temperature stability (within 0.5 mK) can be achieved in about 2 min.

In practice, the method just described leads to oscillations around the set temperature on the order of 3 mK. This effect can be problematic for experiments demanding a temperature to be reached without actually going above it. For example, in Chapter 5, we determine the critical temperature, T_C , of UBe_{13} samples as a function of magnetic field. In these experiments, it is important to reach T_C from the superconducting state only. An overshooting of the temperature above T_C would trap flux inside the sample and affect the determination of T_C . For these experiments, the temperature control was performed by replacing the HP 59501B by a computer-controlled, home-made DAC (built by Jeff Legg of the electronics shop) giving a constant voltage that can be ramped by steps corresponding to less than 0.05 mK. The temperature was increased very slowly (10 mK/hour) while the data was taken continuously. Using this method, the only temperature fluctuations that the sample experiences come from the instabilities of the refrigerator, and are typically less than 0.5 mK in magnitude.

3.2 ac Susceptibility

One of the experimental techniques utilized in the experiments discussed in this dissertation is the (standard) mutual inductance technique. In the first subsection, the hardware used for this technique is described. As will be shown in subsection 3.2.2, the mutual inductance technique permits the measurement of the ac susceptibility of materials. In the case of superconducting materials, the ac magnetic susceptibility of the sample is related to the penetration depth. The study of the penetration depth as a function of temperature for UPt_3 and UBe_{13} is central to this dissertation, as is discussed in Chapter 4 and Chapter 5. Therefore, it is important to derive the relationship between the detected

signal from a mutual inductance experiment and the penetration depth of a superconducting sample. This derivation is given in the second subsection.

3.2.1 Hardware Used for the Mutual Inductance Technique

The circuit used for the mutual inductance measurement is shown in Fig. 3-7. An important feature of our measurement is the use of two PAR 124A (from EG&G) lock-in amplifiers to detect the real and imaginary components of the signal. We also attempted to carry out our measurements with an SR530 from Stanford Research Systems and a 5302 from EG&G, but the PAR 124A provided the highest signal to noise ratio (typically 5000 compared to about 50 for the other two devices). However, two disadvantages with using the PAR 124A exist. First, these lock-in amplifiers can only detect one phase of the ac signal at a time, so two of them had to be used, one for each phase. Second, they are not IEEE interfaced, so an HP voltmeter was introduced, between the lock-in amplifiers and the computer, for data acquisition. Furthermore, the PAR 124A lock-in amplifiers are constant voltage sources; thus, a $47\text{ k}\Omega$ resistor was placed in front of the primary coil to insure that the current, and ac magnetic field produced inside the primary, stayed constant. The drift in the excitation current was monitored by taking data as a function of time and at constant temperature and was found to be negligible.

Another important aspect of our measurements is the fabrication of the coils (primary and secondary). The geometry and dimensions of a typical set of coils are shown in Fig. 3-8. The materials used for these coils are either Vespel Sp-1 polyimide (from Du Pont de Nemours) or phenolic, (available from McMaster-Carr). These materials are easily machinable and give a relatively low background contribution, possessing a weak, if any, temperature dependence. (We note that Vespel Sp-22 was also used, but had a susceptibility that was strongly temperature dependent, most likely due to the graphite present in it.) The primary coil is wound with approximately 500 turns of niobium-titanium superconducting wire (from Niomax Superconductors, wire CNA36/05).

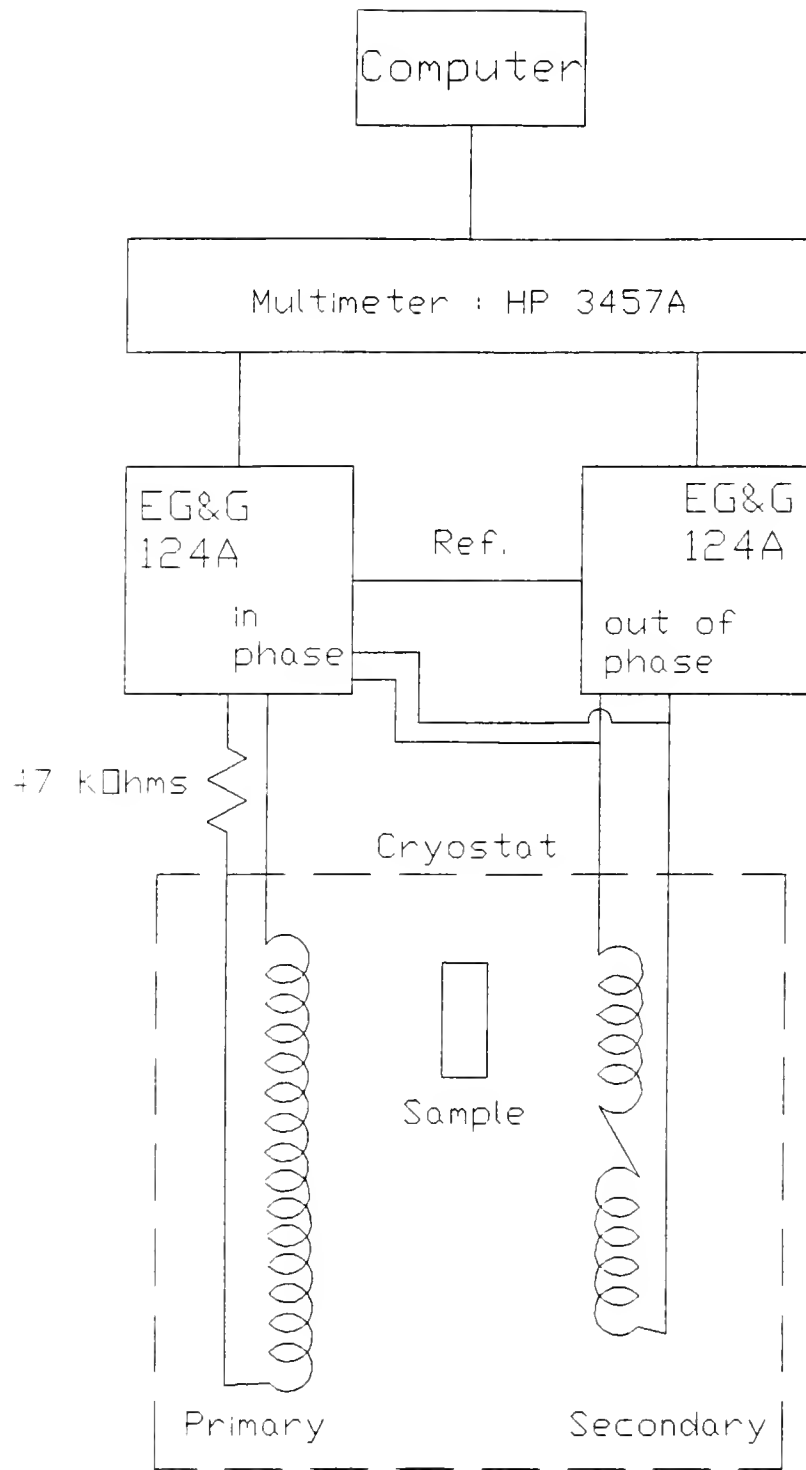


Fig. 3-7. The circuit used for the mutual inductance technique.

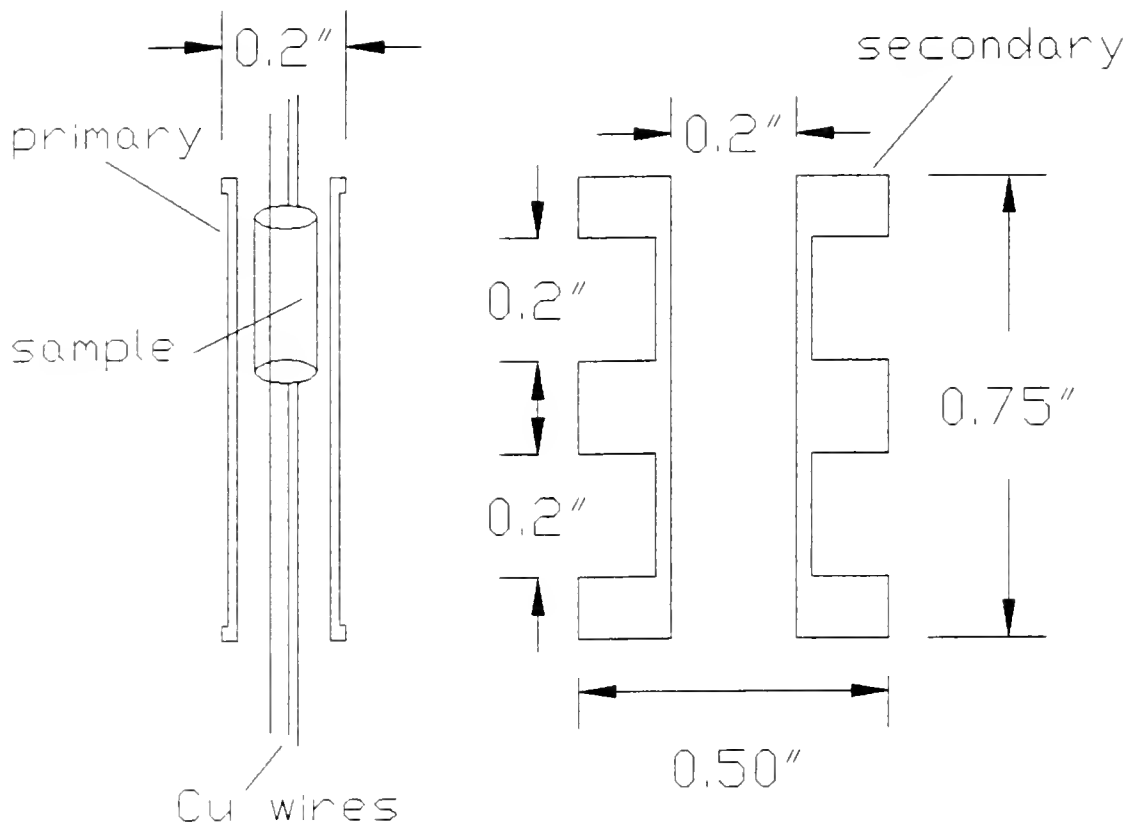


Fig. 3-8. The geometry and dimensions of the primary and secondary coils used for the mutual inductance technique. The primary coil is located inside the secondary coil.

This wire (0.002 inches in diameter) is multifilament and possesses a Cu-Ni matrix. With the excitation level on the lock-in amplifier set on 10 V_{rms}, the ac magnetic field produced at the center of the primary coil is about 10 μT. The secondary coil is wound with approximately 10,000 turns of copper wire (5000 on each half). Because the net currents flowing through the secondary coil are on the order of 1 nA, and the resistance of the coil is about 1 kΩ, the power dissipated in the coil is negligible (1×10^{-15} W).

3.2.2 Principles of the Mutual Inductance Technique

In this section, we show how the mutual inductance technique allows one to measure the penetration depth of a superconductor, $\lambda(T)$. In particular, the relationship between the magnetic susceptibility of a sample, $\chi(T) = \chi'(T) + i\chi''(T)$, and $\lambda(T)$ is reviewed.

When a specimen is located in one of the two counterwound pick-up coils (Fig. 3-7), the signal detected by the lock-in amplifiers corresponds to the difference between the voltage due to $d\Phi/dt$ (Φ is the magnetic flux) in the two pick-up coils, given by

$$V = 2\pi \frac{d}{dt} \left(\int B(r) r dr \right) - i\omega \pi r_s^2 B_{ac} , \quad (3.5)$$

where r_s is the radius of the sample, $\omega = 2\pi f$, and f is the probing frequency. In addition, we have assumed a circular sample cross-section and $B(r,\theta,z) = B(r)$. We may define the magnetic susceptibility χ by

$$\frac{2\pi}{\pi r_s^2} \int B(r) r dr = \mu_0(1 + \chi)H_{ac} , \quad (3.6)$$

where $B_{ac} = \mu_0 H_{ac}$, with μ_0 being the permeability of free space. Substituting Eq. (3.6) into Eq. (3.5) yields

$$V = i \omega \pi r_s^2 B_{ac} \chi . \quad (3.7)$$

In other words, from Eq. (3.7), the detected voltage is directly proportional to the magnetic susceptibility of the sample.

For a normal metal, we know from Maxwell's equations that the field inside the sample must satisfy

$$\nabla^2 B + K^2 B = 0 , \quad (3.8)$$

where $K^2 = i 4\pi\sigma_n\omega/c^2$ and σ_n is the normal metal conductivity. Using the definition of the normal skin depth:

$$\delta(T) = \left[\frac{2}{\mu \sigma_n(T) \omega} \right]^{1/2} , \quad (3.9)$$

we obtain

$$K(T) = \frac{(1 + i)}{\delta(T)} . \quad (3.10)$$

For a cylindrical sample of radius r_s with the field parallel to its axis, Eq. (3.8) can be solved explicitly, giving the textbook result

$$B(r) = B_{ac} \frac{J_0(Kr)}{J_0(Kr_s)} , \quad (3.11)$$

where J_0 is the 0th order Bessel function (Landau and Lifshitz). Substituting Eq. (3.11) into Eq. (3.6) gives the following expression for the magnetic susceptibility:

$$\chi = \chi' + i\chi'' = \frac{1}{4\pi} \left(-1 + \frac{2 J_1(K r_s)}{K r_s J_0(K r_s)} \right), \quad (3.12)$$

where J_1 is the 1st order Bessel function. The Bessel functions J_0 and J_1 for imaginary arguments ($\rho e^{i\phi}$) can be written as

$$J_0(\rho e^{i\phi}) = U_0(\rho, \phi) + i V_0(\rho, \phi), \quad (3.13)$$

where $U_0(\rho, \phi) = \sum_{s=0}^{\infty} (-1)^s \frac{(\rho/2)^{2s}}{(s!)^2} \cos(2s\phi), \quad (3.14)$

$$V_0(\rho, \phi) = \sum_{s=0}^{\infty} (-1)^s \frac{(\rho/2)^{2s}}{(s!)^2} \sin(2s\phi), \quad (3.15)$$

and $J_1(\rho e^{i\phi}) = U_1(\rho, \phi) + i V_1(\rho, \phi), \quad (3.16)$

where $U_1(\rho, \phi) = - \frac{d}{d\rho} [U_0(\rho, \phi) \cos(\phi) + V_0(\rho, \phi) \sin(\phi)], \quad (3.17)$

and $V_1(\rho, \phi) = \frac{d}{d\rho} [U_0(\rho, \phi) \sin(\phi) - V_0(\rho, \phi) \cos(\phi)]. \quad (3.18)$

Equations (3.13) through (3.18) were obtained from National Bureau of Standards (1943). The real and imaginary parts of the susceptibility can then be written as

$$\chi' = \frac{1}{4\pi} [-1 + 2 \frac{\rho \cos(\phi) (U_1 U_0 + V_1 V_0) + \rho \sin(\phi) (V_1 U_0 - U_1 V_0)}{\rho^2 (U_0^2 + V_0^2)}] \quad (3.19)$$

$$\text{and } \chi'' = \frac{1}{4\pi} [2 \frac{\rho \cos(\phi) (V_1 U_0 - U_1 V_0) - \rho \sin(\phi) (V_1 V_0 + U_1 U_0)}{\rho^2 (U_0^2 + V_0^2)}] , \quad (3.20)$$

where, for the normal state, ρ and ϕ are obtained from Eq. (3.10), giving

$$\rho = \frac{r_s}{\delta} ; \quad \text{and} \quad \phi = \tan^{-1}(1) = \frac{\pi}{4} . \quad (3.21)$$

In Fig. 3-9, χ' and χ'' are plotted as a function of r_s/δ . As will be shown in the next section, the shapes of $\chi'(r_s/\delta)$ and $\chi''(r_s/\delta)$ are of significant importance. By measuring both the in-phase component of the output signal and its quadrature, we obtain $\chi'(T)$ and $\chi''(T)$ independently. From Fig. 3-9, we note that for $r_s/\delta < 0.5$, $\chi'(r_s/\delta)$ and $\chi''(r_s/\delta)$ approach zero. This result will be verified in our experiments presented in Chapter 4. For example, sample No. 1 (see section 4.3.1), with $r_s \approx 0.20$ mm and $\delta(T_C, 317 \text{ Hz}) = 2.7$ mm gives $r_s/\delta \approx 0.075 \ll 0.5$, so that no significant signal is observable above T_C (see Fig. 4-13 for example).

Below T_C , the above analysis still holds, but σ_n is replaced by $\sigma_s = \sigma_1 + i\sigma_2$, where σ_1 and σ_2 are the real and imaginary parts of conductivity respectively, and Eq. (3.10) becomes

$$K^2(T) = \frac{i 4\pi \sigma_s(T) \omega}{c^2} = \frac{i 4\pi \sigma_1(T) \omega}{c^2} - \frac{i 4\pi \sigma_2(T) \omega}{c^2} = \frac{2 i}{\delta(T)^2} - \frac{1}{\lambda(T)^2} , \quad (3.22)$$

where $\lambda(T)$ is the penetration depth and is given by

$$\lambda^2(T) = \frac{c^2}{4\pi \sigma_2(T)} . \quad (3.23)$$

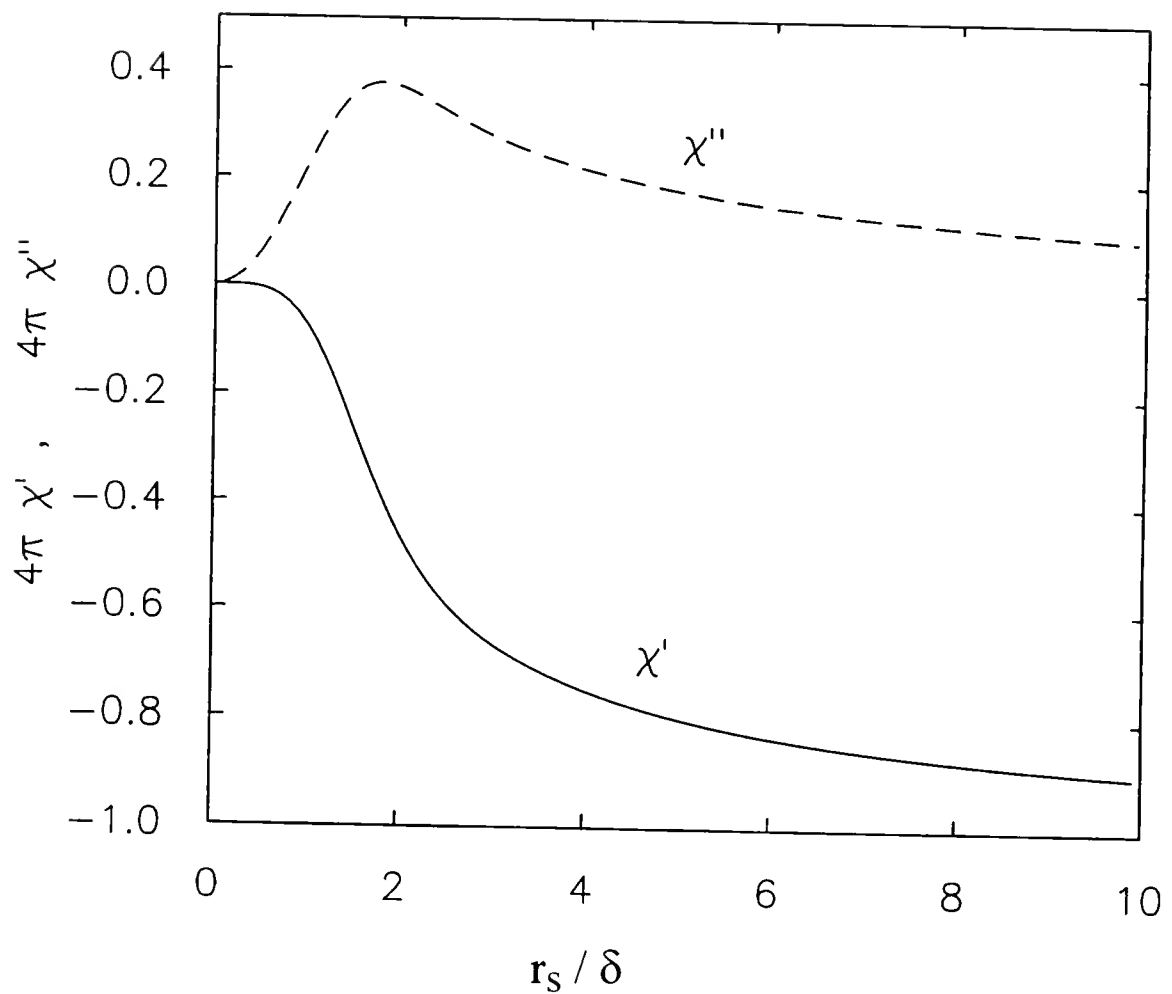


Fig. 3-9. χ' and χ'' as a function of r_s/δ , and calculated from Eqs. (3.19) and (3.20) for the normal state, i.e. $\rho = r_s/\delta$ and $\phi = \pi/4$.

Just below T_c ($T/T_c \approx 1$), both components of the complex conductivity contribute to $\chi'(T)$ and $\chi''(T)$, so that one cannot directly measure $\lambda(T)$ from either $\chi'(T)$ or $\chi''(T)$. In other words, both the magnitude, ρ , and the phase, ϕ , of the imaginary argument in Eqs. (3.19) and (3.20) are functions of $\lambda(T)$ and $\delta(T)$. This effect makes the analysis of the data around T_c difficult. In fact, several different theories exist regarding the microscopic mechanism responsible for the peak in $\chi''(T)$ in the vicinity of T_c , observed in some materials (Maxwell and Strongin, 1963; Khoder, 1983; Hein, 1986). These theories will be discussed in the following subsection. At lower temperatures ($T/T_c \ll 1$), where the real part of the complex conductivity, σ_1 , drops to zero, Eq. (3.22) takes the simple form :

$$K = \frac{i}{\lambda(T)} , \quad (3.24)$$

so that $\rho = \frac{r_s}{\lambda(T)}$ and $\phi = \tan^{-1}(\infty) = \frac{\pi}{2}$. (3.25)

Substituting Eq. (3.25) into Eqs. (3.14), (3.15), (3.17), and (3.18) gives

$$U_0 = \sum_{s=0}^{\infty} \frac{(r/2\lambda)^{2s}}{s!^2} , \quad (3.26)$$

$$V_0 = 0 , \quad (3.27)$$

$$U_1 = 0 , \quad (3.28)$$

$$V_1 = \sum_{s=0}^{\infty} \frac{2s(r/2\lambda)^{2s-1}}{s!^2} . \quad (3.28)$$

Substituting these results into Eqs. (3.19) and (3.20) gives

$$\chi'(T) \approx \frac{1}{4\pi} \left(-1 + 2 \frac{\lambda(T)}{r_s} \right), \quad (3.29)$$

$$\text{and} \quad \chi''(T) = 0. \quad (3.30)$$

Equations (3.29) and (3.30) are the central results of this section. They show that when the quadrature of our experimental output signal, $\chi''(T)$, is zero, the in-phase signal, $\chi'(T)$, is directly proportional to the penetration depth of the superconductor. This result can also be derived by assuming a field distribution inside the superconductor given by

$$B(r) = B_{ac} e^{-(r_s - r)/\lambda(T)}, \quad (3.31)$$

and substituting it in Eq. (3.6). From Eq. (3.7), we know that the output signal is also proportional to the applied ac field, B_{ac} , and to the radius of the sample, r_s . The uncertainties in the exact values of B_{ac} , the gain of the lock-in amplifier, and more importantly r_s , keep us from extracting precise absolute values for $\lambda(T)$. Consequently, our mutual inductance results only enable us to measure $\lambda(T)$ in arbitrary units.

In order to validate our technique, we have measured a number of well characterized superconductors such as Al and Zn. Figure 3-10 shows $\chi'(T)$ and $\chi''(T)$ for a cylindrical specimen ($l = 2.5$ mm, $r_s = 0.2$ mm) of 6N purity aluminum (from Morton Thiokol). The onset transition temperature was observed at 1.180 K which is in excellent agreement with earlier work on aluminum by other groups (McLean, 1962; Tedrow *et al.*, 1971). An important aspect of the data is that $\chi'(T)$ appeared to reach its minimum value just below T_c , i.e. $\chi'(T)$ was temperature independent, within our experimental resolution, from 1.1 K to T_{min} . This result can be explained by an exponentially decaying $\lambda(T)$, with

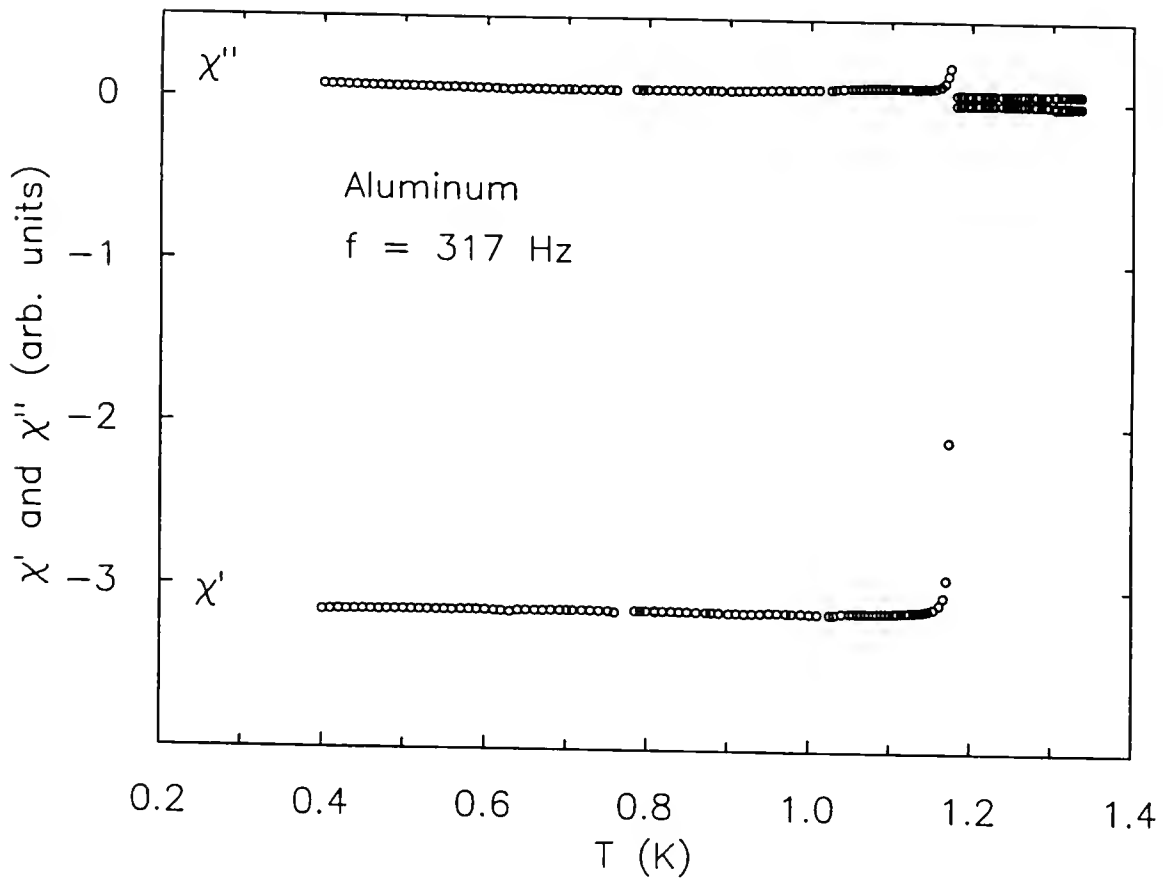


Fig. 3-10. $\chi'(T)$ and $\chi''(T)$ for Al at 317 Hz. The onset transition is 1.180 K. Within our experimental uncertainties, $\chi'(T)$ was temperature independent below 1.1 K.

changes in $\lambda(T \leq 1.1 \text{ K})$ smaller than our experimental resolution. We also performed a measurement on a cylindrical ($l = 3.8 \text{ mm}$, $r_s = 0.95 \text{ mm}$) zinc sample (a standard from National Bureau of Standards). The data on zinc, shown in Fig. 3-11, exhibited a "step-like transition", similar to the aluminum data, Fig. 3-10.

3.2.3 Peak in $\chi''(T)$ in the Vicinity of T_c and in Zero dc Magnetic Field

A great number of measurements of $\chi'(T)$ and $\chi''(T)$ on various superconductors and in zero dc field have indicated the presence of a peak in $\chi''(T)$, located at the midpoint of the transition of $\chi'(T)$. The peak has been observed in conventional superconductors, such as tin, lead-bismuth alloys, and niobium (Maxwell and Strongin, 1963; Strongin *et al.*, 1964, Hein, 1986), but also in organic (Ishida and Mazaki, 1981; Kanoda *et al.*, 1990), heavy fermion (Koziol *et al.*, 1992; Koziol, 1994; Signore *et al.*, 1992; and this work), and high- T_c superconductors (Mazaki *et al.*, 1987; van der Beek and Kes, 1991). The possibility of studying superconductivity through the presence of this peak (as well as its magnitude, anisotropy, temperature and frequency dependences) has motivated a great deal of work on this topic (Maxwell and Strongin, 1963; Gregory *et al.*, 1973; van der Klundert *et al.*, 1973; Khoder, 1983, Hein, 1986; Brandt, 1991; Itzler *et al.*, 1994). The difficulty in understanding this peak comes from the fact that, as was shown in the analysis presented above, both the real and the imaginary parts of the conductivity contribute to $\chi'(T)$ and $\chi''(T)$. In this subsection, three possible explanations for this effect are reviewed.

A simple approach was described by Gregory *et al.* (1973), who considered the peak in $\chi''(T)$ as a purely normal metal effect. In the previous subsection, expressions for $\chi'(T)$ and $\chi''(T)$ were given in Eqs. (3.19) and (3.20), which were used in conjunction with Eq. (3.21) to plot the susceptibility as a function of r_s/δ in normal metals (Fig. 3-9). From this figure, we see that $\chi''(r_s/\delta)$ goes through a peak near $r_s/\delta \approx 1.8$. Given a sample of radius r_s , the ratio r_s/δ is determined by δ only, namely the normal metal skin depth,

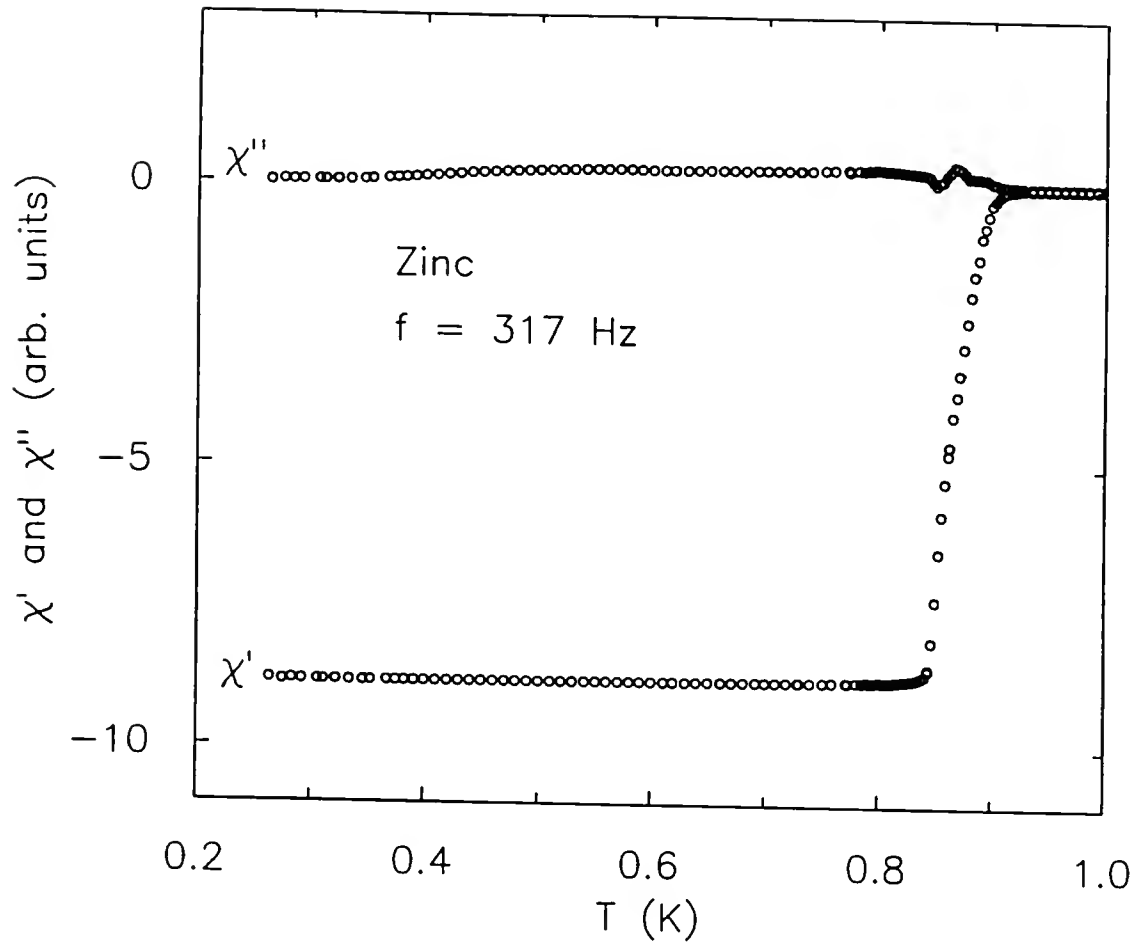


Fig. 3-11. $\chi'(T)$ and $\chi''(T)$ for Zn at 317 Hz. The onset transition is 0.9 K. Within our experimental uncertainties, $\chi'(T)$ was temperature independent below 0.8 K.

defined in Eq. (3.9). For example, a UPt₃ cylindrical sample, of radius 0.2 mm (sample No. 1 in Chapter 4), and of resistivity 0.8 $\mu\Omega\text{cm}$ (just above T_c), has a skin depth of 1.79 mm at 317 Hz (a typical value in our low frequency work), giving $r_s/\delta = 0.11$, to the left of the peak in $\chi''(r_s/\delta)$ shown Fig. 3-9. As the resistivity drops to zero below T_c , the skin depth goes to zero and the ratio r_s/δ approaches infinity. In other words, Gregory *et al.* argued that the peak in $\chi''(T)$ observed in superconductors was simply the peak in $\chi''(r_s/\delta)$ as the ratio r_s/δ goes from a small value (less than 1.8) to infinity, see Fig. 3-9. This scenario is illustrated in Fig. 3-12, where $\chi'(T)$ and $\chi''(T)$ were calculated for the above example and from a resistivity curve (shown in the figure) that one might expect for UPt₃. This explanation for the presence of the peak in $\chi''(T)$ is based solely on normal state electrodynamics and the sample size, but does not require the material to become superconducting. In fact, a few non-superconducting materials exhibit $\chi'(T)$ and $\chi''(T)$ behaviors which look similar to a superconducting transition. For example, it was noted by Gregory *et al.* that Ga-In possesses a peak in $\chi''(T)$ around 25 K, associated with a drop in $\chi'(T)$. However, specific heat and dc magnetization data clearly show that this material is not superconducting at 25 K. This example reminds us that it is prudent to study a material with several different probes before claiming superconductivity. One major argument stands against Gregory *et al.*'s explanation: the peak in $\chi''(T)$ is developed *after* the onset of superconductivity, so the electrodynamics of the superconducting state (namely the complex conductivity) must play a role.

Maxwell and Strongin (1963) proposed a different interpretation, although their explanation is still based on the normal state behavior of $\chi'(r_s/\delta)$ and $\chi''(r_s/\delta)$, and Fig. 3-9. They suggested that the electrodynamics of a superconductor could not produce a peak in $\chi''(T)$, and that both $\chi'(T)$ and $\chi''(T)$ change monotonically through the superconducting transition. To account for observed peak, they proposed that some superconductors (labeled as filamentary superconductors) exhibited traces, or filaments of superconductivity in the normal state, just above T_c . These superconducting inclusions

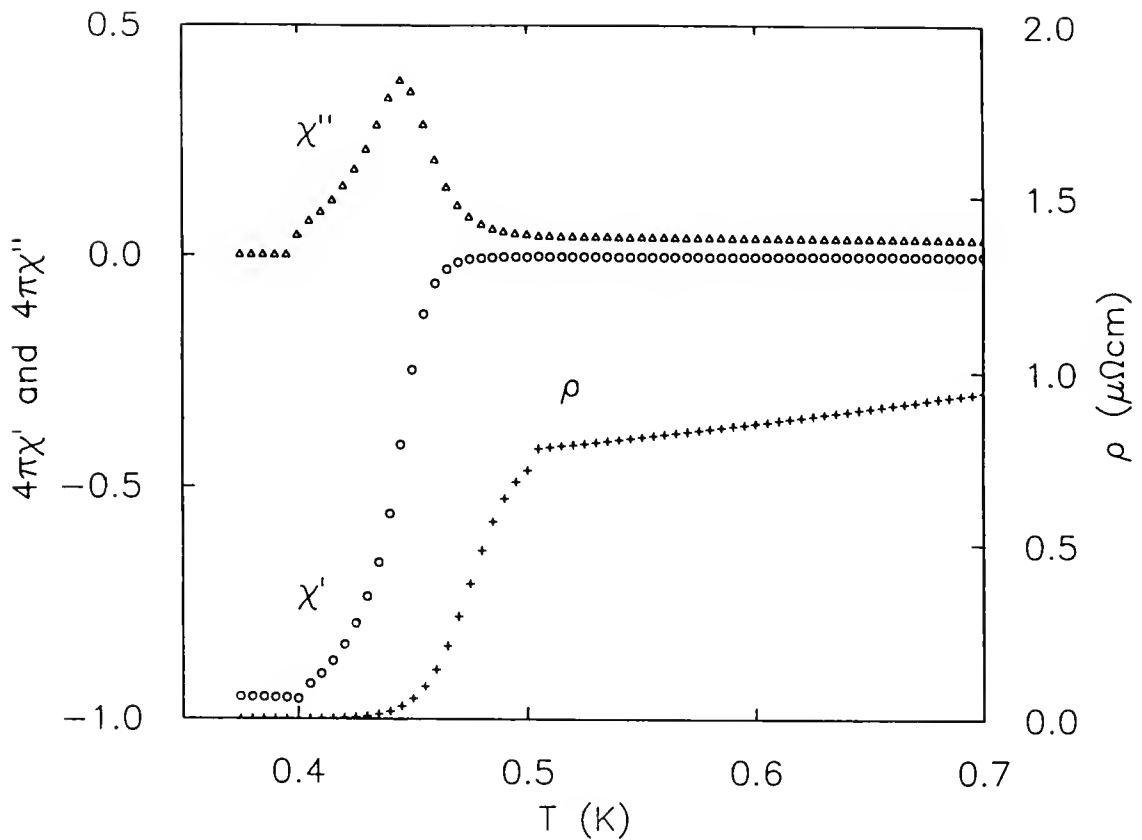


Fig. 3.12. $\chi'(T)$ and $\chi''(T)$ calculated from Eqs. (3.19) and (3.20) using the normal state relation $Kr_S = r_S(1+i)/\delta$ and the resistivity values shown here. Based on these kinds of plots, Gregory *et al.* suggested that the peaks observed in $\chi''(T)$ of superconductors, in the vicinity of T_C , can be simply explained with the electrodynamics of the normal state.

would decrease the average resistivity of the material, thereby increasing the ratio r_s/δ above 1.8 and creating a peak in $\chi''(T)$. Physically, the decrease in resistivity leads to an increase in the current density, which in turn increases dissipation inside the sample so that $\chi''(T)$ increases. As the temperature is lowered further, eddy currents become significant, and through their shielding, decrease the current density and the losses, i.e. $\chi''(T)$ decreases. Thus, this explanation gives a means to differentiate between bulk and filamentary superconductors, provided that the ratio r_s/δ is lower than 1.8 before the appearance of the superconducting inclusions.

Khoder (1983) proposed a third interpretation, which was not based on the normal state properties of $\chi'(T)$ and $\chi''(T)$. He calculated $\chi'(T)$ and $\chi''(T)$ directly from the values of σ_1 and σ_2 predicted by the weak coupling BCS theory. Khoder showed that coherence effects, which cause a peak in σ_1 below T_c (Tinkham, 1975), could account for the peak observed in superconductors. Within this picture, the peak in $\chi''(T)$ arises from the competition between two effects. The first is the ability of the supercurrents to be accelerated, which is represented by $\sigma_1(T)$. The second is the Meissner effect, represented by $\sigma_2(T)$, which reduces the field amplitude in the superconductor and thus prevents the energy absorption. Khoder's conclusion was that all bulk superconductors should exhibit a peak in $\chi''(T)$, although it might be too small to detect experimentally for some materials.

The question on the origin of the peak in $\chi''(T)$ has not been settled yet. It is possible that a combination of the above scenarios actually takes place. The presence of this effect in high- T_c materials has created new interest for this topic. In these materials, dissipation due to flux flow plays an important role, and is most likely related to the observation of the peaks. For superconductors possessing nodes in their energy gap, the finite quasiparticle density below T_c contributes to $\chi''(T)$ and must also be taken into account in the analysis. In conclusion, the behavior of $\chi'(T)$ and $\chi''(T)$ just below T_c is a complex, unsolved problem. Understanding the peak in $\chi''(T)$ should provide information about superconductivity, and this topic should be studied further in the future.

3.3 Tunnel Diode Oscillators

Tunnel diode resonating circuits have been used to study penetration depth, $\lambda(T)$, of various superconductors for a number of years (Tedrow *et al.*, 1971; Varmazis and Strongin, 1974; and Varmazis *et al.*, 1975). In this section, the hardware associated with this technique is presented first, followed by a discussion on how the penetration depth of a superconductor, $\lambda(T)$, can be measured using this method.

3.3.1 Hardware Used for the Tunnel Diode Oscillator Technique

3.3.1.a Circuit

The circuit used for the tunnel diode oscillator (TDO) technique is shown in Fig. 3-13. The voltage divider is comprised of two 1.35 V mercury batteries, and two variable resistors (0-1k Ω and 0-10k Ω) connected in parallel. The 10 k Ω resistor is connected in series with the load. The tunnel diode is connected in parallel with a capacitor, $C_2 = 5 \text{ pF}$, which contributes to the stabilization of the oscillations. The tank circuit is comprised of an inductor, L, inside which the sample is placed, and a capacitor, C_1 , the value of which can be varied to change the resonance frequency of the circuit. The rf signal is amplified (using a model W500K from Tron-Tech) before being read by a frequency counter (model 5385A from Hewlett-Packard), which is IEEE interfaced.

3.3.1.b Coils

The inductors are fabricated from phenolic (available from McMaster-Carr) and are wound with several hundred turns of copper wire. A number of coils, with inductances on the order of 1 μH , were fabricated in order to maximize the packing factor for the differently sized samples.

3.3.1.c Tunnel diodes

A tunnel diode is a heavily doped $p-n$ junction, which combines a tunneling current with a regular diode current to give its unusual I-V curve, shown in Fig. 3-14. The diode

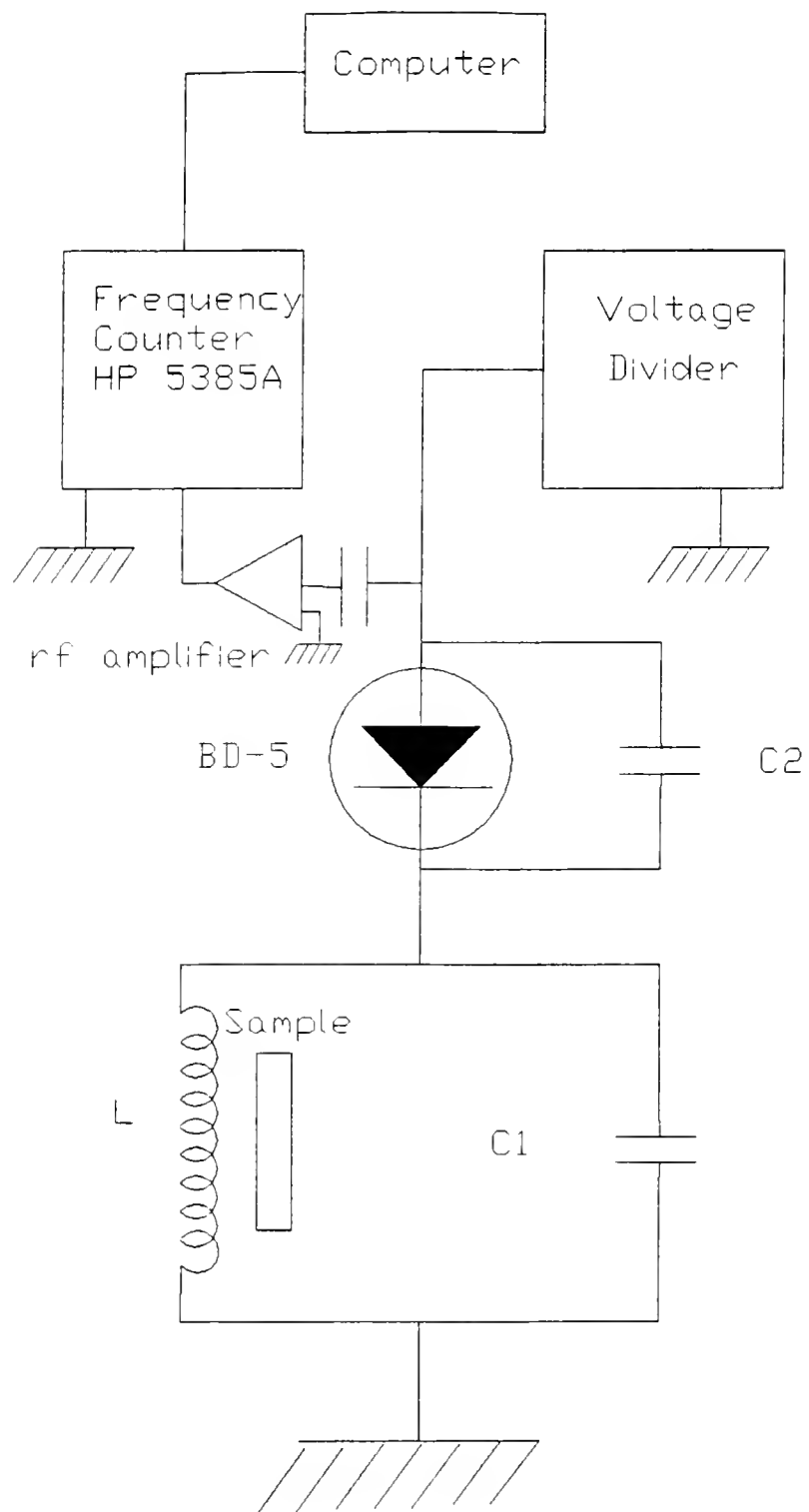


Fig. 3-13. The circuit used for the tunnel diode oscillator technique.

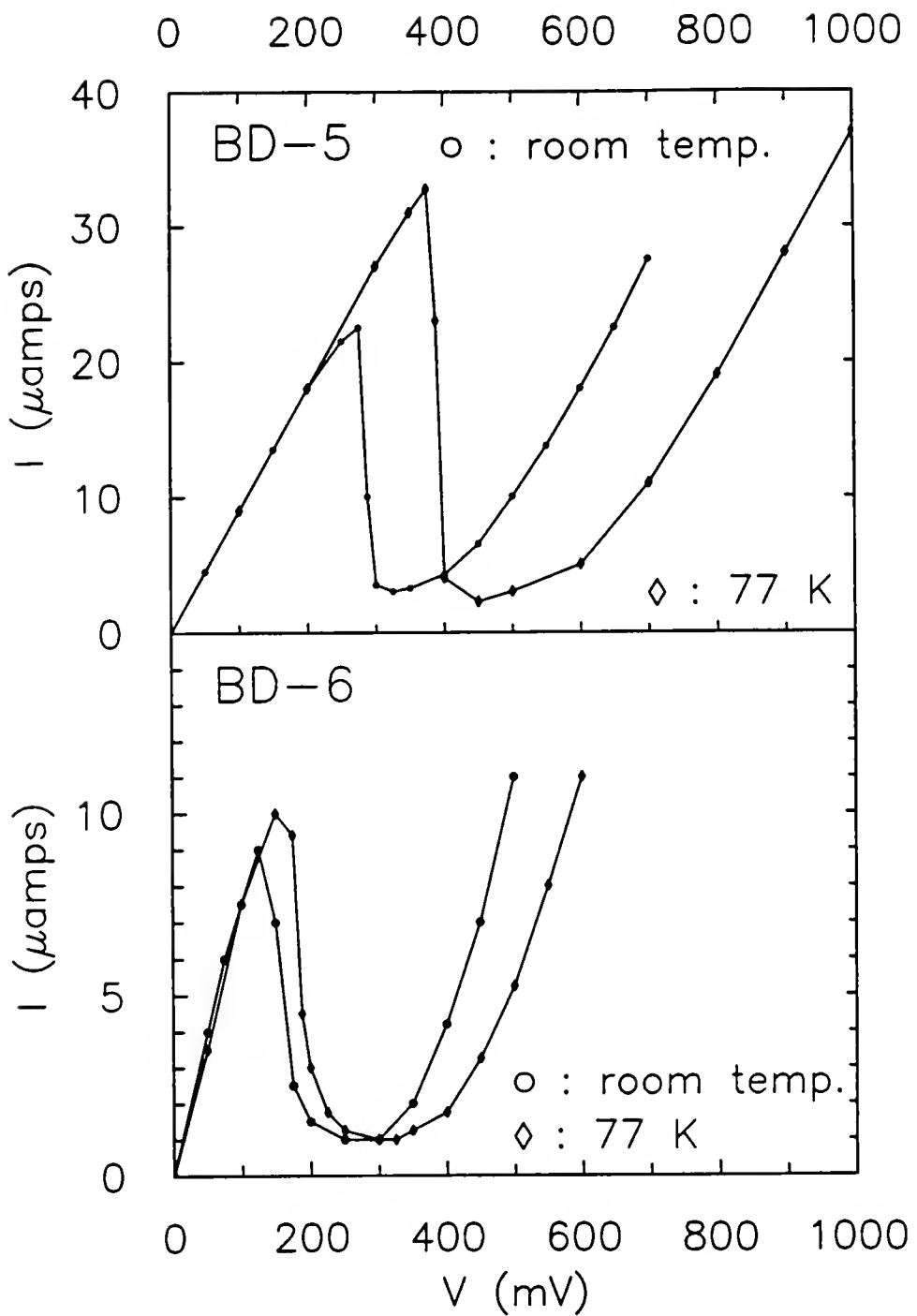


Fig. 3-14. Typical I-V characteristic of tunnel diodes at room temperature (O), and at 77 K (◊). (a) model BD-5 and (b) model BD-6, measured in our laboratory.

can be biased so as to possess an effective "negative resistance". Because of this property, tunnel diodes can be used to build oscillating circuits, amplifiers and other devices, which are discussed in detail by Chow (1964). The tunnel diodes that we use are models BD-5 and BD-6 from Germanium Power Devices (~\$50 each).

3.3.2 Tunnel Diode Oscillators and Penetration Depth

The tunnel diode oscillator operates on the basis of a small bias voltage (≈ 150 mV) being applied across a tunnel diode to keep it within its negative resistance region. The diode then generates a small oscillating current (~ 100 μ A) through a tank circuit connected in series. The specimen to be studied is placed inside the inductor, L, of the circuit. A change in either the penetration depth for $T < T_c$, or the skin depth for $T > T_c$, causes a change in inductance which in turn results in a shift in the resonant frequency. It can be shown that the change in frequency of the oscillator is given by

$$\frac{\Delta f}{f_0} = -\frac{\Delta L}{2L_0} \left(1 - \frac{2}{Q^2}\right) - \frac{\Delta R}{R} \left(\frac{1}{Q^2}\right), \quad (3.32)$$

where R is the resistance of the tank circuit, $Q = 2\pi f L/R$, $\Delta f = f(T_{\min}) - f(T)$, $f_0 = f(T_{\min})$, $\Delta L = L(T_{\min}) - L(T)$, and $L_0 = L(T_{\min})$ (Chow, 1964). Thus, if Q is large enough, the relative change of frequency is simply given by

$$\frac{\Delta f}{f_0} = -\frac{\Delta L}{2L_0}. \quad (3.33)$$

Tedrow (1971) measured the Q of tunnel diode oscillating circuits similar to the one used in our work, and found that if the Q is large enough (≥ 100) to allow oscillations, then it is large enough to make the terms in $1/Q^2$ in Eq. (3.32) negligible, so that Eq. (3.33) can indeed be applied. We qualitatively verified this assertion by performing TDO

measurements on Cu with various size inductors and samples, and found that for small L (low Q) the circuit did not oscillate, but for larger L (high Q) oscillations were stable. Equation (3.33) can also be written as

$$\frac{\Delta f}{f_0} = \frac{\pi r_s \Delta \Lambda}{A}, \quad (3.34)$$

where r_s is the radius of the sample, A is the cross-sectional area between the coil and the sample, and Λ is either the skin depth δ when $T > T_c$, as defined in Eq. (3.9), or the penetration depth λ for $T < T_c$, as defined in Eq. (3.23). Consequently, the experiment consists of monitoring the frequency as a function of temperature.

The disadvantage of this technique, compared to a mutual inductance measurement, is its inability to measure the resistive contribution. On the other hand, one advantage comes from the fact that, in the normal state, $\Delta f / f$ is proportional to $\Delta\delta(T)$. If the resistivity of the sample just above T_c is known, then one can use the normal state data to calibrate the coil and estimate absolute values for $\lambda(T)$.

An additional advantage to this technique is its ability to achieve frequency stability on the order of 5 parts in 10^6 or better. The radio frequency field, B_{rf} , generated inside the inductor was always less than $10 \mu\text{T}$.

To check our method, we have performed several runs on Al and Zn. The data for a cylindrical specimen ($l = 6.3 \text{ mm}$, $r_s = 0.5 \text{ mm}$) of 6N purity Al is shown in Fig. 3-15. The onset transition temperature was observed at 1.175 K, in good agreement with the results of other groups (Behroozi *et al.*, 1974), and with T_c observed in our low frequency measurements, Fig. 3-10. The data fit well the BCS temperature dependence for a non-local superconductor

$$\lambda(T) = \lambda(0) \left[\frac{\Delta(T)}{\Delta(0)} \tanh \left(\frac{3.53 \Delta(T)}{4t \Delta(0)} \right) \right]^{-1/3}, \quad (3.35)$$

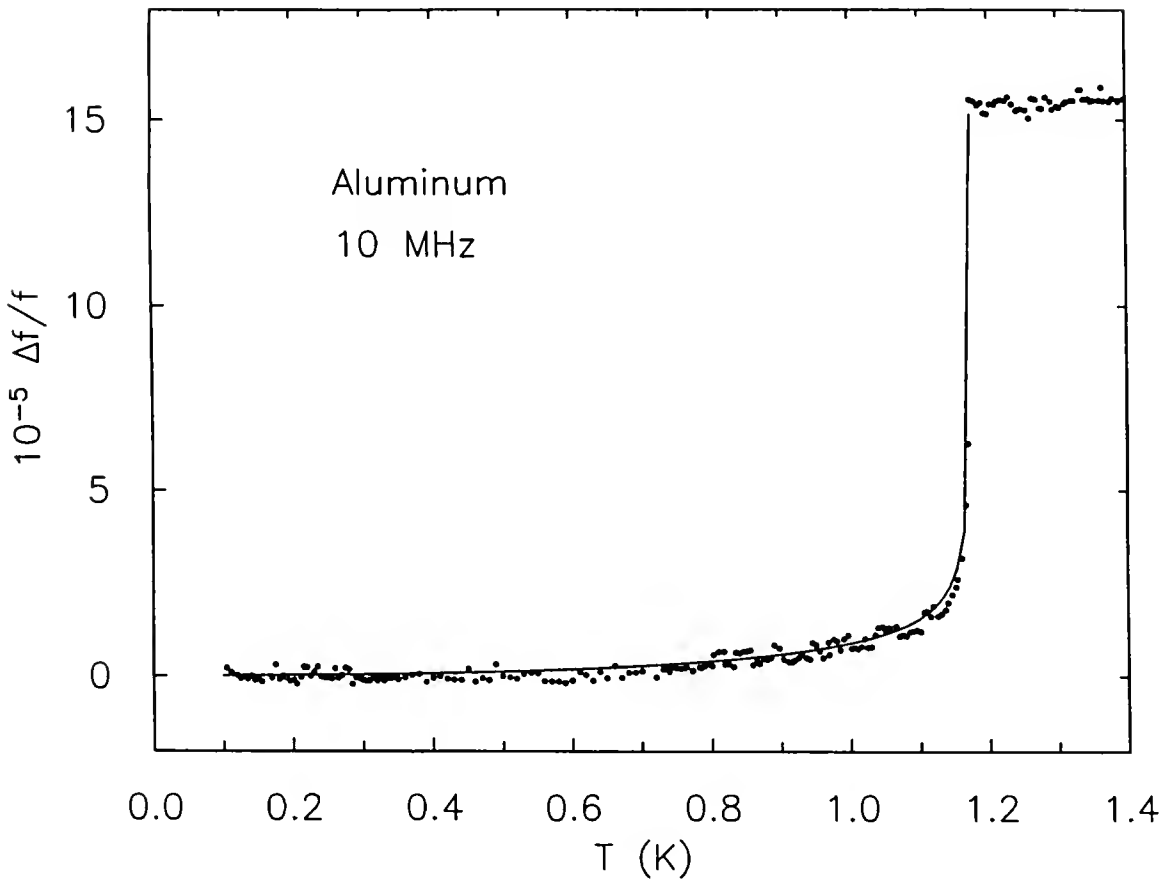


Fig. 3-15. The relative change in frequency, $\Delta f / f = [f(T_{\min}) - f(T) / f(T_{\min})]$, as a function of temperature for Al at 10 MHz. The solid line is a nonlinear least squares fit to the BCS temperature dependence given in the text, (assuming $\lambda(0) = 500 \text{ \AA}$, (Raychaudhuri *et al.*, 1983)). The transition temperature is 1.175 K, in good agreement with the 317 Hz data (Fig. 3-10).

where $2\Delta(t)$ is the BCS energy gap function, $t = T/T_C$, and we have assumed $\lambda(0) = 500 \text{ \AA}$, which is the estimated value for aluminum (Raychaudhuri *et al.*, 1983). The data for zinc is shown in Fig. 3-16, and these results support the preceding discussions.

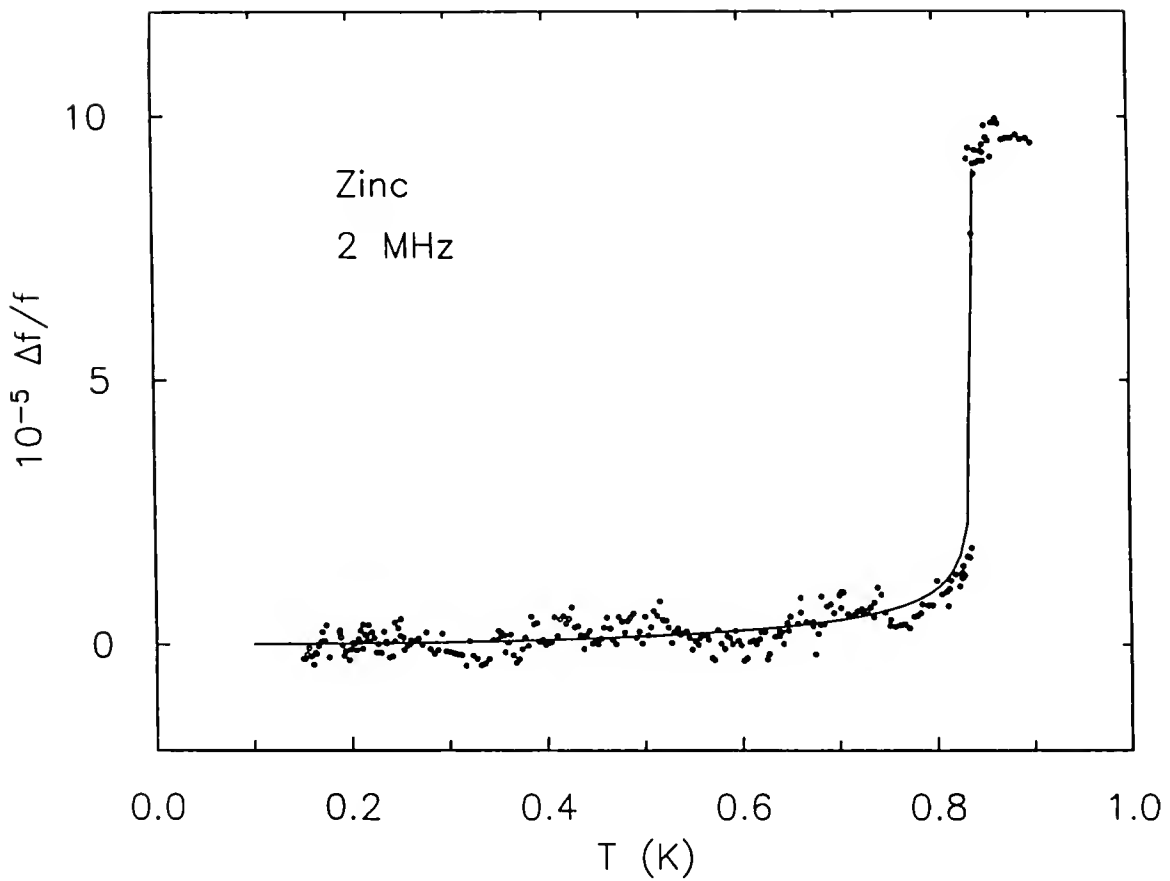


Fig. 3-16. The relative change in frequency, $\Delta f / f = [f(T_{\min}) - f(T) / f(T_{\min})]$, as a function of temperature for Zn at 2 MHz. The solid line is a nonlinear least squares fit to the BCS temperature dependence given in the text, (assuming $\lambda(0) = 290 \text{ \AA}$, (Raychaudhuri *et al.*, 1983)). The transition temperature is 0.84 K.

CHAPTER 4

INDUCTIVE MEASUREMENTS -- UPt₃

In this chapter, the inductive measurements performed on UPt₃ are presented. In section 4.1, a brief theoretical description of the penetration depth, $\lambda(T)$, is given for both conventional and unconventional superconductors. In section 4.2, the results of previous experimental investigations of $\lambda(T)$ for UPt₃ by other groups are reviewed. Next, the fabrication and treatment histories of the various samples used in our study are given (section 4.3). Our results are presented and discussed in sections 4.4 and 4.5. Finally, conclusions from this investigation are drawn.

4.1 Penetration Depth in Superconductors

Since the bulk of the work presented in this chapter relates to measuring the penetration depth of UPt₃, it is important to understand what one learns from such measurements. In the first subsection, the relationships between penetration depth and microscopic quantities, such as the density of superconducting electrons and the energy gap, are presented. The different temperature dependences of the penetration depth predicted by the BCS theory are then given. In the second subsection, the temperature and frequency dependences of $\lambda(T)$ in unconventional superconductors are discussed. Finally, the motivation for studying the penetration depths of various superconductors is summarized.

4.1.1 Conventional Superconductors

A good starting point is to consider the response of superconducting electrons to an external electric field, E . The electrons will experience a force equal to $-eE$, such that

$$m \frac{dv}{dt} = -eE, \quad (4.1)$$

where $-e$ is the electric charge of one electron. Since the current density carried by these electrons is $j = -e v n_s$, Eq. (4.1) can be rewritten as

$$\frac{d}{dt} j = \frac{n_s e^2}{m} E, \quad (4.2)$$

where n_s is the density of superconducting electrons. Substituting Eq. (4.2) into Faraday's law of induction gives the following relation

$$\frac{d}{dt} \left(\nabla \times j + \frac{n_s e^2}{m c} B \right) = 0. \quad (4.3)$$

This relation, together with the Maxwell equation,

$$\nabla \times B = \frac{4\pi}{c} j, \quad (4.4)$$

determines the magnetic field and current densities that can exist within a *perfect conductor*, i.e. zero resistance material, but with a finite homogeneous magnetic field inside. In Eq. (4.4), the time variation is assumed to be so slow that the displacement currents can be neglected.

4.1.1.a The London equation

In order to account for the Meissner effect (zero magnetic field inside the superconducting sample), F. London and H. London proposed that the expression in

parenthesis in Eq. (4.3) had to be not only time-independent, but also equal to zero, so that

$$\nabla \times \mathbf{j} = -\frac{n_s e^2}{m c} \mathbf{B}. \quad (4.5)$$

This expression is called the London equation, and legitimately describes superconductors because it leads directly to the Meissner effect. Equations (4.4) and (4.5) imply that

$$\begin{aligned} \nabla^2 \mathbf{B} &= \frac{4\pi n_s e^2}{m c^2} \mathbf{B}, \text{ and} \\ \nabla^2 \mathbf{j} &= \frac{4\pi n_s e^2}{m c^2} \mathbf{j}. \end{aligned} \quad (4.6)$$

These equations indicate that currents and magnetic fields in superconductors can exist only within a layer of thickness λ_L of the surface, where λ_L , known as the London penetration depth, is given by

$$\lambda_L(T) = \left(\frac{m c^2}{4\pi n_s(T) e^2} \right)^{1/2}, \quad (4.7)$$

where the temperature dependences of $\lambda_L(T)$ and $n_s(T)$ has been explicitly noted. Equation (4.7) states that a measurement of $\lambda_L(T)$ directly gives the temperature dependence of the density of superconducting electrons.

4.1.1.b Temperature dependence of $\lambda_L(T)$

Prior to the BCS theory, temperature dependences of $n_s(T)$ and $\lambda_L(T)$ could not be microscopically predicted. The only insight came from experiments suggesting the empirical function

$$\frac{\lambda_L(T)}{\lambda_L(0)} = \left[1 - \left(\frac{T}{T_c} \right)^4 \right]^{-1/2}, \quad (4.8)$$

which provided good fits to some data for $T/T_c > 0.5$. As the BCS microscopic theory emerged, with its description of a gap in the excitation spectrum at the Fermi level, it became clear that $n_s(T)$ was dependent upon on the structure of this energy gap and its temperature dependence. Using the predicted BCS energy gap, $\Delta(T)$, it became possible to estimate the expected $n_s(T)$ and $\lambda_L(T)$. However, there exists no simple analytical form for $n_s(T)$ in terms of $\Delta(T)$. Nevertheless, one finds $n_s(T) \sim \Delta(T)$ in the limit $T/T_c \ll 1$, and $n_s(T) \sim \Delta^2(T)$ for $T/T_c \approx 1$ (Tinkham, 1975). The temperature dependence of the gap cannot be put into analytical form either, but requires numerical methods. Such numerical calculations have been tabulated by Mühlischlegel (1959), and these exact results, for the weak coupling BCS theory, have been fit to the analytical expression

$$\Delta(T) \approx \Delta(0) \tanh \left\{ \frac{k_B T_c \pi}{\Delta(0)} \sqrt{\frac{2}{3}} (1.43) \left(\frac{T}{T_c} - 1 \right) \right\} \quad (4.9)$$

which is approximately valid for the entire range of T/T_c , and where $\Delta(0) = 1.76 k_B T_c$. For the limits $T/T_c \ll 1$, and $T/T_c \approx 1$, the BCS gap can be put into analytical form, and is given by the expressions

$$\Delta(T) \approx \Delta(0) - (2\pi \Delta(0) k_B T)^{1/2} e^{-\Delta(0)/k_B T} \quad T/T_c \ll 1 \quad (4.10)$$

and

$$\frac{\Delta(T)}{\Delta(0)} \approx 1.74 \left(1 - \frac{T}{T_c}\right)^{1/2}, \quad T/T_c \approx 1 \quad (4.11)$$

(Fetter, 1980; Tinkham, 1975). Equations (4.9) through (4.11) are valid only for the weak coupling limit and for frequencies of the electromagnetic field much less than $\Delta(0)$. Substituting Eq. (4.10) into Eq. (4.7), with the relation $n_s(T) \sim \Delta(T)$, gives for $T/T_c \ll 1$

$$\lambda_L(T) = \lambda_L(0) + \frac{\lambda_L(0)}{2} \left[\frac{2\pi k_B T}{\Delta(0)} \right]^{1/2} e^{-\Delta(0)/k_B T}, \quad (4.12)$$

where

$$\lambda_L(0) = \left[\frac{m c^2}{4\pi e^2 \Delta(0)} \right]^{1/2}. \quad (4.13)$$

Equation (4.12) states that the temperature dependence of the penetration depth expected for a BCS superconductor is exponential. In order to estimate $\lambda(T)$ for the entire temperature range (up to $T/T_c = 1$), one has to rely on numerical calculations. Such a calculation is outlined in Appendix B. The temperature dependence of $\lambda(T)$ from the BCS weak coupling theory (see Appendix B) is shown in Fig. 4-1, where we used Eq. (4.9) for the temperature dependence of the energy gap. Also shown is the same dependence plotted against T^2 , T^3 and T^4 . From this graph, it is clear that $\lambda_L(T)$ is difficult to distinguish from a power law close to T^3 if the data does not go below $T/T_c \approx 0.1$. This fact is important because, as is discussed in the next subsection (4.1.2), a T^3 power law is predicted for certain unconventional gap structures. Furthermore, our measurements for

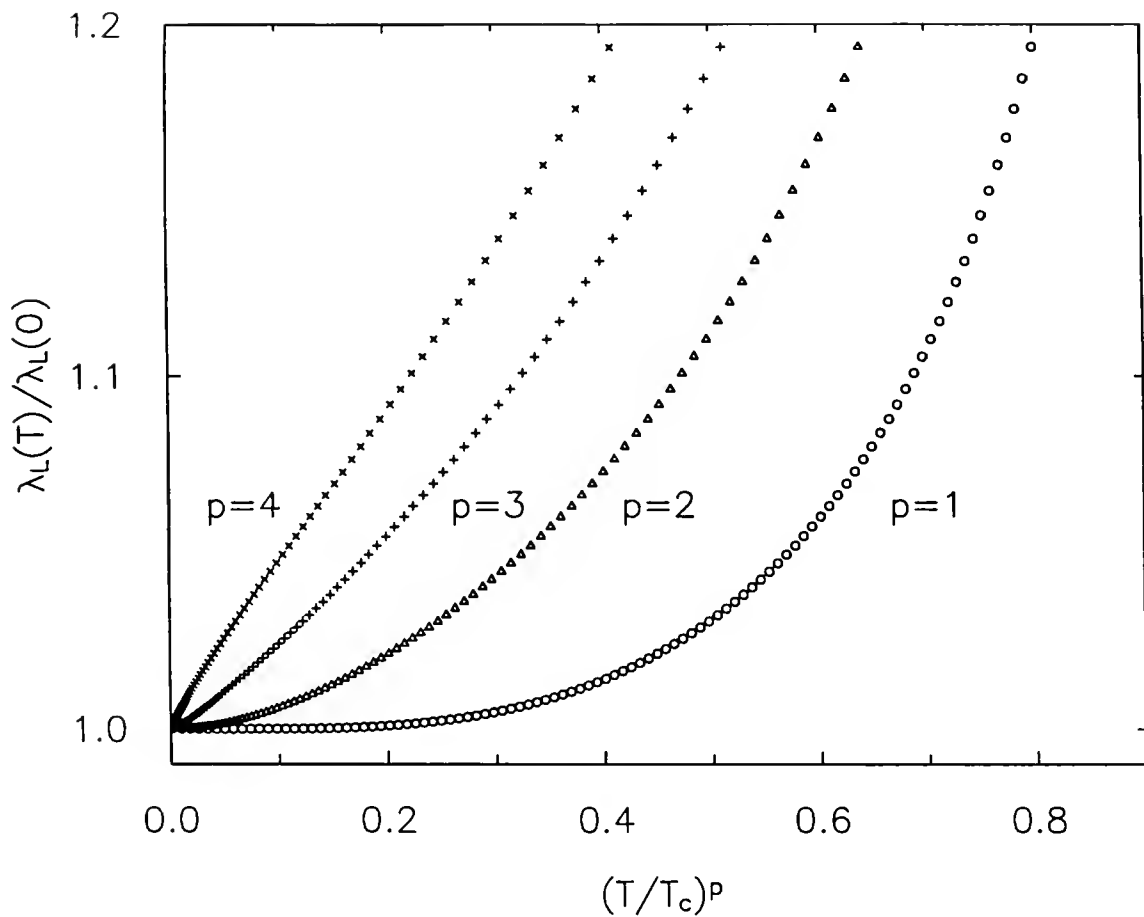


Fig. 4-1. $\lambda_L(T)/\lambda_L(0)$ in the local limit, expected for a conventional weak coupling superconductor (using Eq. (4.9) and the numerical calculation outlined in Appendix B) (o). The temperature dependence is plotted as a function of $(T/T_c)^p$, where $p = 1$ (o), $p = 2$ (Δ), $p = 3$ (+), and $p = 4$ (x). Above $T/T_c = 0.1$, the predicted BCS temperature dependence is close to T^3 and T^4 .

one sample of UBe₁₃ (Chapter 5) indicate that $\lambda_L(T)$ follows a power law close to T^3 , but can also be fitted to the BCS expression.

Another important point from Eq. (4.12) is that the exponential nature of $\lambda_L(T)$ is independent of the field orientation. This isotropic property is due to the fact that the BCS gap is finite everywhere around the Fermi surface. Finally, Eq. (4.12) indicates that $\lambda_L(T)$ is independent of the probing frequency, f , as long as $f \ll \Delta(0)$.

4.1.1.c Local vs. non-local

Equation (4.7) was derived assuming that the electromagnetic fields were slowly varying on a scale of the coherence length, ξ . This assumption holds when $\lambda(0) \gg \xi$, which defines the local or London limit, and which characterizes type II superconductors. It has already been shown in Chapter 2 that UBe₁₃ is strongly type II, so the local limit is appropriate. For UPt₃, our measurements have shown that $\lambda(0) \approx 2 \times 10^4 \text{ \AA}$ (see results on sample No. 1 below). The coherence length has been estimated from measurements of the upper critical field by Chen *et al.* (1984) to be about 100 Å, making UPt₃ a strong type II superconductor as well. Therefore, if UPt₃ had a finite gap surrounding the Fermi surface, one would expect the temperature dependence of the penetration depth to follow the expression given in Eq. (4.7) with $m \rightarrow m^*$.

Type I superconductors, such as aluminum ($\lambda(0) \approx 520 \text{ \AA}$, $\xi \approx 15,000 \text{ \AA}$) and tin ($\lambda(0) \approx 500 \text{ \AA}$, $\xi \approx 3,000 \text{ \AA}$), do not fall into the local limit (Raychaudhuri *et al.*, 1983). For these superconductors, non-local effects have to be included in the calculation of $\lambda(T)$, which then becomes (Tinkham, 1975)

$$\frac{\lambda(T)}{\lambda(0)} = \left[\frac{\Delta(T)}{\Delta(0)} \tanh \frac{\Delta(T)}{2k_B T} \right]^{-1/3}, \quad (4.14)$$

where $\Delta(T)$ is defined in Eqs. (4.9), (4.10), and (4.11).

4.1.2 Unconventional Superconductors

One might expect that the relationship between $n_s(T)$ and $\Delta(T)$ given for a finite energy gap around the entire Fermi surface ($n_s(T) \sim \Delta(T)$ for $T/T_c \ll 1$) would be different for superconductors possessing nodes in their energy gaps. It would follow, therefore, that the temperature dependence of the measured penetration depth, $\lambda(T)$, may not possess the exponential form given by Eq. (4.7). This assumption is indeed correct, as the next subsection will show.

4.1.2.a Temperature dependence

Assuming a spherical Fermi surface, Gross *et al.* (1986) have calculated $n_s(T)$ and $\lambda(T)$ for two different gap structures possessing nodes. The first gap structure, referred to as the axial state, is characterized by point nodes where the z-axis intersects the Fermi surface. The second state, namely the polar state, possesses a line of nodes where the equatorial plane crosses the Fermi surface. In addition, Gross *et al.* calculated the effect of non-magnetic impurity scattering on $\lambda(T)$ for these two states. Their calculations were given in terms of the orientation of the vector potential, \mathbf{A} ($\mathbf{B} = \nabla \times \mathbf{A}$), with respect to the local unit axis of the gap symmetry, \mathbf{l} . These results indicate that $\lambda(T)$ in clean, unconventional superconductors should follow a power law for $T \ll T_c$, so that

$$\lambda(T) \propto T^\eta, \quad (4.15)$$

and these are summarized in Table 4-1. It is important to note that η depends on the orientation of the field with respect to the crystal, in contrast to the situation in a BCS superconductor where the dependence is always exponential regardless of the field orientation. This anisotropy vanishes if sufficient impurity scattering is present, in which case a quadratic dependence is recovered for all orientations.

Table 4-1. Predicted $\lambda(T)$ for $T/T_c \ll 1$ for the axial state and the polar state from Gross *et al.* (1986). The variable \mathbf{A} is the vector potential and \mathbf{l} is the local unit axis of the gap symmetry.

State	$\lambda_{\perp}(\mathbf{A} \perp \mathbf{l})$	$\lambda_{\parallel}(\mathbf{A} \parallel \mathbf{l})$	Impurities
Axial	$\sim T^4$	$\sim T^2$	$\sim T^2$
Polar	$\sim T$	$\sim T^3$	$\sim T^2$

The comparison between these temperature power laws and the measured $\lambda(T)$ for UPt₃ and UBe₁₃ should be made with care, since these predictions represent only first order approximations and are limited by several conditions. First, they were calculated using a spherical Fermi surface, which may not properly describe the actual material, especially in the case of UPt₃, which possesses an hexagonal Fermi surface (Taillefer and Lonzarich, 1988; Julian, Teunissen, and Wiegers, 1992). Second, they represent the first term of a series expansion in T/T_c , which makes these power laws valid only in the limit $T/T_c \rightarrow 0$. Finally, the temperature dependence of the energy gap used in these calculations is an approximation of the BCS weak coupling temperature dependence of the energy gap, which may not be appropriate for either UPt₃ or UBe₁₃.

4.1.2.b Frequency dependence

As will be presented in the next section, some experiments involving UPt₃ have hinted at a possible frequency dependence of $\lambda(T)$. For example, Gross *et al.* (1988) reported $\lambda(T) \sim T^2$ for a dc measurement, while the radio frequency (rf) experiments performed by Gannon *et al.* (1990) indicated that $\lambda(T) \sim T^4$. Furthermore, results from the work of this dissertation also suggest a frequency dependence of $\lambda(T)$ for several UPt₃ samples.

In a superconductor possessing nodes in its energy gap, quasiparticles can be excited at all non-zero frequencies of the probing fields, even at $T = 0$. Therefore, one might conclude that the density of superconducting electrons would be reduced at higher frequencies, thereby increasing the penetration depth (Eq. (4.7)). However, the measuring

frequencies used in the experiments mentioned above are in the range $0 \leq f \leq 40$ MHz, which corresponds to a thermal energy of less than 2 mK. Therefore, a simple increase in quasiparticles cannot adequately account for the difference between dc and rf experiments in the temperature range 50 mK $< T < 250$ mK, which is the region where the measurements showing the frequency dependence were taken.

Putikka, Hirschfeld and Wölfle (1990) suggested a resonant mechanism to account for this frequency dependence (see also Hirschfeld, Wölfle and Einzel, 1988; and Hirschfeld *et al.*, 1989). They proposed that, for a range of frequencies and wave vectors, the response of thermally activated quasiparticles enhances the reactive portion of the currents, so that instead of reducing the Meissner effect, the quasiparticles contributed to it. These authors calculated the magnitude of this effect for the special case of the polar state in the clean limit, with the Poynting vector parallel to the z-axis and the vector potential in the basal plane. Their results suggested that the reactive component of the quasiparticle current had a strong effect on the temperature dependence of $\lambda(T)$. Furthermore, by including the effects of strong impurity scattering, they were able to qualitatively account for the crossover from the T^2 dependence of the dc measurements (Gross *et al.*, 1988) to the T^4 behavior observed at rf frequencies (Gannon *et al.*, 1990), both taken with \mathbf{A} in the basal plane. Although these theoretical calculations are promising, they cannot account for all the reported experimental results. In particular, the frequency dependences presented in this dissertation cannot be explained by the above analysis. It is possible that the mechanism proposed by Putikka, Hirschfeld and Wölfle (1990), applied to an energy gap structure other than the spherical polar state, could account for our results. If so, our investigation of the frequency dependence of $\lambda(T)$ could help identify the energy gap structure for UPt₃. This perspective should motivate future theoretical work on this topic.

4.1.3 Motivation for Studying the Penetration Depth in Superconductors

From the preceding subsections, it is clear that the temperature dependence of the penetration depth can provide a great deal of information about the superconducting state of a material. For instance, the temperature dependence of the density of superconducting electrons can be established, from which information regarding the energy gap structure can be obtained. The ability to measure $\lambda(T)$ as a function of angle and frequency makes this technique a very unique probe.

Measurements of $\lambda(T)$ have been a powerful tool in the study of numerous superconductors. For example, the linear temperature dependence of $\lambda(T)$ in $\text{YBa}_2\text{Cu}_3\text{O}_{7-\delta}$ single crystals has been taken as evidence for non *s*-wave BCS superconductivity (Hardy *et al.*, 1993). Similar measurements performed on Zn-doped $\text{YBa}_2\text{Cu}_3\text{O}_{7-\delta}$ crystals (Achkir *et al.*, 1993), and on thin films (Ma *et al.*, 1993), lead to quadratic temperature dependences, suggesting that, in this system, sample composition and geometry play an important role in the observed temperature dependence of $\lambda(T)$.

4.2 Previous Work on the Penetration Depth of UPt_3

In this section, we review the work of other groups who measured the temperature dependence of the penetration depth, $\lambda(T)$. Only the measurements extending to temperatures below $T/T_c < 0.5$ are discussed. The previous work on the inductive response near T_c will be referred to as needed in the discussion section.

4.2.1 dc Measurements

The first measurements of $\lambda(T)$ were reported by Gross *et al.* (1988) who used a SQUID magnetometer in their experiments. Their results for $0.175 \leq T/T_c \leq 0.5$ indicated a quadratic temperature dependence. As was discussed in the previous section, this quadratic dependence is consistent either with a gap possessing point nodes or with scattering from non-magnetic impurities in an anisotropic pairing state. The presence of point nodes is unlikely since their existence would be in conflict with the ultrasonic and

specific heat results which suggest lines of nodes in the a-b plane (see Chapter 2). Furthermore, the authors reported an unusual paramagnetic signal just below T_C , which they attributed to an inhomogeneous T_C distribution with the highest value on the circumference of the sample. The inhomogeneity of T_C suggests that the sample may not be completely free of impurities.

Groß-Alltag *et al.* (1991) extended the work published earlier by Gross *et al.* (1988) and reported penetration depth measurements for three different samples. All three specimens exhibited quadratic dependences for $\lambda(T)$. For two of the specimens, the probing field was applied parallel to the c-axis, while for the third one, the field was perpendicular to its c-axis. These isotropic results are surprising since other measurements, such as ultrasonic attenuation (Shivaram *et al.*, 1986a) and thermal conductivity (Behnia *et al.*, 1991), exhibit a strong anisotropy between the basal plane and the c-axis. These results, however, are consistent with scattering from non-magnetic impurities causing the quadratic temperature dependence of $\lambda(T)$ for these samples.

4.2.2 Radio Frequency Measurements

Brown *et al.* (1990) published penetration depth results obtained on one of the polycrystalline samples for which Fisher *et al.* (1989) reported a double bump near T_C in the specific heat (see Chapter 2). This specimen is also sample No. 4 described in the next section. Brown *et al.* (1990) used a tunnel diode oscillator (TDO) to measure $\lambda(T)$ as described in Chapter 3. These authors reported a temperature dependence close to T^4 in agreement with the results from Gannon *et al.* (1990) discussed below.

Using a similar TDO method, Gannon *et al.* (1990) measured $\lambda(T)$ for fields parallel and perpendicular to the c-axis. They reported a T^4 dependence for both orientations. This lack of anisotropy in the penetration depth is difficult to reconcile with the transverse ultrasound measurements which clearly showed different temperature dependences for the two orientations.

4.2.3 Muon Spin Relaxation Measurements

Broholm *et al.* (1990) performed muon spin relaxation (μ SR) measurements on single crystals. An advantage of the μ SR technique is that one can extract the absolute value of $\lambda(0)$ and determine $\lambda_{\parallel}(T)$ and $\lambda_{\perp}(T)$ in the same crystal, without re-orienting the sample relative to the muon beam. Furthermore, μ SR is a bulk probe and is not sensitive to the quality of the surface. The main disadvantage, however, is that a large magnetic field, B_{app} , must be applied to the specimen so that the sample is in its mixed state, *i.e.* ($B_{C1} < B_{app} < B_{C2}$). Furthermore, in order to extract $\lambda(T)$, it is important that the quantity measured in a μ SR experiment (the muon spin relaxation rate, σ) be independent of B_{app} . Broholm *et al.* (1990) reported temperature dependences of $\lambda(T)$ in UPt₃ which suggested lines of nodes along the a-b plane and point nodes where the c-axis intersects the Fermi surface. These results are in qualitative agreement with the transverse ultrasonic work by Shivaram *et al.* (1986a). However, subsequent μ SR measurements (Luke *et al.*, 1991, and 1993) raised questions, based on the field dependence of σ , about the validity of the extraction of $\lambda(T)$ by Broholm and coworkers. Luke and his collaborators have suggested that the observed increase in muon spin relaxation rate near T_C was not a result of changes in the penetration depth (as assumed by Broholm *et al.*), but instead, was caused by the second superconducting transition at T_{C2} (see Chapter 2 and Fig. 2-2), most likely indicating the presence of a superconducting phase with finite angular momentum pairing. If this assertion is true, then the results reported by Broholm *et al.* do not reflect the true temperature dependence of $\lambda(T)$ in UPt₃.

4.2.4 Motivation for Studying the Penetration Depth in UPt₃

Three important conclusions can be drawn from the above review of the penetration depth measurements in UPt₃. First, a low frequency measurement (less than 1 MHz) of $\lambda(T)$ on a high quality single crystal, *i.e.* for which non-magnetic impurity scattering is negligible, does not exist. The execution of such a measurement is the

primary motivation behind the work on UPt₃ presented in this dissertation. Second, the frequency of the probing field might play an important role in the observed $\lambda(T)$. Such frequency dependence is minimal for BCS superconductors, but may be a signature of unconventional superconductivity, as was discussed in the previous section. By measuring $\lambda(T)$ using inductive techniques over a wide range of frequencies (32 Hz to 16 MHz), the present work provides the first systematic study of this possible frequency dependence in UPt₃. Finally, the observed temperature dependence of $\lambda(T)$ might be sample dependent. This problem was observed in other properties of UPt₃ and UBe₁₃ and was already discussed in Chapter 2. Thus, another goal of this study is to investigate the effects of surface roughness on the measurements of $\lambda(T)$.

4.3 Sample Histories

During the course of this work, eight different specimens were investigated. Table 4-2 summarizes several of the important properties of each specimen, and additional information about each sample is given in the following subsections. The demagnetization factor, D, given for each sample in Table 4-2, corresponds to the magnetic field orientation used in the measurements, and were estimated from van Duzer and Turner (1981).

4.3.1 Sample No. 1

Sample No. 1 was comprised of single crystals which were grown by Z. Fisk at Los Alamos National Laboratory using a Bi flux from which they were quenched. These needles were first studied inductively before *any* treatment was performed on them. These preliminary results (shown in the next section) indicated a superconducting-like transition around 1.3 K in addition to the superconducting transition around 0.5 K. The exact nature and origin of the 1.3 K transition are unknown. It is possible that a surface phase, such as BiPt ($T_c \approx 1.21$ K (Roberts, 1976)), formed on the surface. The needles were

Table 4-2. Characteristics of the eight UPt₃ samples investigated in this work. In the treatment column, if annealing was performed, the temperature and duration of the annealing are given by the notation: A: (temperature, duration). For more details concerning the various treatments and the fabrication method, refer to the full sample descriptions given in the text.

Sample	Geometry, demag. factor	Dimensions, c-axis orientation	Treatment	References
No. 1	Single crystal needles $D \approx 0.035$	$r_s = 0.2 \text{ mm}$ length = 3 mm c-axis long axis	A: (950°C, 100 hrs.), etched, and polished	Signore <i>et al.</i> , 1991 Signore <i>et al.</i> , 1994a, Signore <i>et al.</i> , 1994b.
No. 2	Single crystal cylinder $D \approx 0.175$	$r_s = 1.25 \text{ mm}$ length = 5 mm c-axis long axis	Not annealed, polished	Gross <i>et al.</i> , 1988, Ellman <i>et al.</i> , 1990, Groß-Alltag <i>et al.</i> , 1991, Schuberth <i>et al.</i> , 1990.
No. 3	Single crystal parallelepiped $D \approx 0.035$	$3.7 \times 0.6 \times 0.6$ mm^3 c-axis 3.7 side	Spark erosion cut, not annealed, not polished	Menovsky <i>et al.</i> , 1983, Vorenkamp <i>et al.</i> , 1990 Koziol, 1994.
No. 4	Polycrystal cylinder $D \approx 0.135$	$r_s = 1 \text{ mm}$ length = 5 mm	A: (950 °C, 90 hrs.)	Fisher <i>et al.</i> , 1989, Brown <i>et al.</i> , 1990.
No. 5	Single crystal parallelepiped $D \approx 0.18$	$2.83 \times 1.47 \times 1.89$ mm^3 c-axis 2.83 side	Spark cut, A: (950 °C, 48 hrs.), polished	Hasselbach <i>et al.</i> , 1990, Adenwalla <i>et al.</i> , 1990, Lin, 1993.
No. 6	Single crystal parallelepiped $D \approx 0.17$	$3.42 \times 3.54 \times 7.42$ mm^3 c-axis 7.42 side	Spark cut, A: (950 °C, 48 hrs.), polished	Schenstrom <i>et al.</i> , 1989, Adenwalla <i>et al.</i> , 1990, Lin, 1993.
No. 7	Single crystal plate $D \approx 0.03$	$2.2 \times 1.8 \times 0.14$ mm^3 c-axis 2.2 side	Spark erosion cut, A: (1200 °C, 40 hrs), not polished	Shivaram <i>et al.</i> , 1986a, Shivaram <i>et al.</i> , 1989, Gannon <i>et al.</i> , 1990
No. 8	Single crystal whiskers $D \approx 0.056$	$r_s \approx 0.1 \text{ mm}$ length $\approx 1 \text{ mm}$	Not annealed, not polished	Lee <i>et al.</i> , 1993

then annealed (100 hours at 950 °C wrapped in Ta foil), etched (about one minute in HCl : HNO₃ (3 : 1)), and subsequently remeasured. After etching, the 1.3 K transition was no longer observable. These crystals were further studied after polishing their surfaces with very fine paper of 0.3 μm grading. Figure 4-2 shows three scanning electron microscope (SEM) pictures of the surfaces at different stages of the treatment. The characteristic length scale of the surface imperfections went from approximately 2 μm to 0.5 μm. In order to further characterize this sample, we measured its resistivity and specific heat. An annealed, etched, unpolished specimen was used in the resistivity and specific heat measurements. A fit of $\rho(T)$ vs. T^2 shows that $\rho(T) = \rho_0 + A T^2$, with $\rho_0 = 0.6 \pm 0.1 \mu\Omega\text{cm}$ and $A = 0.7 \pm 0.1 \mu\Omega\text{cmK}^{-2}$ (Fig. 4-3). The specific heat in the vicinity of T_C is shown in Fig. 4-4. A double jump is observable with a splitting, ΔT_C , of about 50 mK.

4.3.2 Sample No. 2

The first penetration depth measurement reported on UPt₃ was performed by Gross *et al.* (1988) on a single crystal, sample No. 2, using a dc method. The observed T^2 dependence of $\lambda(T)$ was later attributed to the presence of impurities (Groß-Alltag *et al.*, 1991). The specific heat of this sample was also measured down to 10 mK (sample No. 1 of Schuberth *et al.*, 1990), where the data showed an interesting upturn below 50 mK. It is important to note that sound velocity measurements on a different UPt₃ sample down to 5 mK did not show any manifestation of this anomaly (Jin *et al.*, 1992). Earlier specific heat measurements on sample No. 2 showed no signs of a double jump around T_C (Ellman *et al.* 1990). We were interested in this particular sample to determine if we could reproduce the T^2 dependence with our low frequency mutual inductance technique and thereby demonstrate the equivalence between our ac method and the dc measurements of Gross and coworkers.

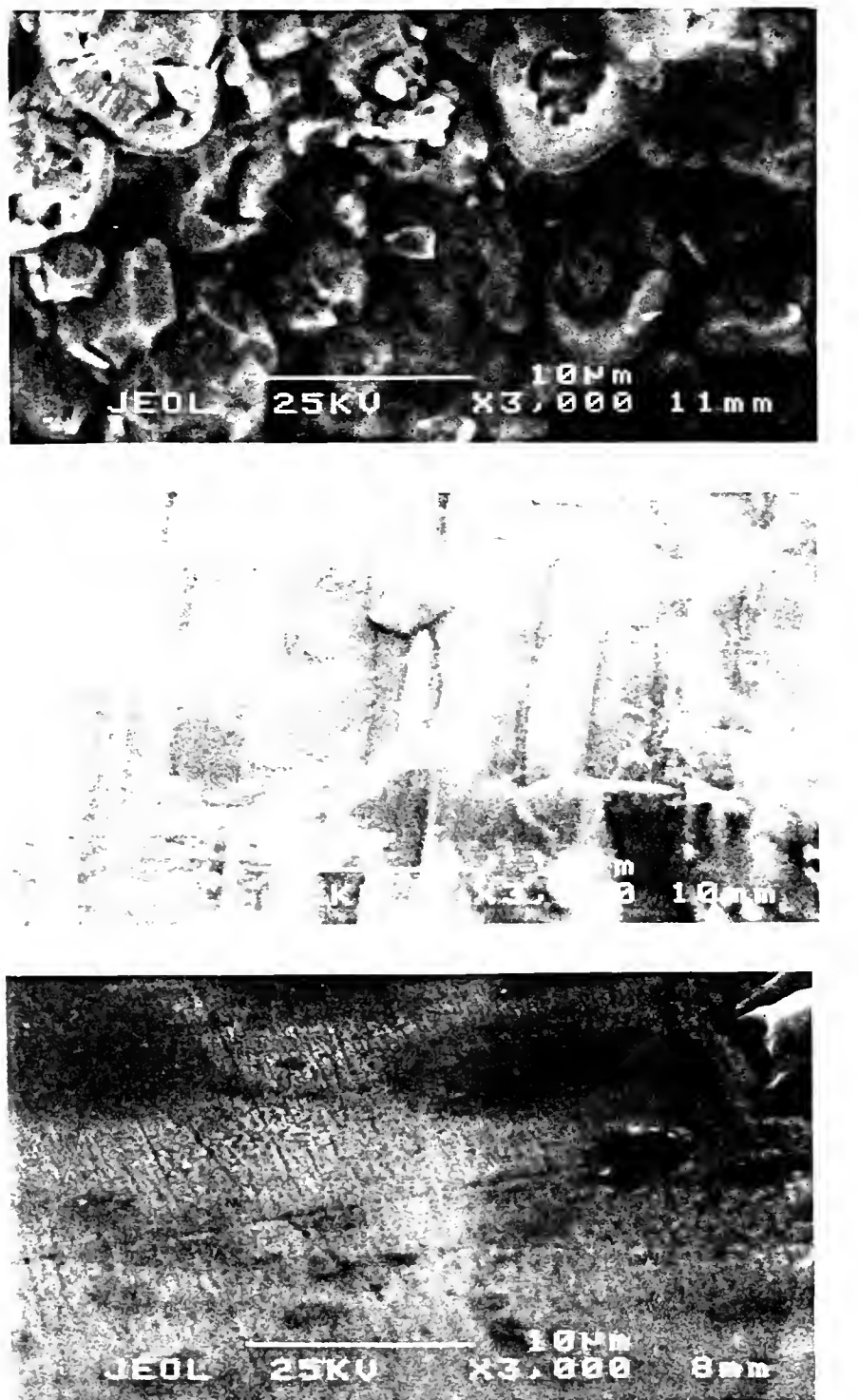


FIG. 4-2. SEM pictures (x 3000 magnification) of the surface of single crystal No. 1 (Table 4-2). (a) As grown; (b) after etching and annealing; (c) after polishing; the length scale of the imperfections improves from about 2 μm to less than 0.5 μm .

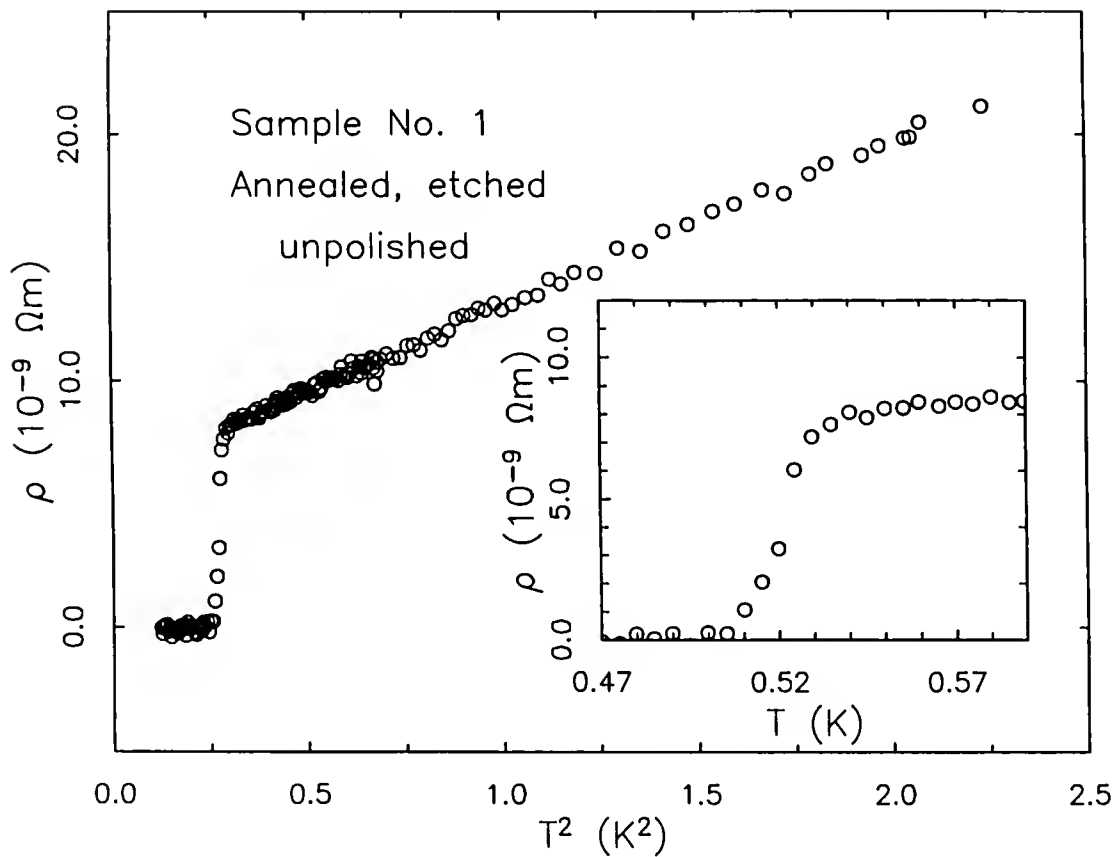


Fig. 4-3. Resistivity as a function of T^2 for sample No. 1 (after annealing and etching, but before polishing). A linear fit to the data indicates that, above T_C , $\rho(T) = \rho_0 + A T^2$, with $\rho_0 = 0.6 \pm 0.1 \mu\Omega\text{cm}$ and $A = 0.7 \pm 0.1 \mu\Omega\text{cmK}^{-2}$. The inset shows $\rho(T)$ in the vicinity of T_C . The onset of the transition is 530 mK. Data taken from Signore *et al.* (1992).

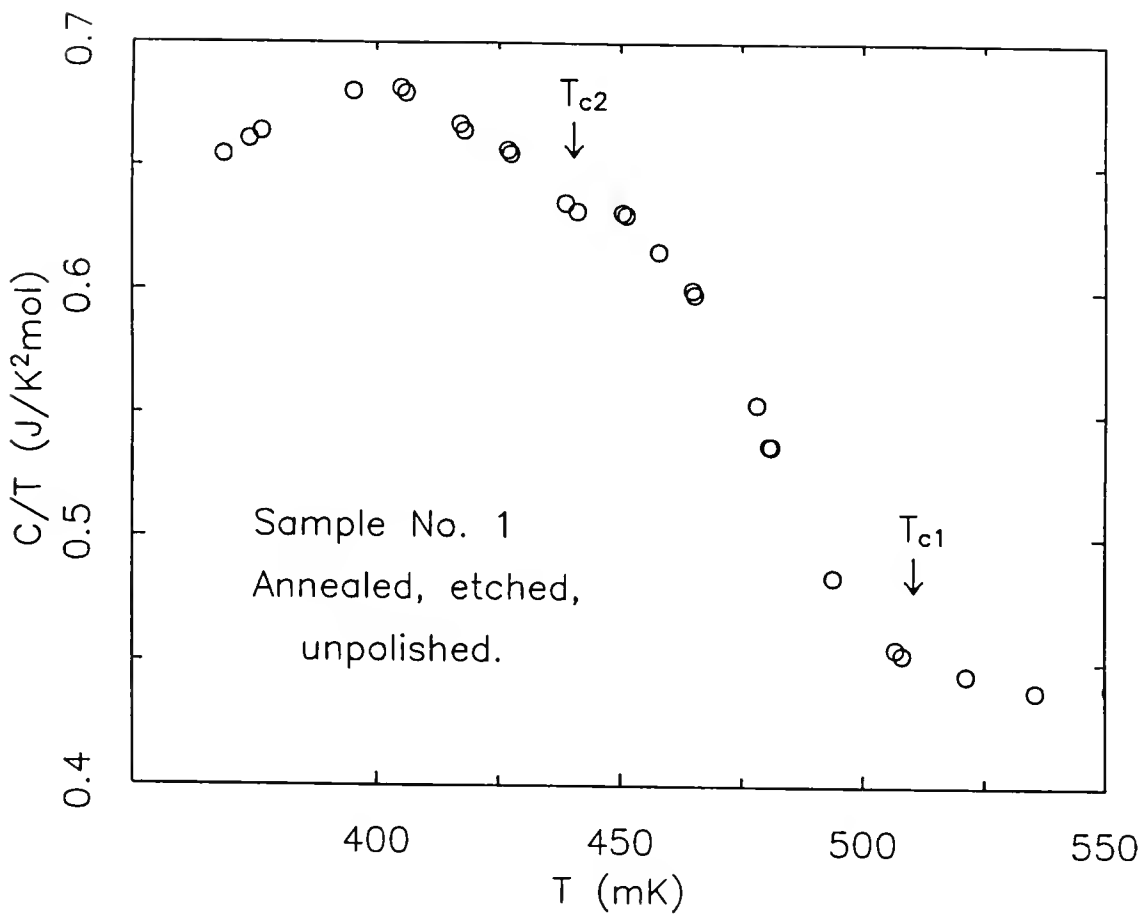


Fig. 4-4. Specific heat as a function of temperature in the vicinity of T_c for Sample No. 1 (after annealing and etching, but before polishing). A double jump is observable with a splitting, ΔT_c , of about 50 mK. Data taken by Bohdan Andraka (unpublished).

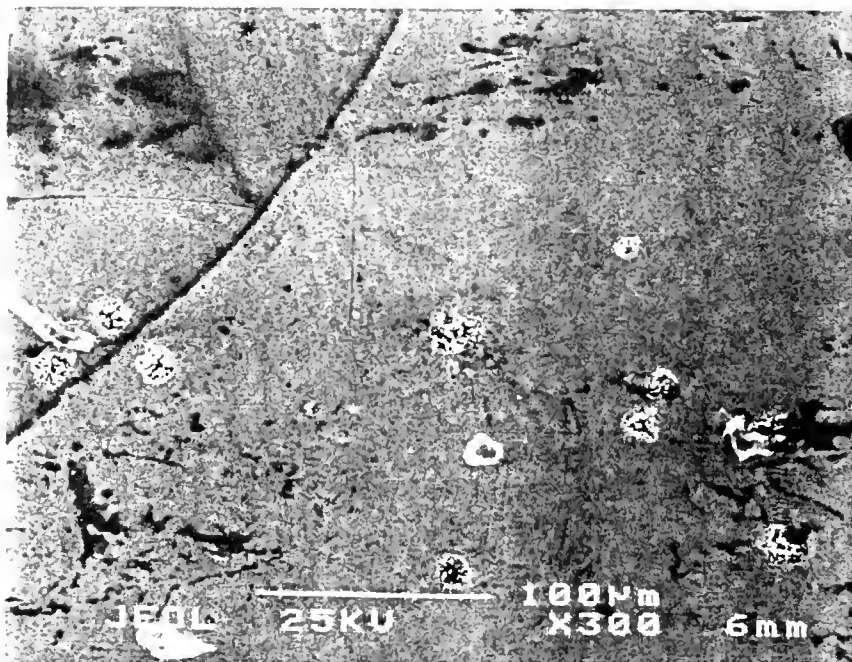
This single crystal was grown by electron beam melting in an ultrahigh-vacuum (pressure not given in the literature) zone refining furnace using uranium that was depleted to less than 100 ppm ^{235}U . The specimen was polished with Korund powder, and SEM pictures of the surface are shown in Fig. 4-5. The characteristic length scale of the surface imperfections were less than 1 μm , except for a number of scattered "pin-holes" shown in Fig. 4-5b. These local defects were 10 to 20 μm in diameter and appeared to be at least 10 μm deep. They covered approximately 5% of the total surface of the sample. This sample was not annealed.

4.3.3 Sample No. 3

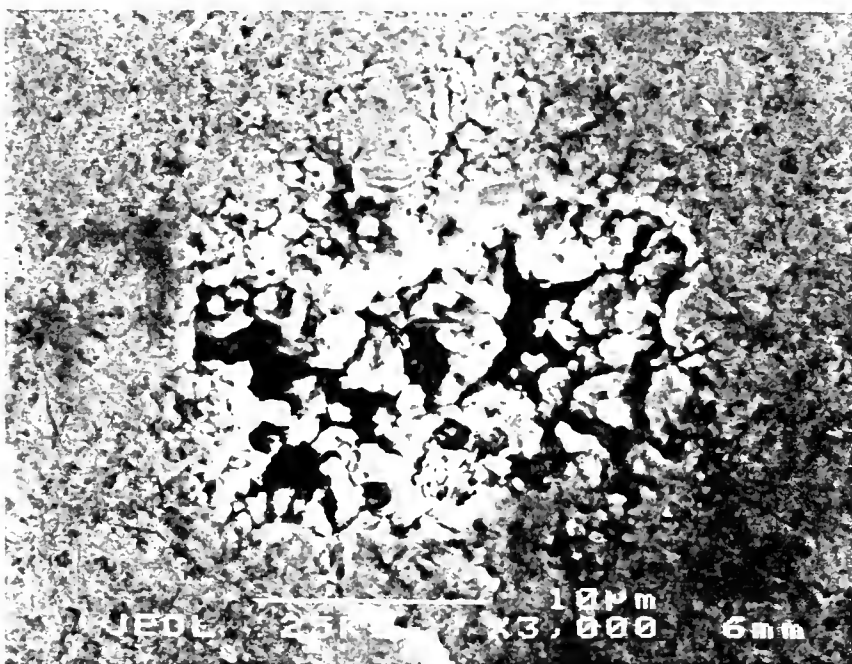
Sample No. 3 was spark erosion cut from a large single crystal grown using a modified Czochalski tri-arc method (Menovsky *et al.*, 1983), and was not annealed. Other specimens originating from the same crystal were annealed and showed a pronounced increase in the double jump in the specific heat data without changing T_C (Vorenkamp *et al.*, 1990). The surface was not treated after the spark erosion process, and SEM pictures of the surface of a sample originating from the same batch as No. 3 are shown in Fig. 4-6. The entire surface is covered with imperfections of size ranging from 1 to 10 μm .

4.3.4 Sample No. 4

Sample No. 4 is the polycrystal in which the double peak in the specific heat was first reported as an intrinsic feature of UPt₃ (sample No. 2 of Fisher *et al.* (1989)). The results on the rf penetration depth have already been published (Brown *et al.* 1990), but the low frequency work has not. Our goal with this sample was to determine if the double peak in specific heat corresponds to any feature in our inductive measurements. This specimen was cut from a large arc-melted polycrystalline ingot, and the surface was not further characterized.

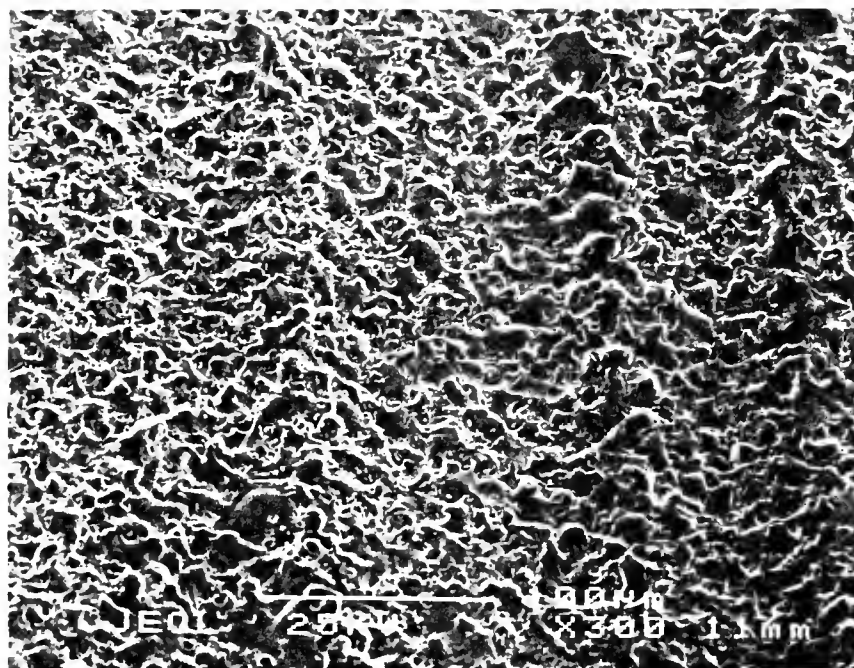


(a)

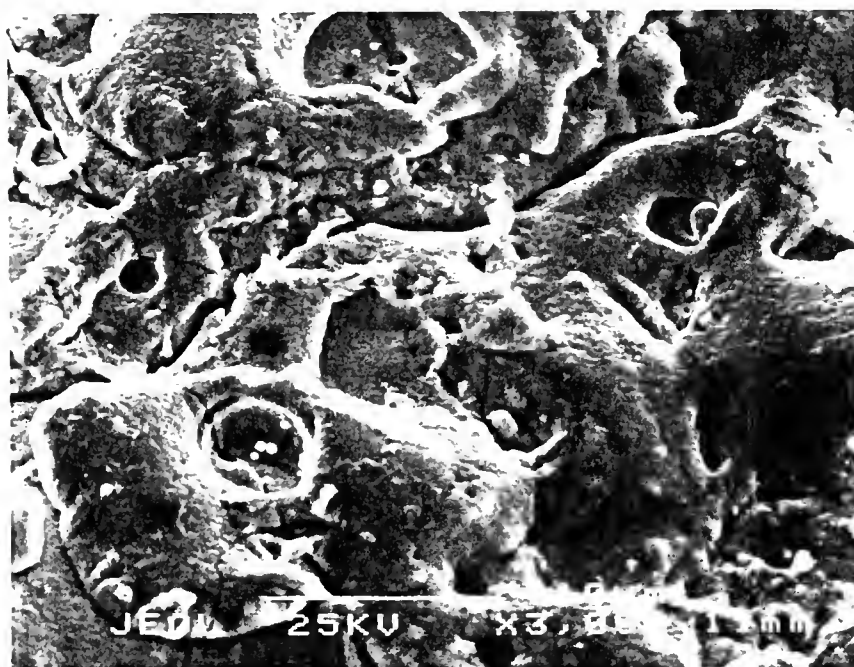


(b)

FIG. 4-5 SEM pictures of the surface of single crystal No. 2 (Table 4-2). (a) x 300 magnification; the length scale of the imperfections is less than 1 μm , except for a few cracks (upper left corner) and scattered "pin-holes" occupying less than 5% of the total surface area. (b) x 3000 magnification, focusing on one of the local defects.

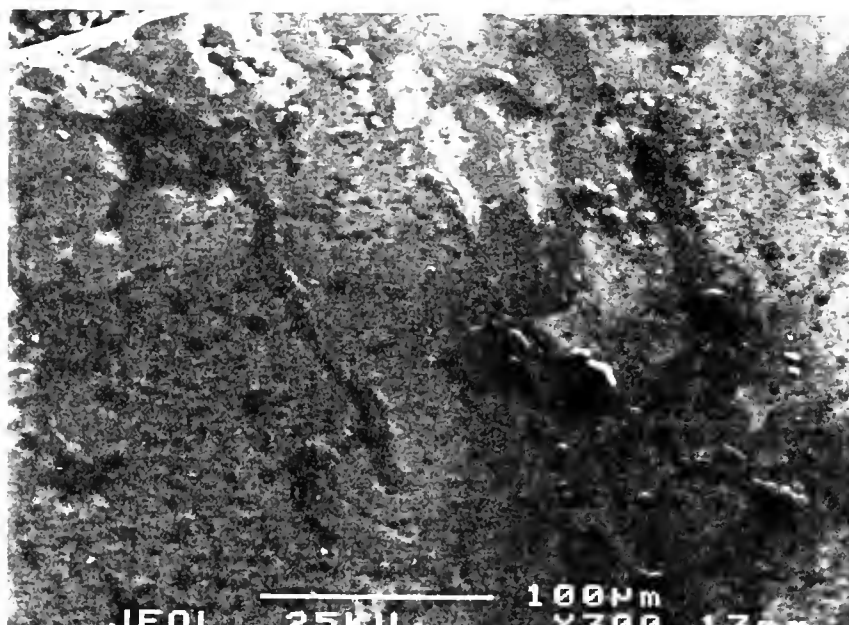


(a)



(b)

FIG. 4-6 SEM pictures of a neighboring piece of sample No. 3 (Table 4-2). (a) x 300 magnification. (b) x 3000 magnification. Imperfections possessing a length scale between 1 and 10 μm cover the entire surface.



(a)



(b)

FIG. 4-7 SEM pictures of single crystal No. 7 (Table 4-2). (a) x 300 magnification.
(b) x 3000 magnification.

4.3.5 Sample No. 5

This single crystal was one of the specimens used in the ultrasonic studies of Adenwalla *et al.* (1990) and Lin (1993). In addition, Hasselbach *et al.* (1990) performed thermal expansion and specific heat measurements which showed a well defined double feature near T_c . This sample was prepared by first mixing high purity uranium and platinum in a stoichiometric ratio in an induction furnace under ultra-high vacuum. A rod was then formed by slow unidirectional cooling. A single crystal was obtained from the rod with the horizontal floating-zone technique. The sample was spark cut out of this rod. Annealing was performed at 950 °C for 48 hours before and after cutting. Finally, the sample was polished to optical quality.

4.3.6 Sample No. 6

This large single crystal was also studied by Adenwalla *et al.* (1990) and Lin (1993) in their ultrasonic work (their sample No. 2). In addition, earlier ultrasonic attenuation was performed by Schenstrom *et al.* (1989) on the same specimen. The growth method and treatments were the same to those of sample No. 5.

4.3.7 Sample No. 7

Sample No. 7 is one of the samples which showed a T^4 dependence for $\lambda(T)$ reported by Gannon *et al.* (1990) from their rf experiments. In addition, the upper and lower critical field for this specimen were measured by Shivaram *et al.* (1986a and 1989). This single crystal was first synthesized in an arc furnace and then vertically zone refined. The sample was then spark erosion cut and briefly etched in HCl : HNO₃. An SEM picture of the surface is shown in Fig. 4-7.

4.3.8 Sample No. 8

This sample is comprised of many (~ 50) small single crystal whiskers embedded in nail polish. Data involving this sample has not been published previously. The whiskers

were quenched out of an arc melted batch of high purity uranium and platinum in a stoichiometric ratio. These specimens were made by W. W. Kim and G. R. Stewart (unpublished) at the University of Florida. This sample was not annealed.

4.4 Results

In this section, the entire set of results obtained from inductive measurements on the eight UPt_3 samples is presented. The section is divided into two parts. The results from the mutual inductance technique (low frequency) are given in the first subsection, while the data obtained from the tunnel diode oscillator experiments (rf frequencies) are presented in the second subsection.

For the seven single crystals, the ac field, \mathbf{B}_{ac} , was oriented parallel to the c-axis of the crystals, so that we report $\lambda_{\perp}(T)$ only, where the symbol " \perp " refers to the vector potential orientation relative to the c-axis (following the notation of Gross *et al.*, 1986). Table 4-3, located at the end of this section, summarizes the different temperature dependences obtained from both techniques.

Unless stated explicitly, all the data presented below were acquired in the following manner. First, the sample was cooled to the lowest temperature in the presence of the Earth's field. At the lowest temperature, the probing ac magnetic field was applied. The temperature was then systematically increased in a manner that avoided large thermal fluctuations (see subsection 3.1.3). In all cases, the experimental runs were performed with and without the specimen. In some cases, a weak temperature dependent background signal was present. This background was fitted to an analytical expression which was used to correct the data.

4.4.1 Mutual Inductance Results

As mentioned in Chapter 3, the mutual inductance data is given in arbitrary units. However, for all samples, the arbitrary units are reported on the same scale, and the

difference in response from sample to sample arises from their various geometries and microscopic differences in $\lambda(T)$.

4.4.1.a Sample No. 1

"As grown" : unannealed, unetched, and unpolished

As mentioned in the previous section, the unannealed, unetched sample No. 1 exhibited a transition around 1.3 K in addition to the superconducting transition around 0.5 K. This anomalous transition was not present after annealing and etching the sample. The "before" and "after" comparison is shown in Fig. 4-8. A second important change, that occurred after annealing and etching sample No. 1, was the appearance of a double feature in the vicinity of T_c . This change is clearly shown in Fig. 4-9, (where the data for the polished sample No. 1 is also shown). The total change in signal across T_c for the raw data was different for each set of measurements, reflecting the fact that a portion of the volume of the sample was lost after each step of the surface treatment. To facilitate the comparison in Fig. 4-9, this total change in signal was normalized to negative one. The observation that a double feature in $\chi'(T)$ near T_c was only present after annealing and etching is reminiscent of specific heat measurements showing a double jump near T_c only after annealing the samples (Vorenkamp *et al.*, 1990, Midgley *et al.*, 1993). Further results presented below strengthen the point that the double feature in our inductive measurements does indeed correspond to the double transition observed in bulk measurements (*e.g.* specific heat and ultrasonic attenuation) of UPt₃.

The inductive response below 600 mK of the as grown sample is shown in Fig. 4-10. The inset of Fig. 4-10a shows a log-log plot for $T/T_c \leq 0.5$. The solid line represents the result of a linear fit and yields $\eta = 1.0 \pm 0.2$, where η is defined in Eq. (4.15) and listed in Table 4-3. The uncertainty in η represents one standard deviation.

Annealed, etched, and unpolished

The results for $\chi'(T)$ and $\chi''(T)$, taken at 317 Hz, are shown in Fig. 4-11. The inset of Fig. 4-11a shows a log-log plot for $T/T_c \leq 0.5$. A linear least squares fit indicates that

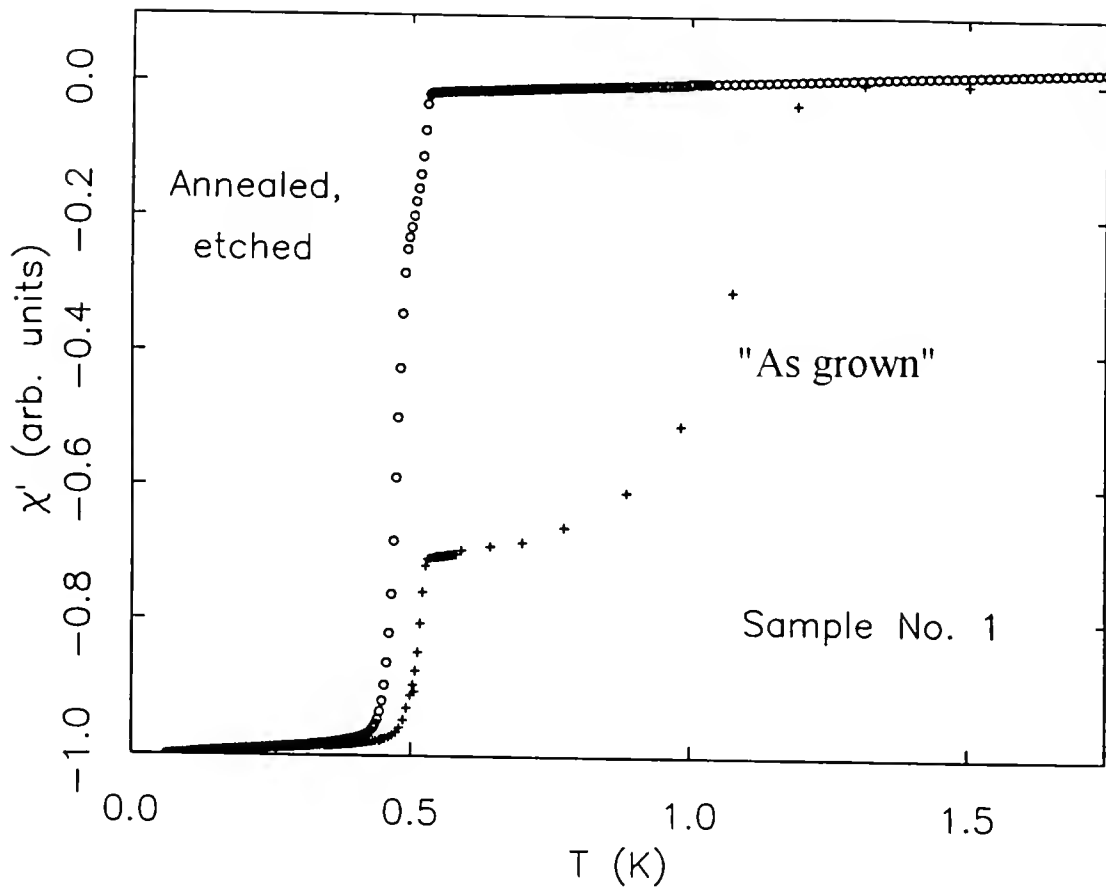


Fig. 4-8. The real part of the susceptibility, $\chi'(T)$, for sample No. 1 in "as grown" (+) and annealed, etched (\circ) conditions. After annealing and etching, the anomalous transition around 1.3 K was no longer observable.

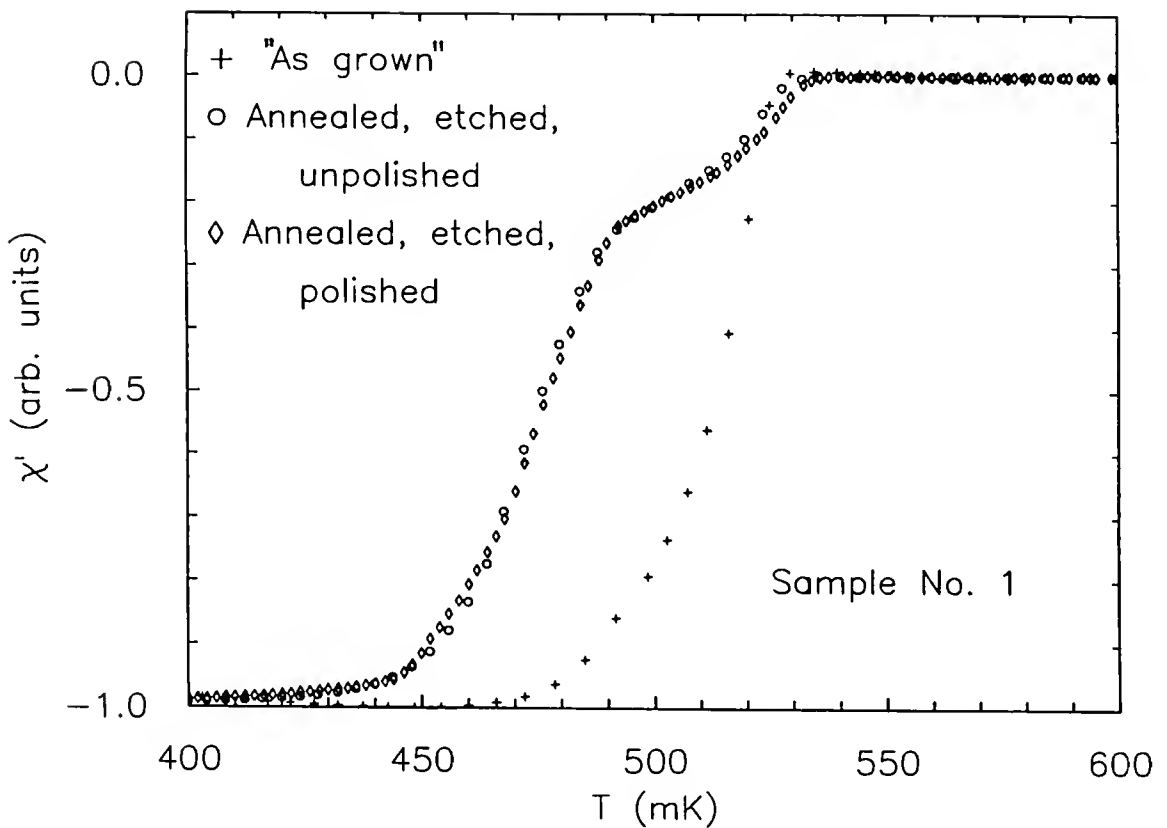


Fig. 4-9. Real part of the susceptibility, $\chi'(T)$, from the mutual inductance (317 Hz) response of single crystal No. 1 in the vicinity of T_c with $B_{ac} \parallel c$ -axis in "as grown" (+), annealed and etched (\circ), annealed, etched, and polished (\diamond) conditions. The total response is normalized to -1. The double transition is observed only after annealing and etching. Furthermore, polishing did not affect significantly the onset of T_c .

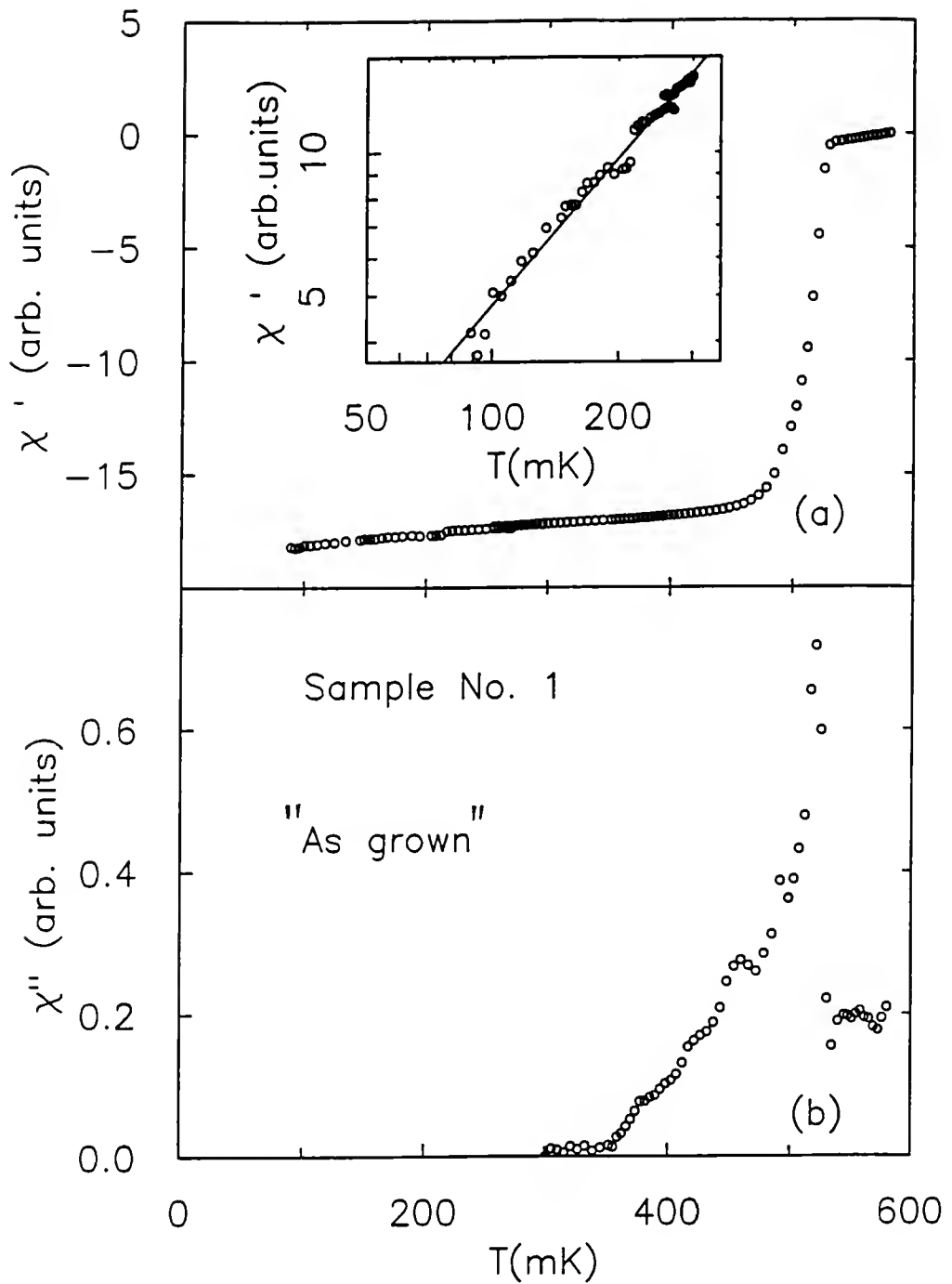


Fig. 4-10. Mutual inductance (317 Hz) data for single crystal No. 1, "as grown", with $B_{ac} \parallel c$ -axis. (a) The real part of the susceptibility, $\chi'(T)$. The kink near T_c is not observable. The inset is a log-log plot of the data for $T/T_c \leq 0.5$. The solid line represents the result of a linear fit and yields a slope $\eta = 1.0 \pm 0.2$. (b) The imaginary part of the susceptibility, $\chi''(T)$. A single peak is observable around T_c . $\chi'(T)$ and $\chi''(T)$ share the same scale of arbitrary units.

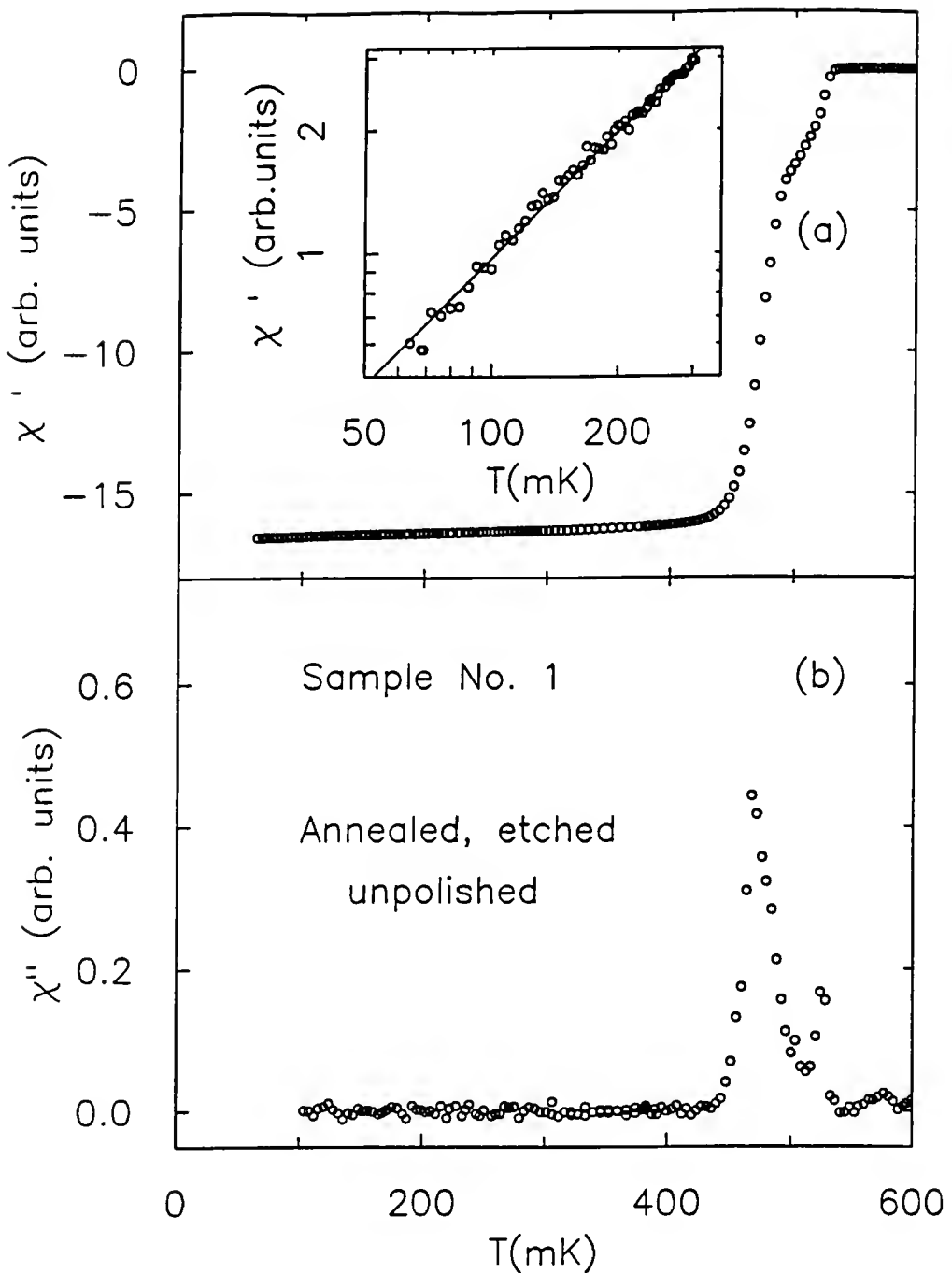


Fig. 4-11. Mutual inductance (317 Hz) data for single crystal No. 1 (annealed, etched, unpolished) with $B_{ac} \parallel c$ -axis. (a) The real part of the susceptibility, $\chi'(T)$. The kink near T_c is clearly observable. The inset is a log-log plot of the data for $T/T_c \leq 0.5$. The solid line represents the result of a linear fit and yields a slope $\eta = 1.0 \pm 0.1$. (b) The imaginary part of the susceptibility, $\chi''(T)$. The same scale of arbitrary units were used for $\chi'(T)$ and $\chi''(T)$.

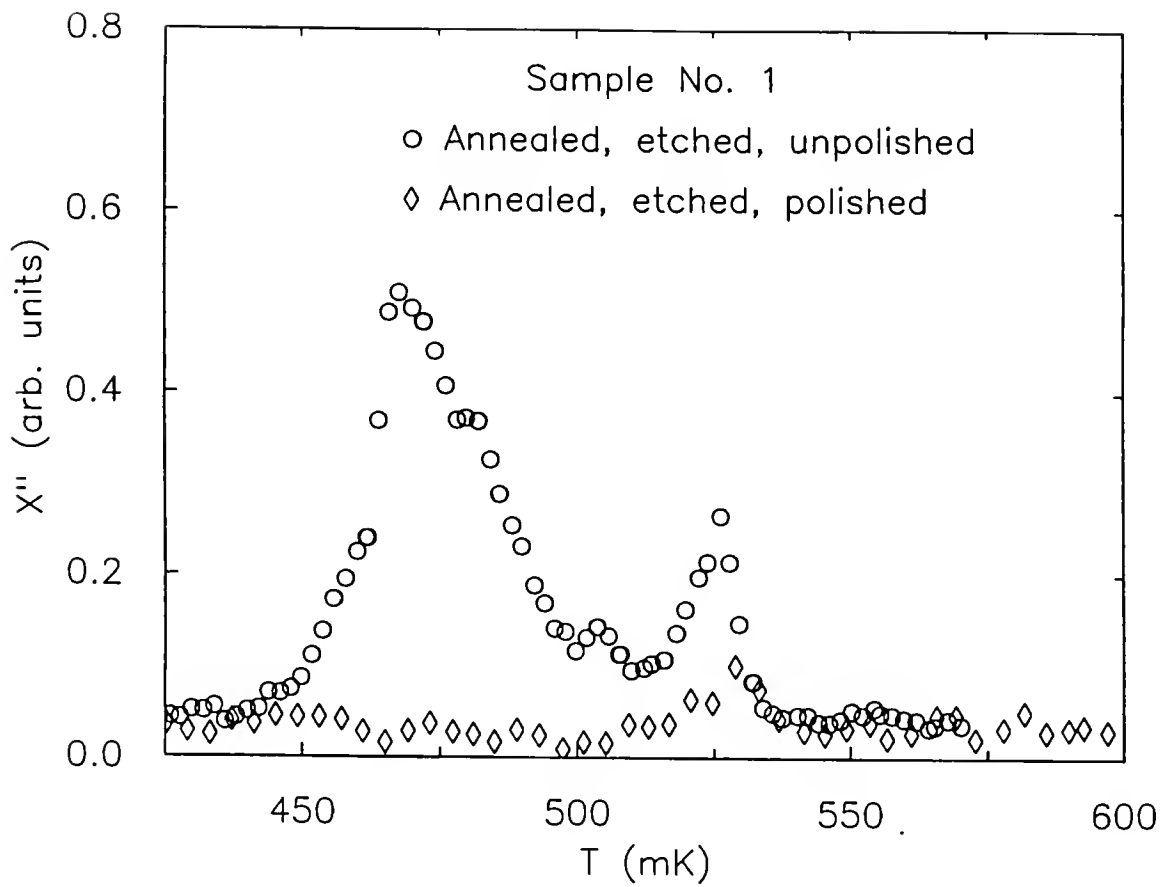


Fig. 4-12. The imaginary part of the susceptibility, $\chi''(T)$ taken at 317 Hz, in the vicinity of T_c and with $\mathbf{B}_{ac} \parallel c$ -axis for single crystal No. 1 before (○) and after (◊) polishing.

the data fall on a straight line with a slope of $\eta = 1.0 \pm 0.1$, where η is defined in Eq. (4.15) and listed in Table 4-3. The double feature in $\chi'(T)$ around T_c corresponds to a double peak in $\chi''(T)$ as shown in Fig. 4-11b. The splitting between the two peaks, ΔT_c , is of roughly the same magnitude as the splitting observed in the specific heat data on the same sample (Fig. 4-4). The double peak in $\chi''(T)$ is better illustrated in Fig. 4-12, which focuses on the data in the vicinity of T_c .

Annealed, etched, and polished

The results for $\chi'(T)$ and $\chi''(T)$, taken at 473 Hz, are shown in Fig. 4-13. The inset of Fig. 4-13a shows a log-log plot for $T/T_c \leq 0.5$. A linear least squares fit indicates that the data fall on a straight line with a slope of $\eta = 1.0 \pm 0.1$, where η is defined in Eq. (4.15) and listed in Table 4-3. Although the kink in $\chi'(T)$ was still present near T_c after polishing, the double peak in $\chi''(T)$ has almost disappeared (Fig. 4-12 and Fig. 4-13b). The decrease in losses at T_c after polishing can be understood as a decrease in the volume where losses take place. The kink in $\chi'(T)$ near T_c was also present for measurements taken at 47.3 Hz, 4.73 kHz, and 31.7 kHz, as shown in Fig. 4-14.

An attempt to study the frequency dependence of the inductive response was made by measuring $\chi'(T)$ from 32 Hz to 6 kHz at two temperatures, 80 mK and 600 mK. These results are shown in Fig. 4-15. Unfortunately, the error associated with retuning the lock-in amplifier at each frequency, and the frequency dependence of the lock-in amplifier gain, lowered the sensitivity below that needed to extract conclusive results. In fact, within our experimental uncertainties, both the normal state and superconducting state data sets lie on straight lines of equal slope.

Previous specific heat measurements on a UPt₃ single crystal, in magnetic fields parallel to the c-axis, showed the two jumps near T_c existing in fields up to 0.75 T, above which only one broad transition could be seen (Hasselbach *et al.*, 1989). These results motivated a study of the kink in $\chi'(T)$, observed in sample No. 1, as a function of magnetic field. The dc field ($0 \leq B_{dc} \leq 1.6$ T) was applied parallel to \mathbf{B}_{ac} and to the c-axis of the

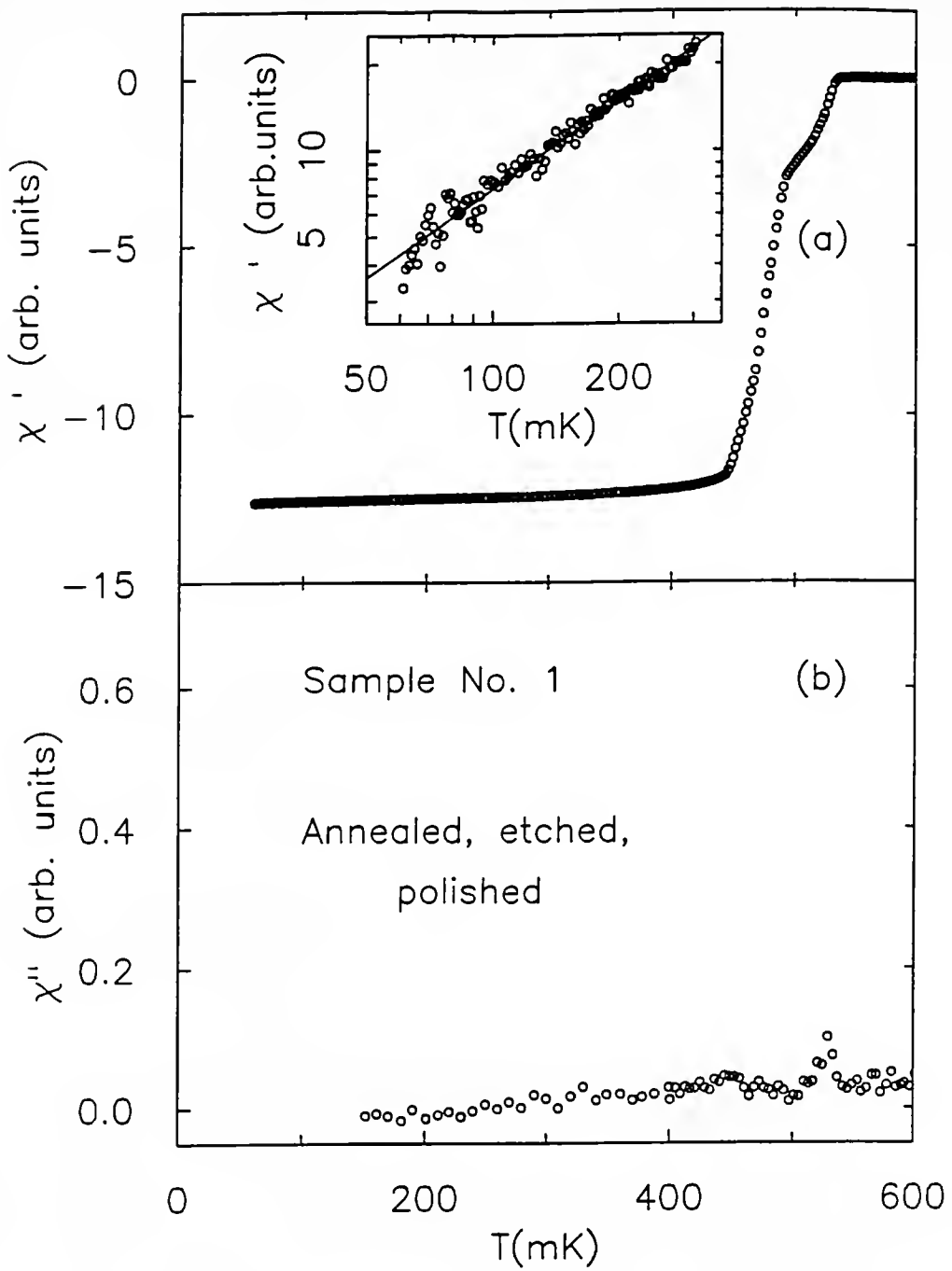


Fig. 4-13. Mutual inductance (473 Hz) data for single crystal No. 1 (annealed, etched, and polished) with $B_{ac} \parallel c$ -axis. (a) The real part of the susceptibility, $\chi'(T)$. The kink near T_C is clearly observable. The inset is a log-log plot of the data for $T/T_C \leq 0.5$. The solid line represents the result of a linear fit and yields a slope $\eta = 1.0 \pm 0.1$. (b) The imaginary part of the susceptibility, $\chi''(T)$. After polishing, the double peak in $\chi''(T)$ is greatly diminished, indicating a decrease in the volume where losses take place.

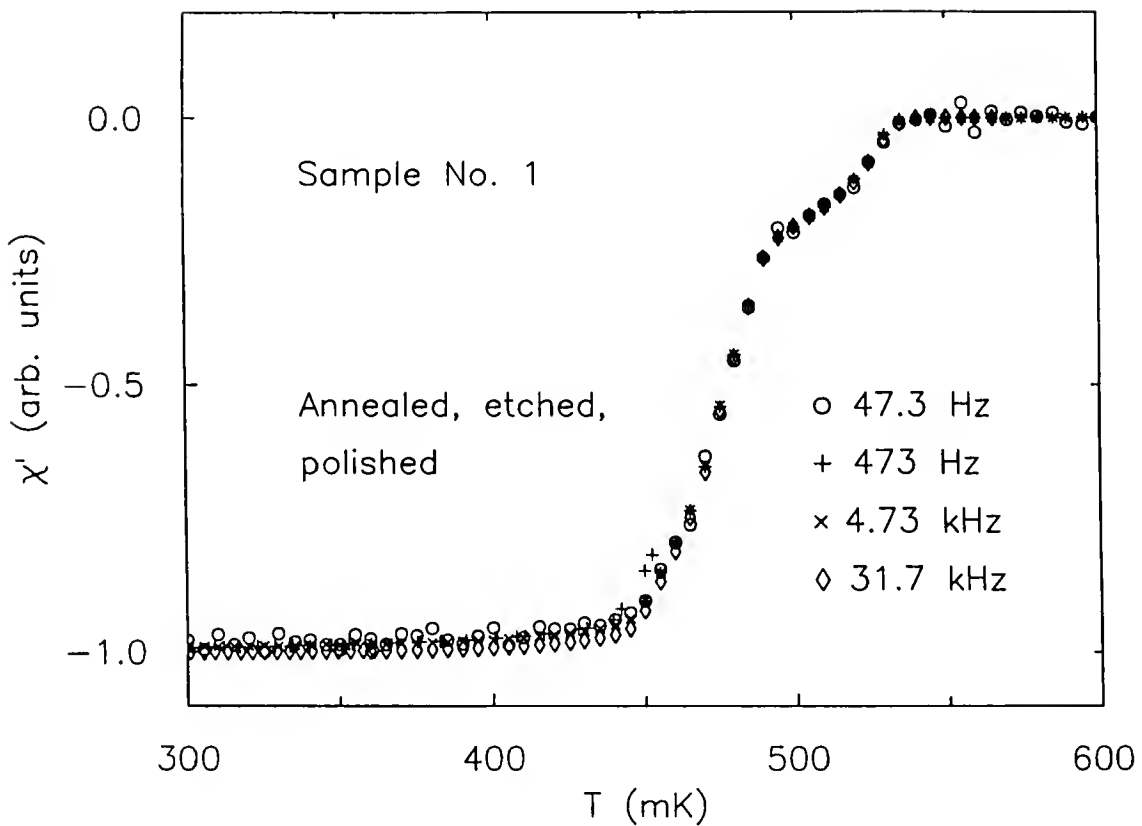


Fig. 4-14. $\chi'(T)$ in the vicinity of T_c , for single crystal No. 1 (annealed, etched, and polished) with $B_{ac} \parallel c$ -axis and for different frequencies : 47.3 Hz (\circ), 473 Hz ($+$), 4.73 kHz (\times), and 31.7 kHz (\diamond). To facilitate the comparison, the total change in signal was normalized to -1.

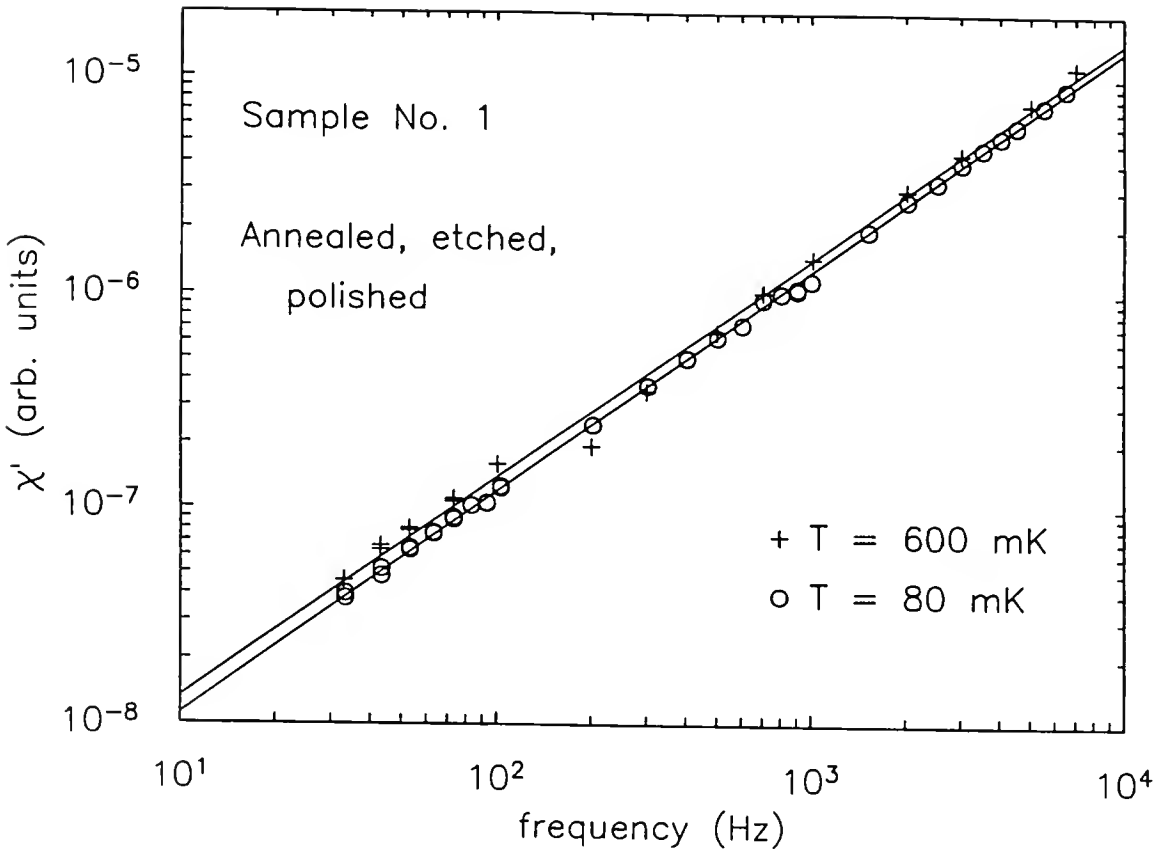


Fig. 4-15. χ' as a function of frequency, from 32 Hz to 6 kHz, on a log-log plot, at constant temperatures (80 mK and 600 mK). The error associated with retuning the lock-in amplifier at each frequency, and the frequency dependence of the lock-in amplifier gain, made the distinction between the data taken in the normal state and the superconducting data difficult. The two lines represent the results of linear fits yielding slope of 1.0 ± 0.1 .

crystal. The resulting phase diagram is presented in Fig. 4-16 (where the circles represent the onset of the first transition and the crosses correspond to the kink in $\chi'(T)$ at the lower transition). Although the B-T phase diagram has been extensively studied, Fig. 4-16 is the first one constructed from inductive measurements. The significance of these results is discussed at length in the next section. Three typical traces used to identify the two transitions at various fields are shown in Fig. 4-17 where the oblique up arrows indicate the data taken under Earth's field cooled conditions, while the oblique down arrows indicate the field cooled (with $B_{ac} + B_{dc}$ on) temperature sweeps.

A second interesting feature came out of these field measurements. For $B_{dc} \geq 1.2$ T, an upturn in $\chi'(T)$ was observable at the lowest temperatures (Fig. 4-18). Although the origin of such a paramagnetic-like signal is unknown, a number of possibilities will be discussed in the next section.

4.4.1.b Sample No. 2

The results on sample No. 2 for $\chi'(T)$ and $\chi''(T)$, taken at 417 Hz, are shown in Fig. 4-19. In this unannealed single crystal, the double feature near T_c was not observed in $\chi'(T)$ or in $\chi''(T)$. Inductive and specific heat measurements by Ellman *et al.* (1990) and Schuberth *et al.* (1990, 1992) have also established a single transition for this sample.

The inset of Fig. 4-19a shows a log-log plot of $\chi'(T)$ for $T/T_c \leq 0.5$. A linear least squares fit indicates that the data fall on a straight line with a slope of $\eta = 2.0 \pm 0.2$, where η is defined in Eq. (4.15) and listed in Table 4-3. This quadratic temperature dependence of $\lambda(T)$ is consistent with results previously reported on this sample by Gross *et al.* (1988), Groß-Altag *et al.* (1991), and Schuberth *et al.* (1990, 1992).

4.4.1.c Sample No. 3

The results on sample No. 3 for $\chi'(T)$ and $\chi''(T)$, taken at 317 Hz, are shown in Fig. 4-20. The onset of the transition for this unannealed single crystal was observed at

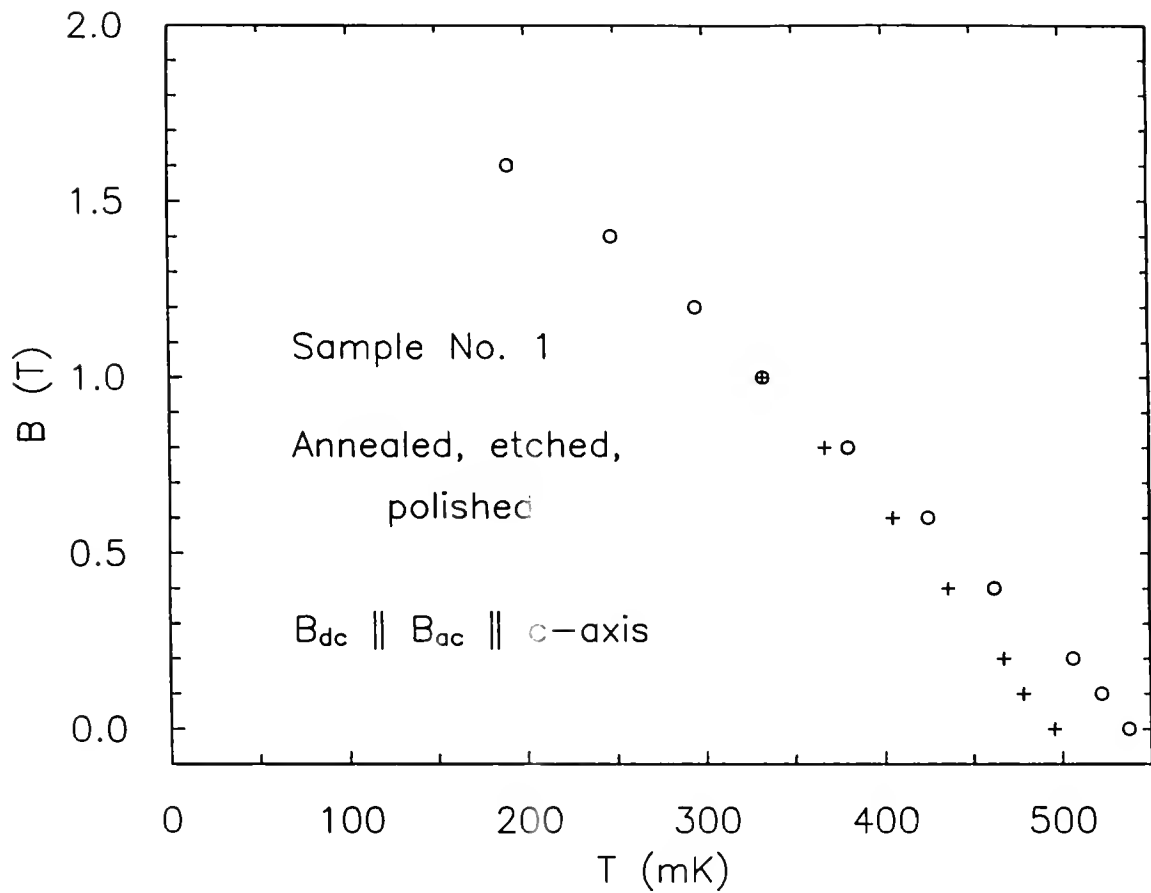


Fig. 4-16. (a) The B-T phase diagram for single crystal No. 1 (annealed, etched, and polished) constructed from the double transition in $\chi'(T)$ from mutual inductance (317 Hz) with $\mathbf{B}_{dc} \parallel \mathbf{B}_{ac} \parallel c\text{-axis}$. The circles represent the onset of the first transition and the crosses correspond to the kink in $\chi'(T)$ at the lower transition.

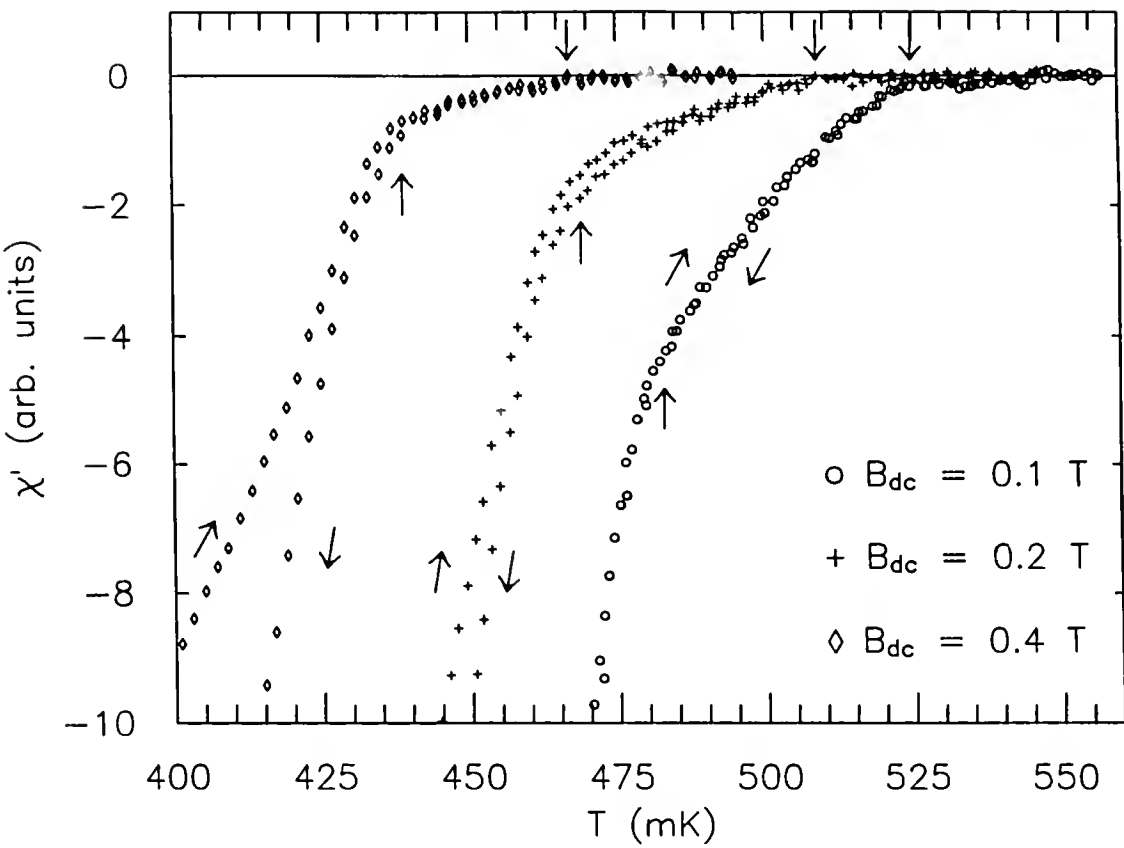


Fig. 4-17. Three typical data traces used to identify the upper and lower transition temperatures of sample No. 1 (annealed, etched, polished). The resultant B-T phase diagram is shown in Fig. 4-16. The oblique arrows represent the direction of the temperature sweeps. The vertical arrows indicate the transition temperatures used in Fig. 4-15.

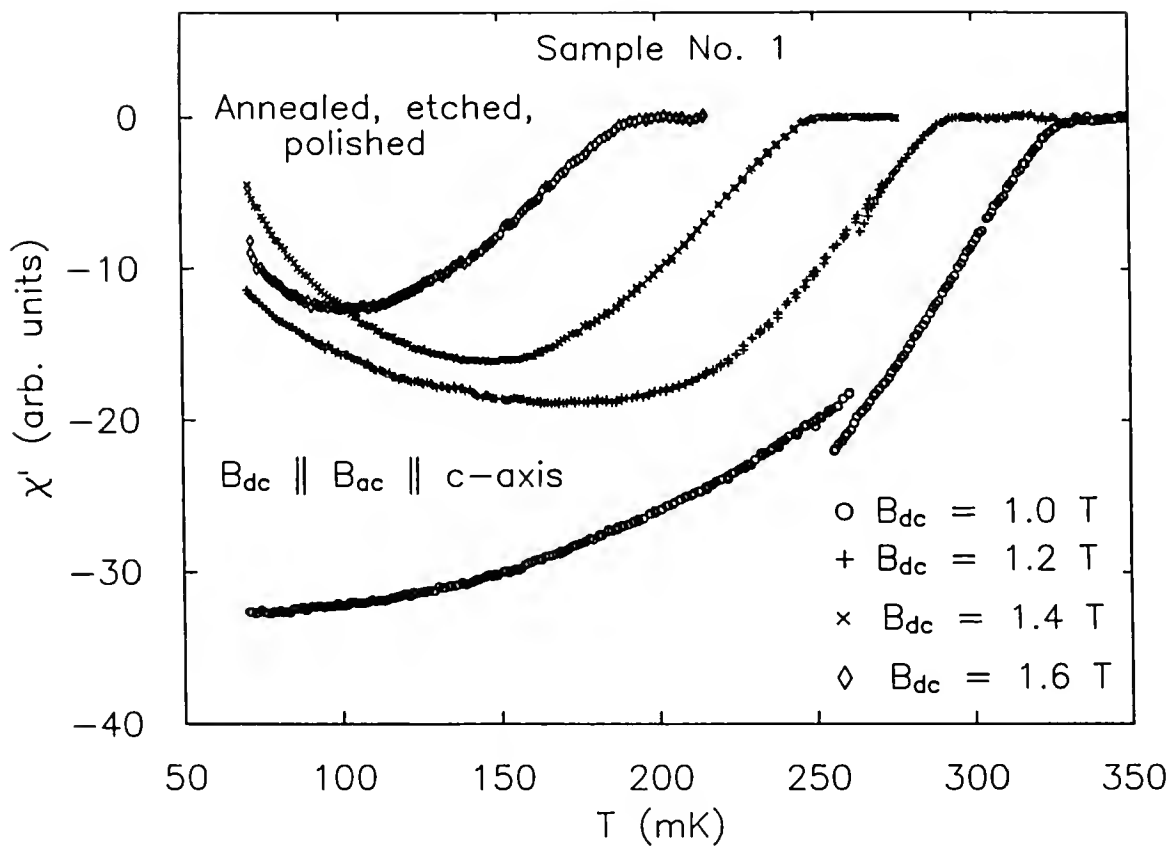


Fig. 4-18. $\chi'(T)$ for sample No. 1 (annealed, etched, polished) for $B_{dc} \geq 1$ T. An upturn is clearly observable for $B_{dc} \geq 1.2$ T.

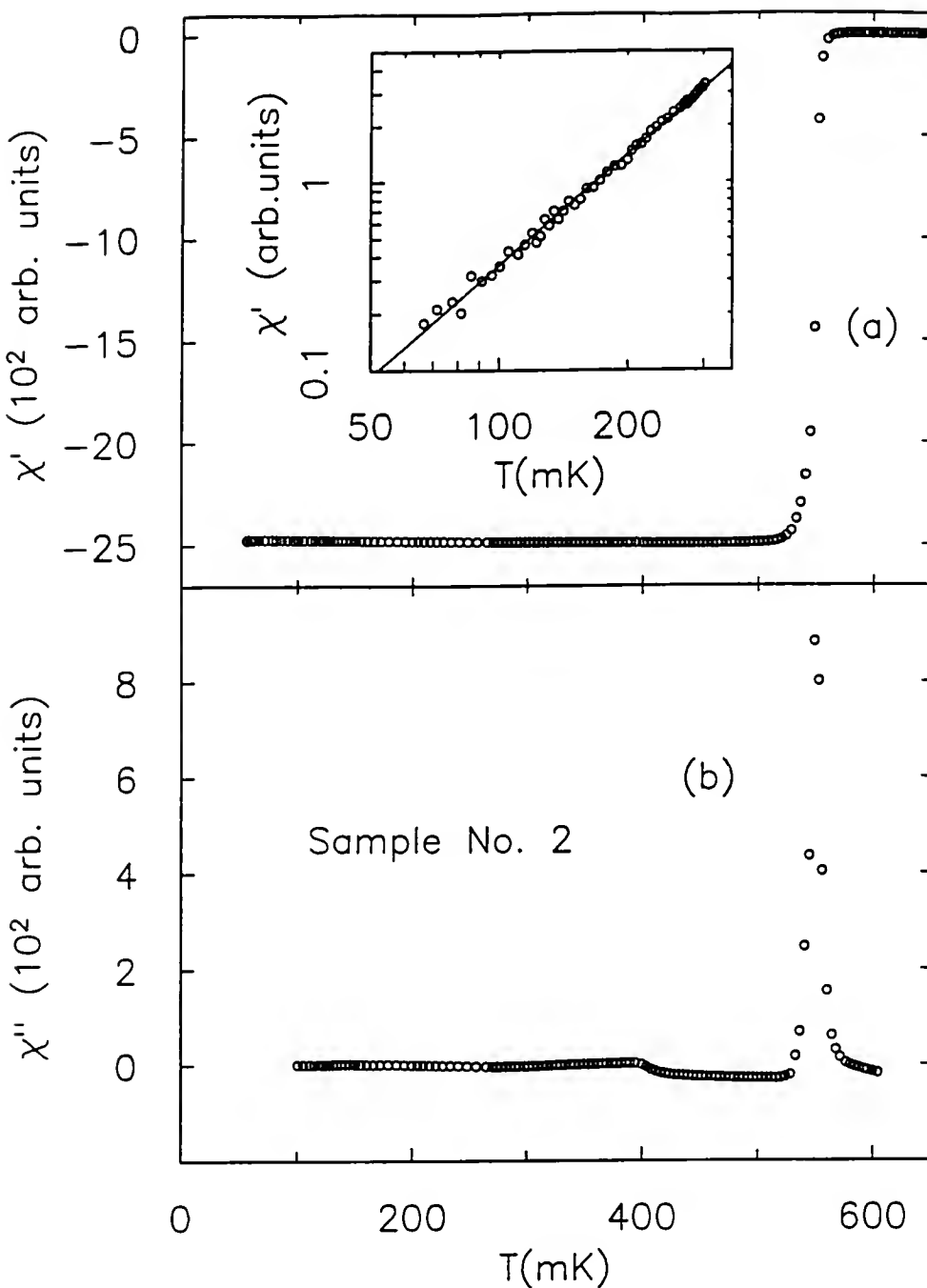


Fig. 4-19. Mutual inductance (417 Hz) data for single crystal No. 2 with $B_{ac} \parallel c$ -axis. (a) The real part of the susceptibility, $\chi'(T)$. The inset is a log-log plot of the data for $T/T_c \leq 0.5$. The solid line represents the result of a linear fit and yields a slope $\eta = 2.0 \pm 0.2$. (b) The imaginary part of the susceptibility, $\chi''(T)$. The double feature near T_c is not observable in either $\chi'(T)$ or $\chi''(T)$. The same scale of arbitrary units were used for $\chi'(T)$ and $\chi''(T)$.

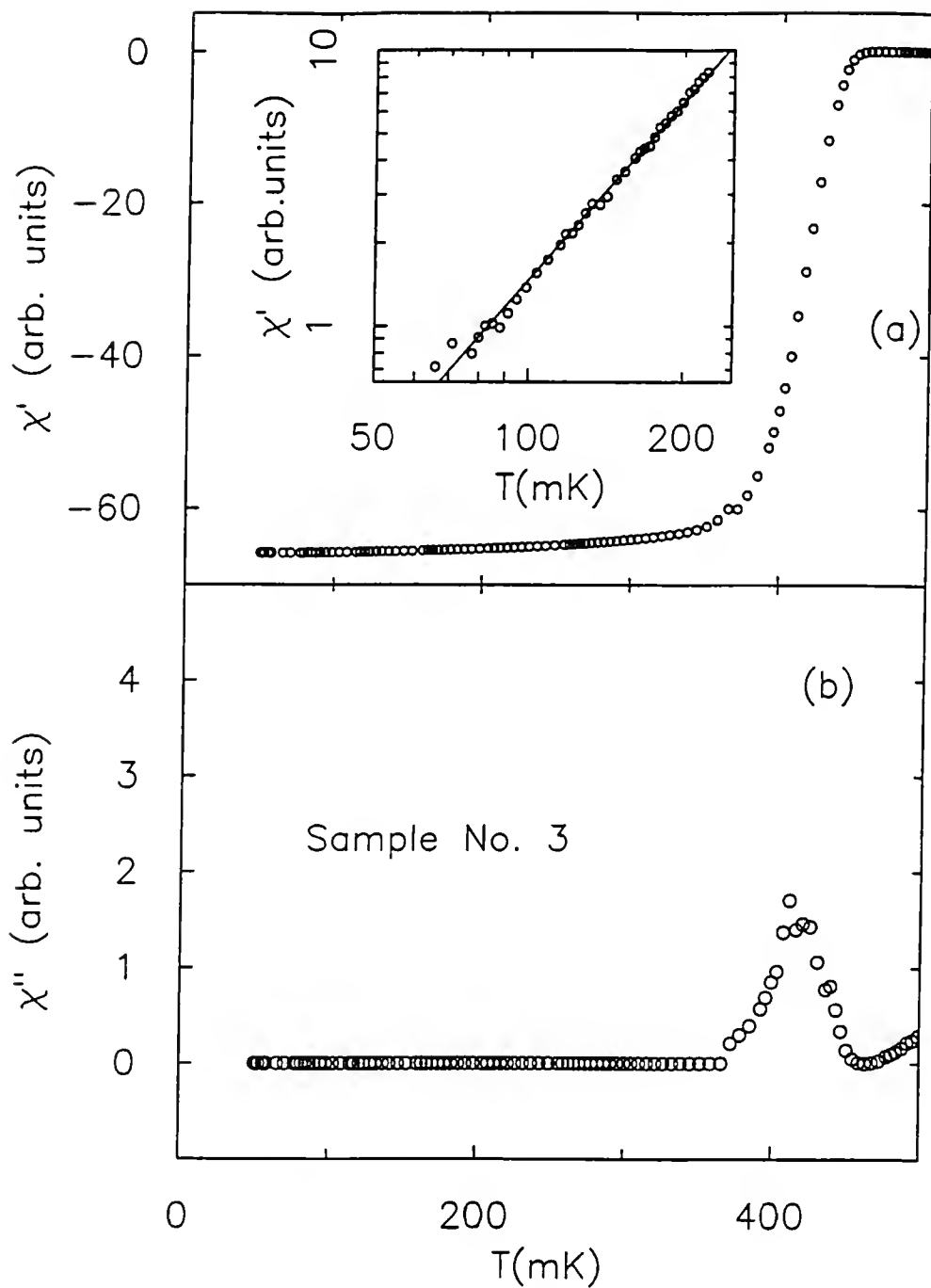


Fig. 4-20. (a) The real part of the susceptibility, $\chi'(T)$, from mutual inductance (317 Hz) with $\mathbf{B}_{\text{ac}} \parallel c$ -axis for sample No. 3. The inset shows a log-log plot of $\chi'(T)$ for $T/T_c \leq 0.5$. The solid line represents the result of a linear fit and yields a slope $\eta = 2.0 \pm 0.1$. (b) The imaginary part of the susceptibility, $\chi''(T)$. The double feature near T_c is not observable in either $\chi'(T)$ or $\chi''(T)$. The same scale of arbitrary units were used for $\chi'(T)$ and $\chi''(T)$.

450 mK, a significantly lower temperature compared to the other samples. The data near T_c did not exhibit a kink in $\chi'(T)$ and showed only one peak in $\chi''(T)$. The inset of Fig. 4-20a shows a log-log plot of $\chi'(T)$ for $T/T_c \leq 0.5$. The solid line represents the result of a linear fit, and yields $\eta = 2.0 \pm 0.1$, where η is defined in Eq. (4.15) and listed in Table 4-3. It is important to note here (a detailed discussion is to follow in the next section) that both samples No. 2 and No. 3 exhibited a quadratic temperature dependence and a single transition at T_c .

4.4.1.d Sample No. 4

The data for $\chi'(T)$ and $\chi''(T)$ on this polycrystalline sample are shown in Fig. 4-21. The double feature in $\chi'(T)$ near T_c corresponds to two peaks in $\chi''(T)$, with a difference in temperature of about 60 mK. This splitting was equal to that observed in the specific heat by Fisher *et al.* (1989), and was on the same order as the splitting reported for sample No. 1. The inset of Fig. 4-21a shows the low temperature ($T/T_c \leq 0.5$) results for $\chi'(T)$ on a log-log plot. For temperatures below 200 mK, $\chi'(T)$ was linear in temperature ($\eta = 1.0 \pm 0.1$, where η is defined in Eq. (4-15) and listed in Table 4-3), while between 200 mK and 300 mK, the data was best fitted to T^3 ($\eta = 3.0 \pm 0.2$).

4.4.1.e Sample No. 5

In Fig. 4-22, the results on sample No. 5 for $\chi'(T)$ and $\chi''(T)$, taken at 317 Hz, are shown. A kink in $\chi'(T)$, and a double peak in $\chi''(T)$ are clearly observable. The magnitude of the splitting, ΔT_c , between the two peaks is on the same order as the splitting observed in samples No. 1 and No. 4. Furthermore, this ΔT_c is consistent with the zero field sound velocity measurements performed on this sample, which showed two transitions separated by about 60 mK (Adenwalla *et al.*, 1990). The inset of Fig. 4-22a shows a log-log plot of $\chi'(T)$ for $T/T_c \leq 0.5$. A linear least squares fit indicates that the data fall on a straight line with a slope of $\eta = 0.9 \pm 0.1$, where η is defined in Eq. (4.15) and listed in Table 4-3.

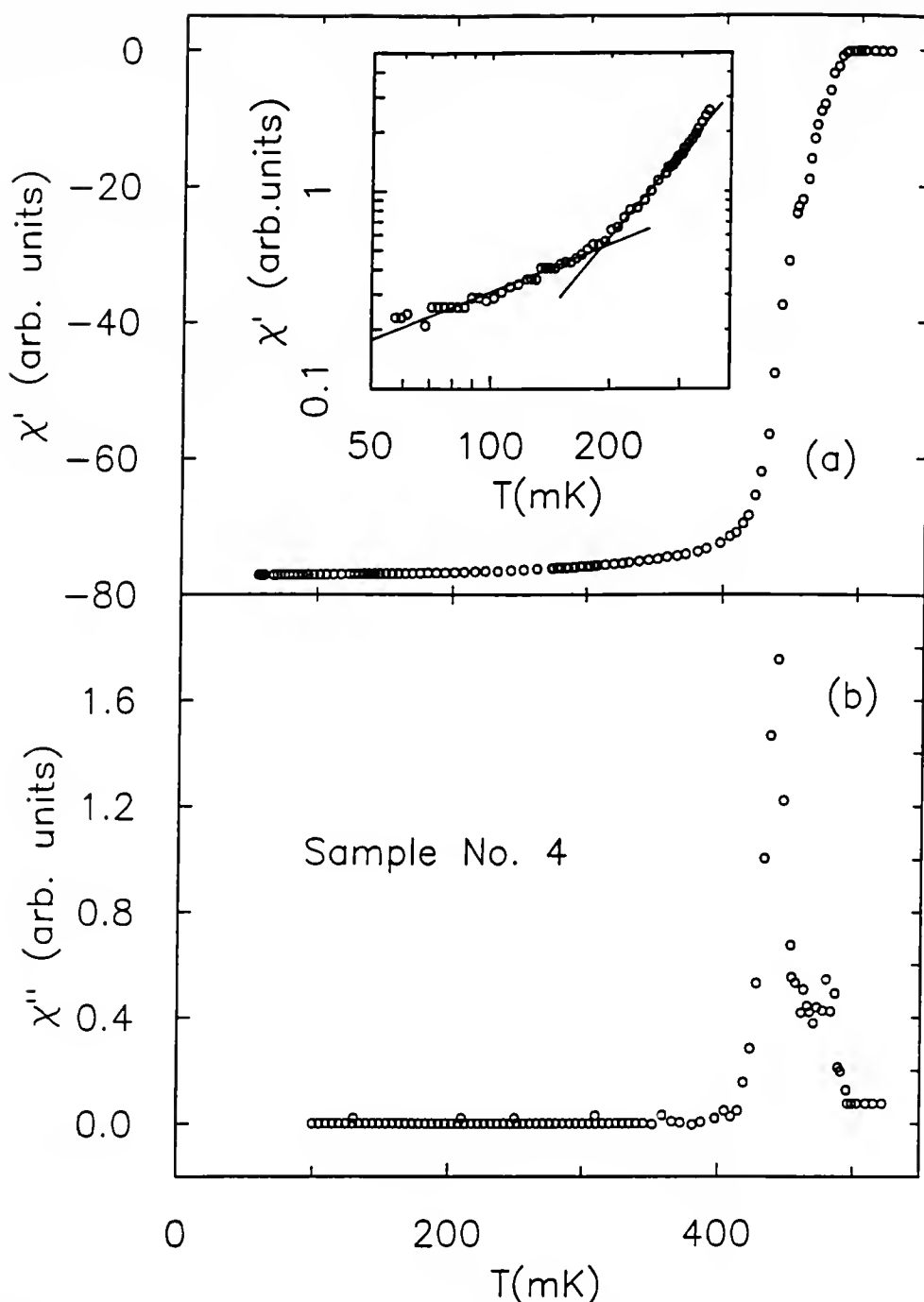


Fig. 4-21. (a) The real part of the susceptibility, $\chi'(T)$, for the polycrystal sample (No. 4) from mutual inductance (317 Hz). The inset shows a log-log plot of $\chi'(T)$ for $T/T_c \leq 0.5$. The solid lines represent the results of linear fits and yield a slope $\eta = 1.0 \pm 0.1$ for $T < 200$ mK, and $\eta = 3.0 \pm 0.1$ for $200 \text{ mK} < T < 300$ mK. (b) The imaginary part of the susceptibility, $\chi''(T)$. The two peaks in $\chi''(T)$ near T_c were separated by 60 mK, a difference which corresponds to the splitting observed in the specific heat by Fisher *et al.* (1989) and was on the same order as that reported for sample No. 1.

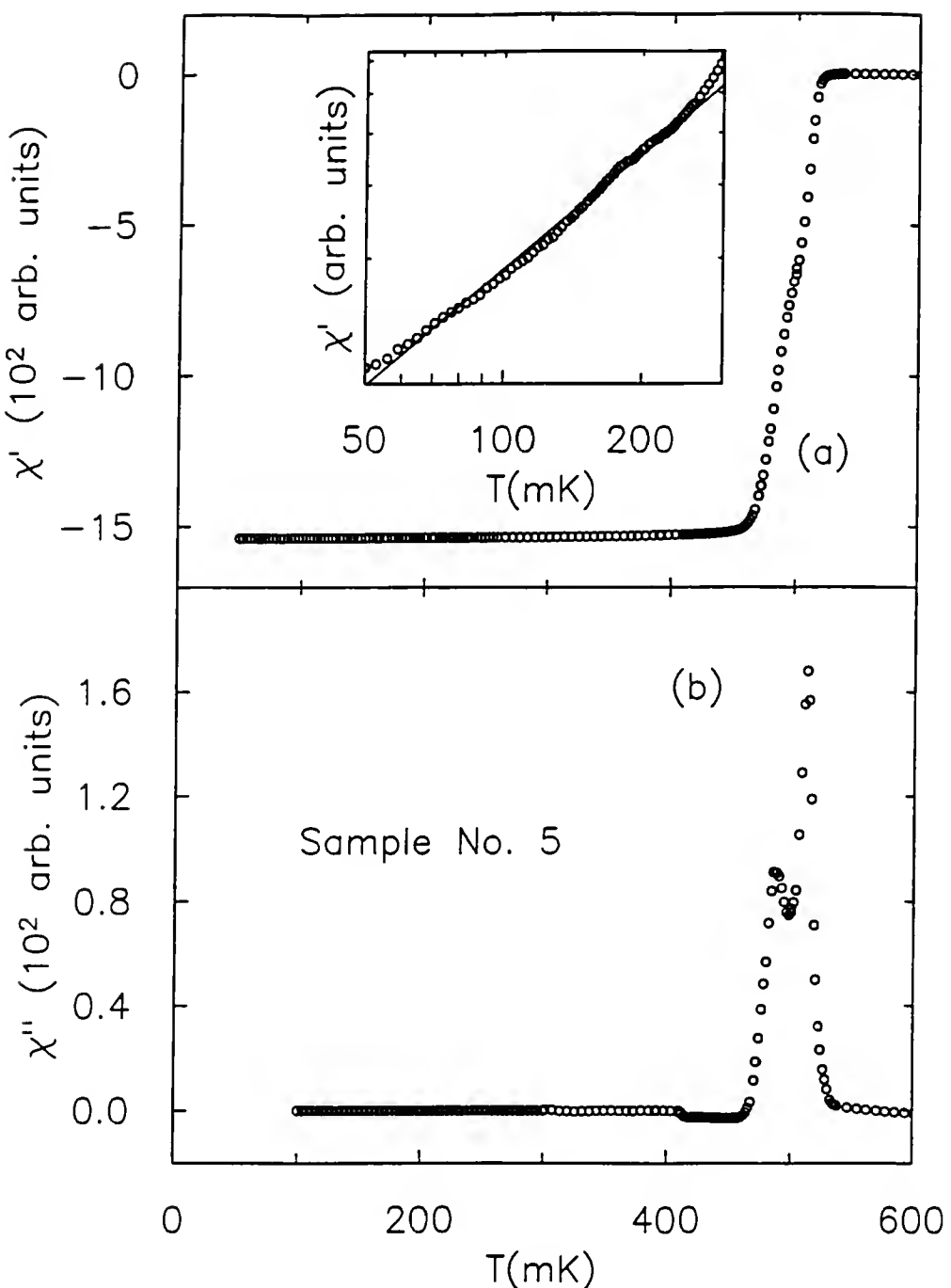


Fig. 4-22. Mutual inductance (317 Hz) data for single crystal No. 5 with $B_{ac} \parallel c$ -axis. (a) The real part of the susceptibility, $\chi'(T)$. The inset is a log-log plot of the data for $T/T_c \leq 0.5$. The solid line represents the result of a linear fit and yields a slope $\eta = 0.9 \pm 0.1$. (b) The imaginary part of the susceptibility, $\chi''(T)$. The double feature near T_c is observable in both $\chi'(T)$ and $\chi''(T)$ and is consistent with the sound velocity measurements on this same sample (Adenwalla *et al.*, 1990). The same scale of arbitrary units were used for $\chi'(T)$ and $\chi''(T)$.

4.4.1.f Sample No. 6

The results on sample No. 6 for $\chi'(T)$ and $\chi''(T)$, taken at 317 Hz, are shown in Fig. 4-23. The kink in $\chi'(T)$ is barely observable. The small "bump" on the right side of the peak in $\chi''(T)$ likely corresponds to a second smaller peak. The magnitude of the splitting, ΔT_C , between the top of the larger peak and the "bump", is on the same order as the double feature in the zero field sound velocity measurements on this sample (Lin, 1993). The inset of Fig. 4-23a shows a log-log plot of $\chi'(T)$ for $T/T_C \leq 0.5$. A linear least squares fit indicates that the data fall on a straight line with a slope of $\eta = 1.0 \pm 0.1$, where η is defined in Eq. (4.15) and listed in Table 4-3.

4.4.1.g Sample No. 7

The results on sample No. 7 are shown in Fig. 4-24 for $\chi'(T)$ and $\chi''(T)$, taken at 317 Hz. The $\chi'(T)$ transition does not exhibit any kink. The data for $\chi''(T)$ is very unusual, with a strong temperature dependence in the normal state, a very broad transition and an upturn below 200 mK. A possible explanation might come from the fact that the sample was mounted in between two pieces of epoxy, which were slid into the coils. This special technique was used only for sample No. 7, in order to assure the orientation of the crystal (of plate geometry) with respect to the field. It is possible that the thermal contraction of the epoxy caused additional strain on the sample and affected the measurements. This explanation is supported by the fact that the sample was found broken into three pieces after the measurements. The inset of Fig. 4-24a shows a log-log plot of $\chi'(T)$ for $T/T_C \leq 0.5$. A linear least squares fit indicates that the data fall on a straight line with a slope of $\eta = 2.1 \pm 0.2$ where η is defined in Eq. (4.15) and listed in Table 4-3.

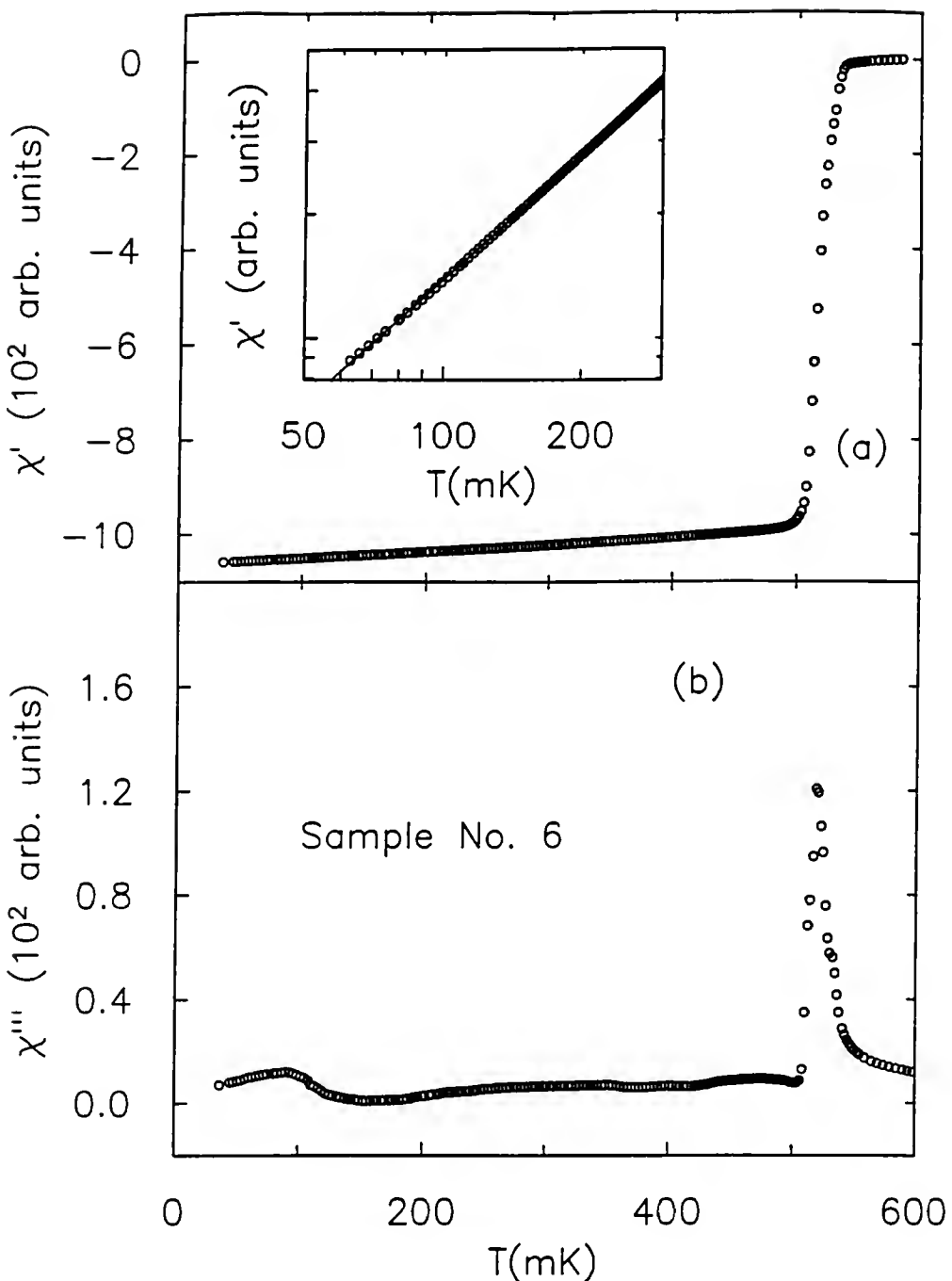


Fig. 4-23. Mutual inductance (317 Hz) data for single crystal No. 6 with $B_{ac} \parallel c$ -axis. (a) The real part of the susceptibility, $\chi'(T)$. The inset is a log-log plot of the data for $T/T_c \leq 0.5$. The solid line represents the result of a linear fit and yields a slope $\eta = 1.0 \pm 0.1$. (b) The imaginary part of the susceptibility, $\chi''(T)$. The double feature near T_c is observable in both $\chi'(T)$ and $\chi''(T)$, although not as clearly as in samples No. 1, No. 4, and No. 5. The ΔT_c obtained from our data is consistent with the sound velocity results of Lin (1993). The same scale of arbitrary units were used for $\chi'(T)$ and $\chi''(T)$.

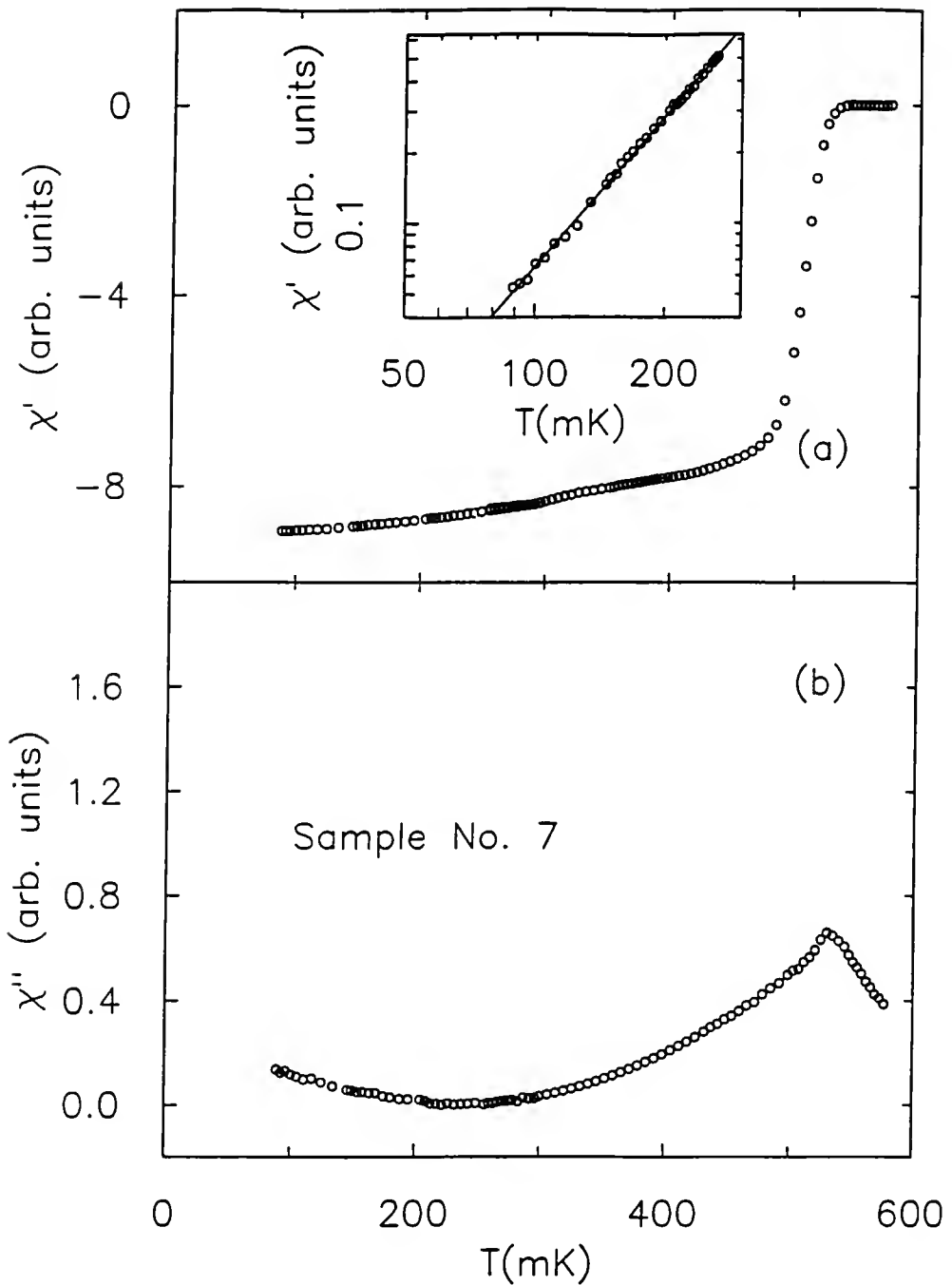


Fig. 4-24. Mutual inductance (317 Hz) data for single crystal No. 7 with $B_{ac} \parallel c$ -axis. (a) The real part of the susceptibility, $\chi'(T)$. The inset is a log-log plot of the data for $T/T_c \leq 0.5$. The solid line represents the result of a linear fit and yields a slope $\eta = 2.1 \pm 0.2$. (b) The imaginary part of the susceptibility, $\chi''(T)$. The double feature near T_c is not observable in either $\chi'(T)$ or $\chi''(T)$. The same scale of arbitrary units were used for $\chi'(T)$ and $\chi''(T)$.

4.4.1.h Sample No. 8

The data taken on sample No. 8 for $\chi'(T)$ and $\chi''(T)$ is shown in Fig. 4-25. This sample exhibited a very broad transition, likely caused by an intrinsic distribution of transition temperatures for these small whiskers. There was no signs of double transitions near T_c . The inset of Fig. 4-25a shows a log-log plot for $T/T_c \leq 0.5$. The solid line represents the result of a linear fit and yields $\eta = 1.3 \pm 0.2$ where η is defined in Eq. (4.15) and listed in Table 4-3.

4.4.2 Resonant Technique Results

In this section, the data from the tunnel diode oscillator measurements are presented by plotting the relative change in frequency, $\Delta f / f$, as a function of temperature, where $\Delta f / f = [f(T_{\min}) - f(T)] / f(T_{\min})$. This expression is justified by Eq. (3.34) which shows that, for $T < T_c$, $\Delta f / f$ is proportional to the changes in the penetration depth. A comparison of the units from sample to sample is not possible, since the inductors, and therefore the area A defined in Eq. (3.34), were different for each sample.

4.4.2.a Sample No. 1

Annealed and etched, and unpolished

Figure 4-26 shows the relative change in frequency on annealed and etched single crystal No. 1, for two different frequencies (3 MHz and 16 MHz) and with $B_{rf} \parallel c\text{-axis}$. Since the normal skin depth was larger for 3 MHz than for 16 MHz, $\Delta f / f$, at T_c , was larger for 3 MHz than for 16 MHz. The inset of Fig. 4-26 shows a log-log plot for $T/T_c \leq 0.5$. The solid lines represent the result of a linear fits and yield $\eta = 2.5 \pm 0.1$ and $\eta = 2.7 \pm 0.1$ for 3 MHz and 16 MHz respectively, where η is defined in Eq. (4-15) and listed in Table 4-3.

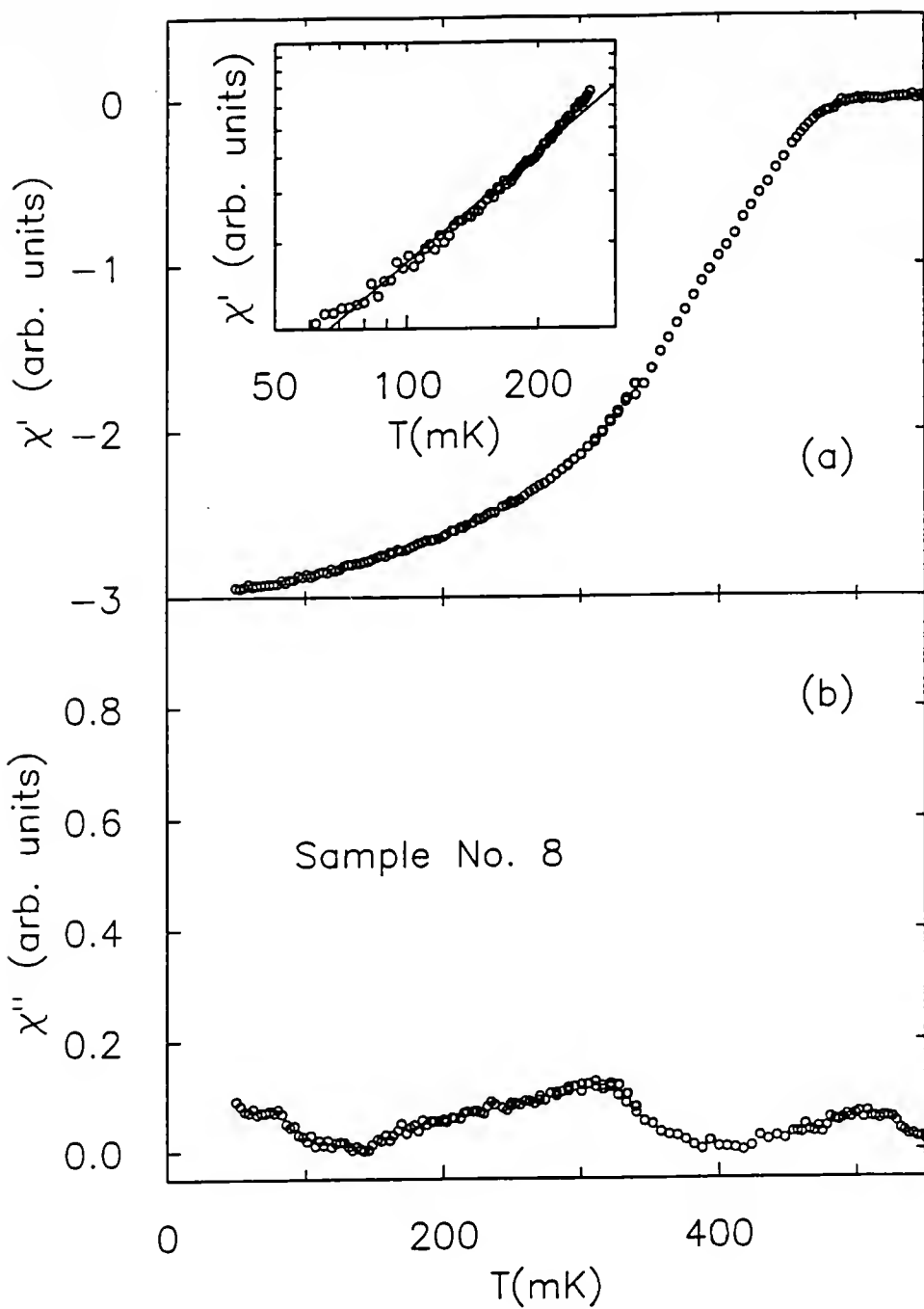


Fig. 4-25. Mutual inductance (317 Hz) data for sample No. 8 with $\mathbf{B}_{ac} \parallel c$ -axis. (a) The real part of the susceptibility, $\chi'(T)$. The inset is a log-log plot of the data for $T/T_C \leq 0.5$. The solid line represents the result of a linear fit and yields a slope $\eta = 1.3 \pm 0.2$. (b) The imaginary part of the susceptibility, $\chi''(T)$. The double feature near T_C is not observable in either $\chi'(T)$ or $\chi''(T)$. The same scale of arbitrary units were used for $\chi'(T)$ and $\chi''(T)$.

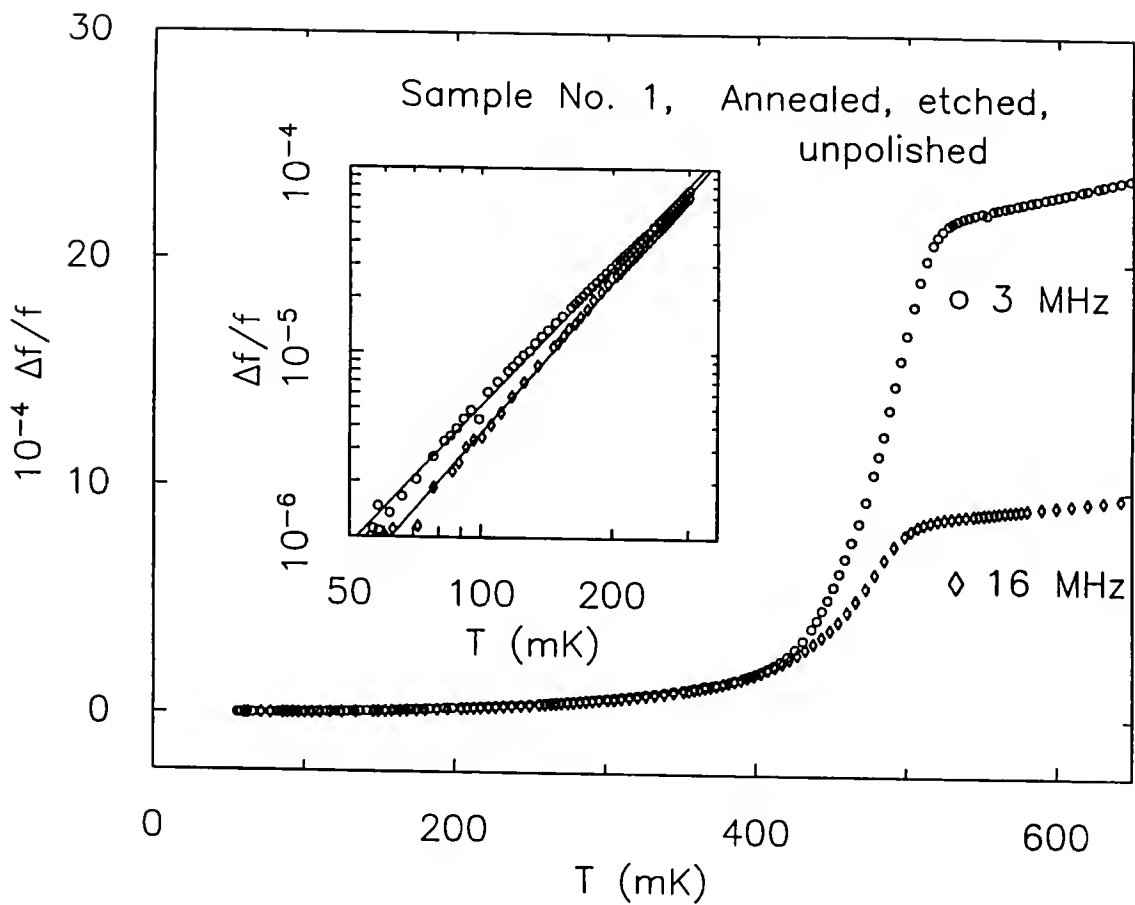


Fig. 4-26. The relative change in frequency $\Delta f / f = [f(T_{\min}) - f(T)]/f(T_{\min})$, as a function of temperature for single crystal No. 1 (annealed, etched, unpolished) at 3 MHz (○) and 16 MHz (◊) and with $\mathbf{B}_{rf} \parallel c$ -axis. The inset shows a log-log plot of $\Delta f / f$ vs. T for $T/T_c \leq 0.5$. The solid lines represent the results of a linear fits which yield a slope $\eta = 2.5 \pm 0.1$ for 3 MHz and $\eta = 2.7 \pm 0.1$ for 16 MHz.

Annealed, etched and polished

Figure 4-27 shows the relative change in frequency on single crystal No. 1 (annealed, etched, and polished), for two different frequencies (6 MHz and 17 MHz) and with $\mathbf{B}_{rf} \parallel c\text{-axis}$. The low temperature data for $f = 6$ MHz is shown in the inset of Fig. 4-27. On a log-log plot, the linear fit indicates that the data falls on a straight line of slope $\eta = 3.7 \pm 0.2$, where η is defined in Eq. (4-15) and listed in Table 4-3. This result indicates that the polishing of the surface caused a significant change in the temperature dependence of $\lambda(T)$. This effect will be discussed in the next section.

4.4.2.b Sample No. 2

The relative change of frequency as a function of temperature is shown in Fig. 4-28 for single crystal No. 2 (Table 4-2) at 5.6 MHz and with $\mathbf{B}_{rf} \parallel c\text{-axis}$. The inset of Fig. 4-28 shows a log-log plot for $T/T_c \leq 0.5$. The solid line represents the result of a linear fit and yields $\eta = 2.4 \pm 0.2$, where η is defined in Eq. (4.15) and listed in Table 4-3.

4.4.2.c Sample No. 3

The relative change of frequency as a function of temperature is shown in Fig. 4-29 for single crystal No. 3 (Table 4-2) at 15 MHz and with $\mathbf{B}_{rf} \parallel c\text{-axis}$. An important point to notice is the large (≈ 50 mK) decrease in T_c onset compared to the low frequency results (Fig. 4-20). This decrease is due to self-heating of the sample near T_c arising from the presence of a significant quantity of quasiparticles near T_c . In addition, this effect is enhanced by the significant surface roughness (i.e. surface resistivity) of this sample compared to others (Fig. 4-6). These effects are discussed in the next section. Although some self-heating may still be present deep in the superconducting state, it should be dramatically reduced. Given this caveat, we have, for completeness, provided a log-log plot of the data for $T/T_c \leq 0.5$ (see inset of Fig. 4-29). The solid line represents

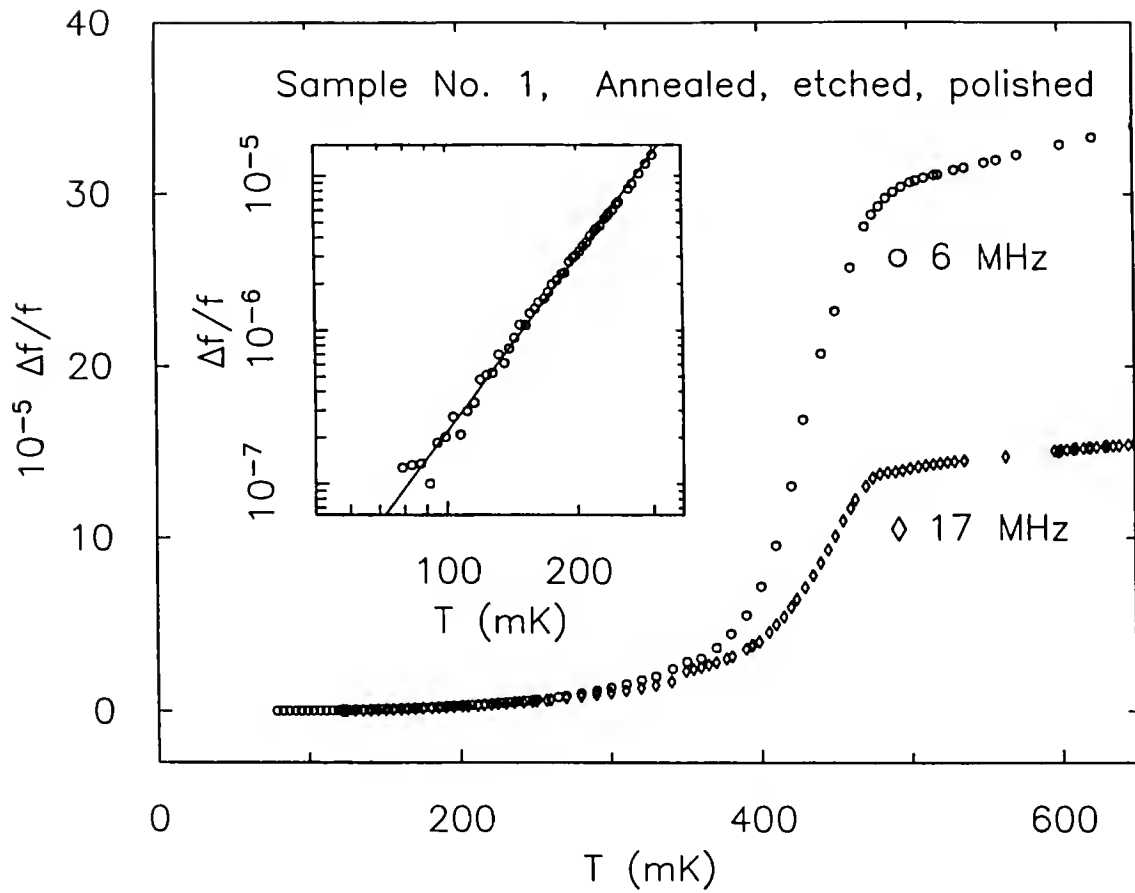


Fig. 4-27. The relative change in frequency $\Delta f / f = [f(T_{\min}) - f(T)] / f(T_{\min})$ as a function of temperature for single crystal No. 1 (annealed, etched, and polished) at 6 MHz (\circ) and 17 MHz (\diamond) with $B_{rf} \parallel c$ -axis. The inset shows a log-log plot of $\Delta f / f$ vs. T for $T / T_c \leq 0.5$. The solid line represents the result of a linear fit and yields a slope $\eta = 3.7 \pm 0.2$.

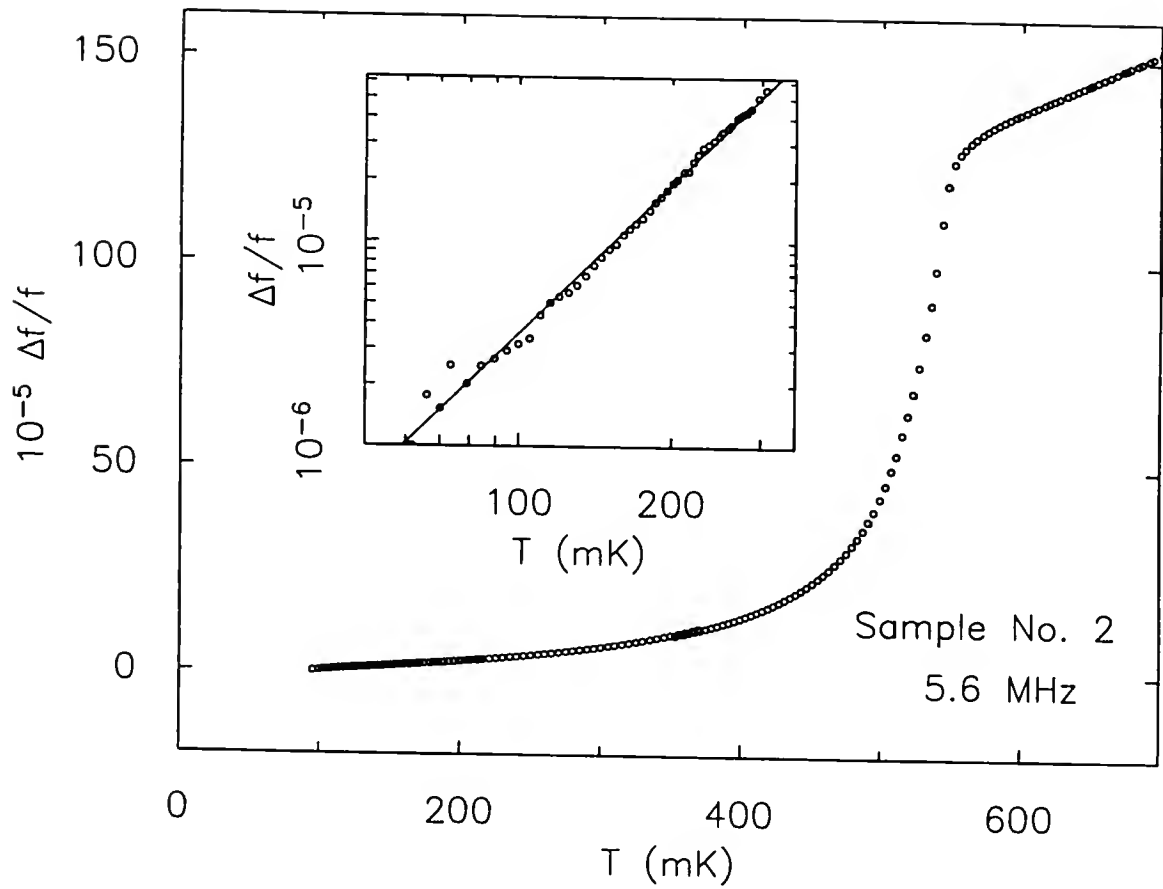


Fig. 4-28. The relative change in frequency $\Delta f / f = [f(T_{\min}) - f(T)]/f(T_{\min})$ as a function of temperature for single crystal No. 2 at 5.6 MHz with $B_{rf} \parallel c$ -axis. The inset shows a log-log plot of $\Delta f / f$ vs. T for $T/T_c \leq 0.5$. The solid line represents the result of a linear fit and yields a slope $\eta = 2.4 \pm 0.2$.

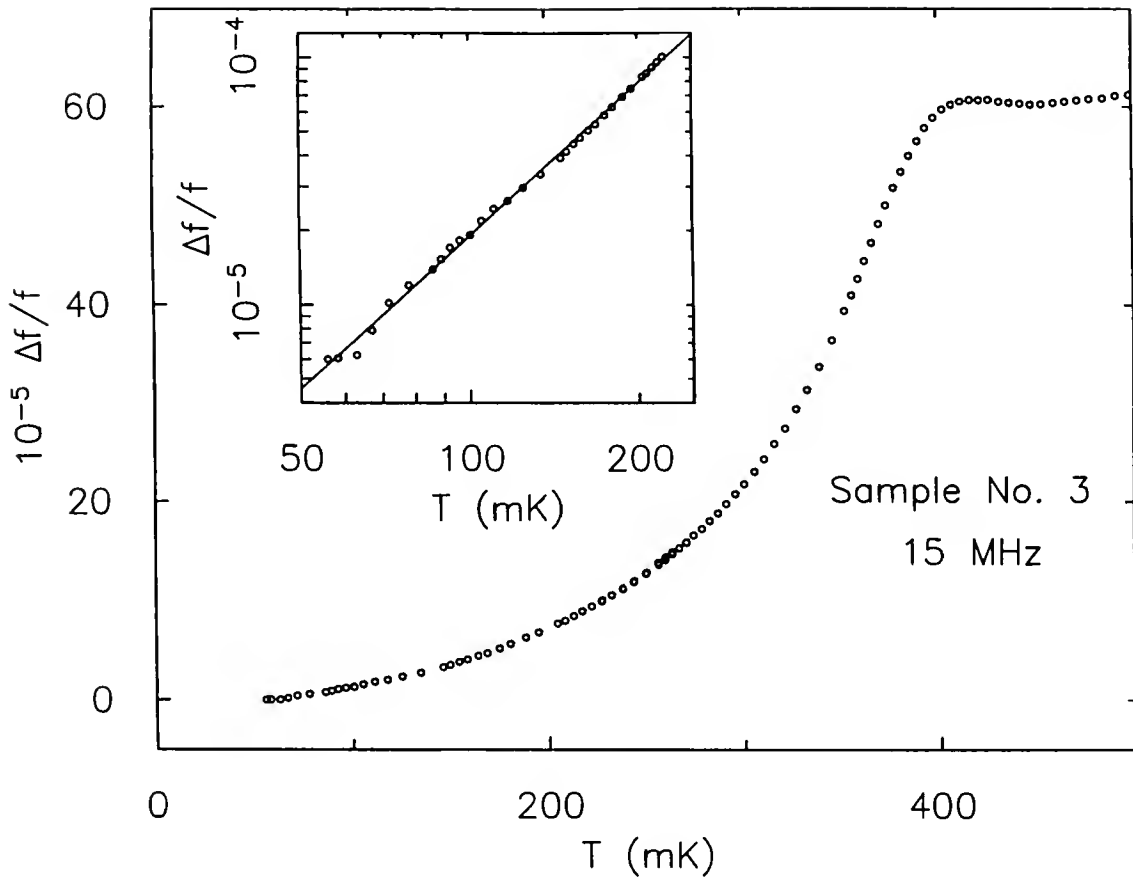


Fig. 4-29. The relative change in frequency $\Delta f / f = [f(T_{\min}) - f(T)]/f(T_{\min})$ as a function of temperature for single crystal No. 3 at 15 MHz with $B_{rf} \parallel c$ -axis. The inset shows a log-log plot of $\Delta f / f$ vs. T for $T/T_c \leq 0.5$. The solid line represents the result of a linear fit and yields slope $\eta = 2.0 \pm 0.2$.

the result of a linear fit and yields $\eta = 2.0 \pm 0.2$, where η is defined in Eq. (4-15) and listed in Table 4-3.

4.4.2.d Sample No. 4

The data for sample No. 4 has already been published by Brown *et al.* (1990). For completeness, their work is reproduced in Fig. 4-30, where $\Delta f / f = [f(T) - f(T_{\min})]/f(T_{\min})$ is plotted as a function of temperature, as opposed to $\Delta f / f = [f(T_{\min}) - f(T)]/f(T_{\min})$. These authors reported a T^4 temperature dependence for $\Delta f / f$.

4.4.2.e Sample No. 5

The relative change of frequency as a function of temperature is shown in Fig. 4-31 for single crystal No. 5 (Table 4-2) at 12 MHz and with $\mathbf{B}_{rf} \parallel c\text{-axis}$. The inset of Fig. 4-31 shows a log-log plot for $T/T_c \leq 0.5$. The solid line represents the result of a linear fit and yields $\eta = 1.8 \pm 0.2$, where η is defined in Eq. (4-15) and listed in Table 4-3.

4.4.2.f Sample No. 6

The relative change of frequency as a function of temperature is shown in Fig. 4-32 for single crystal No. 6 (Table 4-2) at 14 MHz and with $\mathbf{B}_{rf} \parallel c\text{-axis}$. The inset of Fig. 4-32 shows a log-log plot for $T/T_c \leq 0.5$. The solid line represents the result of a linear fit and yields $\eta = 2.0 \pm 0.2$, where η is defined in Eq. (4-15) and listed in Table 4-3.

4.4.2.g Sample No. 7

The data for sample No. 7 has already been published by Gannon *et al.* (1990). For completeness, their work for $\mathbf{B}_{rf} \parallel c\text{-axis}$ is reproduced in Fig. 4-33. These authors reported a T^4 temperature dependence for $\Delta f / f$. However, a linear fit on a log-log plot of their 10 MHz data indicates that, above 140 mK, the data falls on a straight line of slope $\eta = 2.8 \pm 0.2$, where η is defined in Eq. (4-15) and listed in Table 4-3. The temperature

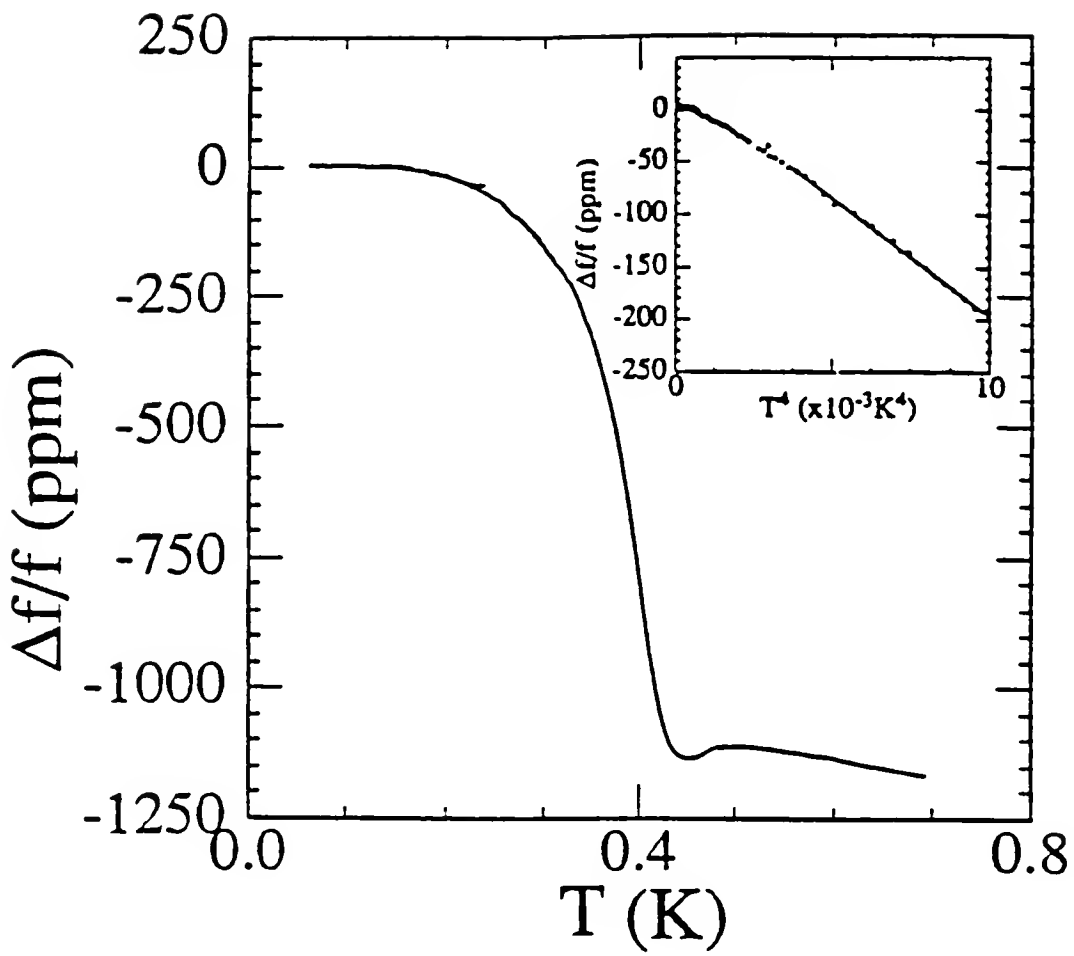


Fig. 4-30. The relative change in frequency $\Delta f / f = [f(T) - f(T_{\min})]/f(T_{\min})$ as a function of temperature for sample No. 4 at 15 MHz. The data is from Brown *et al.* (1990). The inset shows $\Delta f / f$ vs. T^4 for $T/T_c \leq 0.5$.

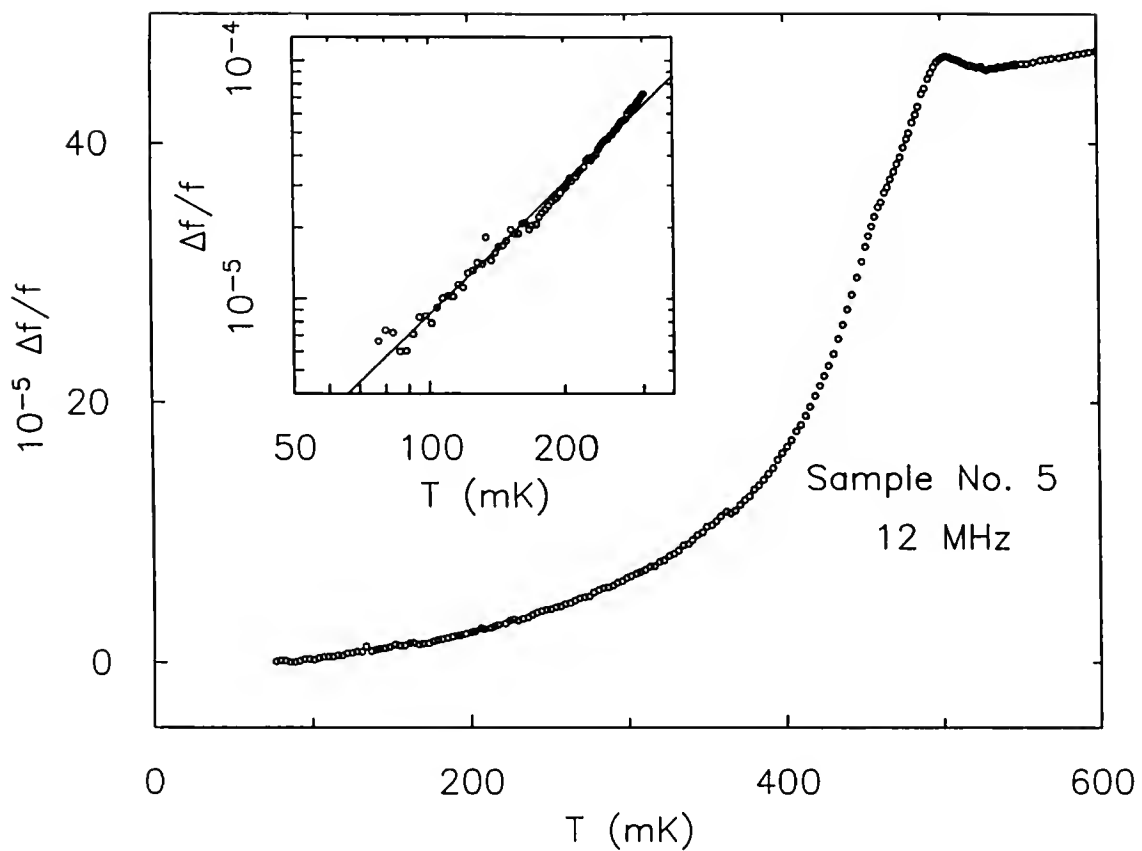


Fig. 4-31. The relative change in frequency $\Delta f / f = [f(T_{\min}) - f(T)] / f(T_{\min})$ as a function of temperature for single crystal No. 5 at 12 MHz with $B_{rf} \parallel c$ -axis. The inset shows a log-log plot of $\Delta f / f$ vs. T for $T/T_c \leq 0.5$. The solid line represents the result of a linear fit and yields slope $\eta = 1.8 \pm 0.2$.

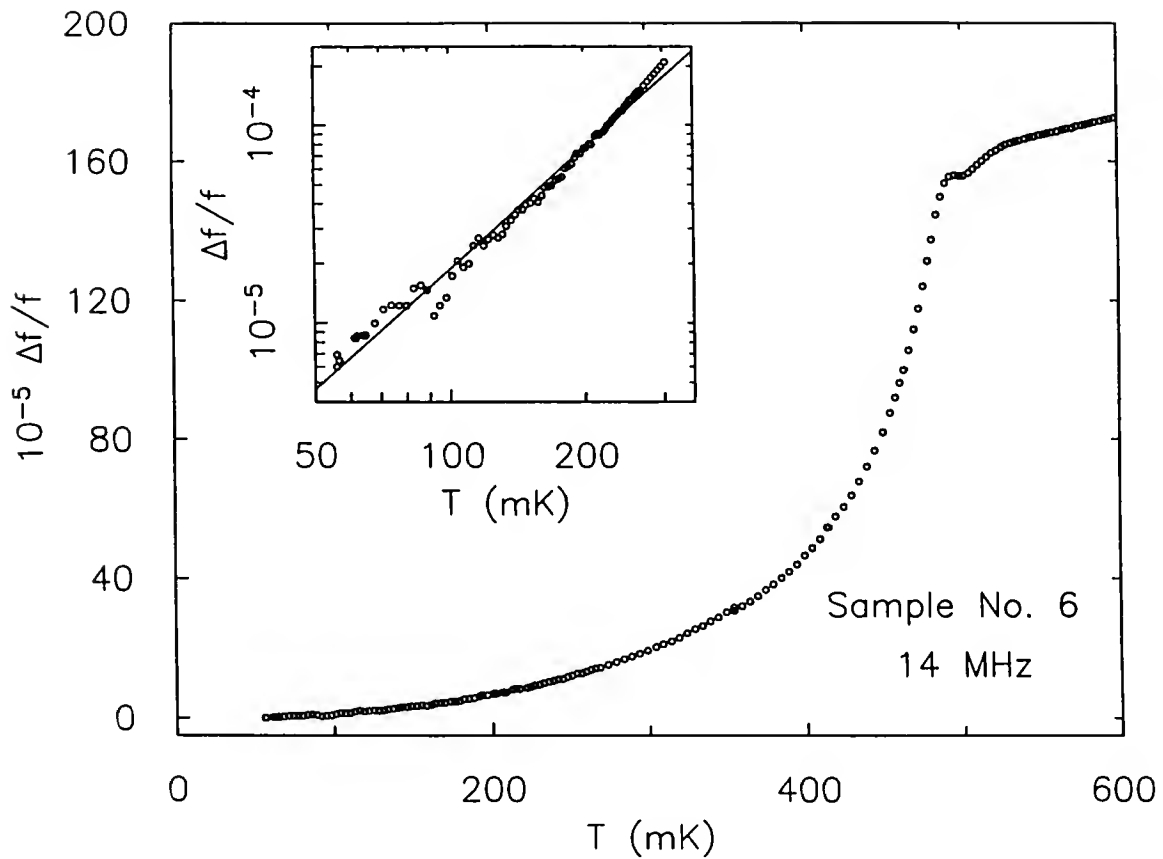


Fig. 4-32. The relative change in frequency $\Delta f / f = [f(T_{\min}) - f(T)]/f(T_{\min})$ as a function of temperature for single crystal No. 6 at 14 MHz with $B_{rf} \parallel c$ -axis. The inset shows a log-log plot of $\Delta f / f$ vs. T for $T/T_c \leq 0.5$. The solid line represents the result of a linear fit and yields a slope $\eta = 2.0 \pm 0.2$.

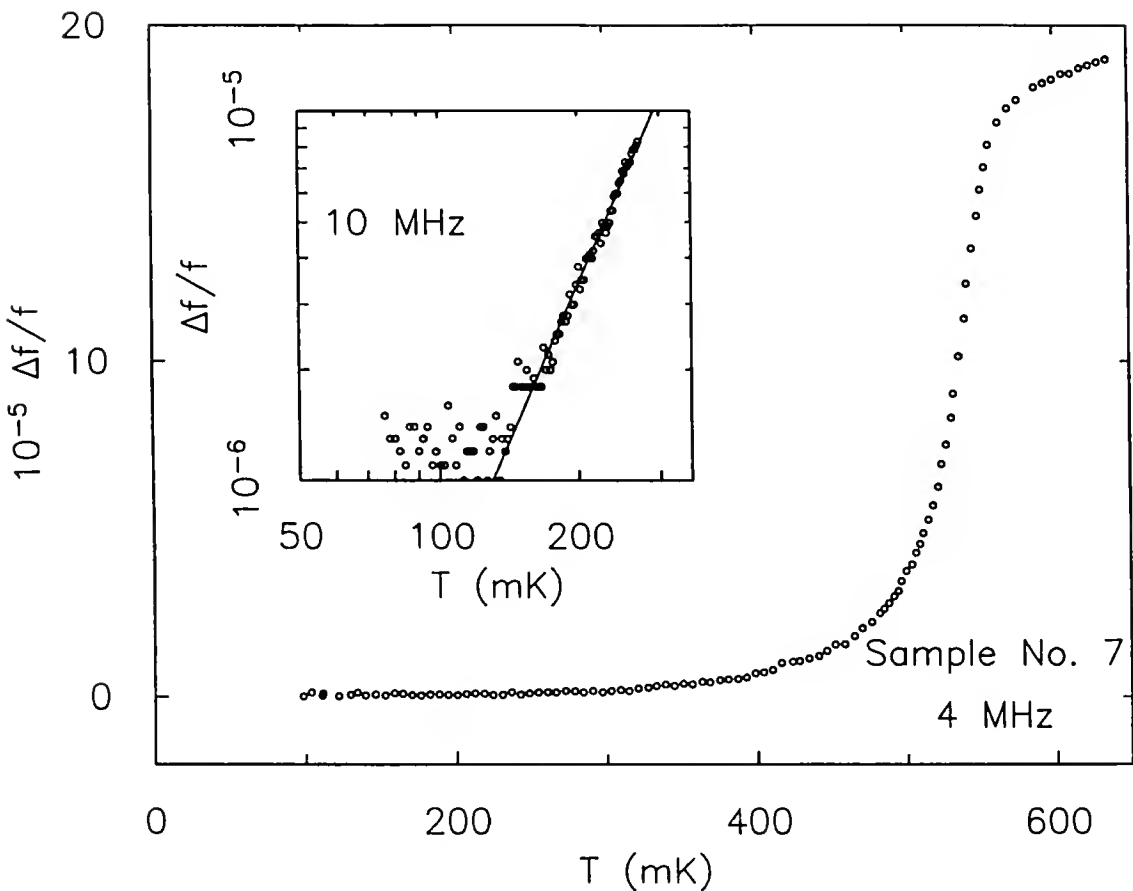


Fig. 4-33. The relative change in frequency $\Delta f / f = [f(T_{\min}) - f(T)] / f(T_{\min})$ as a function of temperature for single crystal No. 7 at 4 MHz with $B_{rf} \parallel c$ -axis. The inset shows a log-log plot of $\Delta f / f$ vs. T for $T/T_c \leq 0.5$ and for 10 MHz. The solid line represents the result of a linear fit and yields a slope $\eta = 2.8 \pm 0.2$. The sample does not seem to cool below 140 mK. The data are from Gannon *et al.* (1990).

Table 4-3. Summary of the temperature dependences obtained from mutual inductance (low frequencies) and tunnel diode oscillator measurements (rf frequencies). η is defined in Eq. (4.15).

Samples	η from low frequencies	η from rf frequencies	double feature in $\chi(T)$
No. 1 as grown	1.0 ± 0.2	no data taken	NO
No. 1 annealed, etched	1.0 ± 0.1	2.6 ± 0.2	YES
No. 1 annealed, etched, polished	1.0 ± 0.1	3.7 ± 0.2	YES
No. 2	2.0 ± 0.2	2.4 ± 0.2	NO
No. 3	2.0 ± 0.1	2.0 ± 0.2	NO
No. 4	1.0 ± 0.1 ($T < 200$ mK)	~ 4.0	YES
No. 5	0.9 ± 0.1	1.8 ± 0.2	YES
No. 6	1.0 ± 0.1	2.0 ± 0.2	YES
No. 7	2.1 ± 0.2	2.8 ± 0.2	NO
No. 8	1.3 ± 0.2	no data taken	NO

independent signal below 140 mK might be due to the fact that the sample is not cooling any further.

4.4.2.h Sample No. 8

Measurements using the tunnel diode oscillator technique on sample No. 8 were not performed since the low frequency data for this specimen showed an unusually broad transition (Fig. 4-25). A distribution of transition temperatures is probably responsible for such broadening, which complicates the analysis of the inductive response in terms of the penetration depth for this sample.

4.5 Discussion

In this section, some of the main results just presented are discussed. The significance of the linear temperature dependence found in several samples is covered first, followed by remarks about the quadratic dependence exhibited by other specimens. The double feature observed in the vicinity of T_c for several samples is considered in the third subsection. Next, the frequency dependence of our results, *i.e.* η from mutual inductances vs. η from tunnel diode measurements, is discussed. Finally, the low temperature upturn in $\chi'(T)$ for fields greater than 1 T is analyzed.

4.5.1 Linear Temperature Dependence of $\lambda(T)$

From the low frequency data for samples No. 1, No. 4, No. 5, and No. 6, *i.e.* Figs. 4-10a, 4-11a, 4-13a, 4-21a, 4-22a, and 4-23a, $\lambda(T)$ is linear in temperature for $T/T_c \leq 0.5$ (Table 4-3). Since, for all these measurements, the probing ac magnetic field was oriented parallel to the c-axis of the crystal, the shielding currents flowed in the basal plane. Therefore, the data suggest that the energy gap possesses a line of nodes in the basal plane, and this arrangement is consistent with the polar state (Gross *et al.*, 1986). This identification is in agreement with thermal conductivity and ultrasonic attenuation

experiments (Behnia *et al.*, 1992; Bishop *et al.*, 1984; Shivaram *et al.*, 1986a). Furthermore, this linearity in $\lambda_{\perp}(T)$, where the symbol " \perp " refers to the vector potential orientation relative to the c-axis (following the notation of Gross *et al.*, 1986), agrees with μ SR measurements by Broholm *et al.* (1990), where a hybrid-state (*i.e.* line nodes in the basal plane and point nodes on the c-axis) was proposed. However, questions have been raised about the validity of the μ SR raw data analysis used to extract $\lambda(T)$ (Luke *et al.*, 1991; 1993). Nevertheless, our work on sample No. 1 does not allow us to comment on the possibility of any gap nodes out of the a-b plane. One might think that insight into this point could be gained by considering the results on sample No. 4, Fig. 4-21a. Gross *et al.* (1986) have shown that, for the polar state, $\lambda(T)$ is linear in temperature for fields parallel to the c-axis and $\lambda(T) \propto T^3$ for fields perpendicular to the c-axis. In a polycrystal (such as our sample No. 4), where both orientations are present, one might expect to see $\lambda(T) \propto T$ dominate at low temperature and $\lambda(T) \propto T^3$ at higher temperatures. The data for sample No. 4, Fig. 4-21a, *qualitatively* suggest that the temperature dependence is linear below 200 mK, and cubic between 200 mK and 300 mK. On the other hand, T^2 and T^4 contributions might also arise if the hybrid-state exists (Gross *et al.*, 1986), and these effects may also be reflected in the data, Fig. 4-21a. Therefore, our measurements cannot differentiate from these various possibilities. We are in a position to state that our results on some samples are consistent with line nodes in the basal plane, and further information about the gap structure out of the basal plane awaits additional experiments.

4.5.2 Quadratic Temperature Dependence of $\lambda(T)$

Our low frequency data on sample No. 2, Fig. 4-19 and Table 4-3, has reproduced the quadratic temperature dependence of $\lambda(T)$ reported by Gross *et al.* (1988) on the same specimen. This result suggests that the dc technique used by these authors is equivalent to our low frequency mutual inductance method. It was in fact this quadratic temperature dependence which motivated Groß-Alltag *et al.* (1991) to study the influence of impurities

on the penetration depth. These authors suggested that $\lambda(T) \propto T^2$ could be explained by the presence of non-magnetic impurities in the sample.

A quadratic temperature dependence was also observed for samples No. 3 and No. 7, Figs. 4-20a and 4-24a. Another common feature between these three specimens is the single transition observed at T_c . It is interesting to note that none of these samples were annealed. A connection between annealing and the presence of double transitions near T_c has already been reported (Vorenkamp *et al.*, 1990; Midgley *et al.*, 1993) and is further emphasized by our results on sample No. 1. Before annealing, sample No. 1 did not show signs of a double transition, but after annealing, the double feature in $\chi'(T)$ was clearly observable. The obvious conclusion from these results is that unannealed specimens possess a quadratic $\lambda(T)$. However, this interpretation is not supported by our work on sample No. 1 (unannealed), (Fig. 4-10), where quadratic temperature dependence is not observed, but rather η (Eq. 4-15) is closer to 1.

4.5.3 Double Feature Near T_c

From the low frequency data on sample No. 1 (annealed, etched, unpolished and annealed, etched, polished), Figs. 4-11, and 4-13, and on samples No. 4, No. 5, and No. 6, Figs. 4-21, 4-22, and 4-23, we also learn that the inductive response of the sample is sensitive to the double transition near T_c . One might, at first, find this result surprising since it is usually thought that once superconductivity occurs, the supercurrents shield the bulk of the sample. This argument is valid for BCS-like superconductors, where the penetration depth is shorter than the coherence length, ξ . A typical example is In where $\lambda(0) \approx 210 \text{ \AA}$ and $\xi \approx 440 \text{ \AA}$. In UPt₃, $\lambda(T \rightarrow 0) \approx 1\text{-}2 \mu\text{m}$, which is much larger than $\xi \approx 100 \text{ \AA}$ (Chen *et al.*, 1984). We therefore expect our probing ac magnetic fields to be sensitive to the bulk superconducting state. Furthermore, the phase diagram constructed from our inductive measurements (Fig. 4-15) provides further evidence that the kinks in $\chi'(T)$ correspond to the transitions observed in experiments studying bulk properties

(specific heat, thermal expansion and sound velocity). Finally, we observed this effect in two different samples which also showed double transitions in their specific heat (samples No. 1 and No. 4), and in two samples exhibiting double transitions in sound velocity measurements (samples No. 5 and No. 6), and we did not observe a kink in the samples that showed a single transition in their specific heats (samples No. 2 and No. 3). It is noteworthy that, this double feature near T_c has been present in $\chi'(T)$ data presented by others, see for example Sulpice *et al.* (1986) and Bruls *et al.* (1990).

4.5.4 High Frequency Effects

4.5.4.a Temperature dependence of $\lambda(T)$

For all samples (with the exception of No. 3 and No. 8), $\lambda(T/T_c < 0.5)$ was different at higher frequencies (≥ 3 MHz) compared to lower frequencies (≤ 4.7 kHz). This result clearly indicates that the previous discrepancy, found from the studies of other groups between low and high frequency measurements (Groß-Alltag *et al.*, 1991; Gannon *et al.*, 1990), was not simply related to the difference in samples used by these different workers. Our work clearly shows that these distinct results must come from either the differences in the methods used to measure $\lambda(T)$ (mutual inductance vs. tunnel diode oscillator) or the intrinsic properties of UPt₃. In the following paragraphs, arguments are given against the former possibility.

In Chapter 3, the procedure for extracting $\lambda(T)$ from mutual inductance and tunnel diode oscillator measurements was described in detail. In the analysis, the important assumption was that the resistive part of the response goes to zero in the superconducting state. The mutual inductance technique allows this assumption to be checked by measuring $\chi''(T)$. In all our measurements, except for sample No. 7, $\chi''(T)$ was essentially zero for temperatures below $T/T_c = 0.5$, the range from which the power laws were extracted. Therefore, our mutual inductance data correspond to the penetration depth, at least for $T/T_c \leq 0.5$. This assertion is supported by our results on sample No. 2 which

agreed with the measurements by Groß-Alltag *et al.* (1991) on the same sample using a dc magnetometer.

We now turn to the tunnel diode oscillator (TDO) technique, which does not directly measure the lossy contribution of the signal. First, it is important to recall the successful results on aluminum presented in Chapter 3 (Fig. 3-15). The aluminum data, taken using the TDO method, was well fitted by the BCS prediction for a type I superconductor of $\lambda(T)$, given by Eq. (4.13). Furthermore, the fitted T_C was within 5 mK of the T_C observed with the mutual inductance method, indicating negligible self-heating from the resistive part of the signal. These results, in addition to the work of other workers using the TDO technique (Tedrow *et al.*, 1971; Varmazis *et al.*, 1974; 1975), justify the use of the TDO method to measure $\lambda(T)$, at least in BCS-like superconductors. However, one might argue that, in superconductors possessing nodes in their energy gap structure, the density of normal electrons does not fall to zero as quickly as in a superconductor with a full gap around the Fermi surface. This assertion is discussed in the next paragraph, and in the context of our results for UPt₃.

In Figure 4-34 the data on sample No. 2, in the vicinity of T_C , for both low and high frequencies are shown. In order to facilitate the comparison, the data was normalized so that the total change in signal between T_C and T_{\min} is unity for both sets of data. Although T_C is nominally the same for both runs, a broadening of the transition was clearly observed for the rf measurement. A large broadening, in addition to a shift in T_C , was also present for sample No. 3, as can be seen by comparing Fig. 4-20 and Fig. 4-29. To understand this effect, let us go back to Eq. (3-34), where we asserted that, below T_C , $\Delta f / f$ was proportional to $\Delta \lambda$. In other words, the surface impedance consists completely of a reactive contribution and no resistive component. Pippard (1947) has shown that this assertion is in general true except near the critical temperature where the presence of normal electrons introduces some resistance to the surface impedance. This resistive contribution gives the measured $\lambda(T)$ a weaker temperature dependence than the actual

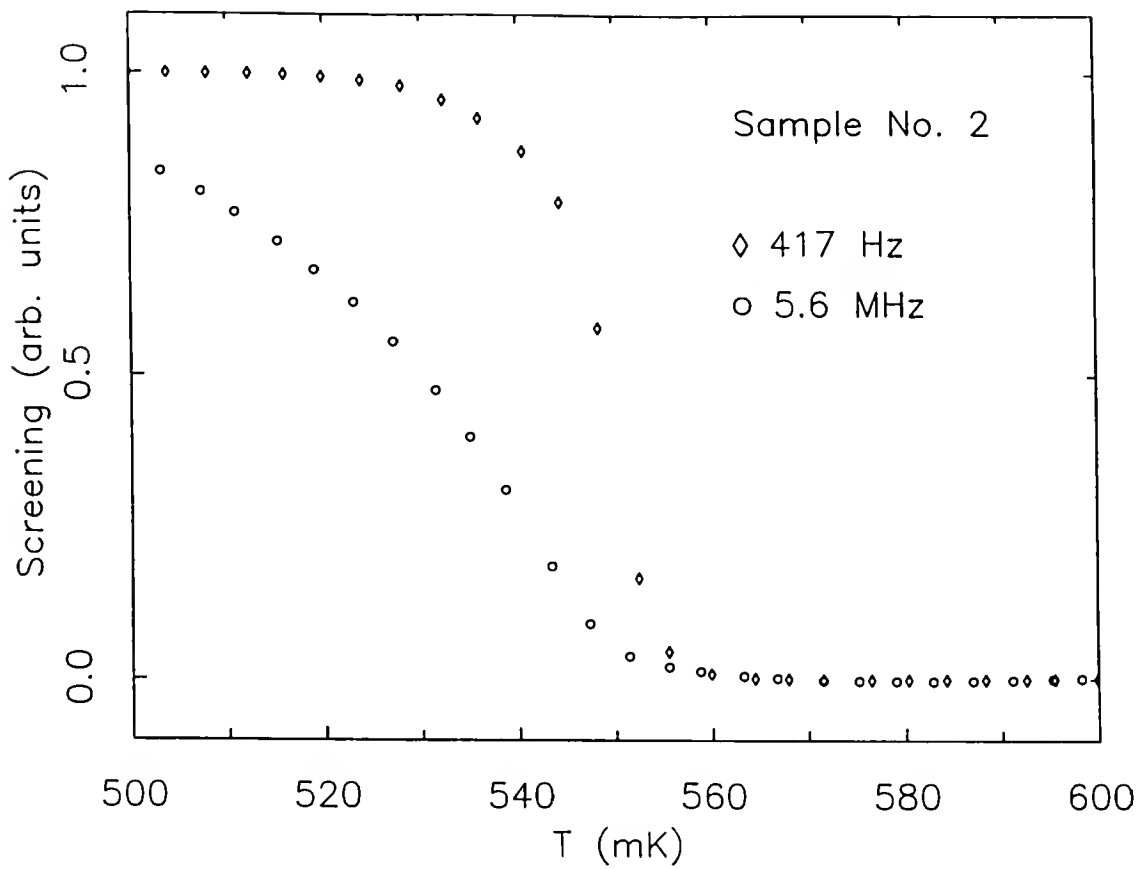


Fig. 4-34. The inductive response for sample No. 2, in the vicinity of T_c , for both low and high frequencies. The data was normalized so that the total change in signal between T_c and T_{\min} is unity for both sets of data. A broadening of the transition was clearly observed for the rf measurement.

$\lambda(T)$, and as a consequence, the transition is broadened. This effect has already been discussed in relation to TDO inductive measurements on UPt₃ by Gannon *et al.* (1990). In superconductors with finite gaps, such as Al, this effect is small because the density of quasiparticles quickly drops below T_C . In UPt₃, however, if we assume that the gap possesses nodes, the decrease of the density of quasiparticles, and of the surface resistance, R_s , is much slower. In fact, the surface resistance of UPt₃ has been studied as a function of frequency by Grimes *et al.* (1991). In their results, a rapid increase of R_s was seen with increasing frequency. This effect is probably also responsible for "washing out" the double feature at T_C for the high frequency data on samples No. 1, No. 4, No. 5 and No. 6. In order to determine precisely the temperature below which this effect becomes negligible, one would have to measure the *rf surface* resistivity. This quantity is likely to be different from sample to sample given their different surface imperfections. It is likely that well polished samples exhibit the lowest surface resistivity at rf frequencies. In fact Grimes *et al.* (1991) reported a surface resistance at 10 MHz and at 0.38 K that was only 1% of R_s at 0.7 K for their polished sample. We, therefore, do not believe that surface resistance effects are significant for well polished samples of low residual resistivity, ρ_0 , such as sample No. 1 of our study, which was polished and possessed a relatively low value for ρ_0 (Fig. 4-3).

Finally, consider our polished sample No. 1. At rf frequencies, this specimen exhibited temperature dependences close to T^4 (Fig. 4-27). The only theoretical effort to reconcile these measurements with the linear dependence, obtained from the mutual inductance data (low frequencies), has been proposed by Hirschfeld *et al.* (1988, 1989, 1992) and Putikka *et al.* (1990). Unfortunately, the assumptions in their analysis do not fully apply to our experimental conditions. For example, they predicted a frequency dependence in the clean limit, i.e. anomalous skin effect regime, or near the crossover $\lambda(T \rightarrow 0) \leq \ell$, where ℓ is the mean free path (from Eq. (2.7), $\ell \approx 2000 \text{ \AA}$ in UPt₃). Since

neither one of these conditions applied to our samples ($\lambda(T \rightarrow 0) \approx 20000 \text{ \AA}$), the answer of the frequency dependence in UPt₃ remains to be given.

4.5.4.b Peak around T_C in the rf measurements

For samples No. 3, No. 4, and No. 5, a peak is observed around T_C for the rf measurements (Figs. 4-29, 4-30, and 4-31), while this feature is not present for samples No. 1, No. 2, and No. 7 (Figs. 4-26, 4-27, 4-28, and 4-33). In this section, we discuss the nature of this peak, and argue that it is related to the size of the skin depth at T_C, $\delta(T_C)$ defined in Eq. 3.9, relative to the sample radius, and to the magnitude of the penetration depth, $\lambda(T)$, just below T_C.

Such peaks have already been reported for conventional superconductors, such as Ta (type I) and Nb (type II), and have been explained in terms of a crossover between the divergent penetration depth and the finite skin depth at T_C (Varmazis and Strongin, 1974; Varmazis, Imry, and Strongin, 1976; Klein *et al.*, 1994). On the other hand rf measurements on Sn (Schawlow and Devlin, 1959) and Al (McLean, 1962) did not reveal any feature around T_C. Furthermore, the effect was also observed in rf measurements of UPt₃ by Gannon *et al.* (1990) who reported a broad peak around T_C for their 6.3 MHz and 10 MHz data. In Fig. 4-35, our results for the rf measurements on Sample No. 1 (annealed, etched, and polished) are shown for two different frequencies. The 6 MHz data, also shown in Fig. 4.27, do not exhibit any feature near T_C, but the 33 MHz data, for the same sample, clearly do. This result suggests that the appearance of the peak is not sample dependent, but is likely to be related to the size of the skin depth at T_C, which decreases with frequency (Eq. 3.9), relative to the sample size.

Just below T_C, the penetration depth diverges, so that the magnetic field penetrates most of the sample. Above T_C, the skin depth determines the amount of field penetration. At low enough frequencies, and for small samples, $\delta(T_C)$ may become equal or greater than the sample size. In this case, the field penetrates most of the sample above and below

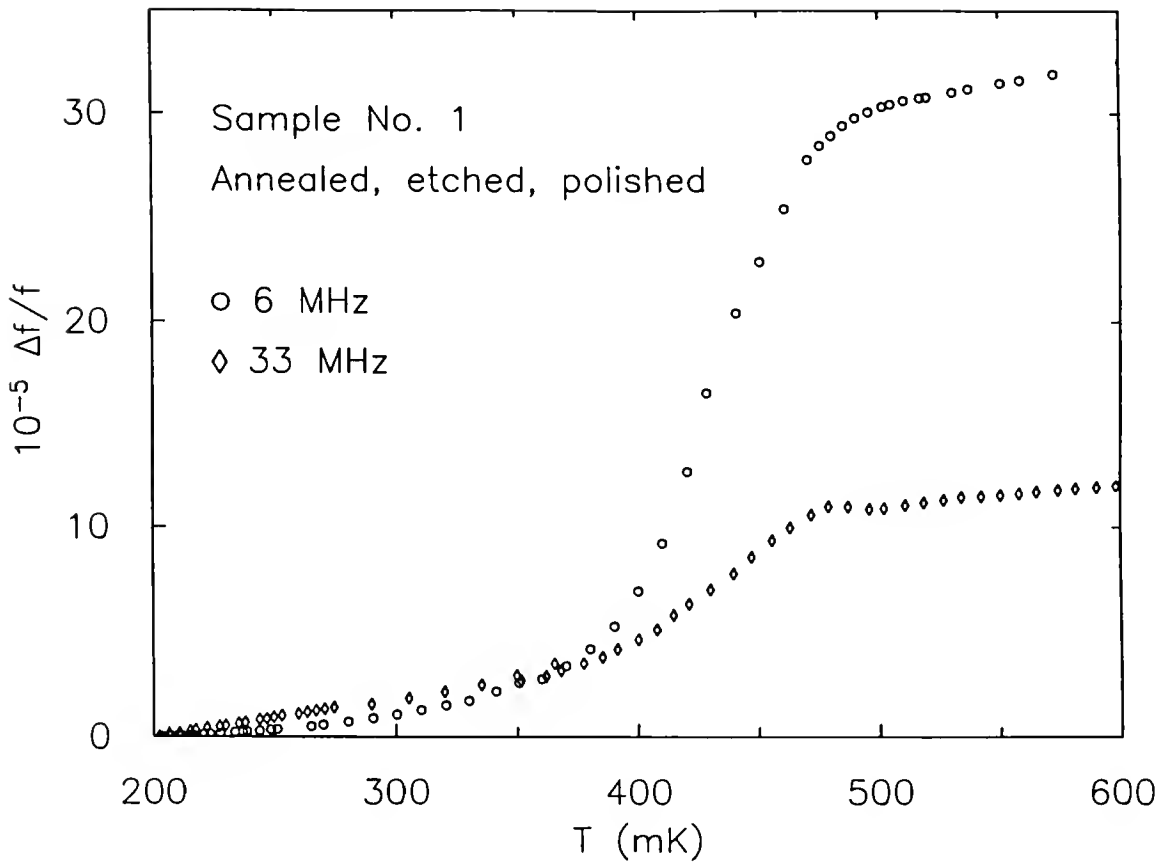


Fig. 4-35 The relative change in frequency $\Delta f / f = [f(T_{\min}) - f(T)] / f(T_{\min})$ as a function of temperature for single crystal No. 1 (annealed, etched, polished) at 6 MHz (○) and 33 MHz (◊) with $B_{rf} \parallel c$ -axis. A peak around T_c is observable only for the 33 MHz data.

T_C , and no peak is observed. At higher frequencies, $\delta(T_C)$ may become much smaller than the radius of the sample, so that the flux through the sample increases as the temperature drops below T_C , causing a peak in the inductive response. The radius of sample No. 1 is $r_S = 0.2$ mm, and we estimate $\delta(T_C, 3 \text{ MHz}) \approx 50 \mu\text{m}$, so that a small peak would be observable with enough sensitivity. At 33 MHz, with $\delta(T_C, 33 \text{ MHz}) \approx 10 \mu\text{m}$, the effect becomes more significant and observable in our measurements.

4.5.5 Upturn in $\chi'(T)$ for $B_{dc} \geq 1.2 \text{ T}$

In this subsection, we discuss the upturn of $\chi'(T)$ observed below 200 mK, in sample No. 1 (annealed, etched, and polished), and for fields greater than 1 T. The traces are shown in Fig. 4-18 and represent the only inductive results ever reported on superconducting UPt₃ for fields above 1 T. These results were surprising since one would expect a monotonic decrease in $\chi'(T)$ as $T \rightarrow 0$, and a decrease in the total change in signal, $\Delta\chi'(T)$, between T_C and the minimum temperature, T_{min} , with increasing magnetic field since $\Delta\chi'(T)$ is a measure of the amount of flux in the sample. We recall that the data was taken in zero field cooled conditions (there are no field cooled data available) and with a probing frequency of 317 Hz (any potential frequency dependence was not investigated). Furthermore, we note that $\chi''(T)$ was temperature independent below T_C .

To allow for the analysis of the upturn in $\chi'(T)$, the superconducting transition was subtracted from the raw data and plotted in Fig. 4-36, for $B_{dc} = 1.4$ T. More specifically, the temperature dependence of the signal corresponding to the superconducting transition was assumed to be quadratic below T_C . This assumption was supported by the quadratic dependence of $\chi'(T)$ observed for the $B_{dc} = 1$ T.

A possible interpretation for the upturn is that it arises from the background temperature dependence of the coil and of the copper wires, on which the sample was G. E. varnished. However, this possibility is not supported by the response of a temperature sweep, taken at $B_{dc} = 2$ T, of the coil in the absence of the specimen but with

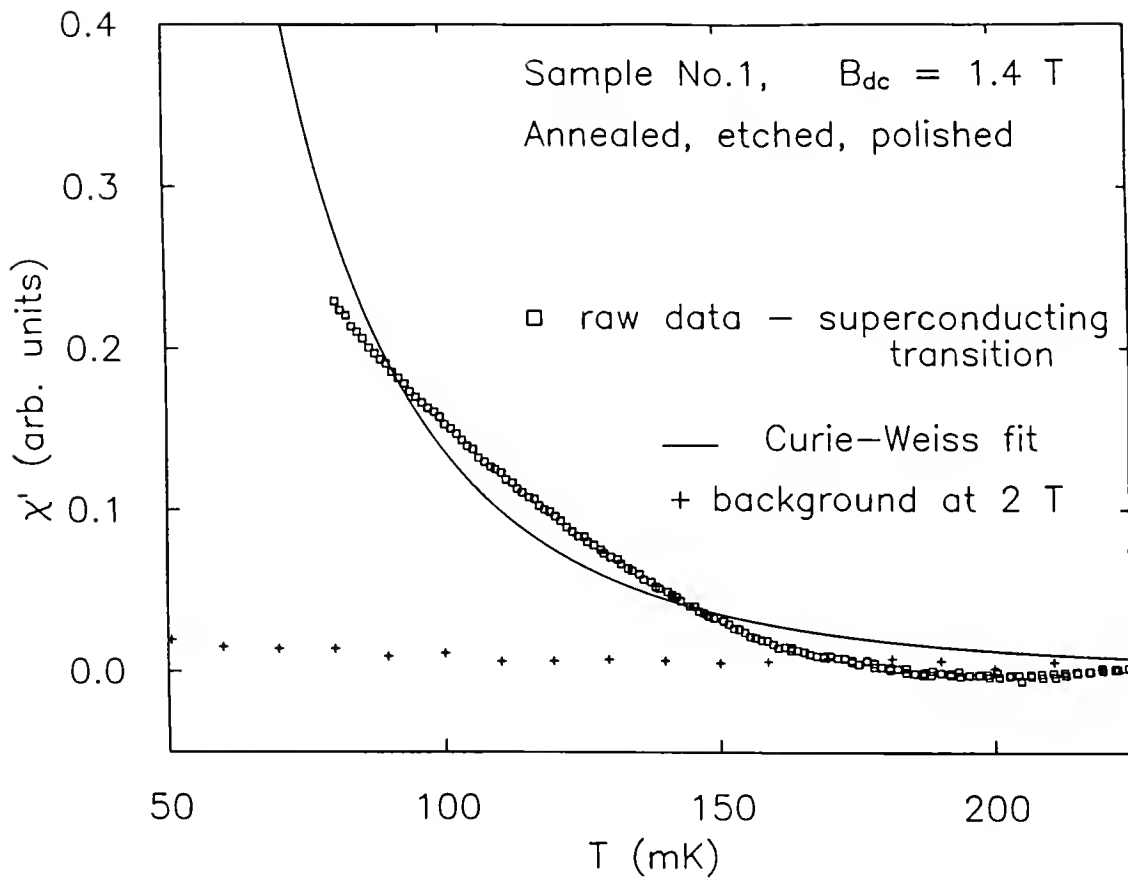


Fig. 4-36. The upturn in $\chi'(T)$ for $B_{dc} = 1.4$ T (\square). The superconducting transition was subtracted from the raw data (see text). The line represents an attempt to fit the upturn to a Curie-Weiss law. The temperature dependence of the background (coil and copper wires) for $B_{dc} = 2$ T is shown (+).

similar copper wires used for the thermal anchoring of sample No. 1. This data is shown in Fig. 4-36, and indicate that the background temperature dependence is negligible compared to the signal observed in the presence of the sample. The upturn is, therefore, intrinsic to sample No. 1.

A second interpretation is the presence of magnetic impurities, which, at low temperatures and high magnetic fields can provide a paramagnetic signal. However, this explanation cannot account for the sudden appearance of the upturn for $B_{dc} \geq 1.2$ T, and the complete absence of any paramagnetic signal in the 1 T sweep (Fig. 4-18). Furthermore, if impurities caused the paramagnetic signal, one would expect the onset temperature of this upturn to increase with field. This prediction is in conflict with the observation of a decrease in onset temperature with increasing field (Fig. 4-18). In addition, the temperature dependence of the magnetic susceptibility arising from impurities might follow a Curie-Weiss law, i.e. $\sim 1/(\Theta - T)$, where Θ is the Curie-Weiss temperature. In Fig. 4-36, an attempt to fit the data to such a temperature dependence is shown, and indicates that the upturn does not follow a Curie-Weiss law.

A third possible interpretation is an intrinsic feature of the superconducting state of UPt₃. The phase diagram shown in Fig. 2-3, for fields parallel to the c-axis, indicates the presence of a transition line around 1.2 T for temperatures below 200 mK. Schenstrom *et al.* (1989) have suggested that this transition line between the B and C phases (see Fig. 2-3) corresponds to a structural transition of the flux lattice (FL), known as H_{FL}, in which the symmetry changes. From this phase diagram, it is clear that, for our measurements below 200 mK, the sample is in one phase for $B_{dc} \geq 1.2$ T, and in a different phase for $B_{dc} < 1.2$ T, explaining the fact that we obtain different responses above and below 1.2 T. However, with this interpretation, the low temperature increase observed in our measurements for fields above 1.2 T, would indicate an increase in total flux penetrating the sample as the specimen is *cooled* through the higher field phase. The reason for such an increase of flux in the low temperature/high field phase as the

temperature decreases is not clear, although it could be related to the possibility that our method may not establish an equilibrium flux distribution as the temperature is swept. This idea is further discussed in the next paragraph.

A fourth explanation for the upturn in $\chi'(T)$ is related to flux motion inside the sample. As mentioned above, the sample was first cooled to T_{\min} in the Earth's field, the magnetic field was then slowly increased (0.03 T/min) to the set point, so as to not generate any heating, and subsequently (within 15 min) the temperature was increased at a rate of about 0.75 mK/min. It is possible that the equilibrium distribution of vortices was never established at the lowest temperatures, and that the upturn corresponds to a time relaxation toward the equilibrium configuration. This assertion is qualitatively supported by the work of Pollini *et al.* (1990 and 1991) who reported magnetization measurements on UPt₃ suggesting the presence of strong flux motion, even at millikelvin temperatures (7 mK). Although their experiments were performed for $B_{dc} \leq 3.3$ mT, *i.e.* in the C phase (Fig. 2-3), this effect might also be present in the B phase. A simple experiment that could shed light on this issue is to measure χ' as a function of time, at fixed field and fixed temperature. Unfortunately, we did not perform this experiment. However, it is possible to plot our data (temperature not held constant) as a function of the time elapsed during the measurement. In Fig. 4-37, $\chi'(time)$ is shown for $B_{dc} = 1.2$ T, $B_{dc} = 1.4$ T, $T < 125$ mK, and where time = 0 refers to the time at which the magnetic field reaches its set point. The data was fit to

$$\chi'(T) = \chi(0) + I e^{-\alpha t}, \quad (4-16)$$

where t is time and $\chi(0)$, I and α are fitting parameters. The results of the fits (lines in Fig. 4-37) gave the following values for α : $\alpha = 1.153 \times 10^{-4}$ sec⁻¹ for $B_{dc} = 1.2$ T, and $\alpha = 1.775 \times 10^{-4}$ sec⁻¹ for $B_{dc} = 1.4$ T.

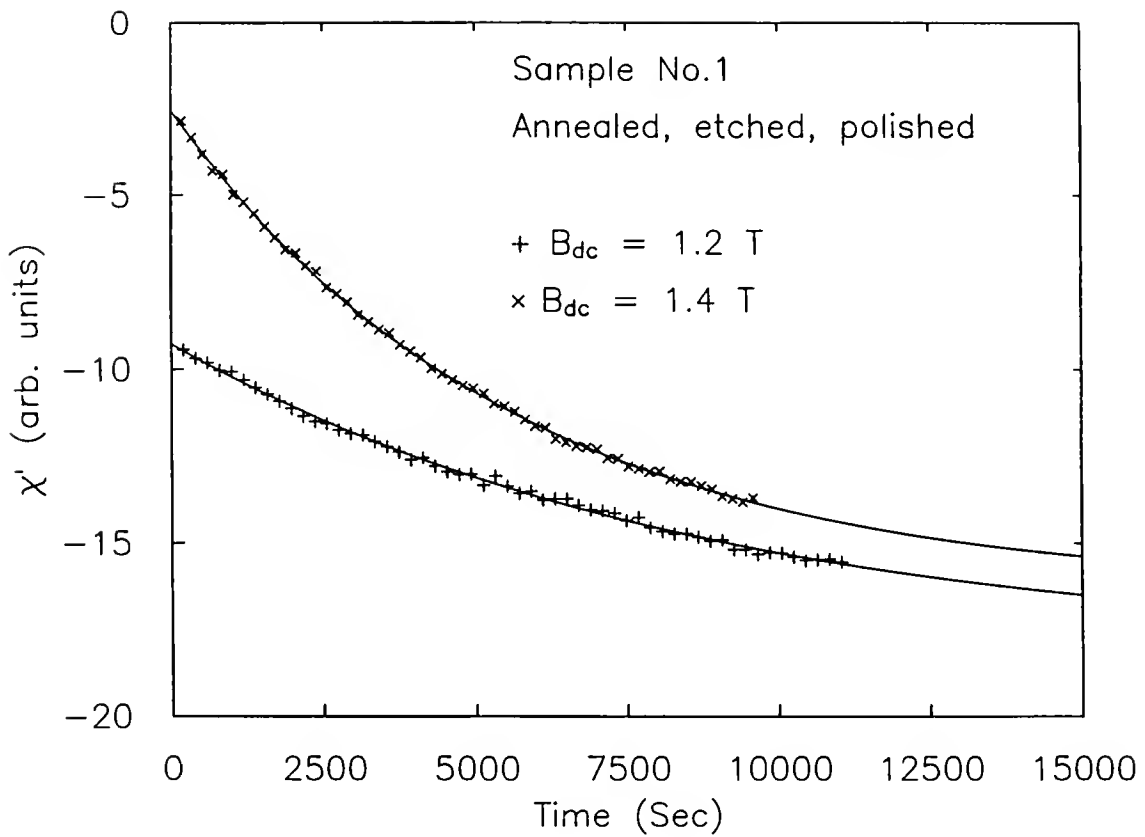


Fig. 4-37 χ' as a function of time for sample No. 1 (annealed, etched, polished), for $B_{dc} = 1.2 \text{ T}$ (+), $B_{dc} = 1.4 \text{ T}$ (\times), with $B_{dc} \parallel c\text{-axis}$. The lines are the results of fits to Eq. (4-16). The data shown are for $T \leq 125 \text{ mK}$.

Although we consider this fourth possibility to be the most plausible explanation of the effect, future investigations, such as field cooled traces of $\chi'(T)$, will be needed to elucidate this phenomenon.

4.6 Conclusions

The first important conclusion drawn from our low frequency measurements is that the temperature dependence of the penetration depth of UPt₃ is linear for currents flowing in the a-b plane and for $T/T_c \leq 0.5$. This finding is consistent for all annealed, high quality samples, showing a double transition in the vicinity of T_c. This result strongly suggests that the energy gap possesses lines of nodes in the basal plane.

The second conclusion is that the double feature near T_c, observed in our low frequency inductive measurements, corresponds to the same double transition observed with bulk measurements such as specific heat, thermal expansion, and sound velocity/attenuation. This conclusion contradicts the statement, often reported, that this feature is an extrinsic property of UPt₃.

The third conclusion is the fact that the temperature dependence of the penetration depth in UPt₃ is frequency dependent, even for frequencies two orders of magnitude less than the frequency corresponding to the maximum of the energy gap. We believe that this frequency dependence is an intrinsic property of the superconductivity in UPt₃ and arises from its unconventionality.

CHAPTER 5

INDUCTIVE MEASUREMENTS -- UBe₁₃

Several of the main results presented and discussed in this chapter relate to the upper critical field, $B_{c2}(T)$, of UBe₁₃. For this reason, this chapter begins with a short theoretical discussion of $B_{c2}(T)$, followed by an overview of earlier measurements of $B_{c2}(T)$ performed on UBe₁₃ by other groups. In the third section, the sample histories of the three UBe₁₃ specimens studied in our work are given. Next, the results of our measurements on these crystals are presented. The subsequent discussion section analyzes the main experimental results and is followed by the conclusions drawn from our work.

5.1 Upper Critical Magnetic Fields in Superconductors

One of the goals of this section is to discuss the theoretically expected temperature dependence of $B_{c2}(T)$ for a strong type II superconductor, which UBe₁₃ is, since $\kappa > 100$ (Chapter 2). Before discussing these points, it is important to briefly review the definition of $B_{c2}(T)$, its relation to the lower critical field, $B_{c1}(T)$, and the meaning of type I and type II superconductors.

5.1.1 Type I, Type II, $B_{c1}(T)$ and $B_{c2}(T)$

Type I refers to superconductors possessing a complete Meissner effect up to the "thermodynamical critical field", H_c , given in the weak coupling BCS theory near T_c by

$$H_c(T) \approx 2.42 \gamma^{1/2} T_c [1 - (T/T_c)^2], \quad (5.1)$$

where T_c is the superconducting transition temperature, and γ is the electronic specific heat coefficient per unit volume. The normal state is restored at $H_c(T)$, and complete magnetic-flux penetration takes place abruptly. The normal-superconducting transition in zero field is second order, while it is first order in finite fields. The Ginzburg-Landau parameter $\kappa \approx \lambda(0)/\xi$ (where $\lambda(0)$ is the penetration depth at $T = 0$, and ξ is the coherence length) can be used to differentiate between type I ($\kappa < 1/\sqrt{2}$) and type II ($\kappa > 1/\sqrt{2}$).

A type II superconductor also exhibits a complete Meissner effect up to a lower critical field, $B_{c1}(T)$, which, for $\kappa \gg 1$, follows the same temperature dependence as $H_c(T)$ (Eq. (5.1)), but with a reduced zero temperature value (Tinkham, 1975). As the field is increased above B_{c1} , the flux gradually penetrates, forming a lattice of supercurrent vortices enclosing the flux lines. It is important to note that in this mixed state, the bulk of the sample remains in the superconducting state. The mixed state persists until the upper critical field, B_{c2} , is reached. Because of the difficulty in applying the BCS microscopic theory to the mixed state of type II superconductors, the temperature dependence of the upper critical field is often calculated within the Ginzburg-Landau (GL) formalism (Tinkham, 1975). This approach is reviewed in the next section and compared to experimental results obtained for niobium.

5.1.2 $B_{c2}(T)$ for Type II Superconductors

The first temperature dependence of $B_{c2}(T)$ was proposed by Abrikosov (1957), who made use of the GL theory of superconductivity and proposed that

$$B_{c2}(T) = \kappa \sqrt{2} H_c(T), \quad (5.2)$$

where $H_c(T)$ is defined in Eq. (5.1). It was latter pointed out by Gor'kov (1960) that B_{c2} / H_c , in Eq. (5.2), should be temperature dependent, and that the upper critical field was better described by

$$B_{C2}(T) = [1.77 - 0.43 (T/T_C)^2 + 0.07 (T/T_C)^4] \propto H_C \quad (5.3)$$

This calculation, referred to as the GLAG (Ginzburg-Landau-Abrikosov-Gor'kov) theory, is only valid in the clean limit ($\ell \gg \xi_0$), and in the local limit, *i.e.* $\lambda(T) \gg \xi_0$, which is always satisfied for $T/T_C \rightarrow 1$.

In Fig. 5-1, the data for experimentally measured $B_{C2}(T)$ of niobium (Butler, 1980) is fitted to Eq. (5.3), (solid line). The discrepancy between the measured values and the ones predicted by the GLAG theory, Eq. (5.3), underlines the fact that several effects have been neglected in the calculation. The GLAG theory was subsequently refined by various authors to handle the "dirty" limit ($\ell \rightarrow 0$) (Maki, 1964; de Gennes, 1964), arbitrary values of ℓ (Hefland and Werthamer, 1966), electron spin effects of Pauli limiting and spin orbit scattering (Werthamer *et al.*, 1966), and non-local corrections (Hohenberg and Werthamer, 1967). The results of these refining calculations for $B_{C2}(T)$ cannot be put into analytical form and must be generated by numerical calculations.

In niobium, the mean free path has been reported to be on the order of 5000 Å (Williamson, 1970), while the zero temperature coherence length was estimated by Varmazis and Strongin (1974) to be around 360 Å, so that the clean limit of the GLAG theory (Eq. 5-3) should apply. Furthermore, Pauli limiting, which arises from the Zeeman energy of the electron spin in a magnetic field, is negligible for niobium. This assertion is based on the fact that the paramagnetic critical field, H_p , is given by (Clogston, 1962)

$$H_p = 1.84 T_C \text{ [in Tesla]}, \quad (5.4)$$

which is ≈ 16.5 T for niobium, more than an order of magnitude larger than the observed critical field.

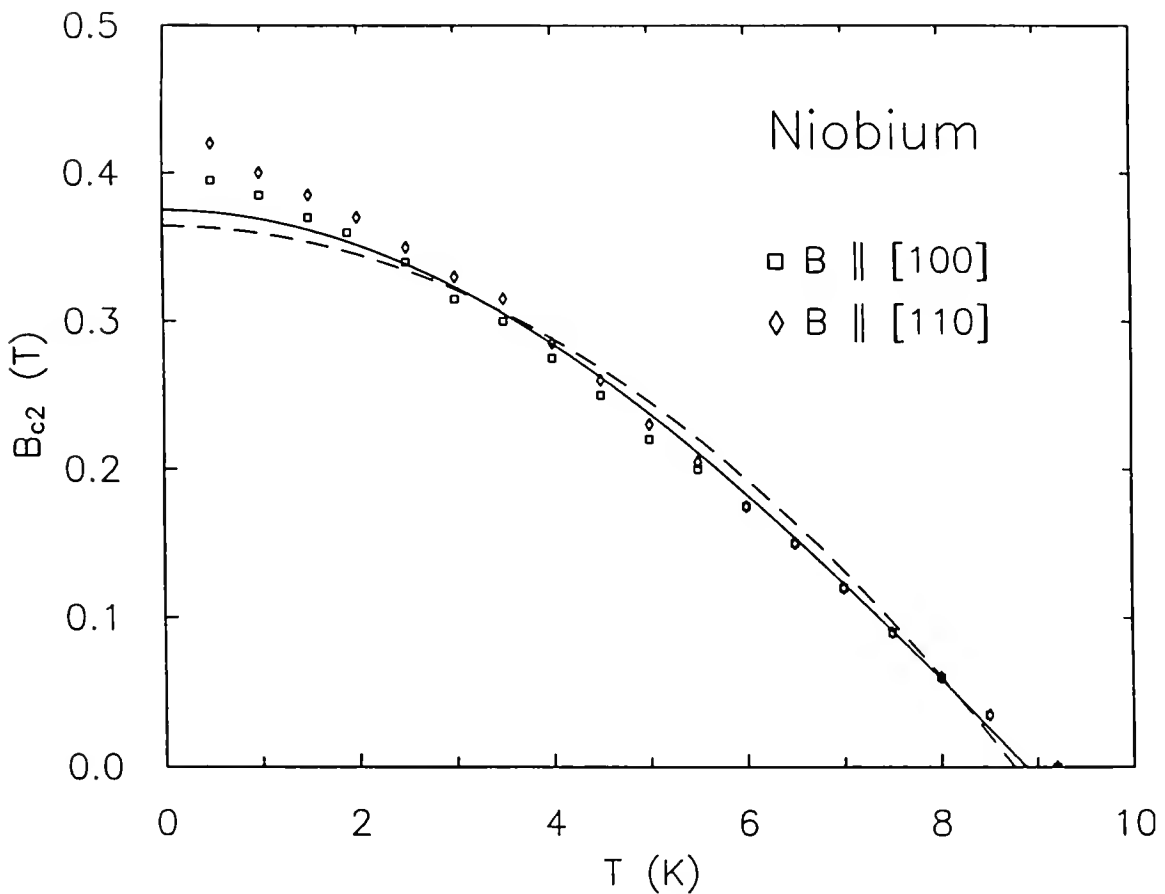


Fig. 5-1. The upper critical field of niobium, for fields parallel to the [100] direction (\square), and fields parallel to the [110] direction (\diamond); data from Butler (1980). The full line represents the result of a fit to Eq. (5.3) for the [100] data. The broken line represents the result of a fit to Eq. (5.2) for the same data.

In order to improve the fit of the data to the GLAG theory, the important correction is the inclusion of non-local effects. Hohenberg and Werthamer (1967) showed that, taking these effects into consideration, the anisotropy of the normal metal Fermi surface will cause an anisotropy in B_{c2} as $T/T_c \rightarrow 0$. In fact, Butler (1980) performed a calculation of B_{c2} taking into account the anisotropy in the Fermi surface and the Fermi velocities for Nb (cubic lattice), and was able to successfully fit the data shown in Fig. 5-1 for both orientations of the field.

In UBe₁₃, which also has a cubic lattice, a similar anisotropy in B_{c2} , arising from Fermi surface anisotropies, can be expected at the lowest temperatures. In addition, Pauli limiting might play a role in UBe₁₃ for the high field region since the value of $B_{c2}(0)$ is around 9 T and $H_p \approx 1.6$ T (Maple *et al.*, 1985). Finally, the clean limit may not be achieved since, as was discussed in Chapter 2, it is not clear whether UBe₁₃ is in the dirty or the clean limit.

In unconventional superconductors, the anisotropy of the energy gap may induce an additional anisotropy in $B_{c2}(T)$. The relationship between the angular dependence of $B_{c2}(T)$ and the symmetry of the superconducting gap parameter has been discussed in detail by Gor'kov (1987), who suggested that this anisotropy could be observed in cubic crystals in the limit $T/T_c \rightarrow 1$. For this reason, it is believed that the observation of anisotropy in $B_{c2}(T)$ of UBe₁₃ for this low field region would strongly suggest unconventional superconductivity, while an absence of anisotropy would be inconclusive (Rainer, 1988). Anisotropy in the limit $T/T_c \rightarrow 0$ is more difficult to analyze because of the normal metal Fermi surface anisotropies which play a role in this region, as was discussed for Nb above. To account for this normal metal effect, a good knowledge of the Fermi surface in UBe₁₃ is necessary. Furthermore, anisotropy in the Pauli limiting effect may cause some anisotropy in B_{c2} for the higher fields (Decroux and Fisher, 1982). For these reasons, our study focuses on the low field region.

5.2 Previous Work on the Upper Critical Field of UBe₁₃

In this section, the previous work published by other groups on the upper critical field of single crystal UBe₁₃ is reviewed. In addition, the reported results on the anisotropy of B_{c2}(T) for T/T_c → 1 are discussed in detail.

5.2.1 B_{c2}(T) of Single Crystal UBe₁₃

Maple *et al.* (1985) reported the first measurements of B_{c2}(T) for UBe₁₃ single crystals. Their results, shown in Fig. 5-2, indicated an enormous initial slope ($-dB_{c2}/dT|_{T_c} \approx 42$ T/K), suggesting unconventional superconductivity. The authors stated that their data did not follow the prediction of the GLAG theory, even after adjusting for the dirty limit and spin orbit scattering. Although Maple *et al.* suggested the need for further theoretical work to explain their data in terms of unconventional superconductivity, they acknowledged that the negative curvature between 0.7 K and 0.85 K could be simply viewed as an effect of Pauli limiting.

The upper critical field was also studied by Schmiedeshoff, Fisk and Smith (1992) who found results very similar to those reported by Maple *et al.* In addition, these authors claimed that, for both their single and polycrystalline samples, two kinks existed in B_{c2}(T) and were evidence of additional phase transitions in UBe₁₃. The search for these additional phases was motivated by the model of Rauchschwalbe (1987) for the second transition observed in thoriated UBe₁₃, and discussed in Chapter 2. However, Schmiedeshoff and coworkers acknowledged that the kinks were difficult to observe, especially in the single crystal. Therefore, their conclusions should be taken with caution.

Two additional studies of B_{c2}(T) on single crystals UBe₁₃ were published by Alekseevskii *et al.* (1986) and Aliev *et al.* (1991). These workers reported results on the anisotropy of B_{c2}(T) in the limit T/T_c → 1. Since one of the important results of our work relates to the presence or absence of this anisotropy, it is important to review in detail the measurements performed by these two groups.

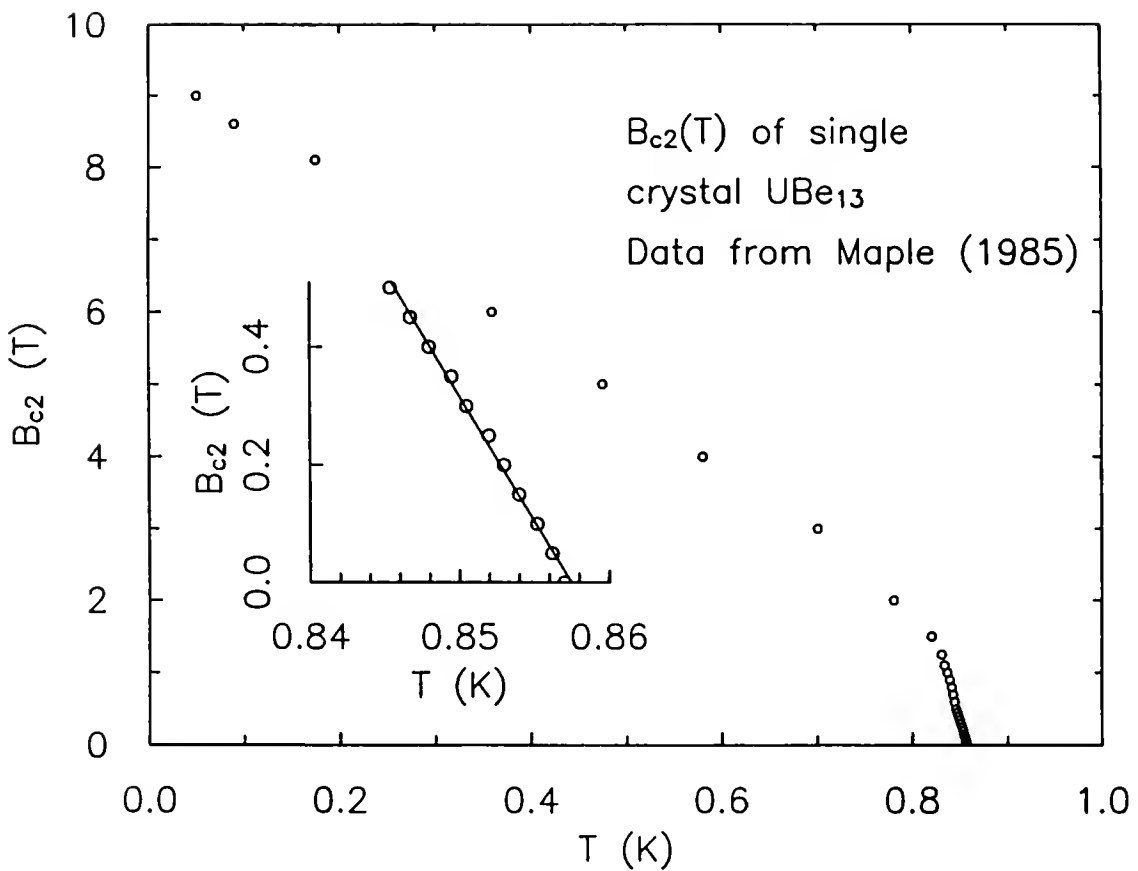


Fig. 5-2. $B_{c2}(T)$ for a single crystal specimen of UBe_{13} . The data are from Maple *et al.* (1985). The inset shows $B_{c2}(T)$ in the limit $T/T_c \rightarrow 1$. The line is the result of a linear fit, indicating that the data fall on a straight line of slope 42 T/K.

5.2.2 Anisotropy of $B_{c2}(T)$ for $T/T_c \rightarrow 1$

Alekseevskii *et al.* (1986) performed magnetoresistance measurements on single crystals UBe_{13} for fields parallel to the [100] and [110] directions. Their samples were grown using a method similar to the one used for our crystals, namely slow cooling a melt of high purity components in an aluminum flux (see next section). However, unlike to our specimens, the samples studied by Alekseevskii *et al.* were polished, but not annealed. These authors reported that the surfaces of their samples consisted of many oriented crystals of about $10\text{ }\mu\text{m}$ in size, and that cracks could be observed along the [110] direction. The $B_{c2}(T)$ values were determined as the midpoint of the resistive transition curves. For both orientations, the current was perpendicular to the applied field and parallel to the [100] direction. The data are shown in Fig. 5-3a. The x-axis is labeled T/T_c (as opposed to T) because the zero field transition temperature for the [110] orientation was lower than the one for the [100] orientation by about 50 mK. The authors suggested that this difference in T_c was related to an anisotropy in impurity and defect distributions. Although the data does not extend below $B = 0.8\text{ T}$ (except for the $B = 0$ point), Alekseevskii *et al.* reported an isotropic $B_{c2}(T)$ in the limit $T/T_c \rightarrow 1$, a result, they claimed, that could be explained by the impurity anisotropy. As discussed in detail below, our results will refute this assertion. Briefly, we report an isotropic $B_{c2}(T)$ for $T/T_c \rightarrow 1$ (with a much higher density of points) associated with an isotropic T_c ($B = 0$). Furthermore, microphotographs of our samples did not reveal the presence of a multitude of small crystals existing on the surface. Therefore, from our results, the isotropic character of $B_{c2}(T)$ is not related to an anisotropy in impurity distribution.

Aliev *et al.* (1991) extended the aforementioned work by measuring the anisotropy of $B_{c2}(T)$ for single crystals similar to the ones used by Alekseevskii *et al.*, and for the same field orientations, but with an emphasis on the low field region as $T/T_c \rightarrow 1$. Their method of determining $B_{c2}(T)$ was also the midpoint of the resistive transition, and their results are shown in Fig. 5-3b. Their findings indicated a strong anisotropy in $B_{c2}(T)$.

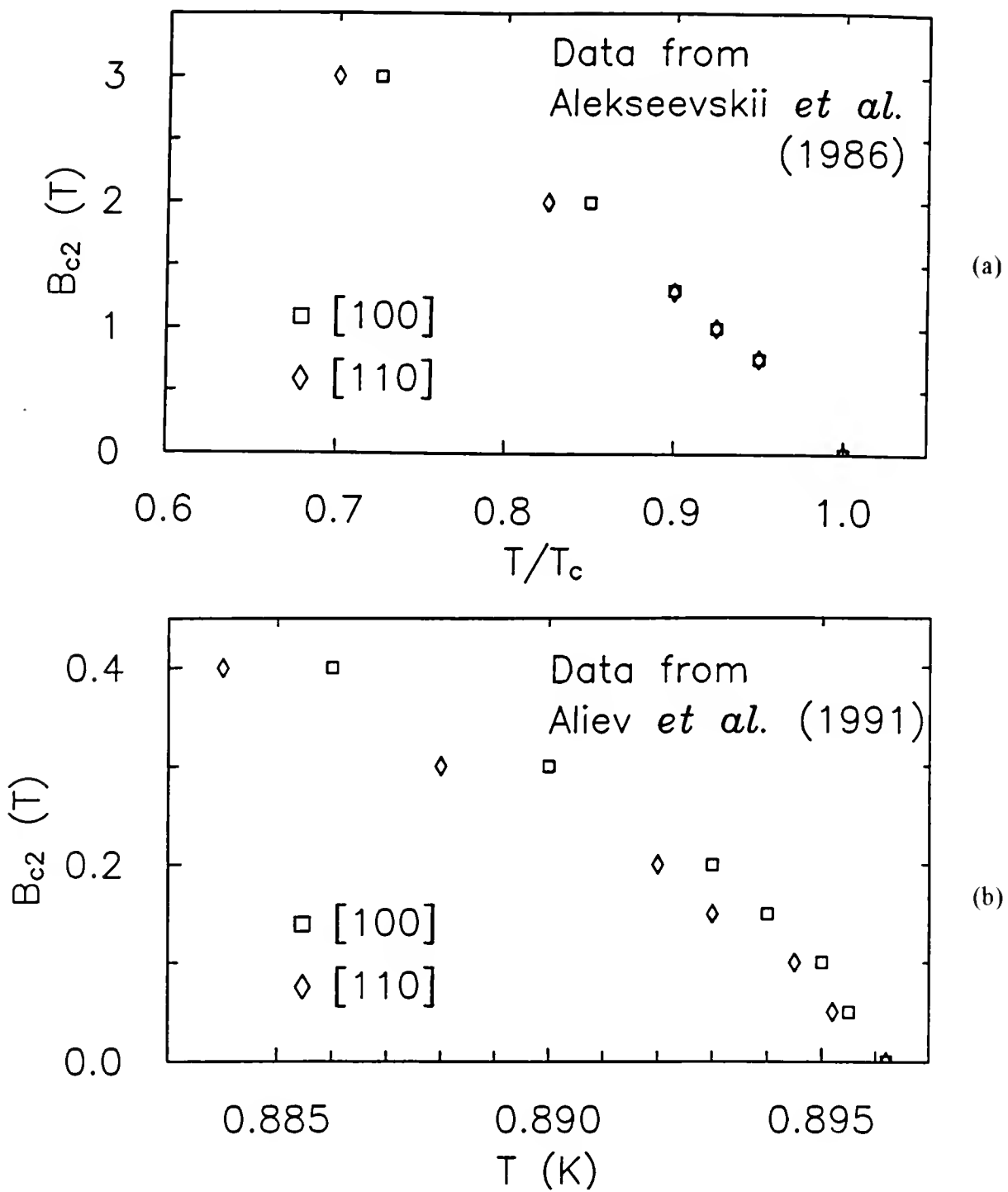


Fig. 5-3. $B_{c2}(T)$ of UBe_{13} in the limit $T/T_c \rightarrow 1$ for fields parallel to the [100] orientation (\square) and the [110] orientation (\diamond). (a) Data from Alekseevskii *et al.* (1986). (b) Data from Aliev *et al.* (1991). The samples were not annealed.

down to the lowest fields measured. It is interesting to note that, contrary to what Alekseevskii *et al.* reported for similar samples, the T_c in zero field was identical for both orientations. An additional result found by Aliev *et al.* is a rapid change in the derivative dk/dT , (where k is the thermal conductivity), by a factor of 1.3 near 8.5 K. The authors associated this change in slope with an increase in the antiferromagnetic correlation length, consistent with the magnetostriction results by Kleiman *et al.* (1990) discussed in Chapter 2.

5.2.3 Our Motivation for Studying $B_{c2}(T)$ in UBe₁₃

One of the goals of our study was to establish whether high quality, *annealed* samples of UBe₁₃ exhibited the anisotropy of $B_{c2}(T)$ reported by Aliev *et al.*. Furthermore, in view of the sample dependence associated with the 8 K anomaly (see Chapter 2), we measured the magnetic susceptibility, $\chi(T)$, near this temperature, for several specimens and found several (one of which is sample No. 1) devoided of any trace of the transition and two (samples No. 2 and No. 3) which showed small kinks in their slope $d\chi/dT$ near 8 K (see next section). Our objective was to study the influence of the presence of such an anomaly on the anisotropy of $B_{c2}(T)$, and, therefore, on the superconductivity of UBe₁₃, by measuring $B_{c2}(T)$ for these three crystals and for fields parallel to the [100] and [110] orientations. As discussed below, in the process of looking for the anisotropy of $B_{c2}(T)$, we have found a number of other interesting results, such as the appearance (for sample No. 3) of a transition line, within the superconducting state. Finally, our measurements allowed us to establish the temperature dependence of the penetration depth of UBe₁₃ in zero field.

5.3 Sample Histories

Our single crystals were obtained by slow cooling a melt of high purity components placed in a BeO crucible which contained aluminum flux. The aluminum flux

was removed with NaOH. Samples No. 1 and No. 2 originate from the same batch, while sample No. 3 comes from a different batch prepared with a different amount of aluminum and with a faster cooling rate. Table 5-1 summarizes their characteristics.

Table 5-1. Characteristics of the three UBe₁₃ single crystals studied in this work.

Samples	Mass (mg)	Dimensions (mm)	% of Al flux (by molar volume)	Growth cooling rate	T _c (H=0)
No. 1	13.55	2.4 × 1.65 × 1.0	92%	2.5 C/hr 1200-900 C	903 mK
No. 2	5.89	1.65 x 1.3 x 1.0	92%	2.5 C/hr 1200-900 C	901.5 mK
No. 3	18.83	2.5 x 1.9 x 1.65	90%	5 C/hr 1400-900 C	849.3 mK

The samples were annealed together for six months at 1000 C. During annealing, the crystals were placed in a BeO crucible with a piece of Be. The crucible was surrounded by Ta foil, and the ensemble was kept in a quartz tube while held in vacuum. The specimens were nearly cubic in shape, and X-ray analysis on sample No. 1 indicated that the faces of the cube were along the [100] direction. Scanning electron microscope (SEM) pictures of the three samples revealed that samples No. 1 and No. 2 had similar surface characteristics. They both had a roughness on the order of 0.5 μm. A large number of spherical particles of diameter on the order of 3 μm were scattered across their surface. This feature can be seen in Figs. 5-4 and 5-5. The surface of sample No. 3 looked much rougher relative to the surfaces of samples No. 1 and No. 2, with grain-like particles ranging from 1 to 50 μm in size. This surface roughness can be seen in Fig. 5-6.

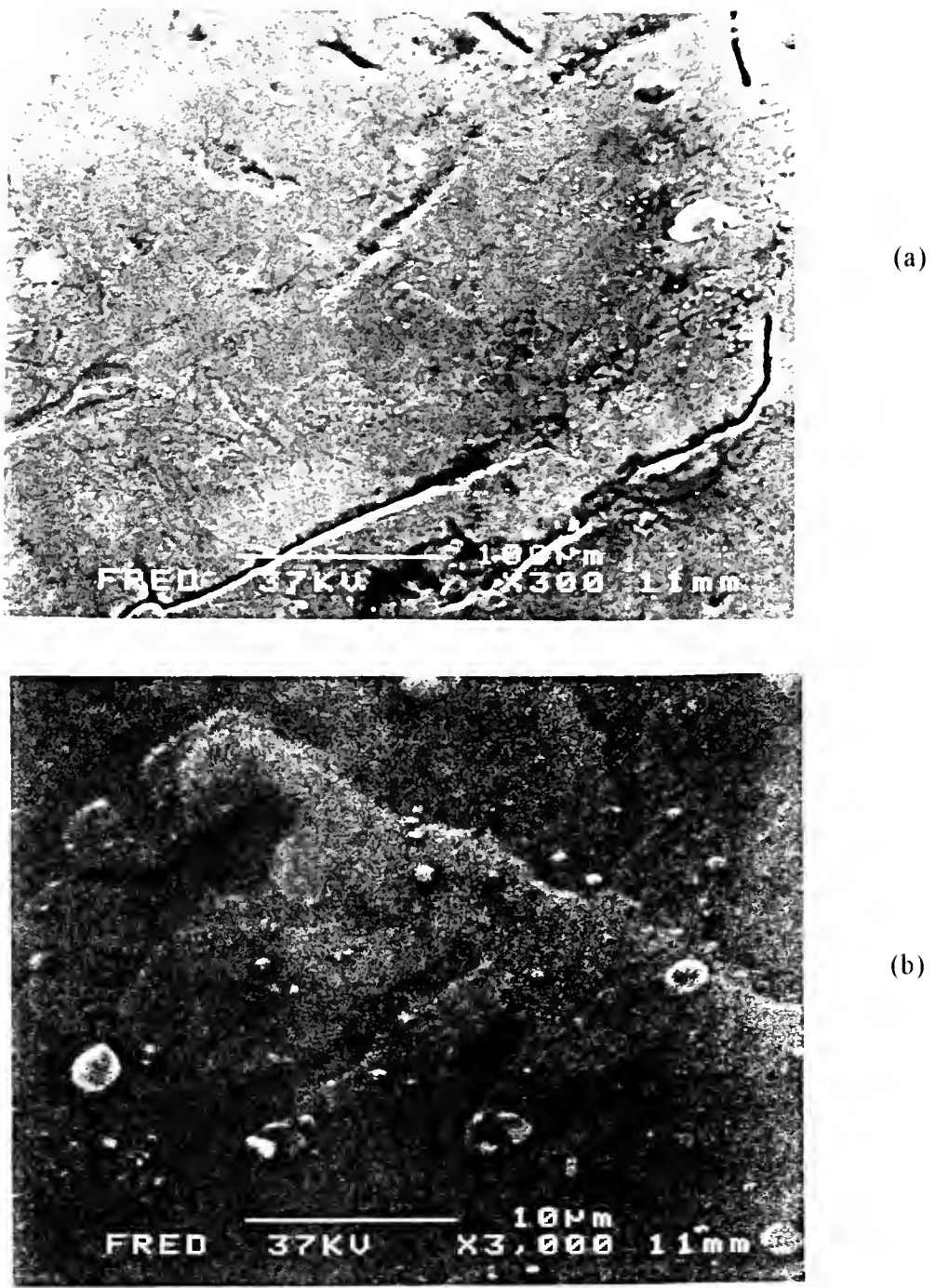


Fig. 5-4. SEM pictures of the surface of sample No. 1. (a) 100 μ m scale. (b) 10 μ m scale.

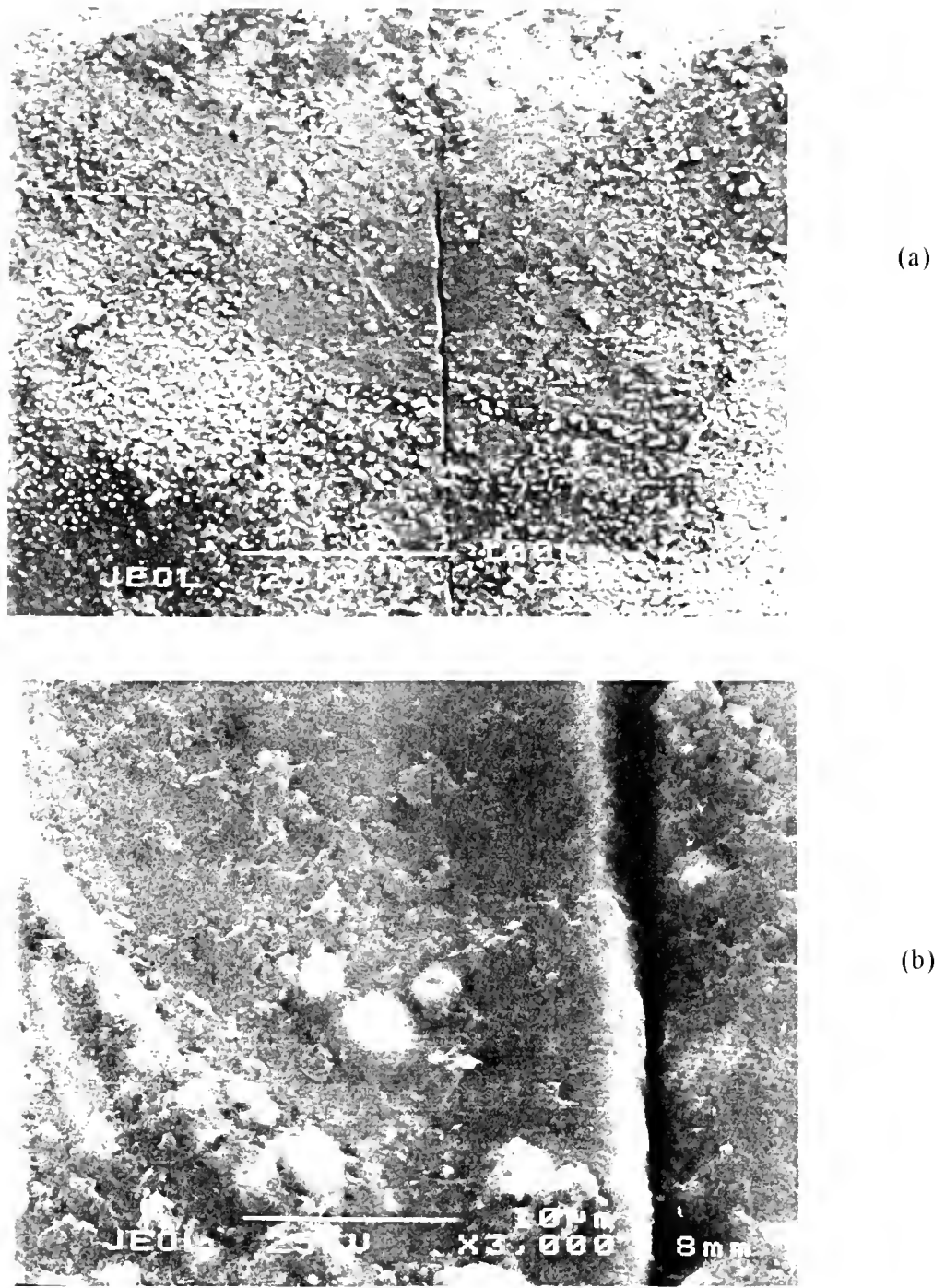


Fig. 5-5. SEM pictures of the surface of sample No. 2. (a) 100 μm scale. (b) 10 μm scale.

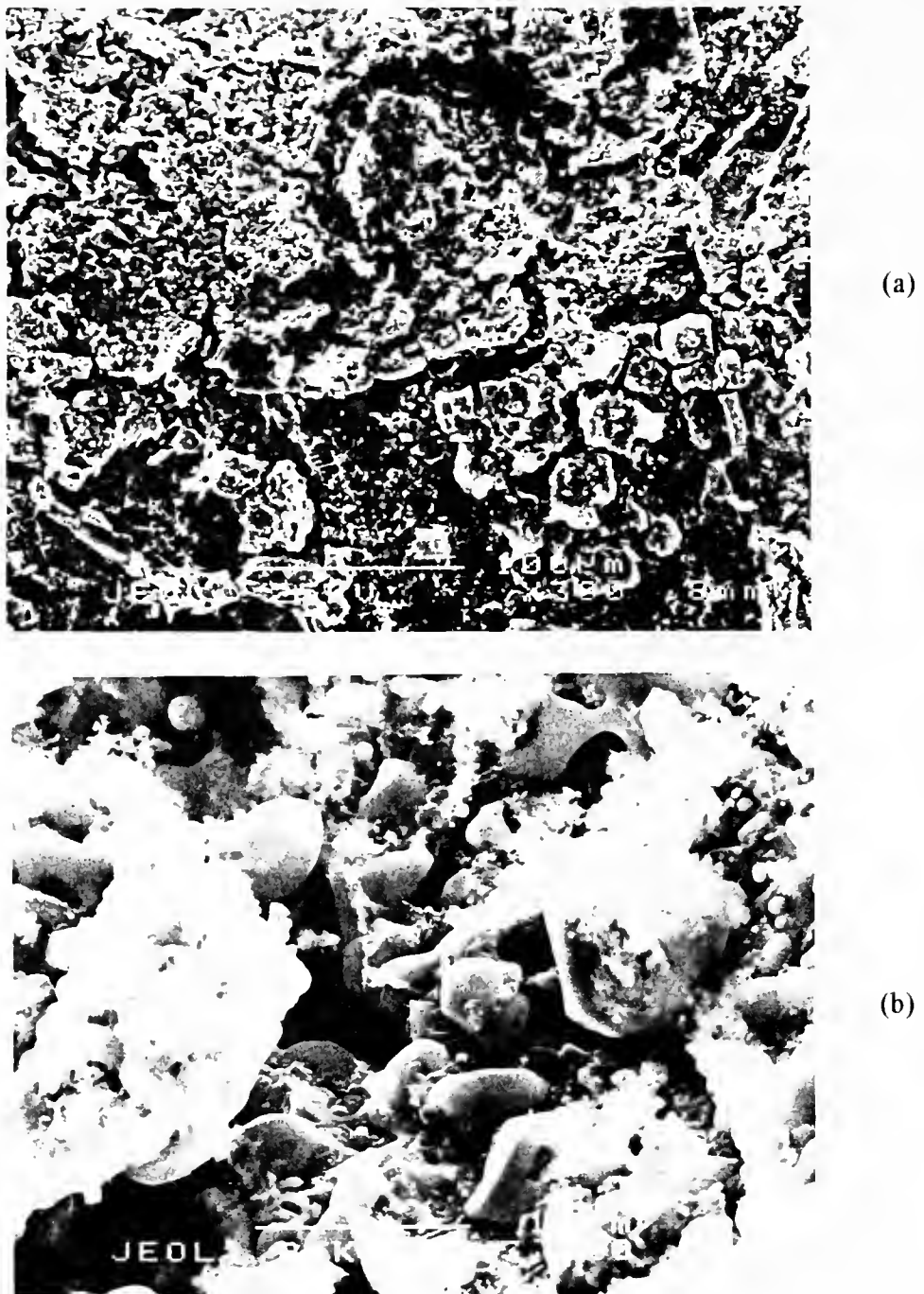


Fig. 5-6. SEM pictures of the surface of sample No. 3. (a) 100 μm scale. (b) 10 μm scale. The surface looks much rougher relative to the surfaces of samples No. 1 (Fig. 5-4) and No. 2 (Fig. 5-5), with grain-like particles ranging from 1 to 50 μm in size. Prior to taking the SEM pictures, the samples were washed in acetone and reagent alcohol, so as to remove any dust, grease or varnish from the surface.



(a)



(b)

Fig. 5-7. SEM pictures of the surface of sample No. 3 after polishing. (a) 100 μm scale. (b) 10 μm scale. Evidently, the surface defects seen in Fig. 5-6 do not penetrate into the bulk of the sample.

Prior to taking the SEM pictures, the samples were washed in acetone and reagent alcohol, so as to remove any dust, grease or varnish from the surface. A small area of the surface of sample No. 3 was polished and is shown in Fig. 5-7. We note that all the results presented in this chapter are for the unpolished specimen. These SEM pictures indicate that the surface defects, observed prior to polishing, do not penetrate into the bulk of the sample. We also performed electron probe microanalysis, with a JEOL Superprobe 733, on samples No. 2 and No. 3 to look for the presence of Al and Na. This analysis, for which the sensitivity level was a few ppm, did not reveal any traces of these two elements for either sample.

5.4 Results

This section is divided into three parts. First, the results on the normal state susceptibility (around 8 K) for the three samples are presented. As mentioned before, these measurements were performed in order to identify which sample, if any, possessed an anomaly around 8 K. In the next subsection, our measurements of $B_{C2}(T)$ are presented, with an emphasis on the $T/T_c \rightarrow 1$ limit. The last subsection concentrates on the zero field temperature dependence of the penetration depth obtained for two of our samples (No. 1 and No. 3).

5.4.1 Normal State Susceptibility

The magnetic susceptibility in the normal state (4 K - 17 K) was measured with a Quantum Design SQUID magnetometer which belongs to Professor G. R. Stewart. The measurements were performed with the help of Dr. B. Andraka and W. W. Kim. The data were taken in an applied field of 0.5 T and are shown in Figs. 5-8 through 5-10. Of the ten specimens whose high temperature susceptibility was studied, only two samples (listed as No. 2 and No. 3) showed any sign of an anomaly near 10 K. In fact, as will be shown below, this possible anomaly is only present in a subtle manner. At first glance, from

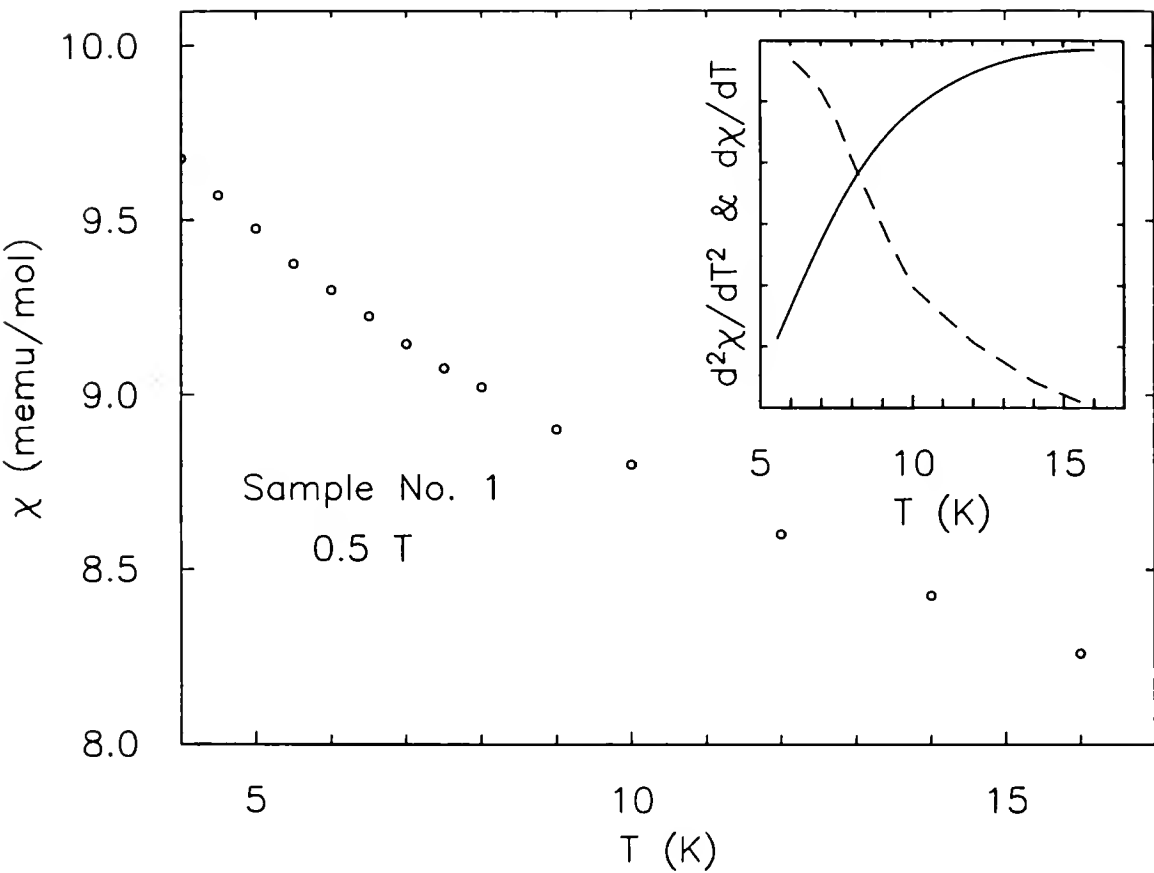


Fig. 5-8. $\chi(T)$ of sample No. 1 in the normal state in an applied field of 0.5 T. The inset shows the first (solid line) and second (broken line) derivative of $\chi(T)$ with respect to T . All three curves are smooth, indicating that any potential magnetic transition, if it exists, is not detectable in this temperature range.

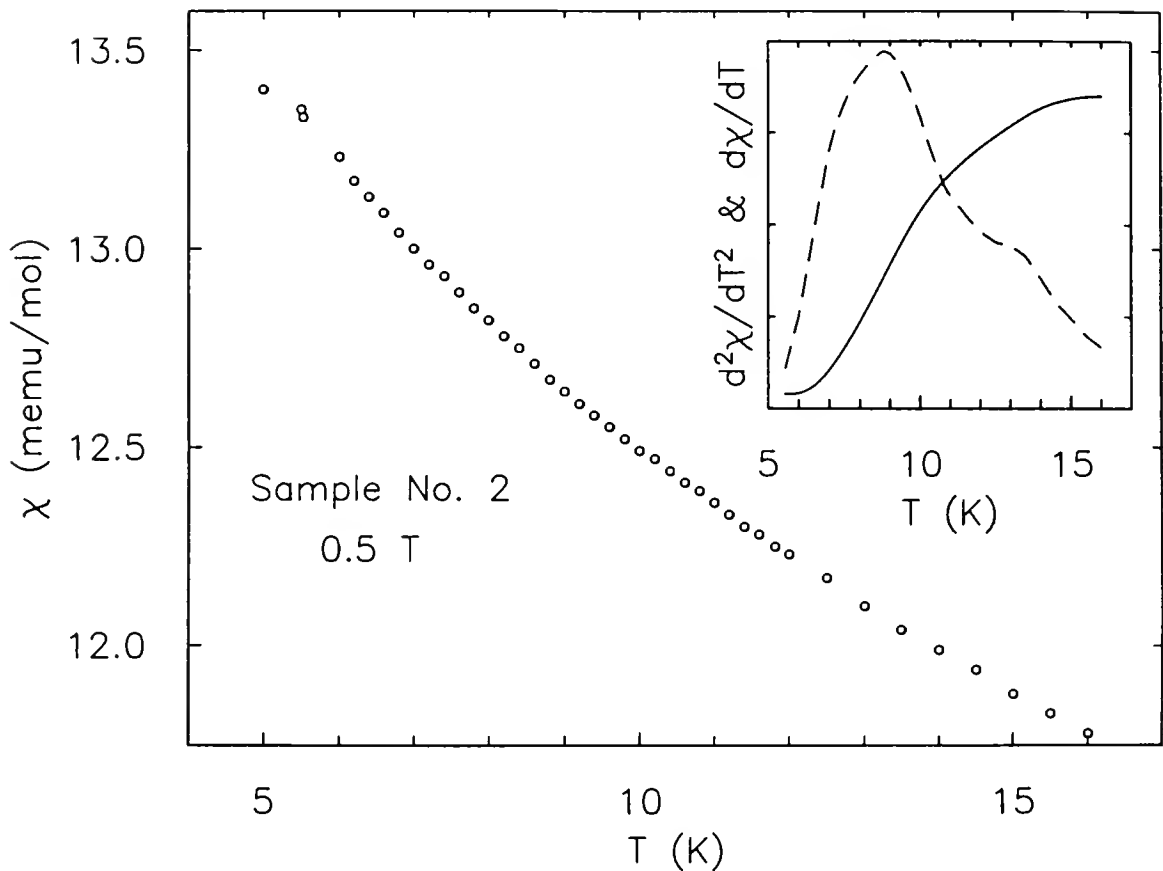


Fig. 5-9. $\chi(T)$ of sample No. 2 in the normal state in an applied field of 0.5 T. The inset shows the first (solid line) and second (broken line) derivative of $\chi(T)$ with respect to T . The second derivative curve indicates a large bump around 9 K associated with the leveling of $\chi(T)$ at lower temperatures, and a small anomaly around 13 K.

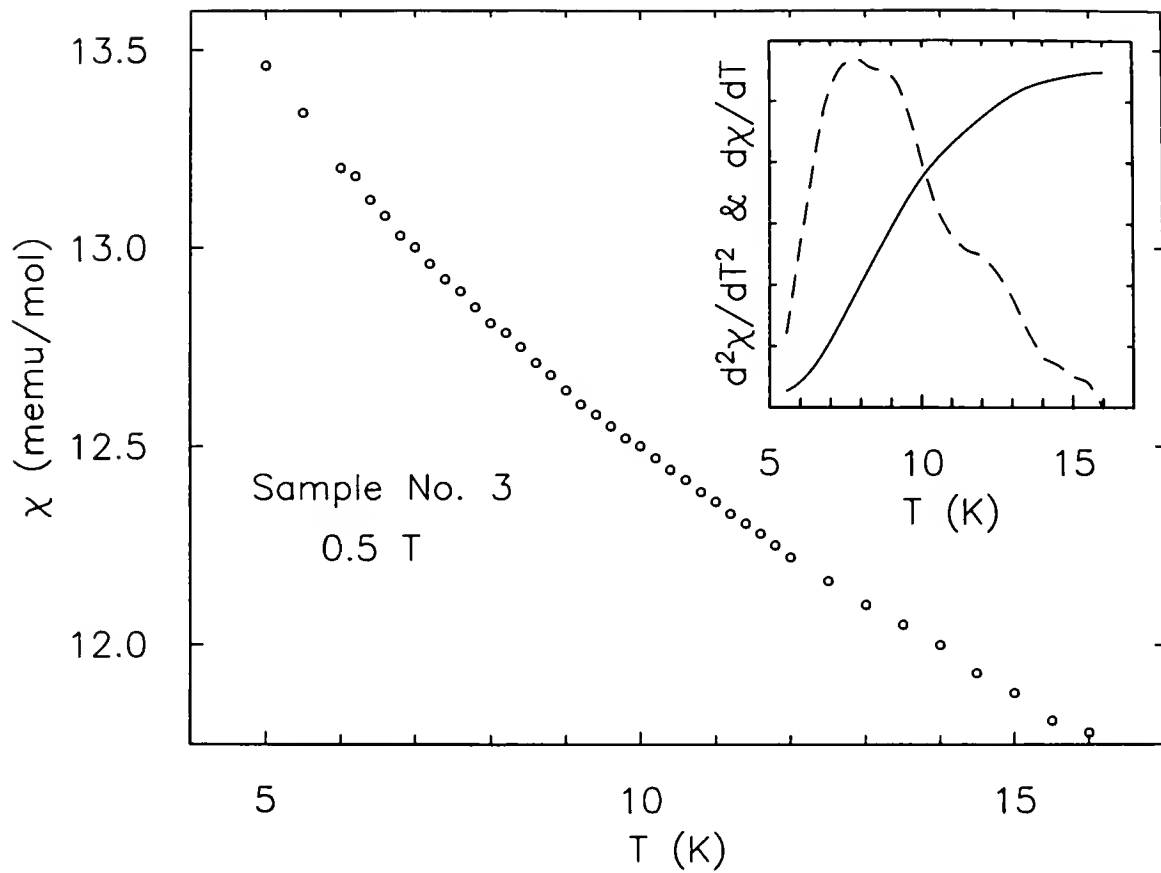


Fig. 5-10. $\chi(T)$ of sample No. 3 in the normal state in an applied field of 0.5 T. The inset shows the first (solid line) and second (broken line) derivative of $\chi(T)$ with respect to T . The second derivative curve indicates a large bump around 8 K associated with the leveling of $\chi(T)$ at lower temperatures, and a small anomaly around 12 K.

Figs. 5-8 through 5-10 none of the samples exhibit any strong anomaly within the temperature range swept. However, after plotting (in the insets) the derivative, $d\chi/dT$, and the second derivative, $d^2\chi/dT^2$, samples No. 2 (Fig. 5-9) and No. 3 (Fig. 5-10) appear to possess a large bump in $d^2\chi/dT^2$ near 8 K. This large bump is believed to reflect the fact that $\chi(T)$ levels off just above T_c . The sign change in the curvature of $\chi(T)$ produces a peak in $d^2\chi/dT^2$. This large bump is likely present for sample No. 1 as well, but at slightly lower temperatures. However, Samples No. 2 and No. 3 exhibit an additional, and anomalous bump in $d^2\chi/dT^2$ near 13 K and 12 K, respectively. This subtle feature is absent for sample No. 1. Therefore, a comparison of the superconducting properties between sample No. 1 and samples No. 2 and No. 3 might allow us to extract information about the role played by the normal state anomaly (near 12-13 K in our samples) on the superconducting state of UBe₁₃.

We note that these derivatives represent the derivatives of a spline fit which was allowed to deviate from the data points by a value that corresponds to the scatter in the data. Furthermore, the presence of the small anomalies in samples No. 2 and No. 3 are not dependent on the parameters used for the spline fits from which the derivatives were calculated. Therefore, the kinks observed in these curves are statistically significant. However, it is important to note that these anomalies are rather small, barely above the sensitivity of the measurements, and therefore are somewhat subjective. The anomalies observed by Aliev *et al.* were much more pronounced, although the comparison is not straightforward since they did not measure magnetic susceptibility, but thermal conductivity and resistivity. The lack of a pronounced anomaly in the normal state does *not* reflect a poor quality in our samples, on the contrary, samples which are considered of the highest quality do not exhibit any anomalous transition, even using high sensitivity measuring techniques (de Visser *et al.*, 1992a, 1992b; Clayhold *et al.*, 1993).

5.4.2 Phase Diagrams

In this subsection, the phase diagrams constructed from our inductive measurements on our three samples are presented. An important aspect in constructing a phase diagram is the manner in which the values of $B_{C2}(T)$ were determined. The first part of this subsection addresses this point. In the second part, the phase diagrams are presented, followed by the data obtained from magnetic field sweeps.

5.4.2.a Determination of $B_{C2}(T)$

The values of $B_{C2}(T)$ were determined by sweeping the temperature and keeping the magnetic field, B_{dc} , constant by placing the superconducting magnet into its persistent mode. We therefore identified $B_{C2}(T)$ at a point $T_c(B_{dc} = \text{constant})$. For each temperature sweep at constant field, the sample was first cooled to a suitably low temperature (typically 50 mK) in the Earth's magnetic field. The dc field was then slowly ramped up to its set point without significant warming of the specimen. The temperature was slowly increased above $T_c(B)$ at a rate of 10 mK per hour. We define T_c as the temperature where the diamagnetic signal changed from its normal state value to its temperature dependent behavior in the superconducting state. In other words, we first fit the normal state data to a straight line and then looked for the first deviation of the data from the fit. This procedure allowed us to locate the temperature at which the last remnant of bulk superconductivity vanished. The traces used in the determination of $T_c(B)$ for the three samples and for different orientations are shown in Figs. 5-11 through 5-16 for $B_{dc} \leq 0.5$ T. The data for $\chi'(T)$ for $B \geq 1$ T are shown in Figs. 5-17 through 5-22.

Another important experimental aspect is the manner in which we achieved the two orientations of the specimens with respect to the dc magnetic field. The crystals were oriented with the field before each run. Our technique required that, between runs, the

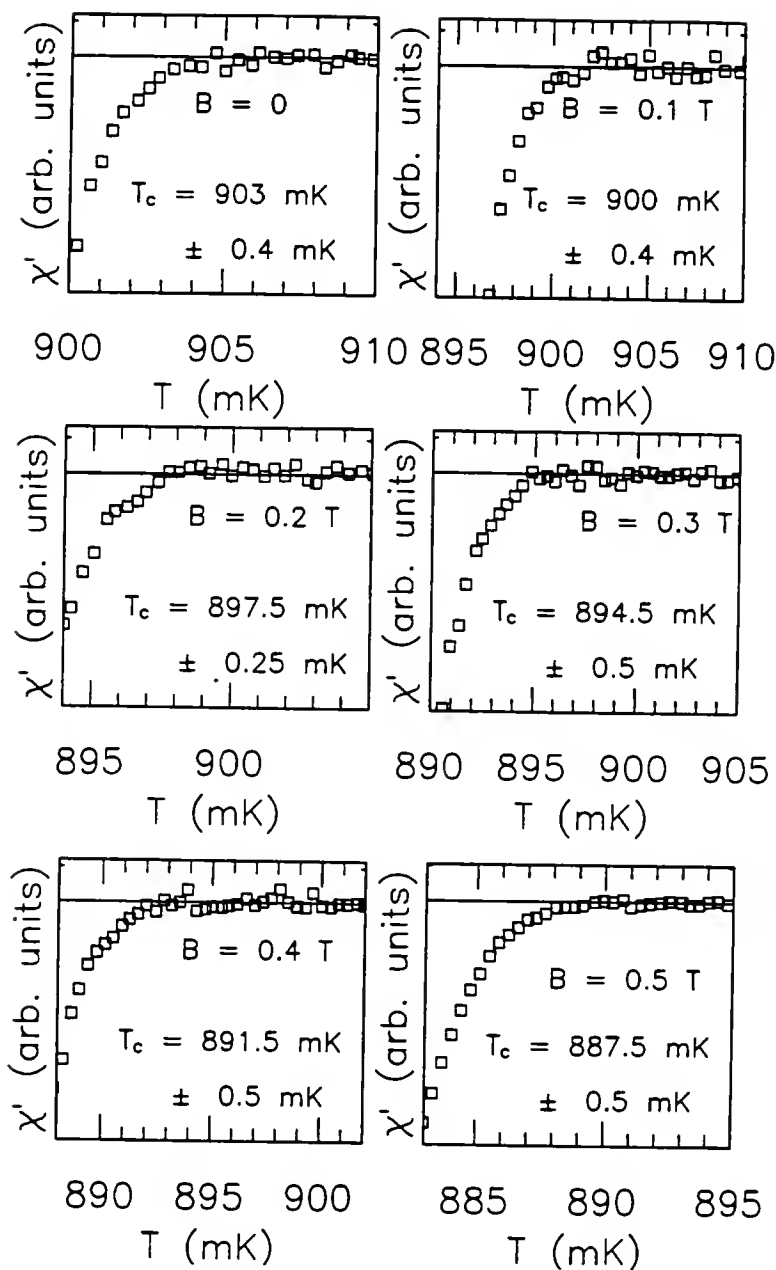


Fig. 5-11. $\chi'(T)$ for sample No. 1 for the applied dc field, \mathbf{B}_{dc} , parallel to the [100] direction, and for $B_{dc} \leq 0.5$ T. The fit to the normal state data was subtracted from the raw data, and the first deviation of the data from zero was identified as $T_c(B)$.

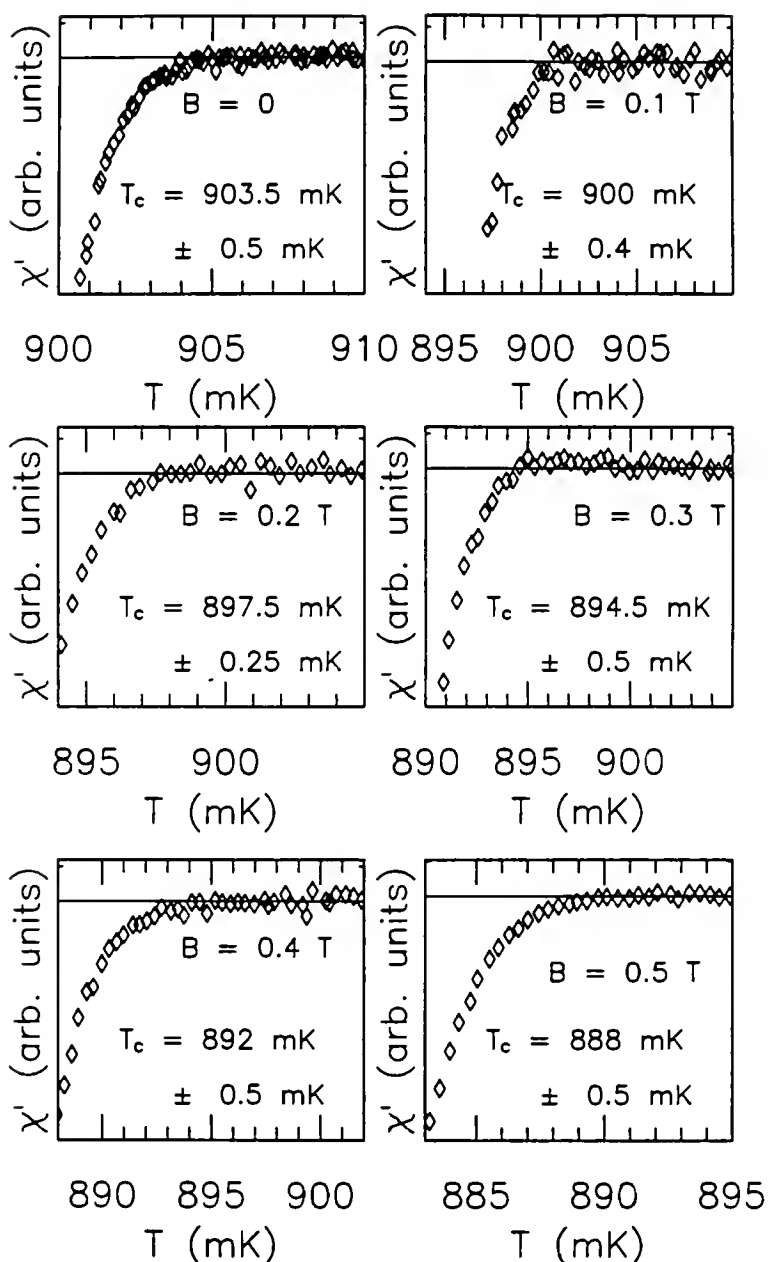


Fig. 5-12. $\chi'(T)$ for sample No. 1 for the applied dc field, \mathbf{B}_{dc} , parallel to the [110] direction, and for $B_{dc} \leq 0.5$ T. The fit to the normal state data was subtracted from the raw data, and the first deviation of the data from zero was identified as $T_c(B)$.

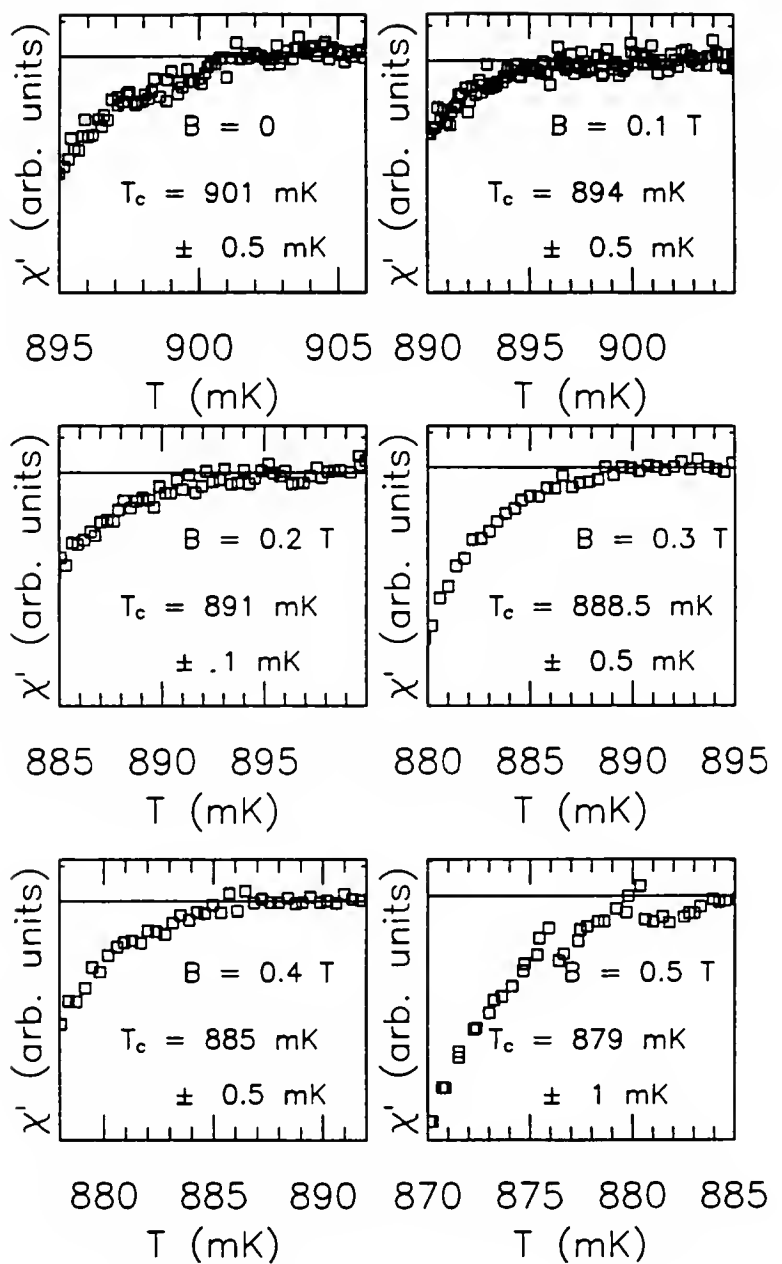


Fig. 5-13. $\chi'(T)$ for sample No. 2 for the applied dc field, \mathbf{B}_{dc} , parallel to the [100] direction, and for $B_{dc} \leq 0.5$ T. The fit to the normal state data was subtracted from the raw data, and the first deviation of the data from zero was identified as $T_c(B)$.

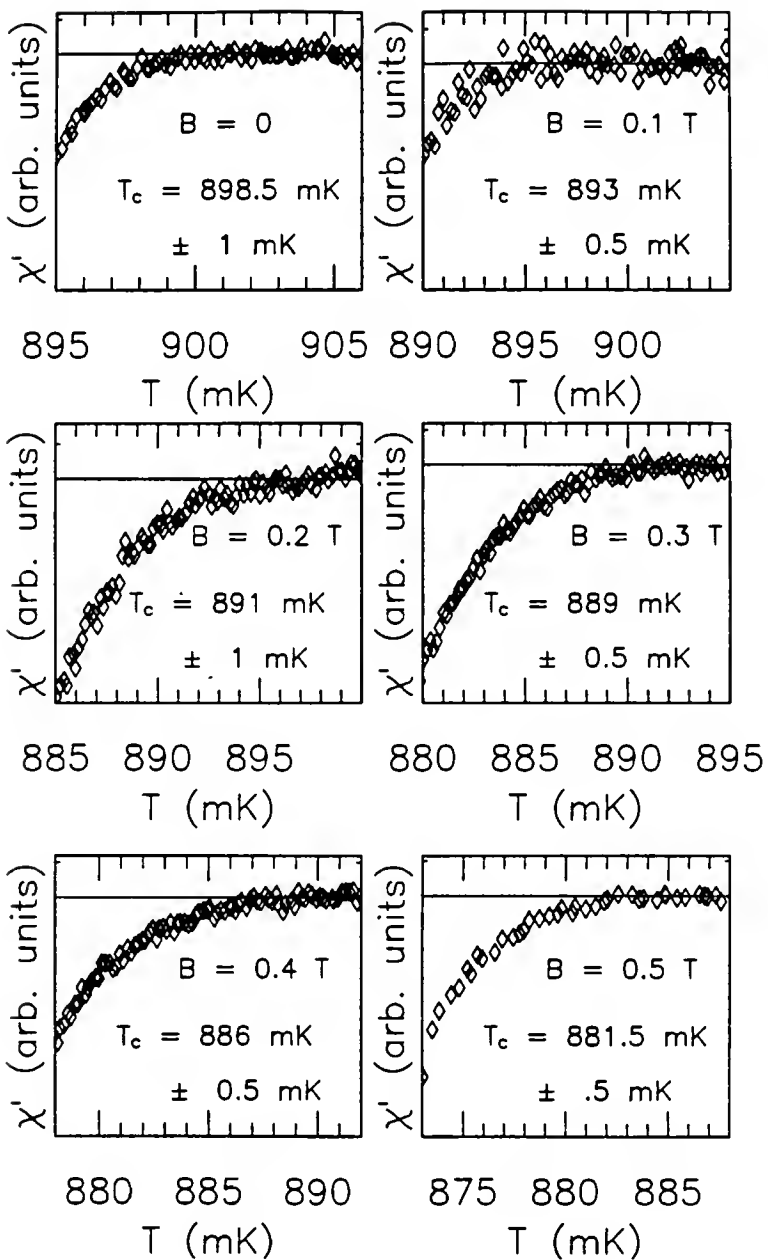


Fig. 5-14. $\chi'(T)$ for sample No. 2 for the applied dc field, \mathbf{B}_{dc} , parallel to the [110] direction, and for $B_{dc} \leq 0.5$ T. The fit to the normal state data was subtracted from the raw data, and the first deviation of the data from zero was identified as $T_c(B)$.

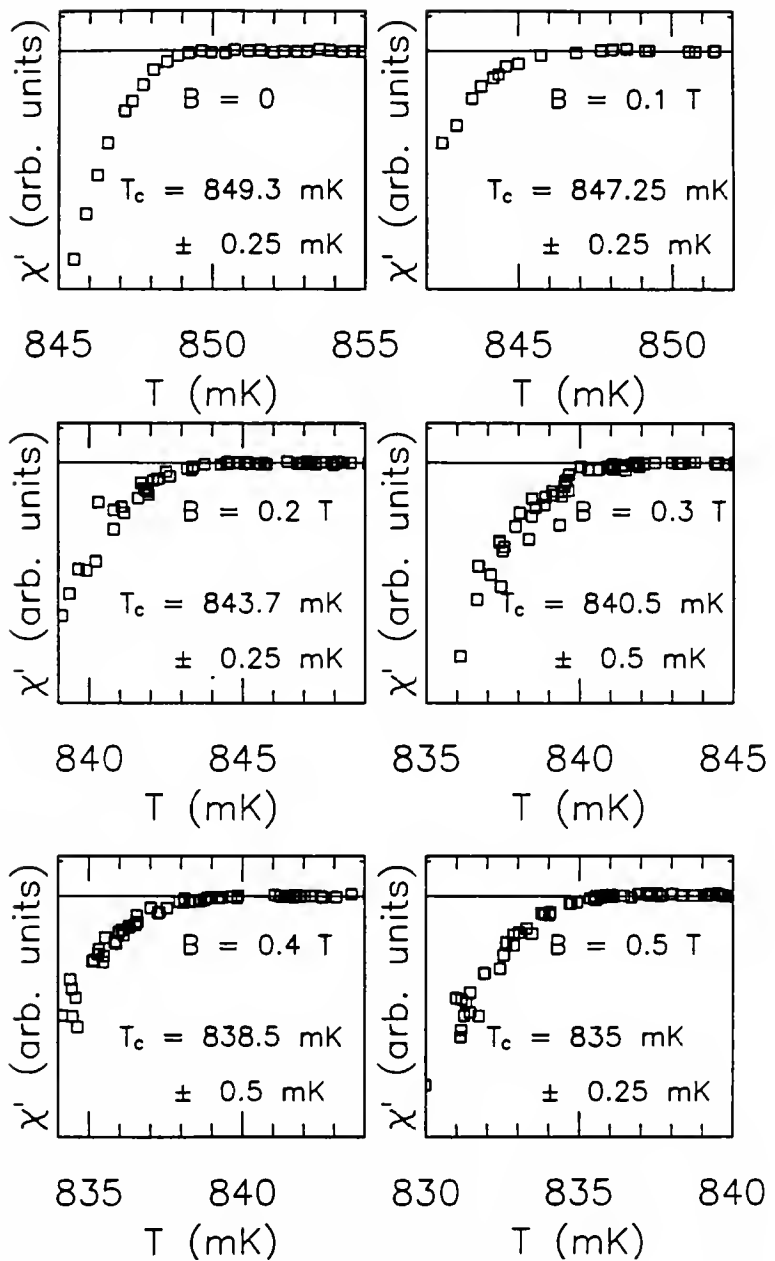


Fig. 5-15. $\chi'(T)$ for sample No. 3 for the applied dc field, \mathbf{B}_{dc} , parallel to the [100] direction, and for $B_{dc} \leq 0.5$ T. The fit to the normal state data was subtracted from the raw data, and the first deviation of the data from zero was identified as $T_c(B)$.

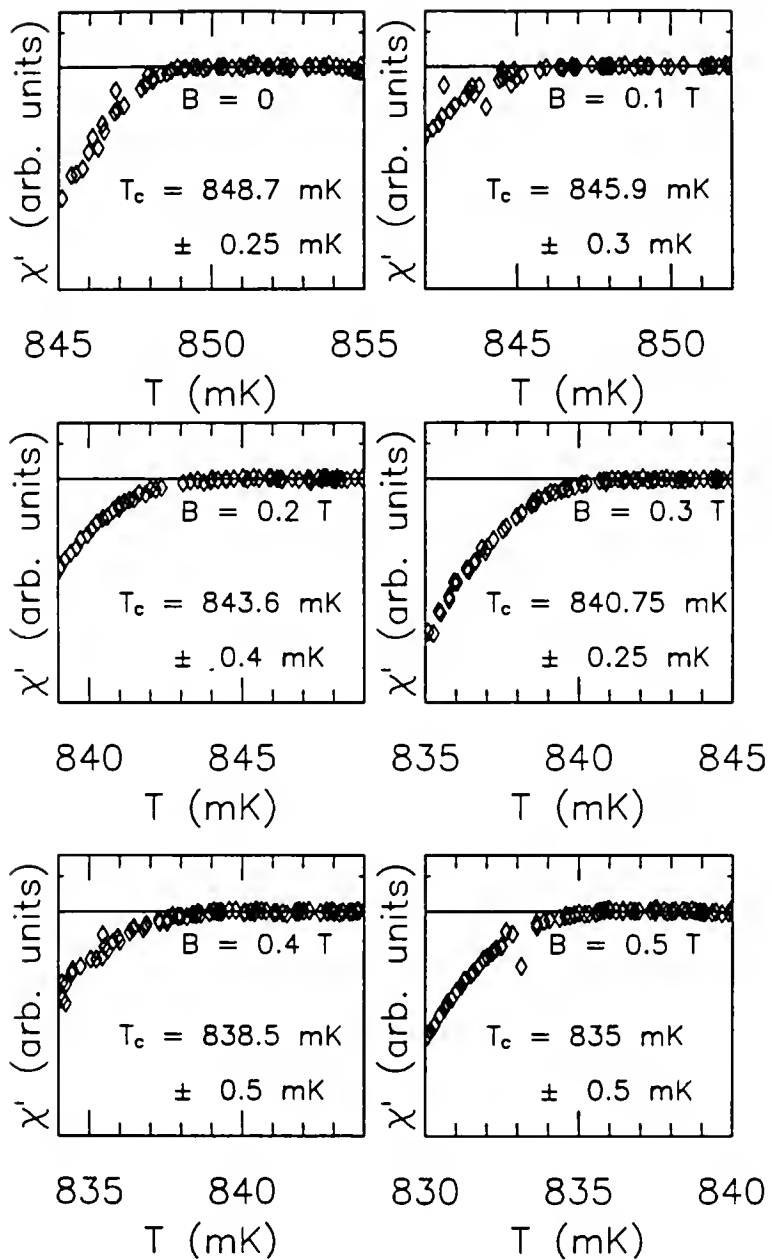


Fig. 5-16. $\chi'(T)$ for sample No. 3 for the applied dc field, \mathbf{B}_{dc} , parallel to the [110] direction, and for $B_{dc} \leq 0.5$ T. The fit to the normal state data was subtracted from the raw data, and the first deviation of the data from zero was identified as $T_c(B)$.

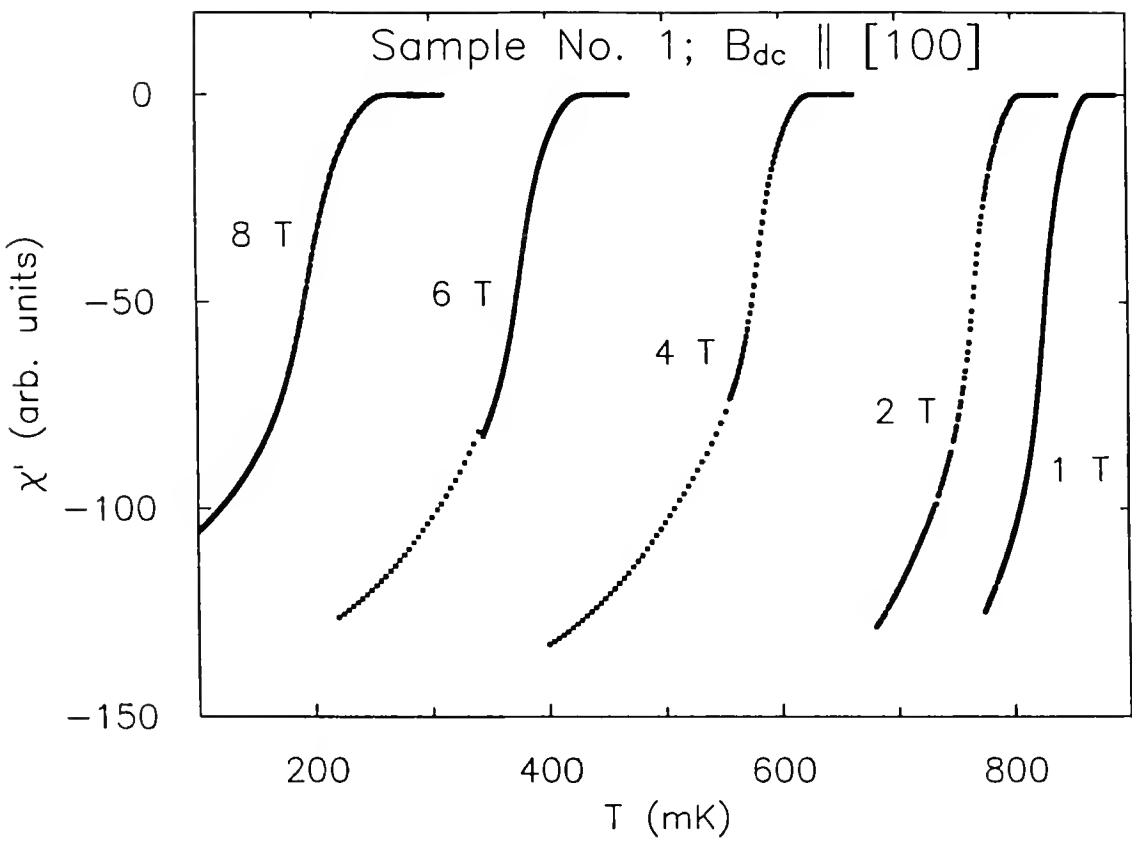


Fig. 5-17. $\chi'(T)$ for sample No. 1 for the applied dc field, B_{dc} , parallel to the [100] direction, and for $B_{dc} \geq 1$ T.

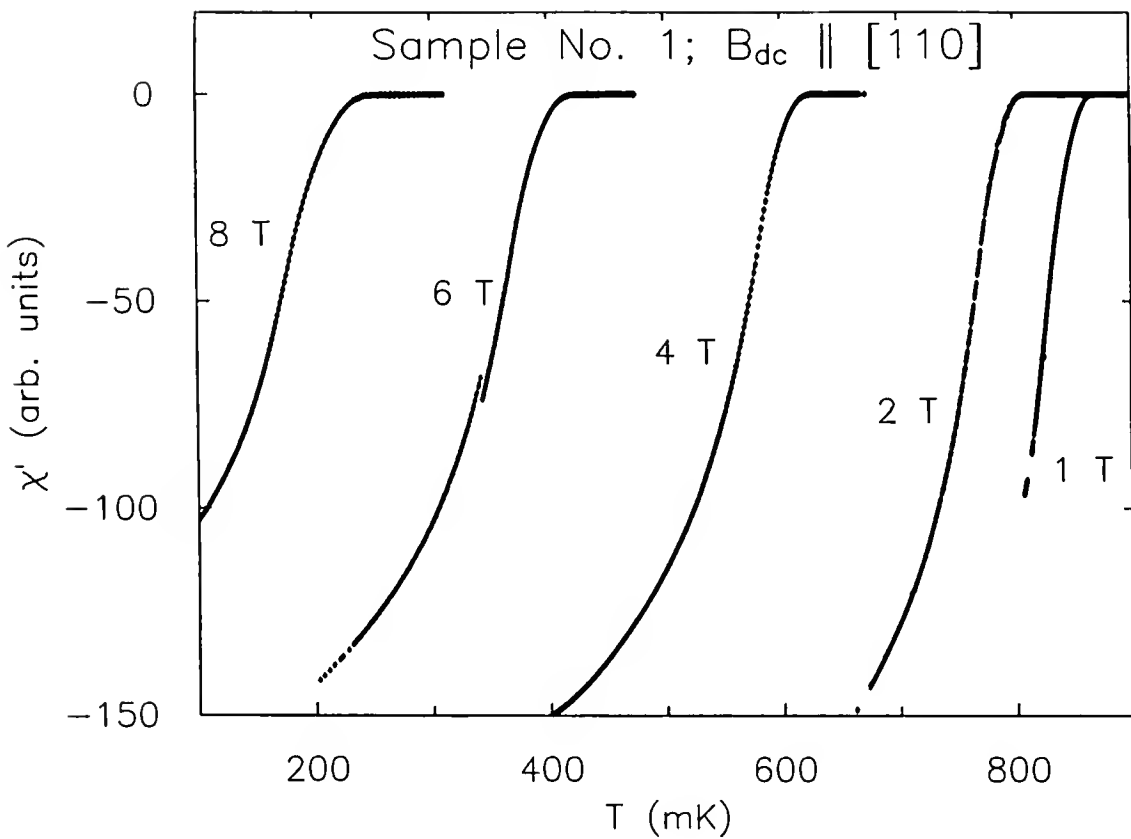


Fig. 5-18. $\chi'(T)$ for sample No. 1 for the applied dc field, B_{dc} , parallel to the [110] direction, and for $B_{dc} \geq 1$ T.

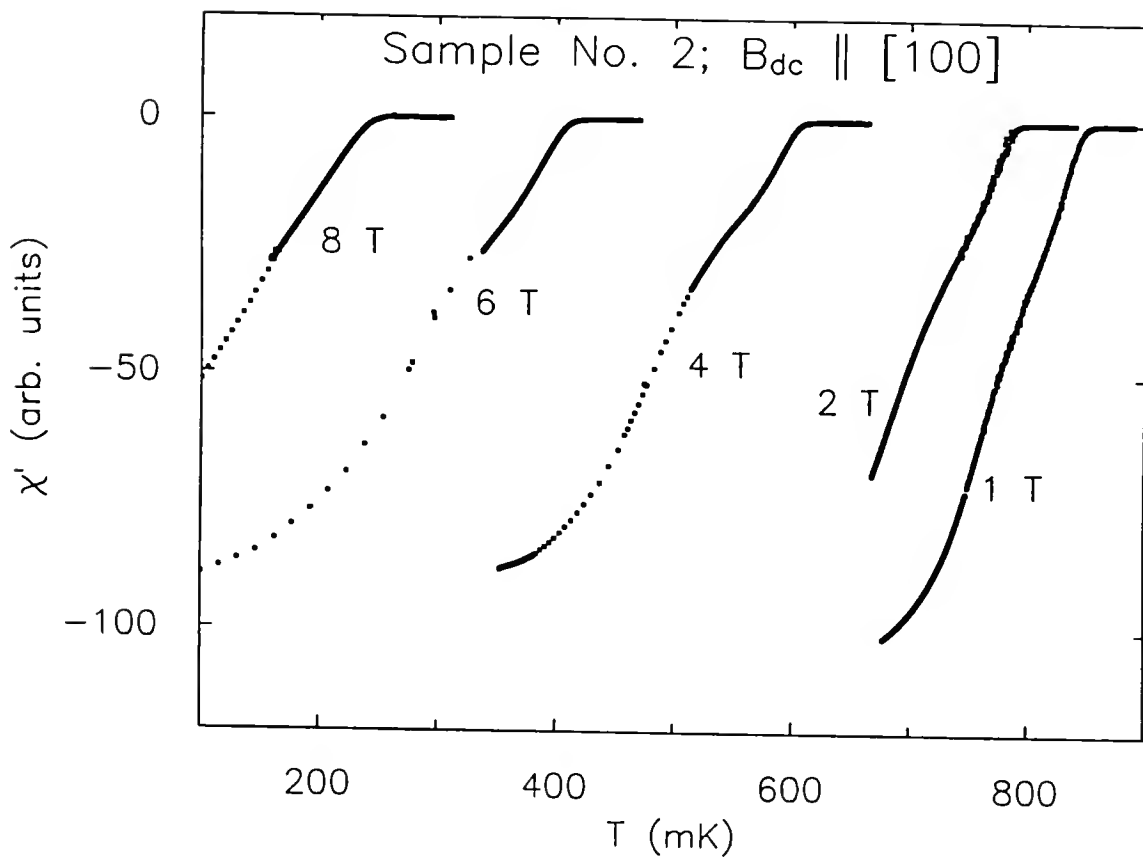


Fig. 5-19. $\chi'(T)$ for sample No. 2 for the applied dc field, B_{dc} , parallel to the [100] direction, and for $B_{dc} \geq 1$ T.

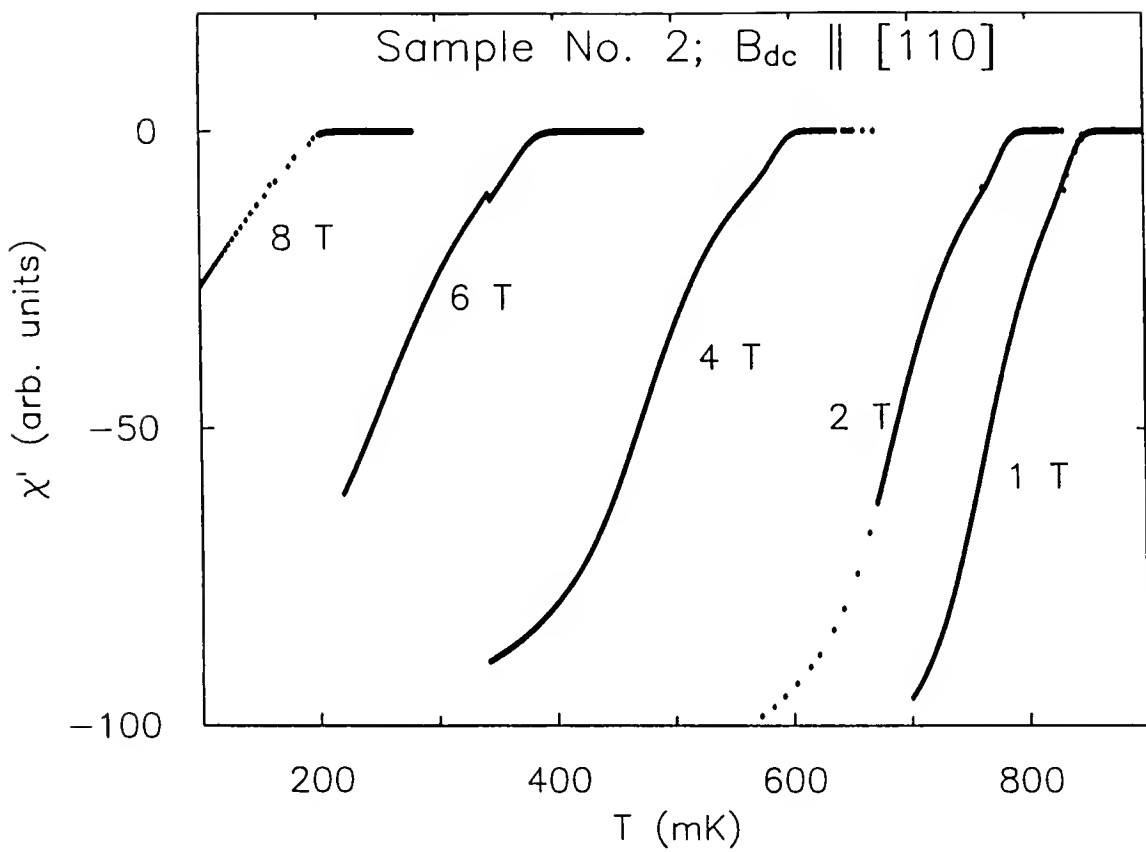


Fig. 5-20. $\chi'(T)$ for sample No. 2 for the applied dc field, B_{dc} , parallel to the [110] direction, and for $B_{dc} \geq 1$ T.

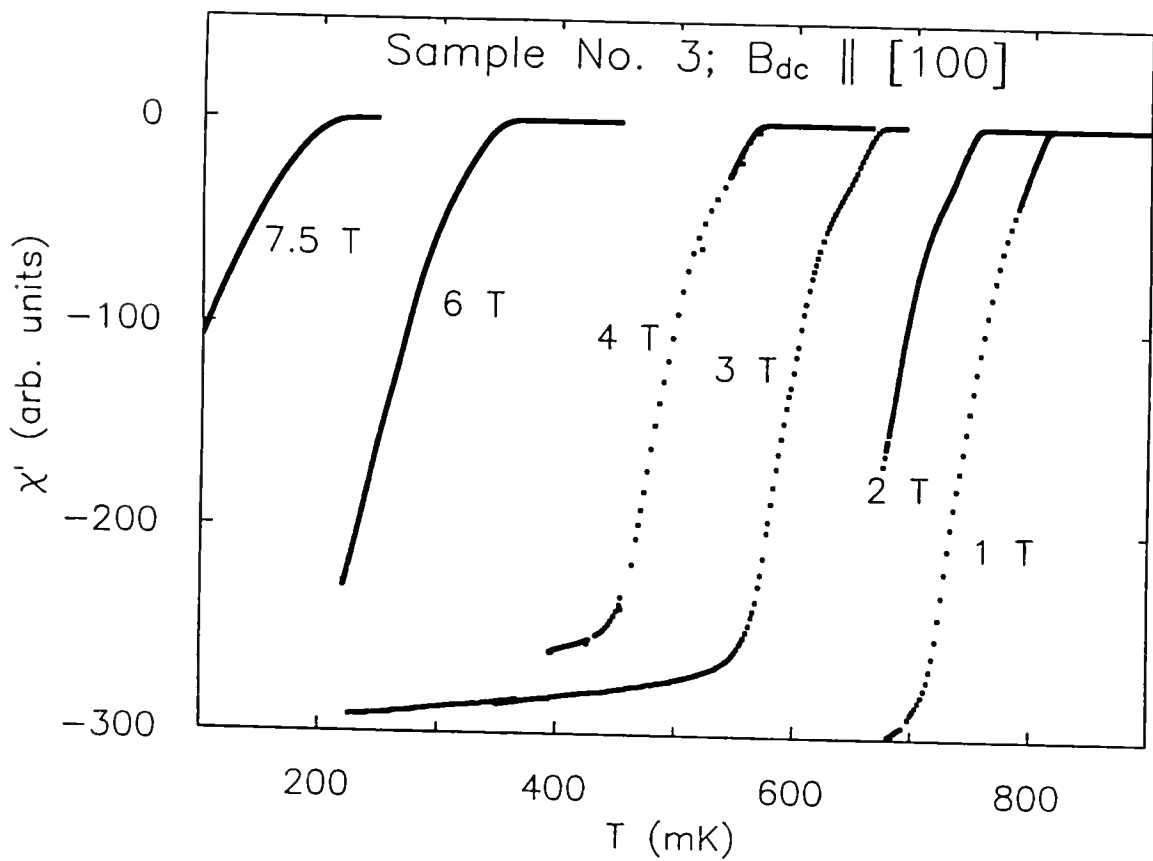


Fig. 5-21. $\chi'(T)$ for sample No. 3 for the applied dc field, B_{dc} , parallel to the [100] direction, and for $B_{dc} \geq 1$ T.

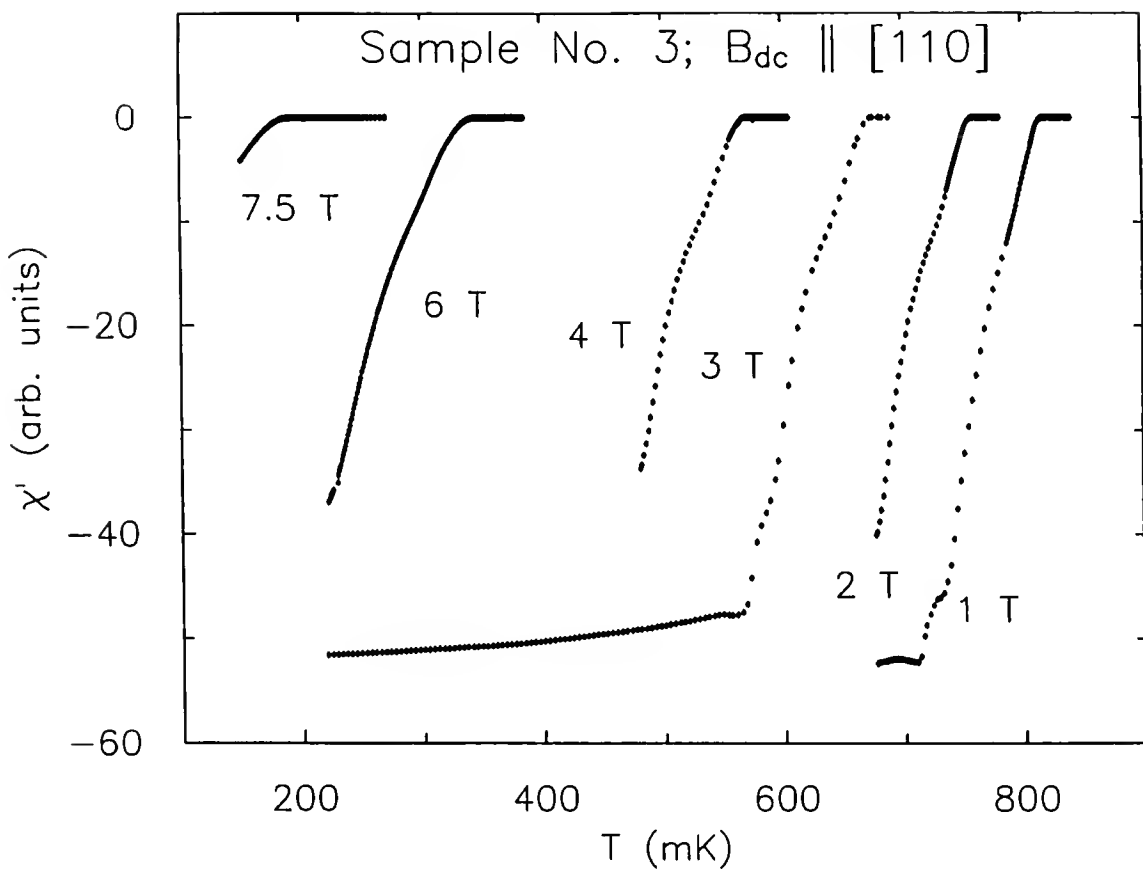


Fig. 5-22. $\chi'(T)$ for sample No. 3 for the applied dc field, B_{dc} , parallel to the [110] direction, and for $B_{dc} \geq 1$ T.

varnish, holding the sample to the copper wires (used for thermal anchoring), be removed. The samples were then rotated, and varnished back on the copper wires. To ensure that we could reproduce the thermal anchoring of the sample from run to run, we used the same crystal orientation ([100]) twice, after dismounting, for one of the specimens (sample No. 1). The data around the transition temperature are shown in Fig. 5-23 for zero field. The transition temperature of 903 mK was reproducible to within the experimental errors (0.5 mK). This result demonstrates that our mounting technique does not introduce additional uncertainties in the identification of T_c .

5.4.2.b Phase diagrams

The values of $B_{c2}(T)$, obtained from the method described above, allow us to construct the B-T phase diagrams for the three samples. These diagrams are shown in Figs. 5-24 through 5-26. The common feature among the three samples is the lack of anisotropy in the limit $T/T_c \rightarrow 1$, as can be seen in the insets of the figures. This finding, central to our study, will be discussed in detail in the next section.

Another interesting result is the fact that sample No. 3, which possesses the lowest zero field T_c of 849.3 mK (compared to 903 mK and 901.5 mK for samples No. 1 and No. 2, respectively), exhibits the highest slope, $dB_{c2}(T) / dT \approx -34.5$ T/K, while the slopes for samples No. 1 and No. 2 were -32.8 T/K and -25.5 T/K, respectively. The combination of a low T_c and a high $B_{c2}(T)$ slope near $T/T_c \approx 1$ is characteristic of type II superconductors with impurities, which decrease T_c , and increase flux pinning, thereby increasing the upper critical field. This effect has been observed in BCS superconductors such as niobium (Rosenblum and Autler, 1964).

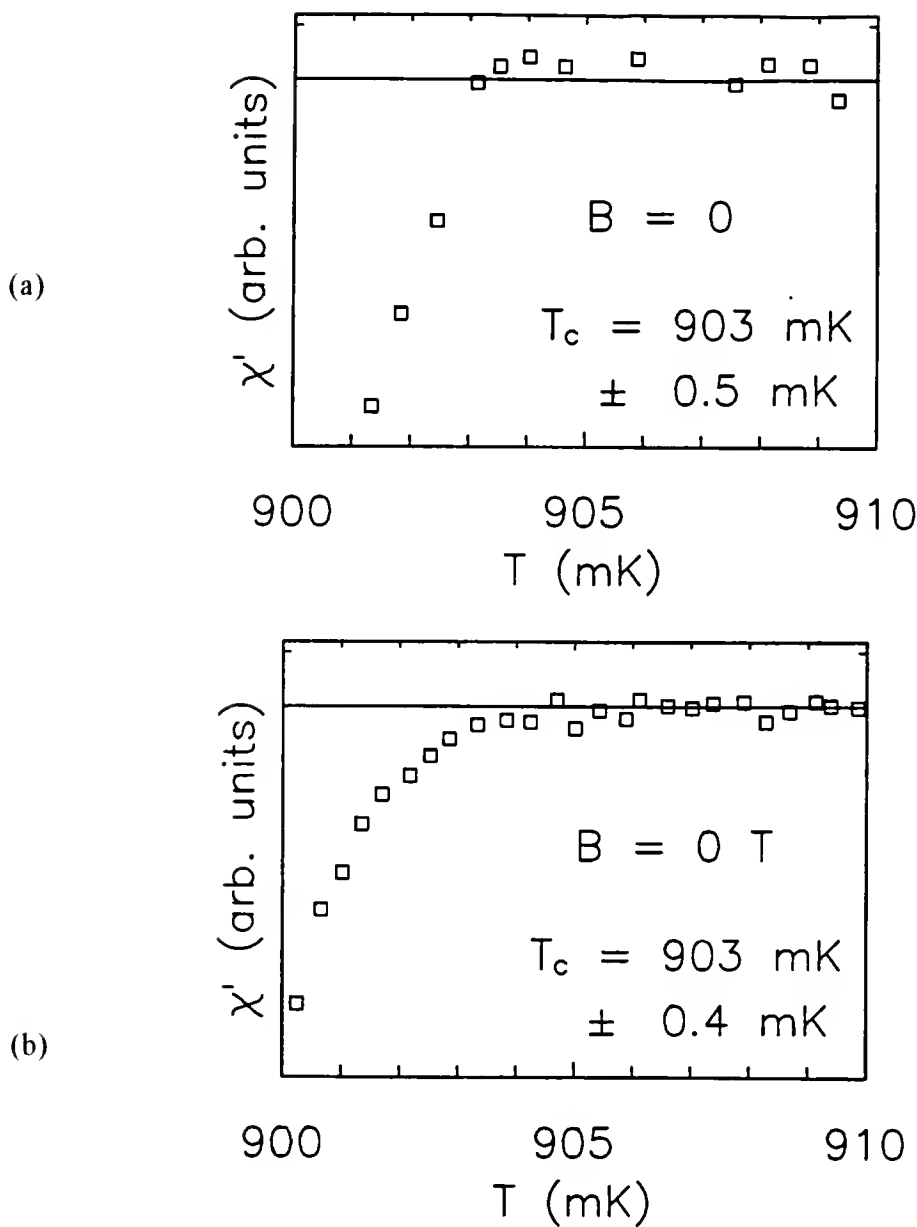


Fig. 5-23. $\chi'(T)$ of sample No. 1 in the vicinity of T_c , with $B_{dc} = 0$, and the probing field parallel to the [100] orientation. The data shown in (a) and (b) were taken under identical conditions, but in two different runs, with dismounting-remounting of the sample in between the runs. The transition temperature was reproducible to within the experimental errors. This result demonstrates that our mounting technique does not introduce additional uncertainties in the identification of T_c .

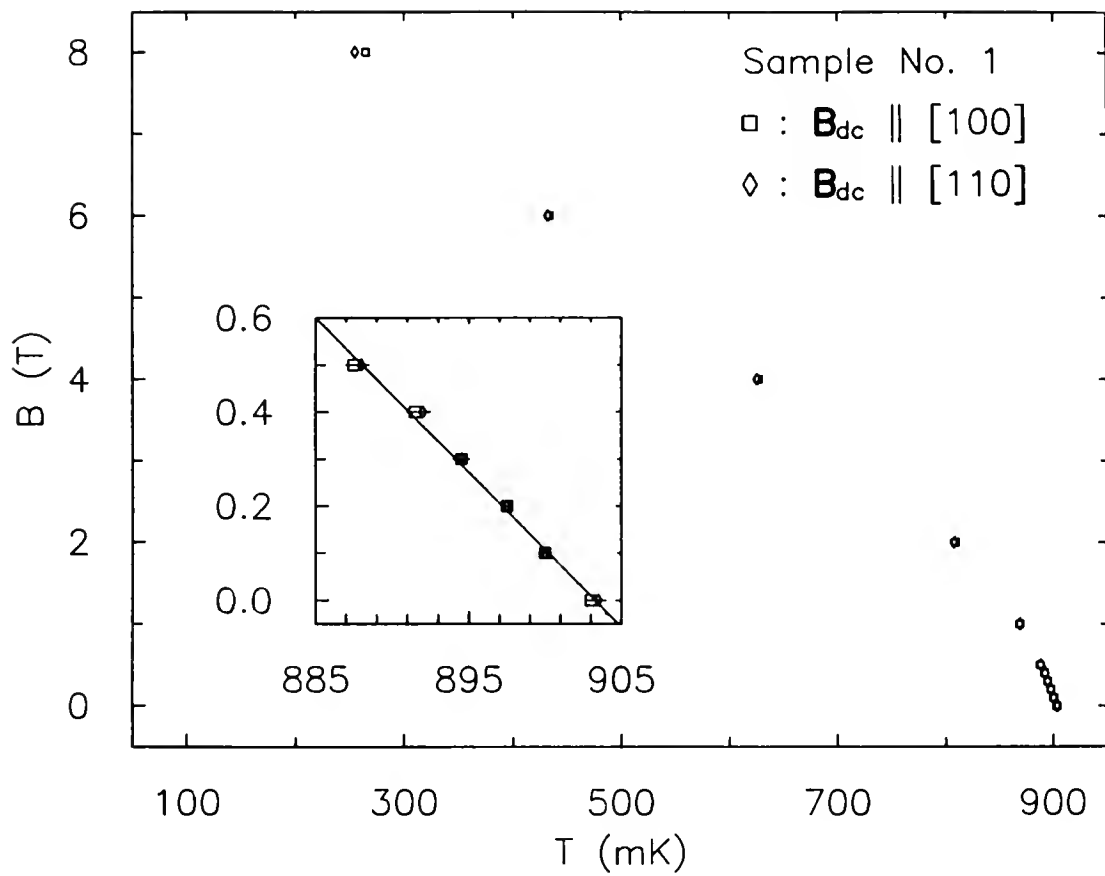


Fig. 5-24. The B-T phase diagram for sample No. 1 with $\mathbf{B}_{dc} \parallel [100]$ direction (\square), and $\mathbf{B}_{dc} \parallel [110]$ direction (\diamond). The inset focuses on the data in the limit $T/T_c \rightarrow 1$. The solid line is the result of a linear fit which indicates that the data fall on a straight line of slope $d\mathbf{B}_{c2}(T)/dT = -32.8 \pm 0.5 \text{ T/K}$.

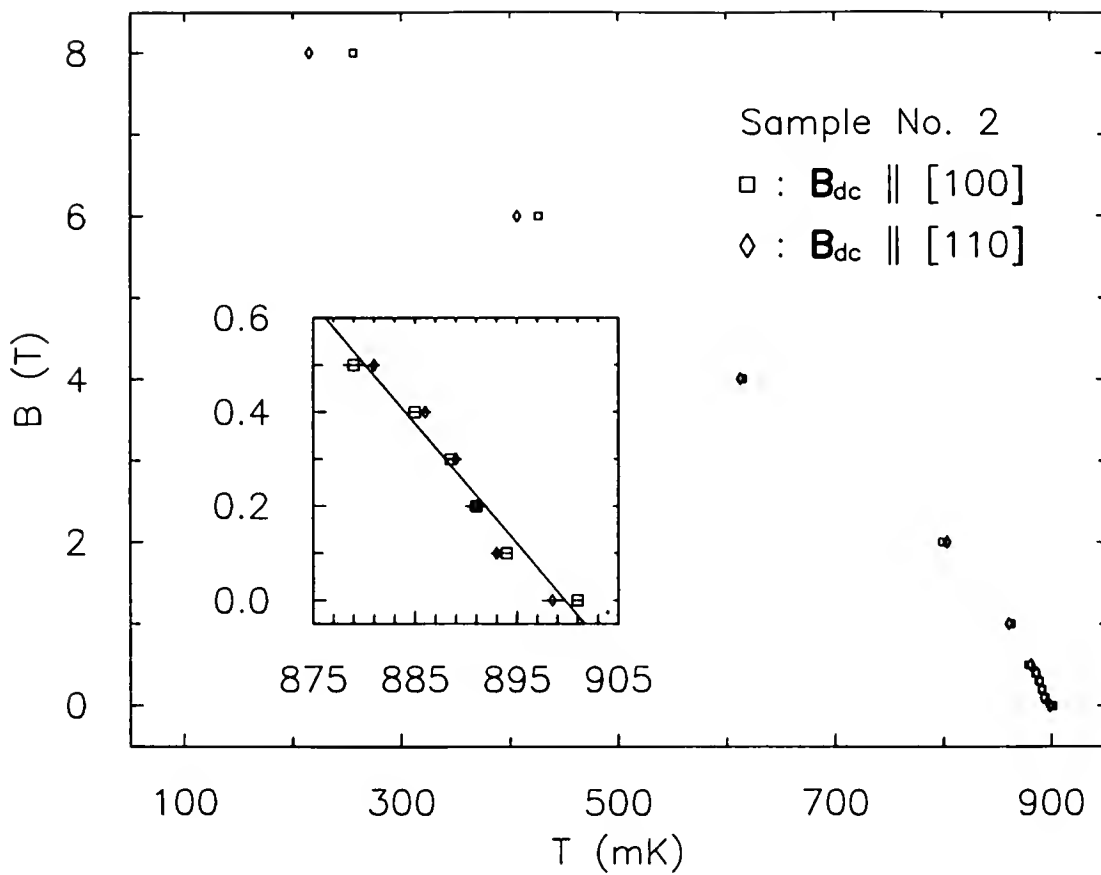


Fig. 5-25. The B-T phase diagram for sample No. 2 with $\mathbf{B}_{dc} \parallel [100]$ direction (\square), and $\mathbf{B}_{dc} \parallel [110]$ direction (\diamond). The inset focuses on the data in the limit $T/T_c \rightarrow 1$. The solid line is the result of a linear fit which indicates that the data fall on a straight line of slope $d\mathbf{B}_{c2}(T)/dT = -25.5 \pm 1.0 \text{ T/K}$.

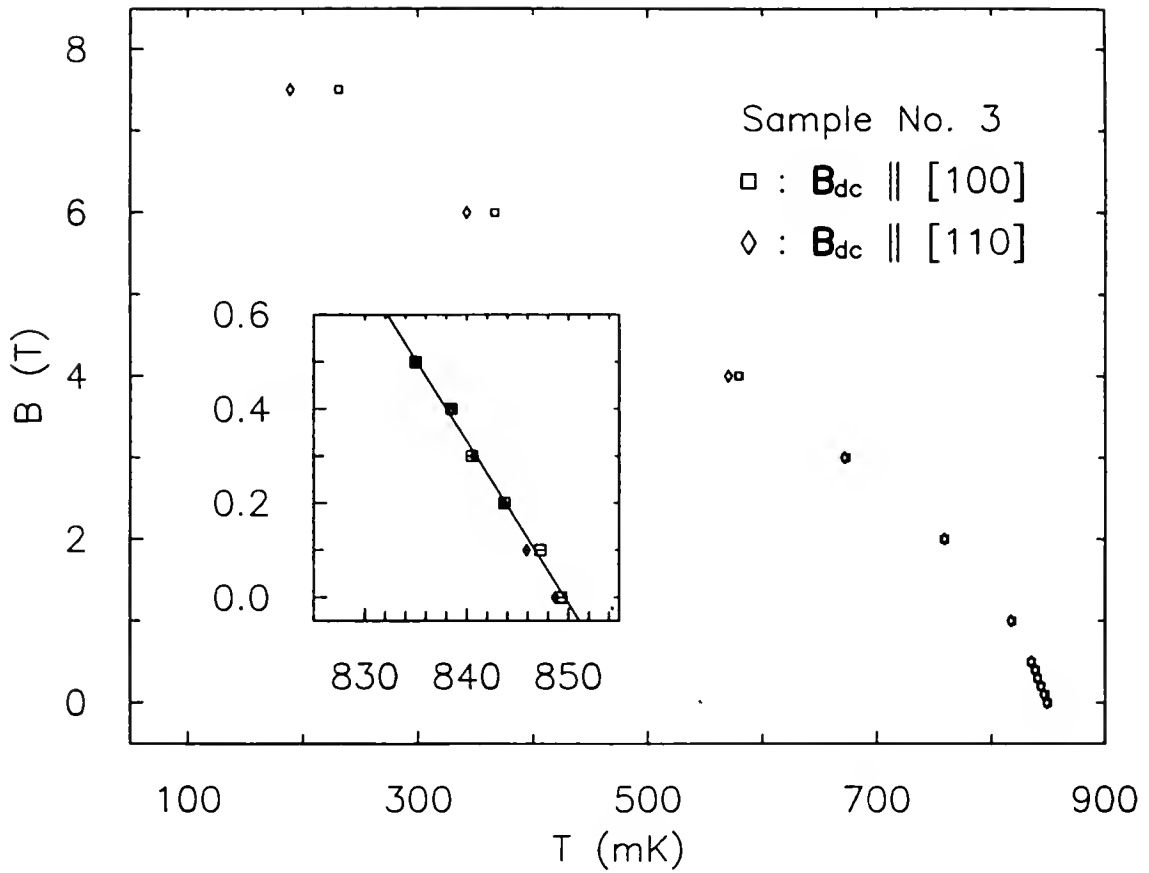


Fig. 5-26. The B-T phase diagram for sample No. 3 with $\mathbf{B}_{dc} \parallel [100]$ direction (\square), and $\mathbf{B}_{dc} \parallel [110]$ direction (\diamond). The inset focuses on the data in the limit $T/T_c \rightarrow 1$. The solid line is the result of a linear fit which indicates that the data fall on a straight line of slope $d\mathbf{B}_{c2}(T)/dT = -34.5 \pm 0.5 \text{ T/K}$.

5.4.2.c $\chi'(B)$ at constant temperatures

In addition to our temperature sweeps at constant magnetic fields, we performed a series of magnetic field sweeps at constant temperature. The initial motivation for this measurement came from the report by Ellman *et al.* (1991) of a second transition line, within the superconducting state, observed in the specific heat as a function of field at constant temperature. The transition line reported by Ellman *et al.* was nearly constant in field (parallel to the temperature axis in a B vs. T plot) and was, therefore, difficult to observe from temperature sweeps. Our results obtained for samples No. 1 and No. 2 are shown in Figs. 5-27 and 5-28, where there is no obvious presence of any second transition below $B_{C2}(T)$. However, both samples exhibit a double bump in $\chi''(B)$ near B_{C2} , which corresponds to a kink in $\chi'(B)$. This double structure is best seen for sample No. 2 around 3.75 T (Fig. 5-28). This observation is probably related to the fact that, due to the parallelepiped shape of the samples, the field is not homogeneously distributed around the surface. Consequently, parts of the specimen (edges and corners) experience fields greater than $B_{C2}(T)$ and become normal, while the rest of the sample stays superconducting. The coexistence of normal and superconducting volumes within one sample is known as the intermediate state. Similar behavior of $\chi'(B)$ has been observed in niobium (Bertman and Strongin, 1964) and was also accounted for by the intermediate state. We note that, since our criterion for T_C is the onset of superconductivity, this effect does *not* affect the determination of T_C and the phase diagrams (Figs. 5-24, 5-25, and 5-26).

Magnetic field sweeps on sample No. 3 revealed a different and interesting feature in $\chi'(B)$. Three sweeps, for fields parallel to the [100] direction and performed at 100 mK, 175 mK and 250 mK (Figs. 5-29, 5-30 and 5-31), indicated a bump in $\chi'(B)$ below the upper critical field transitions. This effect is different from the one discussed in the previous paragraph since, for sample No. 3, $\chi'(B)$ goes through a maximum which cannot

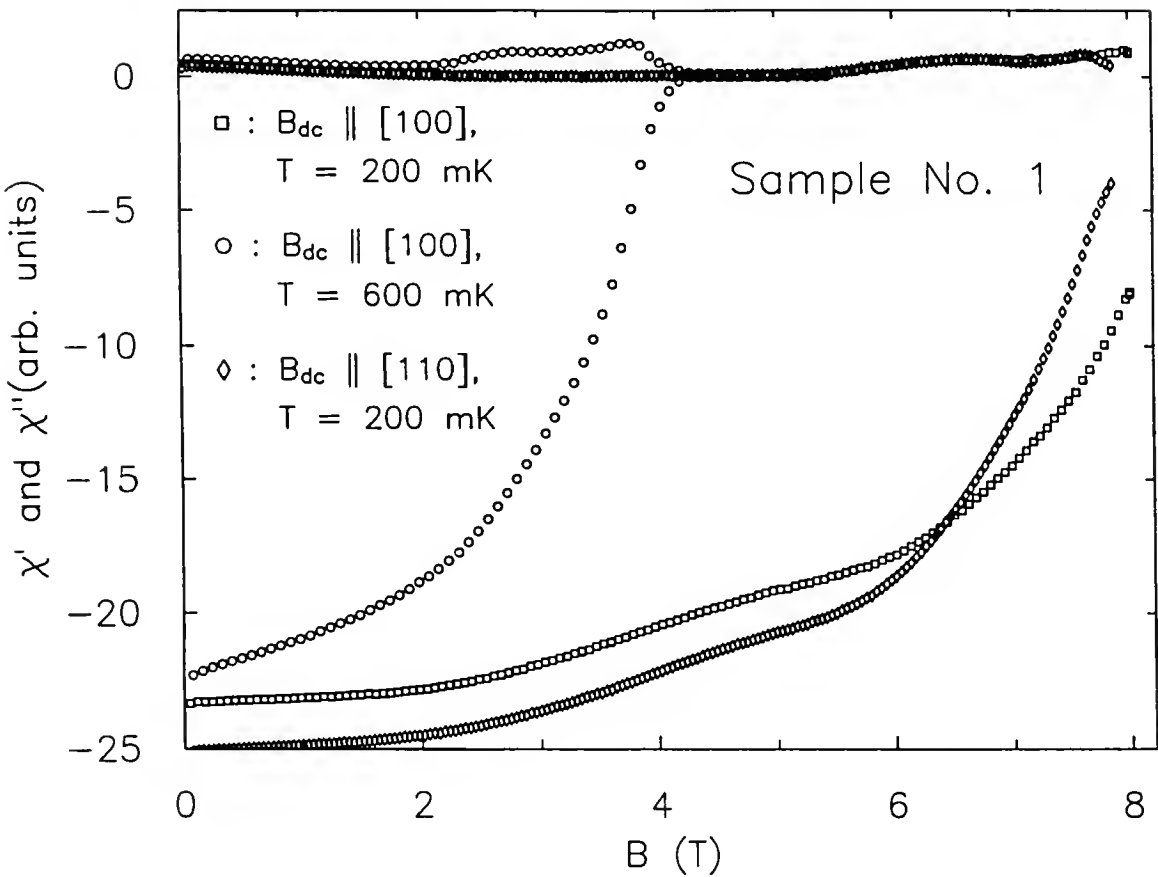


Fig. 5-27. $\chi'(B)$ and $\chi''(B)$ for sample No. 1 for the applied dc field, \mathbf{B}_{dc} , parallel to the [100] direction and at constant temperature $T = 200 \text{ mK}$ (\square), $\mathbf{B}_{dc} \parallel [100]$, $T = 600 \text{ mK}$ (\circ); and $\mathbf{B}_{dc} \parallel [110]$, $T = 200 \text{ mK}$ (\diamond). For the 200 mK sweeps, $B_{c2}(200 \text{ mK})$ is greater than 8 T.

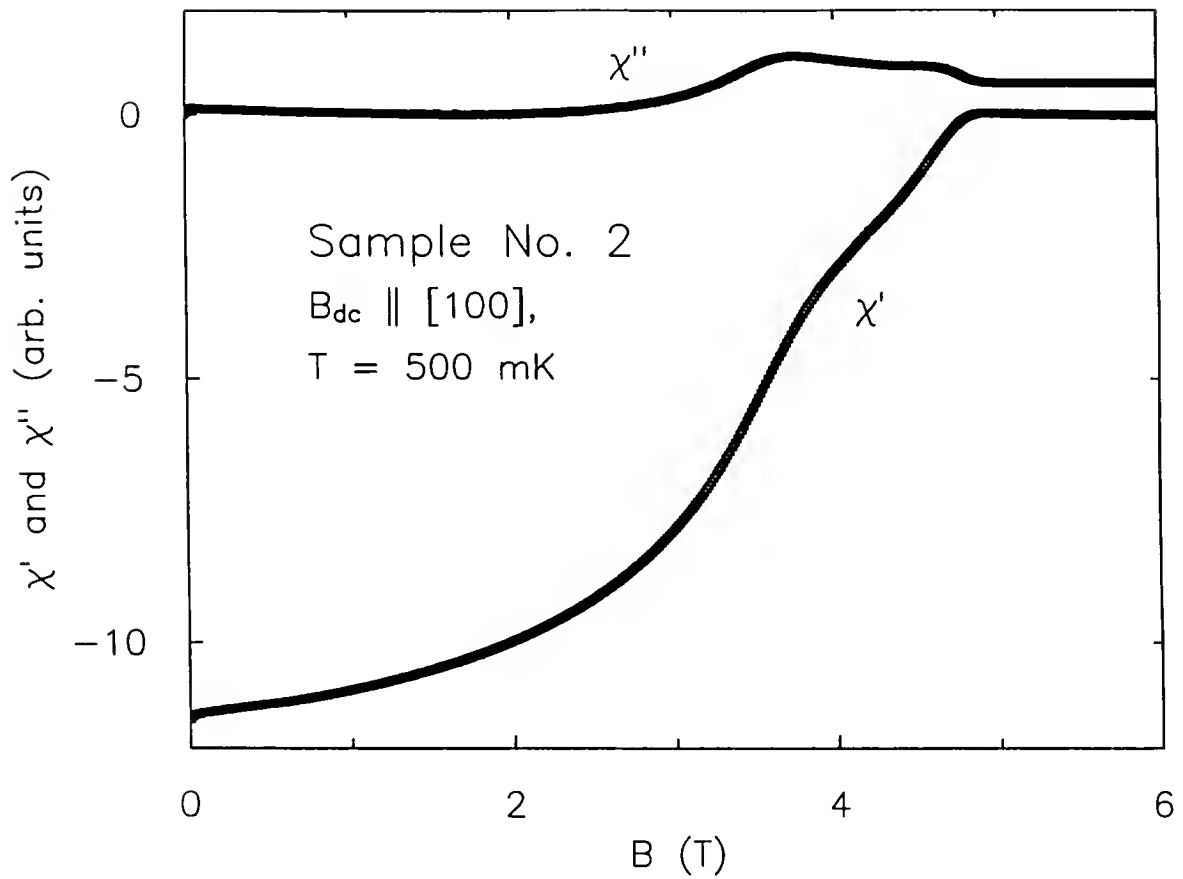


Fig. 5-28. $\chi'(B)$ and $\chi''(B)$ for sample No. 2 with $\mathbf{B}_{dc} \parallel [100]$, $T = 500$ mK.

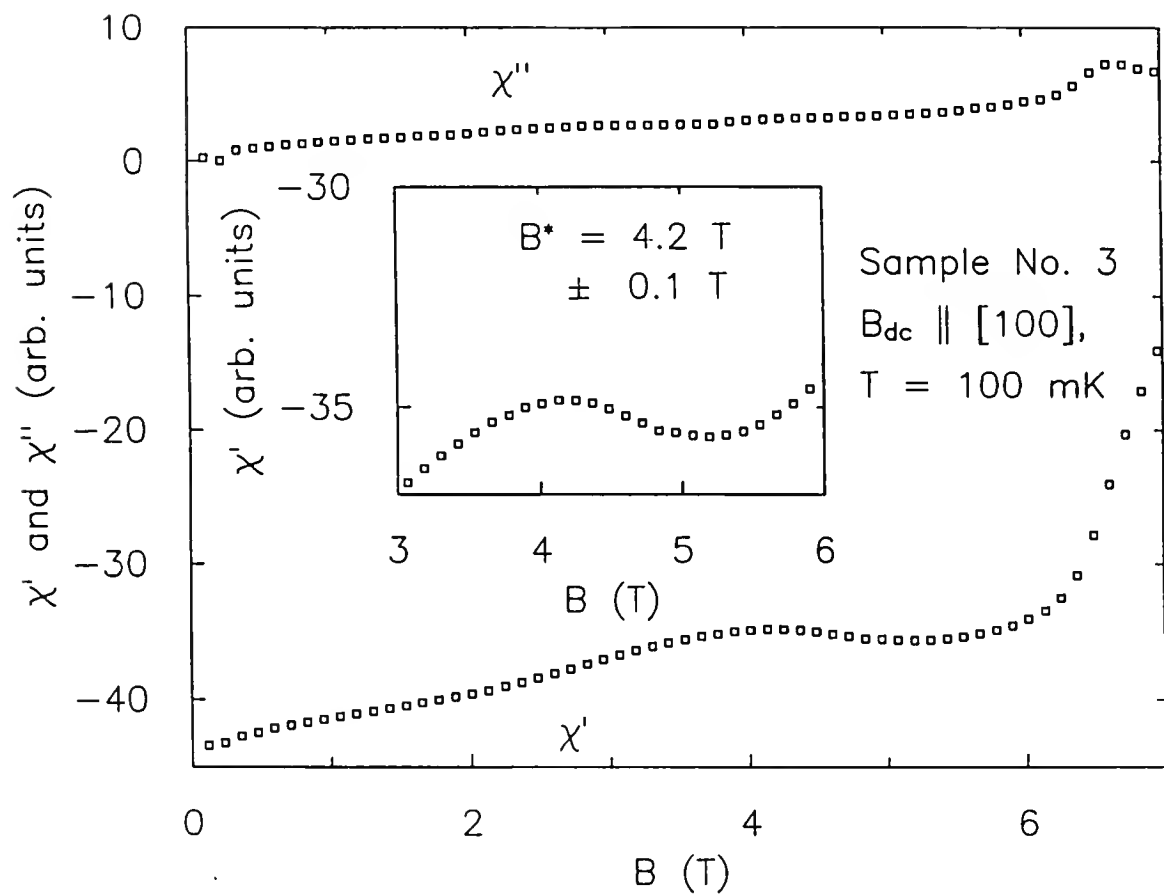


Fig. 5-29. $\chi'(B)$ and $\chi''(B)$ for sample No. 3 with $\mathbf{B}_{dc} \parallel [100]$, $T = 100$ mK. The inset shows the anomaly in $\chi'(B)$ around $B^* = 4.2$ T.

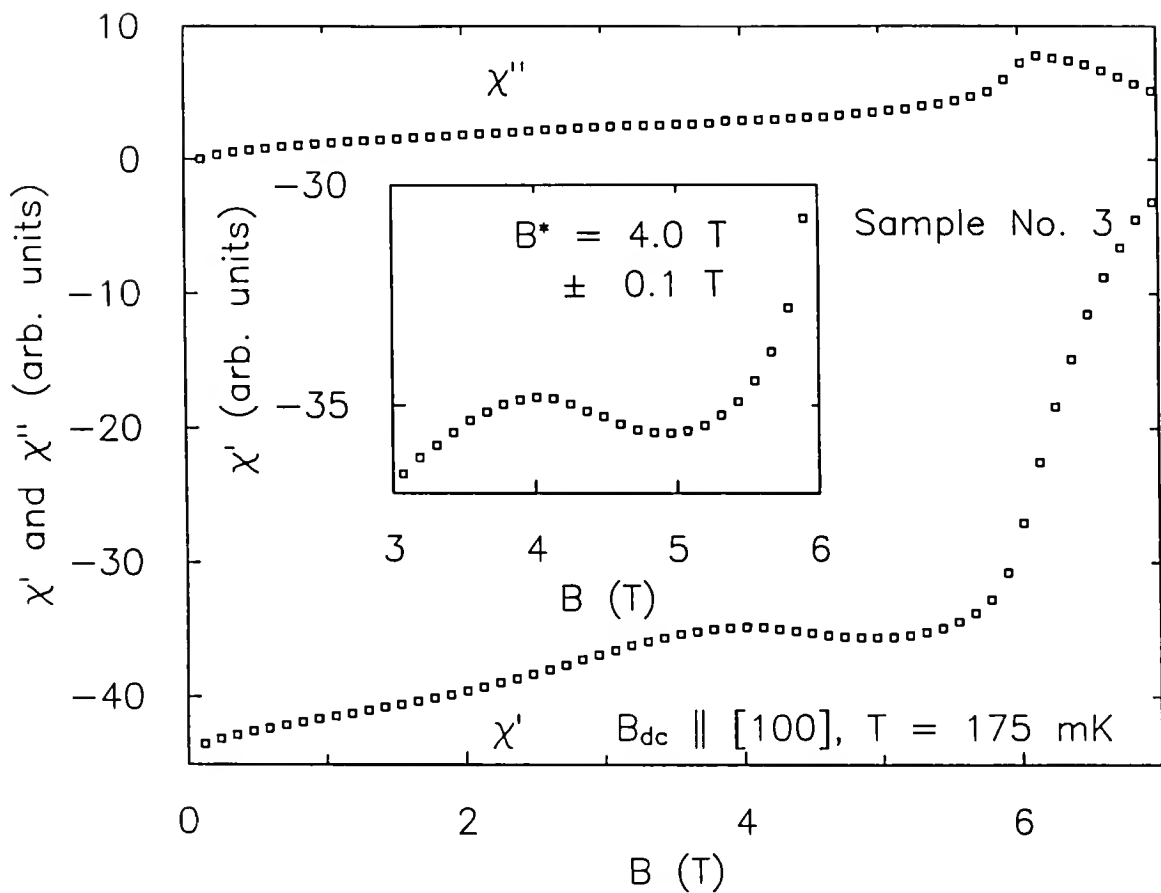


Fig. 5-30. $\chi'(B)$ and $\chi''(B)$ for sample No. 3 with $B_{dc} \parallel [100]$, $T = 175$ mK. The inset shows the anomaly in $\chi'(B)$ around $B^* = 4.0$ T.

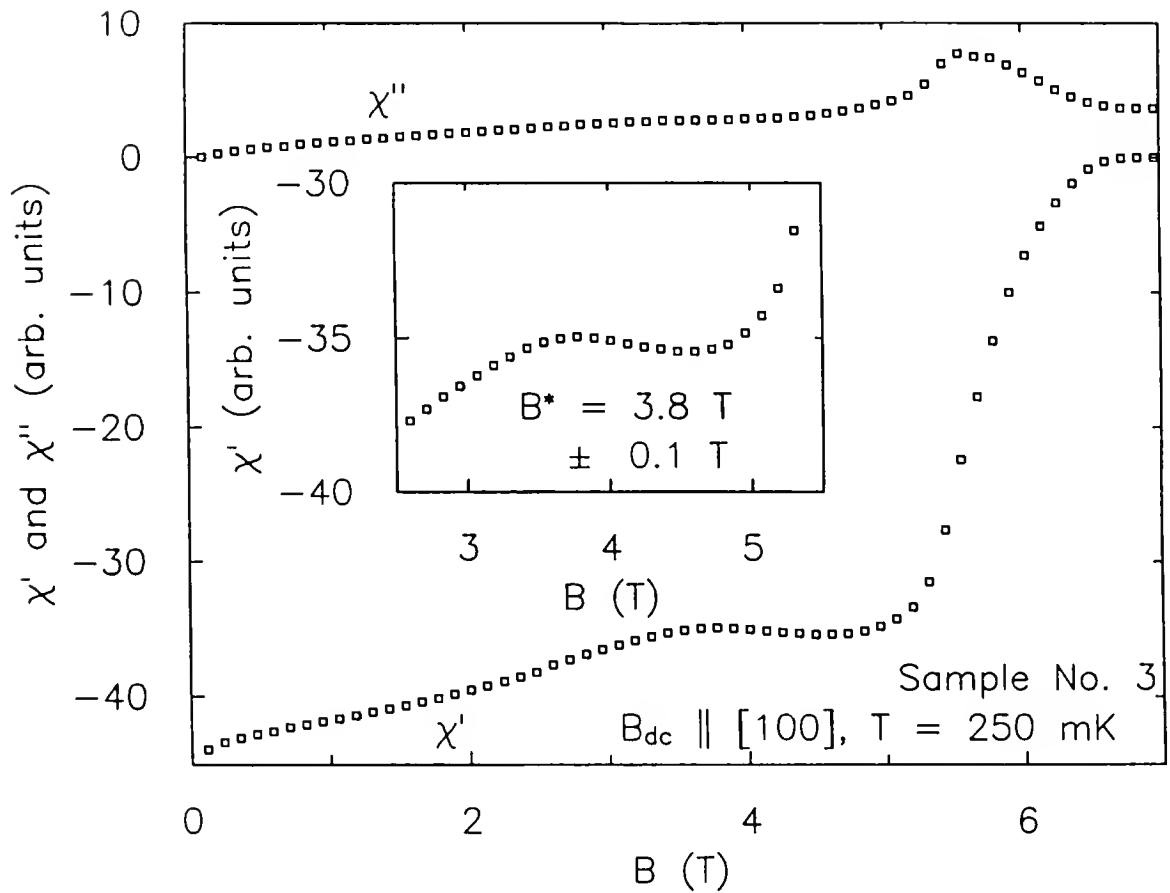


Fig. 5-31. $\chi'(B)$ and $\chi''(B)$ for sample No. 3 with $\mathbf{B}_{dc} \parallel [100]$, $T = 250$ mK. The inset shows the anomaly in $\chi'(B)$ around $B^* = 3.8$ T.

be explained in terms of the intermediate state. The insets of Figs. 5-29 through 5-31 focus on the magnetic field range for which these bumps occurred. In order to map out the B-T diagram of this feature, the peak of the bump, labeled B^* and indicated in the insets, was identified for our various sweeps. For the 400 mK field sweep (Fig. 5-32), the proximity of the upper critical field transition made the identification of B^* ambiguous. This difficulty motivated us to try a temperature sweep at constant field ($B = 3$ T), shown in Fig. 5-33. Although the feature was barely observable for this temperature sweep, we suggest a temperature, T^* , at which the peak of the bump occurs. In view of the difficulty in observing the anomaly for fields lower than 3 T and temperatures higher than 400 mK, we stopped our measurements for this orientation of the crystal and began measuring $\chi'(B)$ for fields parallel to the [110] orientation. These measurements revealed that T^* was clearly observable down to $B = 0$ T. The results of these field and temperature sweeps, for the field parallel to the [110] orientation, are shown in Figs. 5-34 through 5-41, where B^* and T^* are indicated in the insets. The phase diagram constructed from these values of B^* and T^* is shown in Fig. 5-42, where the upper critical field is also plotted for comparison. In the next section, the nature of this anomaly is argued to be related to flux line depinning and to be an extrinsic feature of the superconductivity in UBe₁₃.

5.4.3 Temperature Dependence of the Penetration Depth

The temperature dependence of the penetration depth, $\lambda(T)$, was obtained with a mutual inductance technique identical to the one described in Chapter 3. We studied $\lambda(T)$ of sample No. 1 with the probing ac magnetic field parallel to the [100] and [110] orientations. These results are shown in Figs. 5-43 through 5-46. We also measured $\lambda(T)$ of sample No. 3 for the ac field parallel to the [100] orientation, and this data are shown in Figs. 5-47 and 5-48.

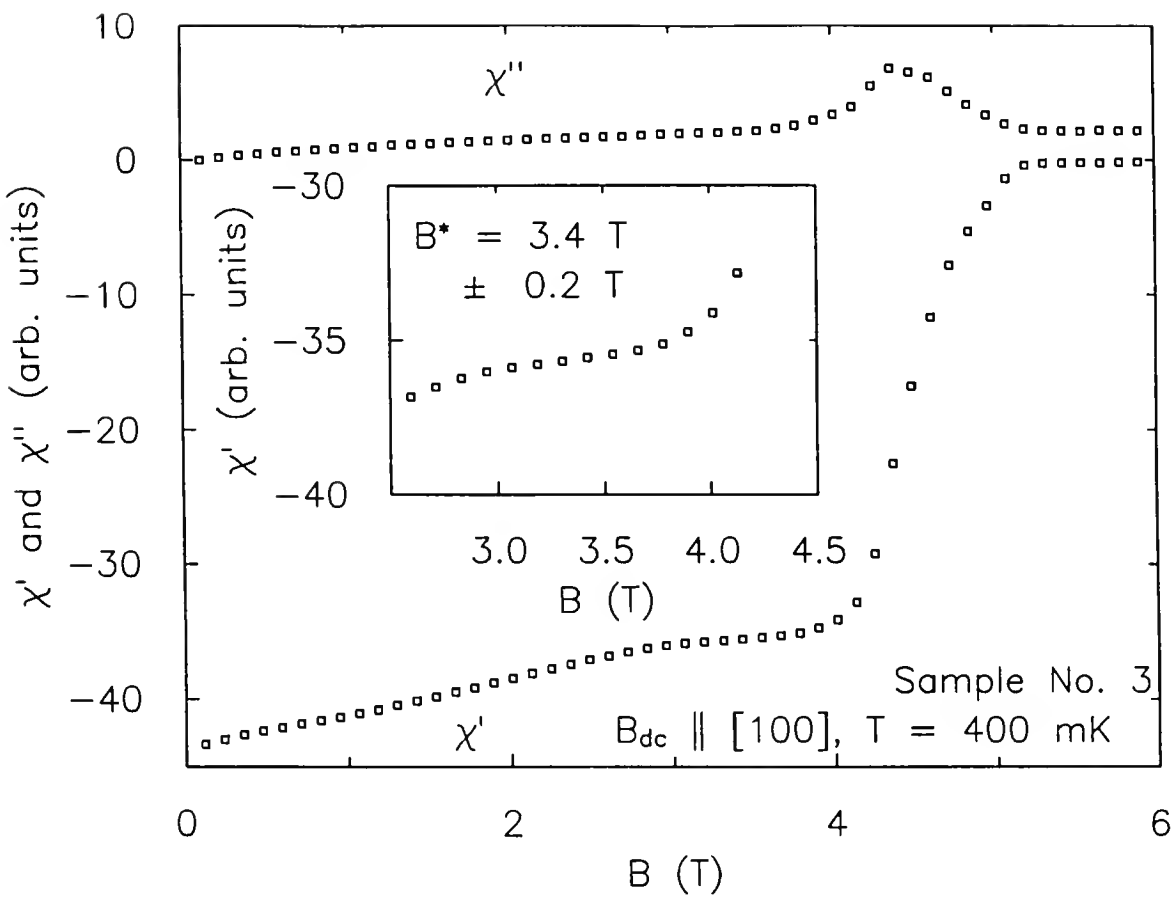


Fig. 5-32. $\chi'(B)$ and $\chi''(B)$ for sample No. 3 with $B_{dc} \parallel [100]$, $T = 400$ mK. The inset shows the anomaly in $\chi'(B)$ around $B^* = 3.4$ T.

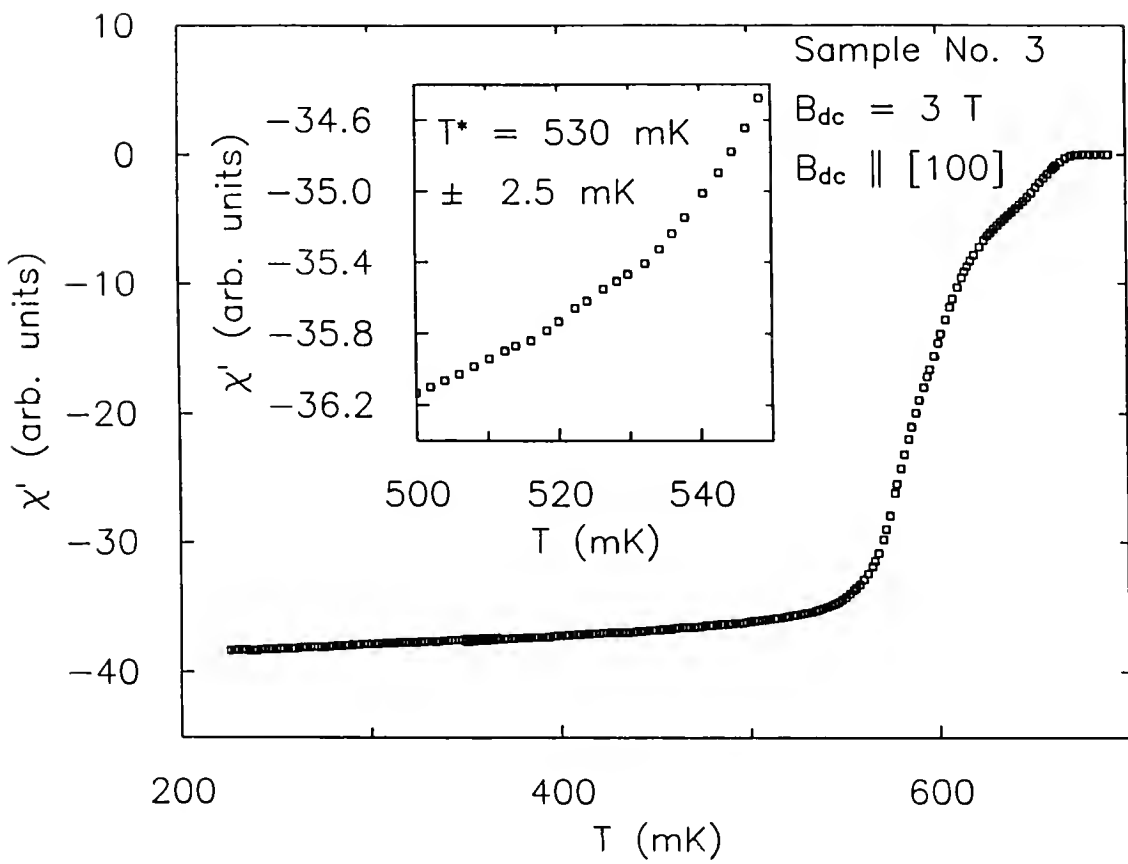


Fig. 5-33. $\chi'(T)$ for sample No. 3 with $B_{dc} \parallel [100]$ and for $B_{dc} = 3 \text{ T}$. The inset shows the anomaly in $\chi'(T)$ around $T^* = 530 \text{ mK}$.

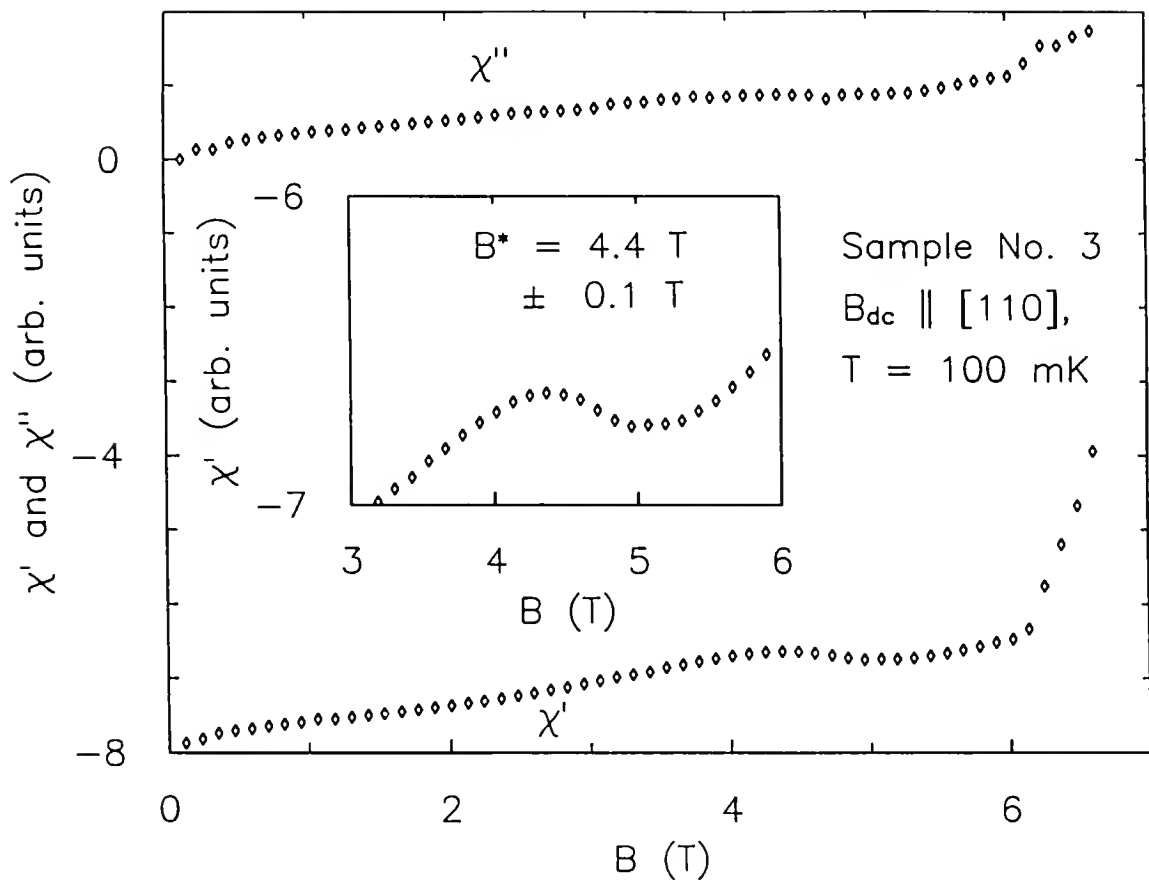


Fig. 5-34. $\chi'(B)$ and $\chi''(B)$ for sample No. 3 with $B_{dc} \parallel [110]$, $T = 100$ mK. The inset shows the anomaly in $\chi'(B)$ around $B^* = 4.4$ T.

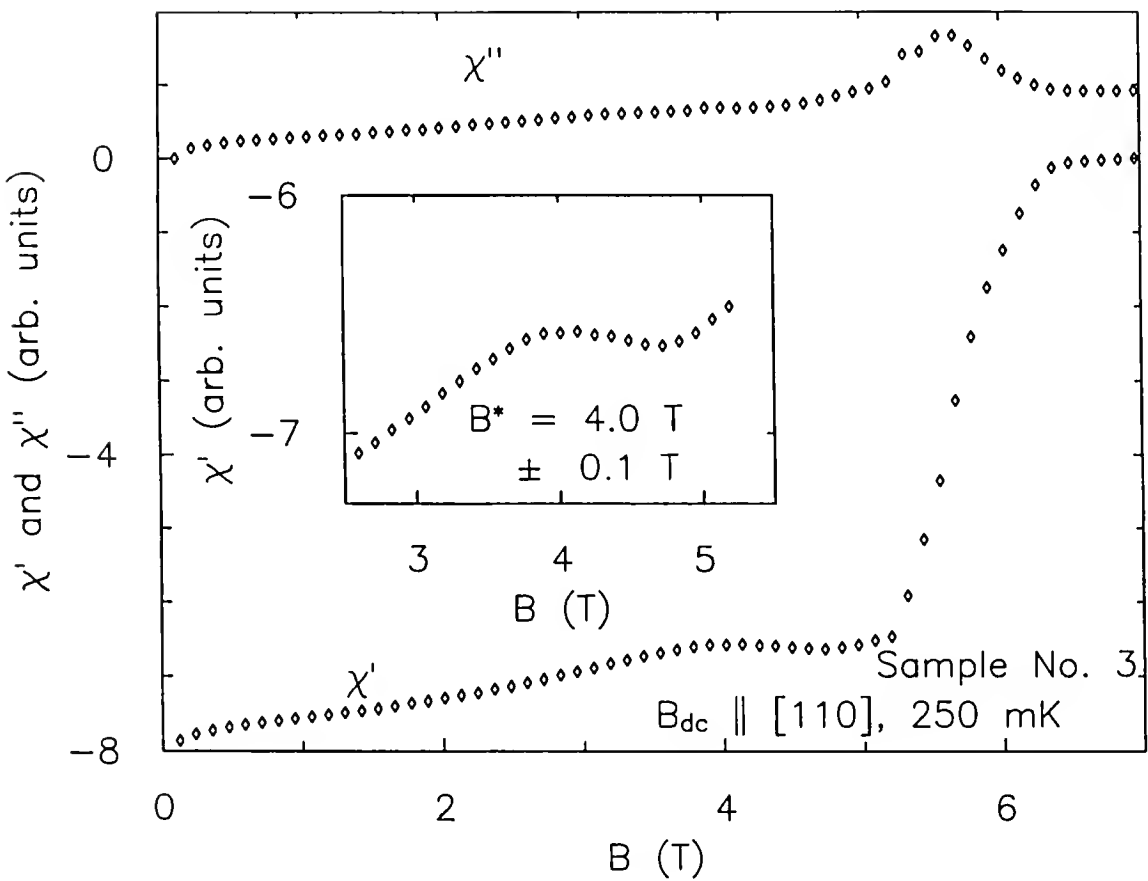


Fig. 5-35. $\chi'(B)$ and $\chi''(B)$ for sample No. 3 with $B_{dc} \parallel [110]$, $T = 250 \text{ mK}$. The inset shows the anomaly in $\chi'(B)$ around $B^* = 4.0 \text{ T}$.

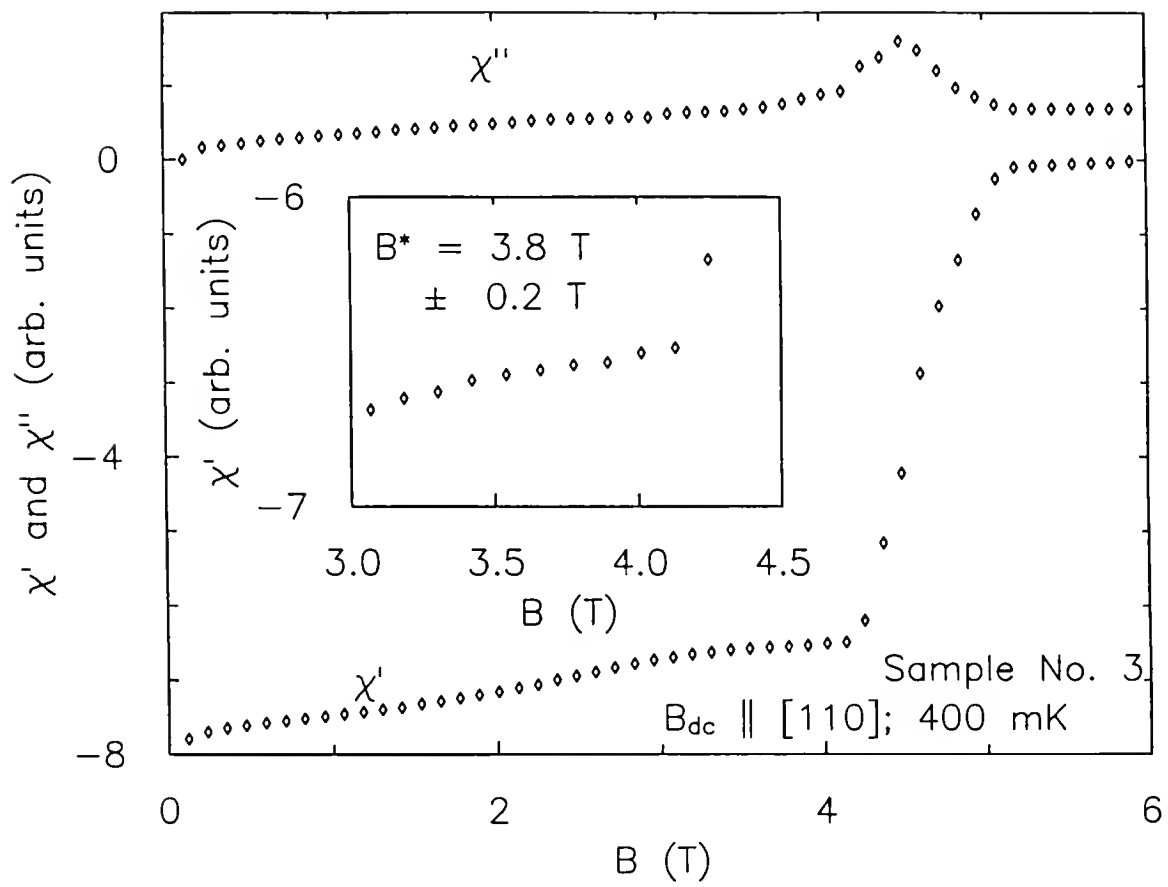


Fig. 5-36. $\chi'(B)$ and $\chi''(B)$ for sample No. 3 with $\mathbf{B}_{dc} \parallel [110]$, $T = 400 \text{ mK}$. The inset shows the anomaly in $\chi'(B)$ around $B^* = 3.8 \text{ T}$.

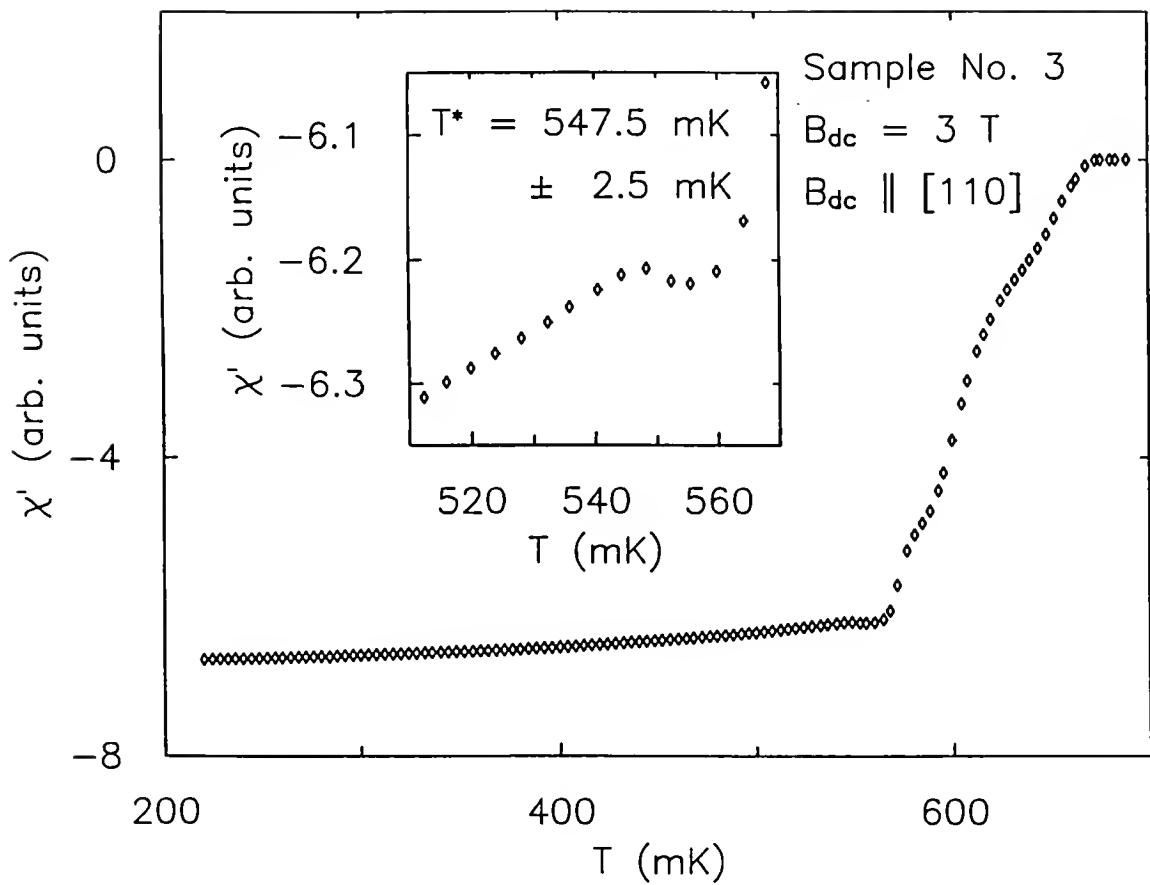


Fig. 5-37. $\chi'(T)$ for sample No. 3 with $B_{dc} \parallel [110]$ and for $B_{dc} = 3 \text{ T}$. The inset shows the anomaly in $\chi'(T)$ around $T^* = 547.5 \text{ mK}$.

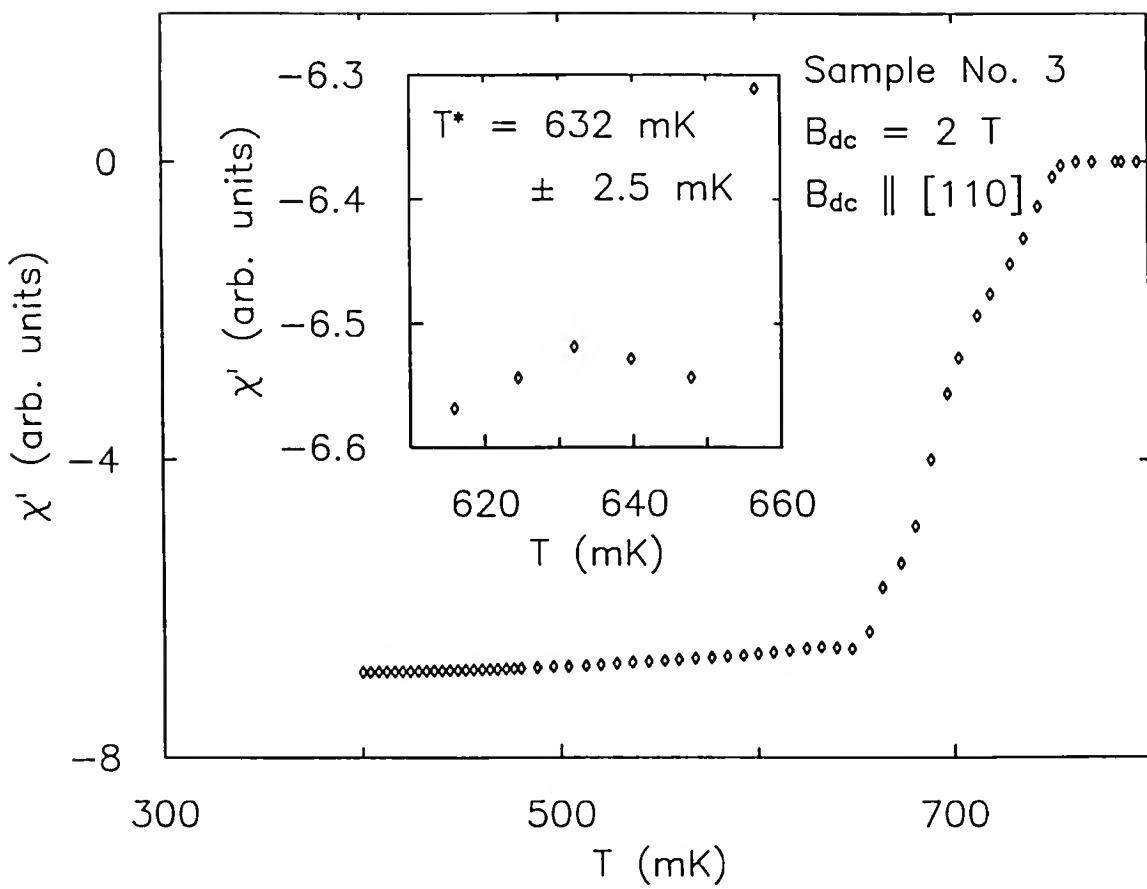


Fig. 5-38 $\chi'(T)$ for sample No. 3 with $B_{dc} \parallel [110]$ and for $B_{dc} = 2 \text{ T}$. The inset shows the anomaly in $\chi'(T)$ around $T^* = 632 \text{ mK}$.

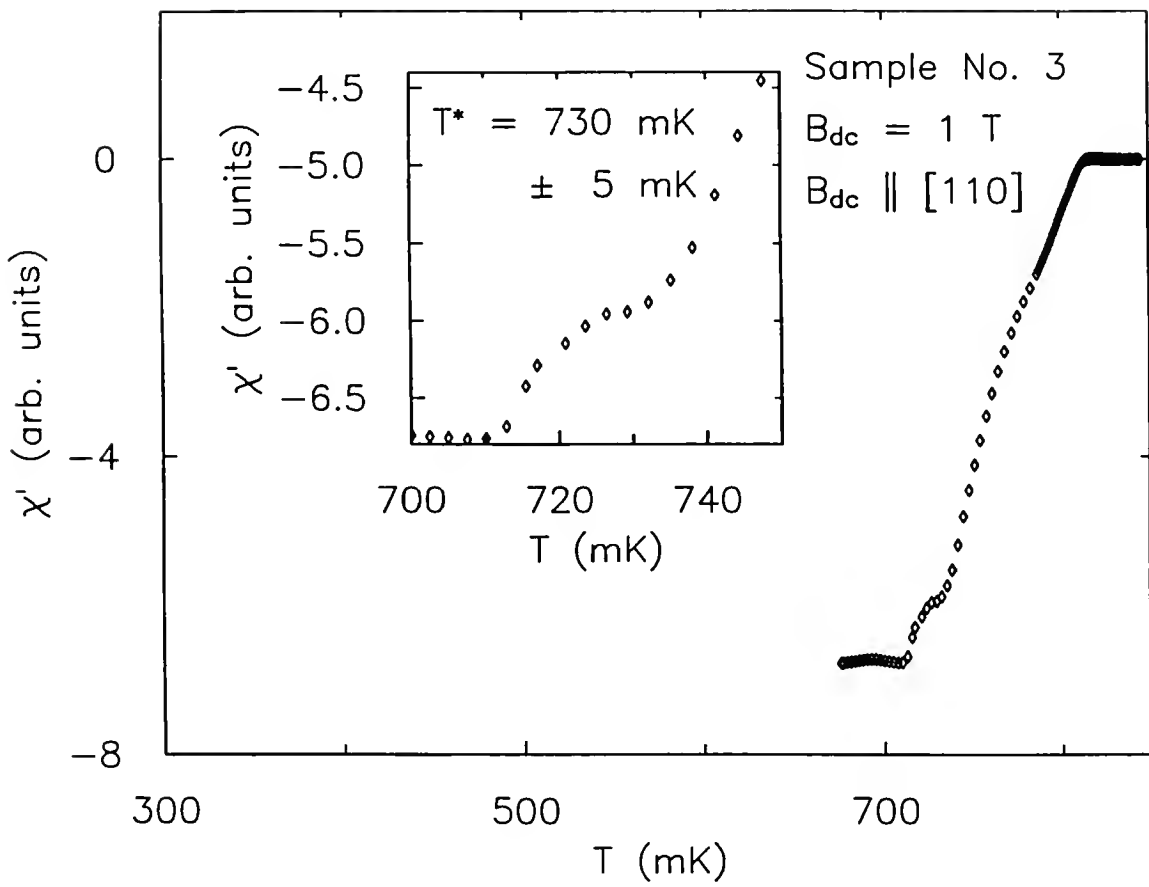


Fig. 5-39. $\chi'(T)$ for sample No. 3 with $B_{dc} \parallel [110]$ and for $B_{dc} = 1 \text{ T}$. The inset shows the anomaly in $\chi'(T)$ around $T^* = 730 \text{ mK}$.

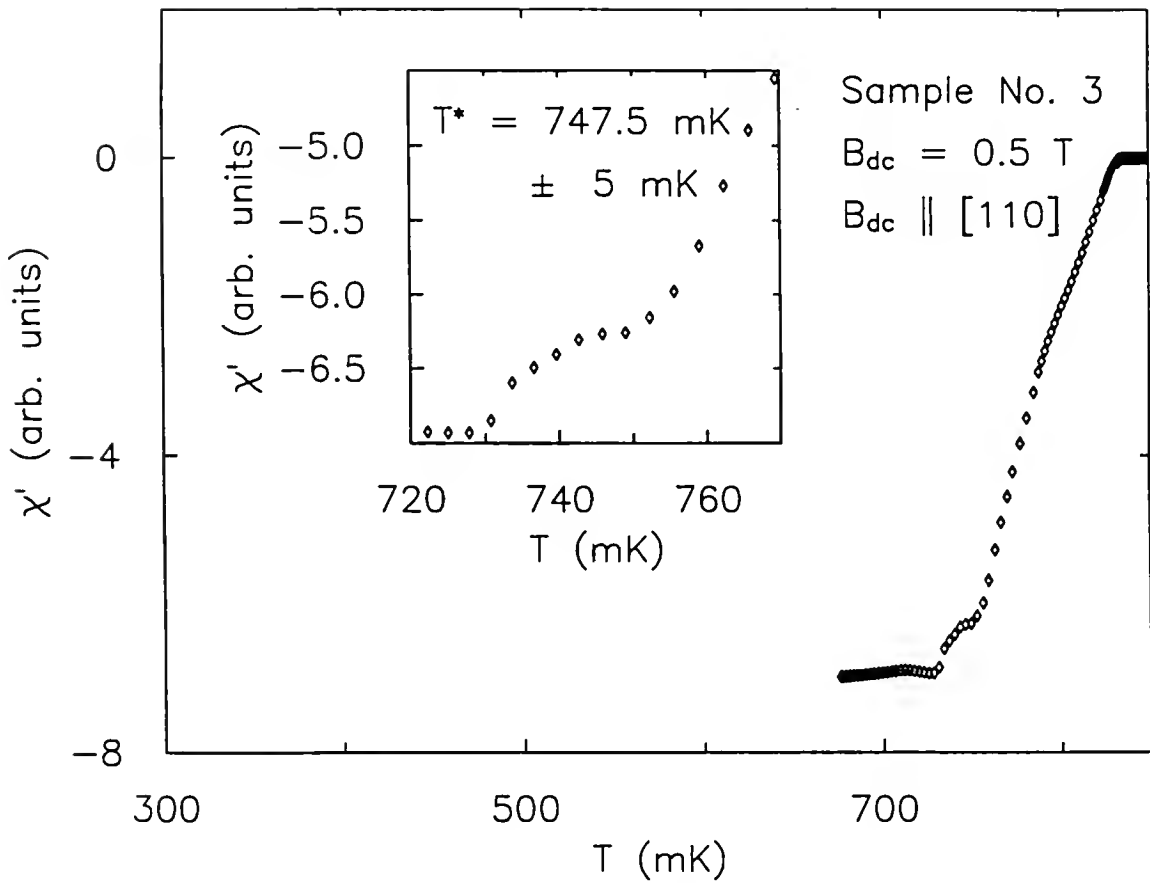


Fig. 5-40. $\chi'(T)$ for sample No. 3 with $B_{dc} \parallel [110]$ and for $B_{dc} = 0.5 \text{ T}$. The inset shows the anomaly in $\chi'(T)$ around $T^* = 747.5 \text{ mK}$.

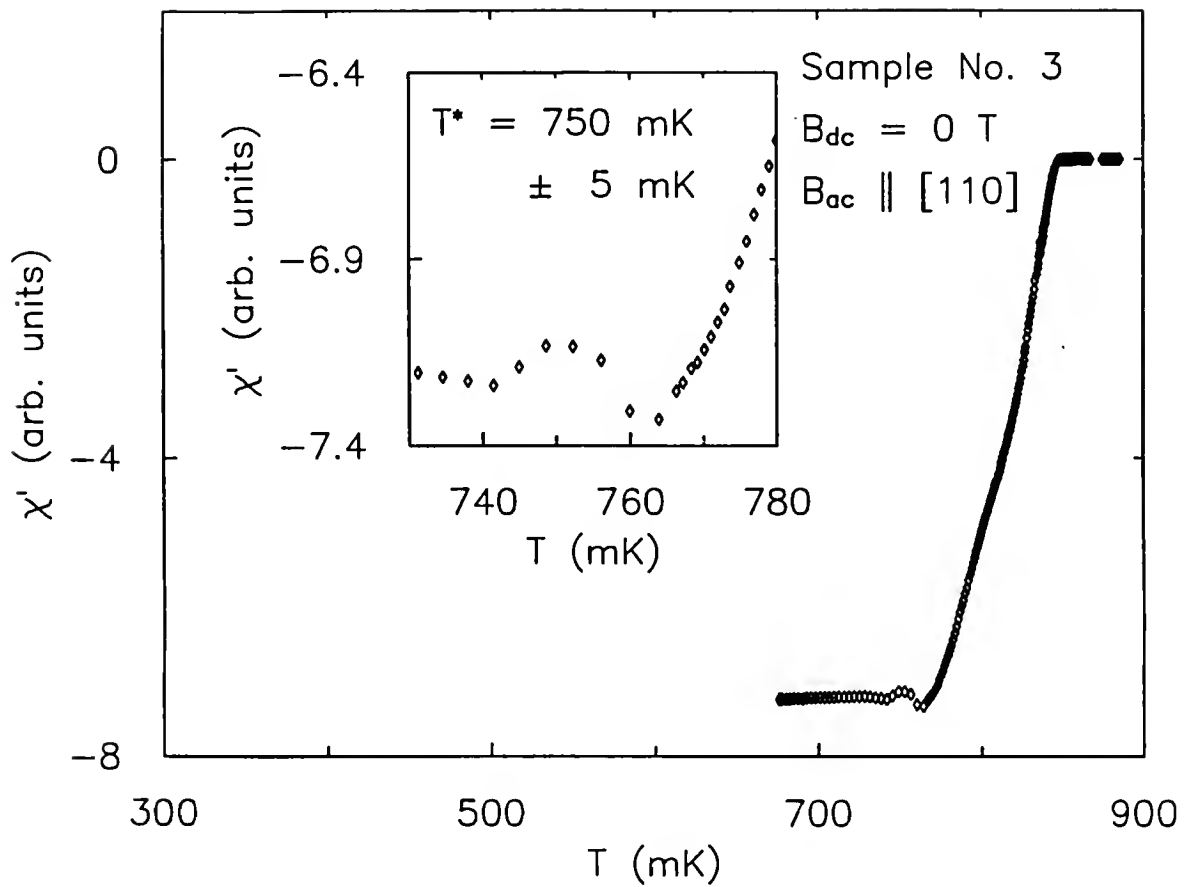


Fig. 5-41. $\chi'(T)$ for sample No. 3 with $B_{dc} = 0 \text{ T}$, $B_{ac} \parallel [110]$. The inset shows the anomaly in $\chi'(T)$ around $T^* = 750 \text{ mK}$.

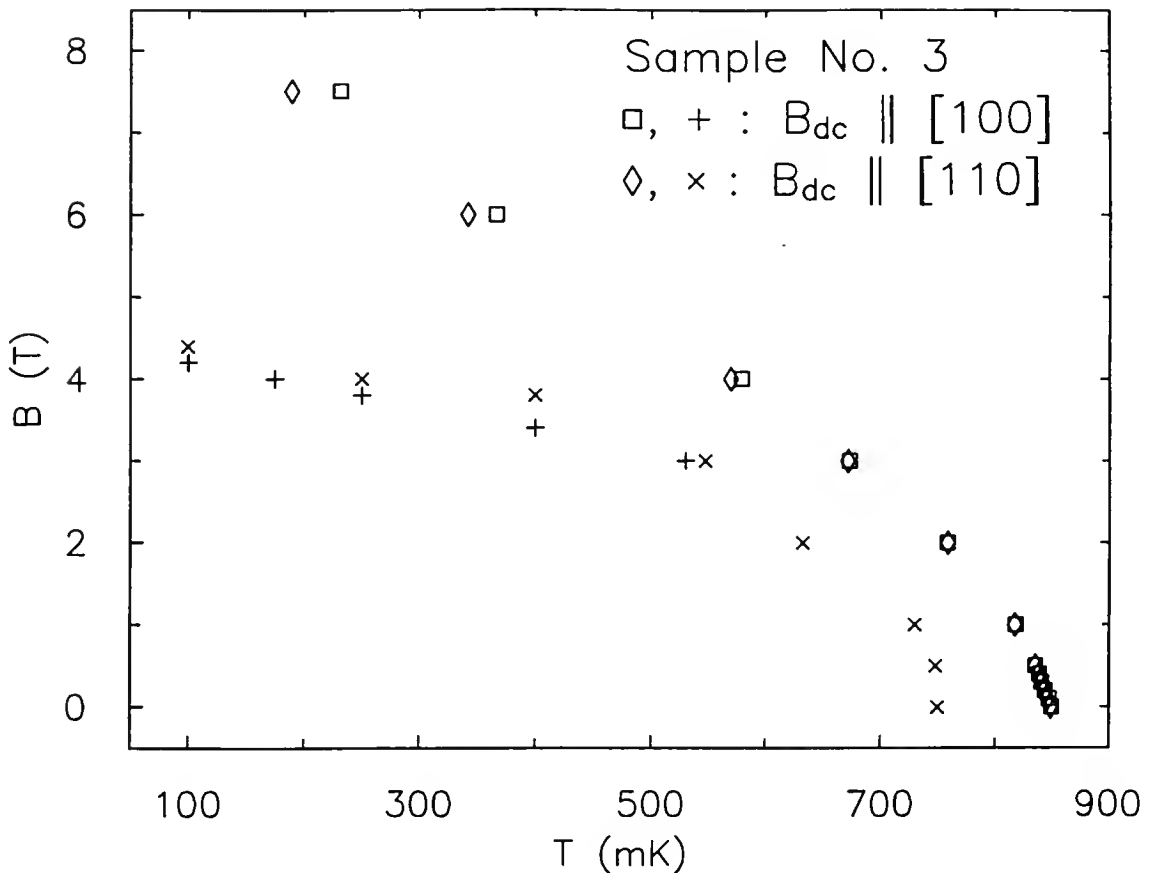


Fig. 5-42. The B-T phase diagram of the anomaly for sample No. 3. The data correspond to: (1) the maxima of the bumps observed in the field sweeps (B^*) from Figs. 5-29 through 5-32 for $B_{dc} \parallel [100]$ (+) and Figs. 5-34 through 5-36 for $B_{dc} \parallel [110]$ (x); and (2) the maxima of the bumps observed in the temperature sweeps (T^*) from Fig. 5-33 for $B_{dc} \parallel [100]$ (+) and Figs. 5-37 through 5-40 for $B_{dc} \parallel [110]$ (x). Also shown, is the upper critical field of sample No. 3 for $B_{dc} \parallel [100]$ (□) and $B_{dc} \parallel [110]$ (◊). The error bars are less than the size of the symbols.

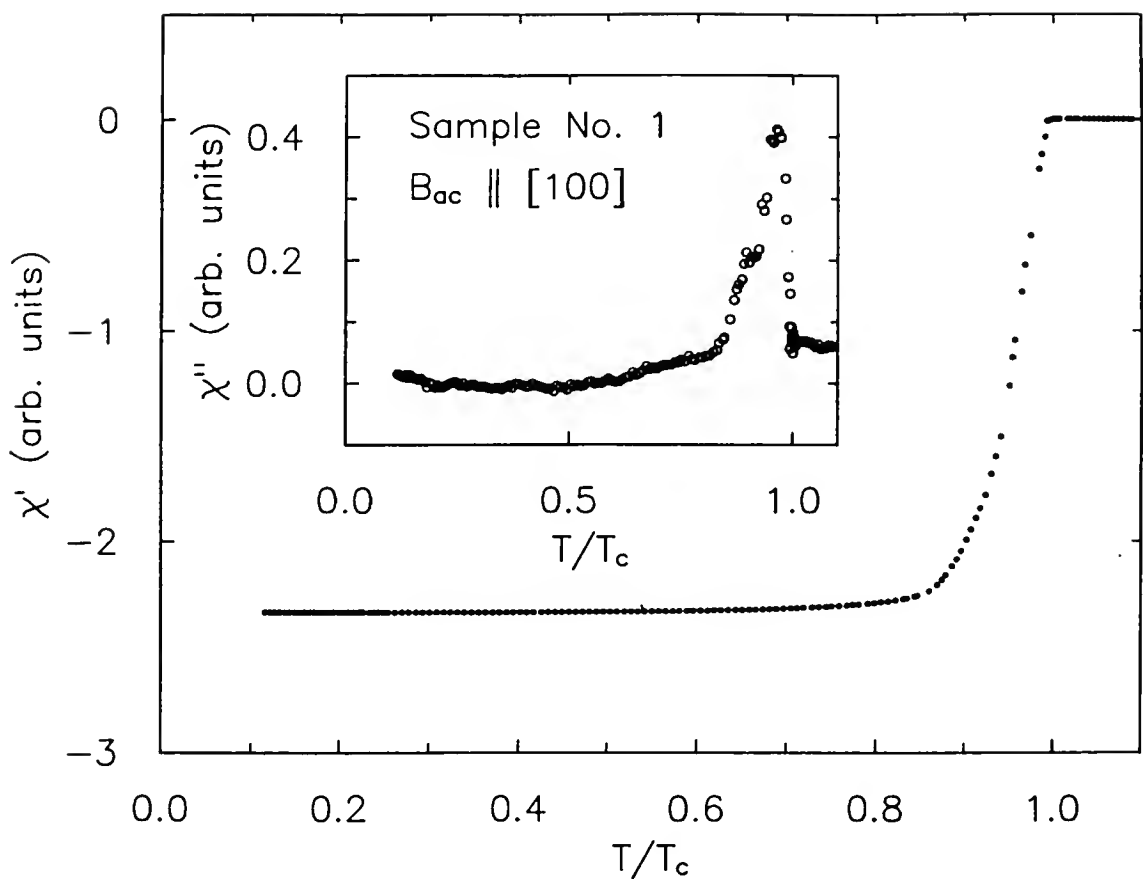


Fig. 5-43. $\chi'(T)$ and $\chi''(T)$ (inset) for sample No. 1 with the probing field parallel to the [100] direction.

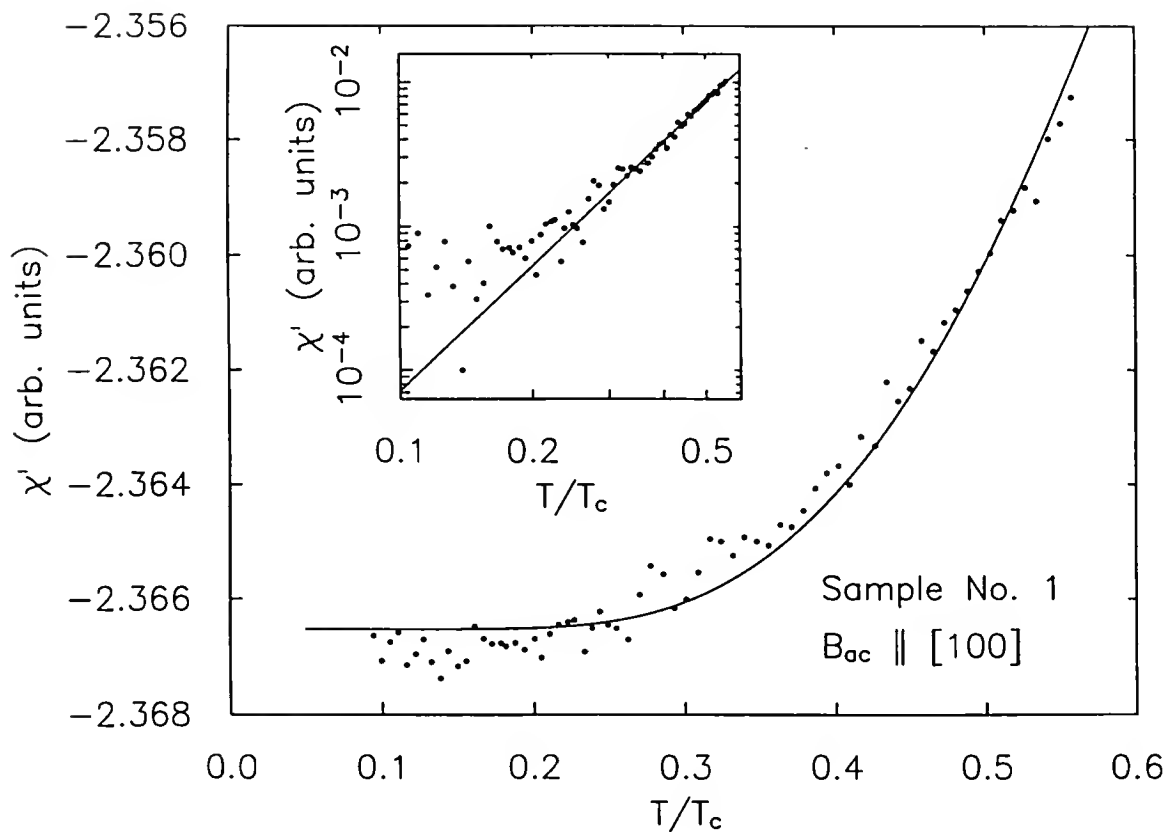


Fig. 5-44. $\chi'(T)$ for sample No. 1 with the probing field parallel to the [100] direction and for $T/T_c < 0.6$. The line corresponds to a fit to the BCS weak coupling theory (see text). The inset shows a log-log plot. The linear fit indicates that the data approximately fall on a straight line of slope 2.9 ± 0.5 .

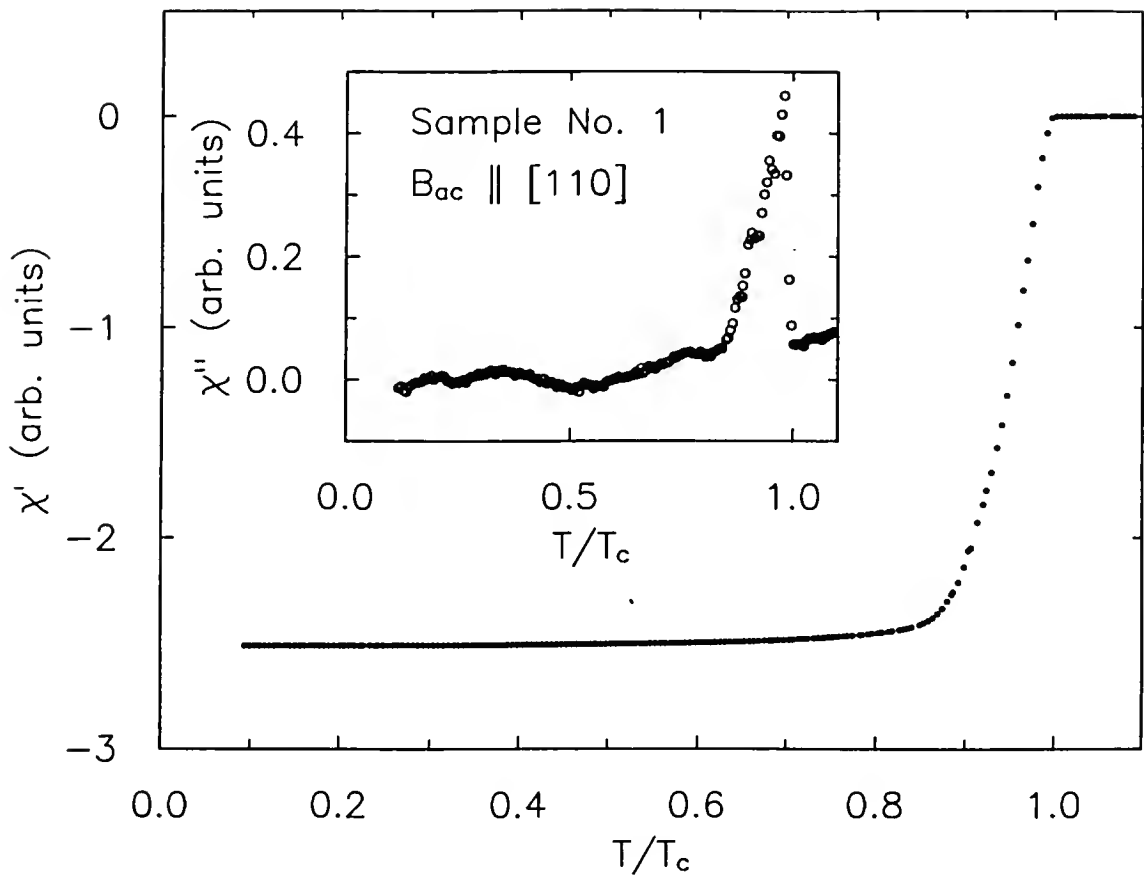


Fig. 5-45. $\chi'(T)$ and $\chi''(T)$ (inset) for sample No. 1 with the probing field parallel to the [110] direction.

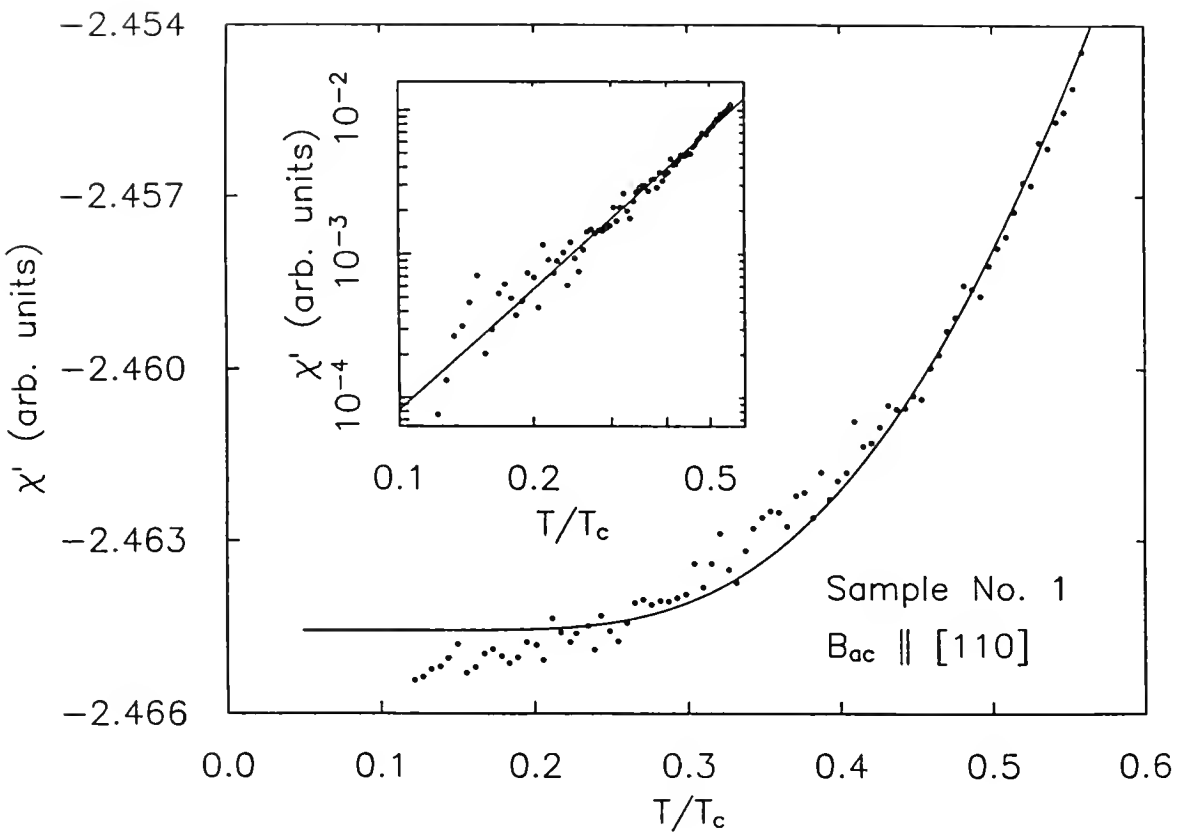


Fig. 5-46. $\chi'(T)$ for sample No. 1 with the probing field parallel to the [110] direction and for $T/T_c < 0.6$. The line corresponds to a fit to the BCS weak coupling theory (see text). The inset shows a log-log plot. The linear fit indicates the data fall on a straight line of slope 2.8 ± 0.2 .

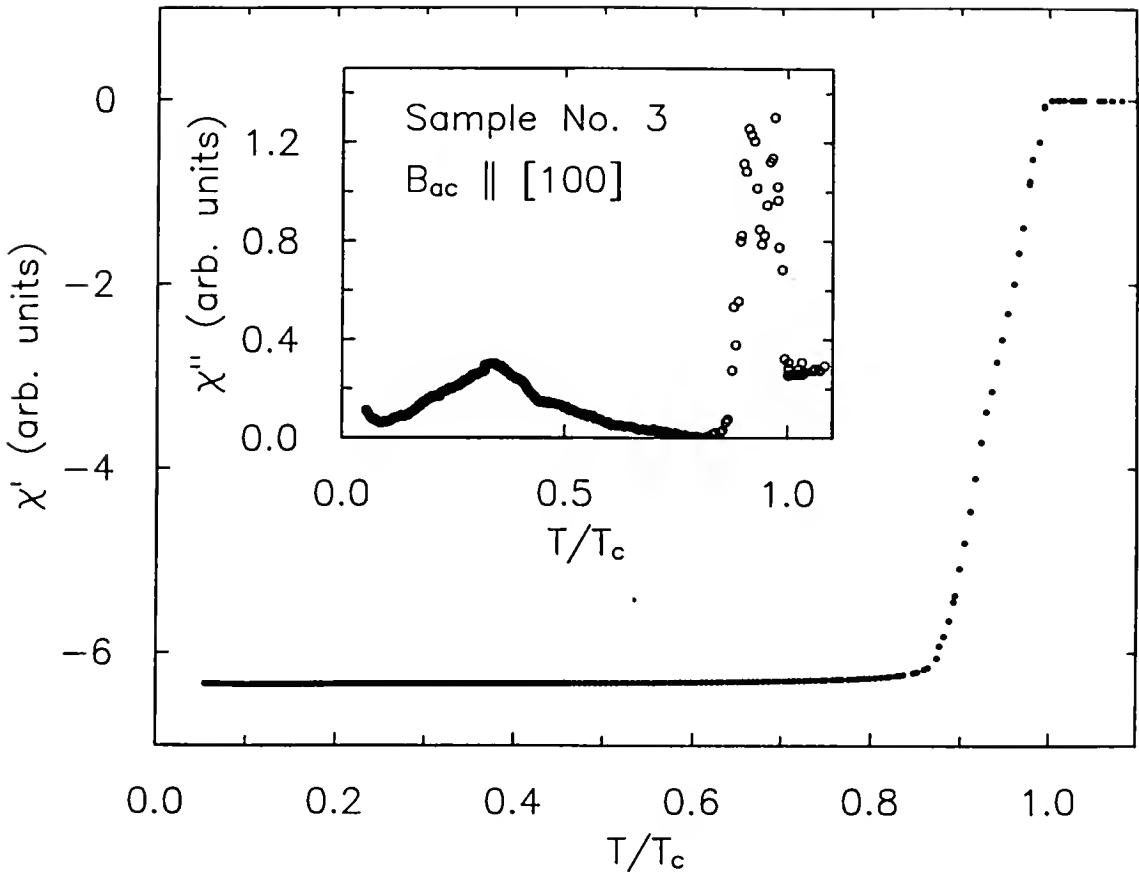


Fig. 5-47. $\chi'(T)$ and $\chi''(T)$ (inset) for sample No. 3 with the probing field parallel to the [100] direction.

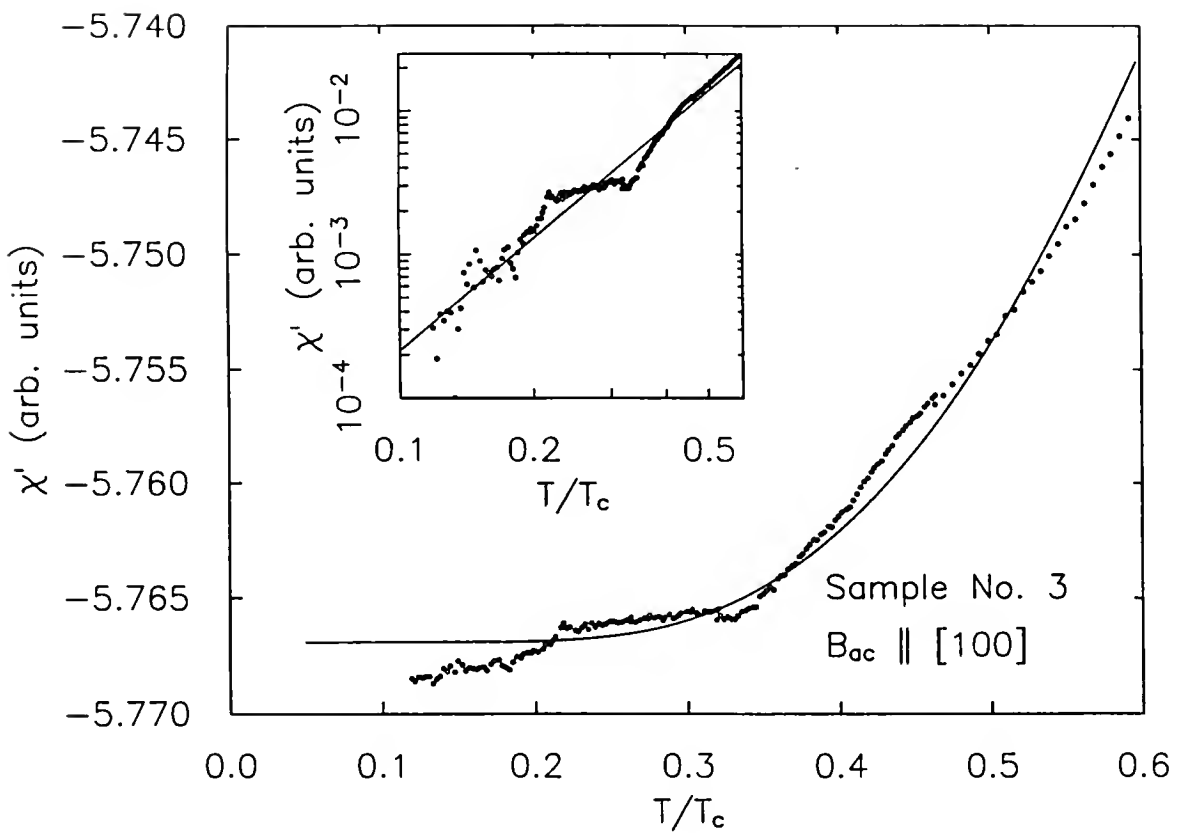


Fig. 5-48. $\chi'(T)$ for sample No. 3 with the probing field parallel to the [100] direction and for $T/T_c < 0.6$. The line corresponds to a fit to the BCS weak coupling theory (see text). The inset shows a log-log plot. The linear fit indicates the data fall on a straight line of slope 2.6 ± 0.2 .

Figures 5-43, 5-45 and 5-47 show $\chi'(T)$ and $\chi''(T)$ for the entire temperature range studied, while Figs. 5-44, 5-46 and 5-48 show the data for $T/T_C \leq 0.6$. For these low temperature traces, the data for the reactive response ($\chi'(T)$) is fitted to $\lambda(T)$ given by the weak coupling BCS theory (Appendix B). We note that the results of the fits are insensitive to the value of the specific heat jump at the transition temperature, $(\Delta C/C_n)_{T_C}$, for $1 \leq (\Delta C/C_n)_{T_C} \leq 2$. It was shown in Section 3.2.2 that when $\chi''(T) = 0$, then $\chi'(T) \sim \lambda(T)$. The insets of Figs. 5-44, 5-46 and 5-48 show log-log plots of the data. Linear fits indicate that the temperature dependences of samples No. 1 (both orientations) and No. 3 are close to T^η , $2.5 < \eta < 3$. This is not surprising since the exponential temperature dependence predicted by the BCS theory is very close to T^3 for $T/T_C > 0.1$. This point was already made in Chapter 4 (Fig. 4-1). A T^3 temperature dependence is also consistent with the presence of line nodes in the energy gap structure (Gross *et al.* 1986). However, within this interpretation, some anisotropy is expected, in contrast to the T^η , $\eta \approx 3$, dependence observed for sample No. 1 for the probing ac magnetic field parallel to the [100] and [110] directions. It is, therefore, not clear from our results on the temperature dependence of $\lambda(T)$ whether UBe₁₃ is a conventional or unconventional superconductor.

5.5 Discussion

In this section, the main results presented above are discussed. First, the isotropic results on $B_{C2}(T)$ in the limit $T/T_C \rightarrow 1$ for our three samples (Figs. 5-24 through 5-26) are discussed, along with arguments explaining the discrepancy between these results and those reported by Aliev *et al.* (1991) (see Fig. 5-3). Second, the anomaly below $B_{C2}(T)$, observed for sample No. 3 (Figs. 5-29 through 5-42) is analyzed. Third, the temperature dependence of $\lambda(T)$ obtained from our $\chi'(T)$ in zero field is considered.

5.5.1 Isotropic $B_{c2}(T)$ in the limit $T/T_c \rightarrow 1$

An important result from our measurements is the fact that, within our experimental uncertainties, the upper critical field is isotropic in the limit $T/T_c \rightarrow 1$. As mentioned earlier in this chapter, Gor'kov (1987) has discussed the presence of anisotropy in $B_{c2}(T)$ in the low field regime for unconventional superconductors. Our results do not, however, rule out unconventional superconductivity in UBe₁₃. First, it is possible that the anisotropy exists, but cannot be observed with our experimental sensitivity. For instance, if the anisotropy is less than 0.5 mK at 0.5 T, our measurements would not detect it. Second, some unconventional superconducting state may give an isotropic $B_{c2}(T)$, as was mentioned by Burlachkov (1985).

From the values of the slope of $B_{c2}(T)$ in the limit $T/T_c \rightarrow 1$, and following the procedure outlined by Maple *et al.* (1985), for weak coupling superconductors in the dirty limit, one can estimate the coherence length, ξ , of UBe₁₃. Using the value of $dB_{c2}(T)/dT = -32.8 \pm 0.5$ T/K found for sample No. 1, we estimate $\xi \approx 156 \pm 5$ Å. From the slopes of $B_{c2}(T)$ for sample No. 2 (-25.5 ± 0.5 T/K) and sample No. 3 (-34.5 ± 0.5 T/K), we estimate $\xi \approx 227 \pm 5$ Å and $\xi \approx 148 \pm 5$ Å, respectively. These values are in agreement with the one reported by Maple *et al.* (142 Å), with the exception of the result from sample No. 2.

We now discuss the discrepancy between our results (isotropic $B_{c2}(T)$ in the limit $T/T_c \rightarrow 1$) and the ones reported by Aliev *et al.* (1991), (Fig. 5-3). There exist several possible explanations for this discrepancy. First, our three samples were annealed, while the specimens that Aliev *et al.* measured were not. It is possible that an anisotropic distribution of impurities give rise to an anisotropic $B_{c2}(T)$. This assertion could be checked by annealing the crystals studied by Aliev *et al.* and remeasuring the upper critical field.

Second, since Aliev *et al.* identified $T_c(B)$ from resistive transitions, it is possible that the anisotropy of the magnetoresistance of UBe₁₃ played a role in their determination

of the upper critical field. In fact, Alekseevskii *et al.* (1986) reported anisotropic magnetoresistance results, for field greater than 4 T and around 2 K. To our knowledge, a careful study of the anisotropy of the magnetoresistance near T_c , and at low field, has not been reported.

A third possible explanation is related to the well known phenomenon of flux flow resistance in type II superconductors (Tinkham, 1976). As a current, I , (this is the current used to measure resistivity), flows through a type II superconductor placed in a magnetic field, B_{dc} , ($B_{dc} > B_{c1}$), the flux lines experience a Lorentz force

$$\mathbf{F} = I \times \frac{1}{c} \mathbf{B}_{dc}, \quad (5.5)$$

where c is the speed of light. Due to this force, the flux lines will tend to move transverse to the currents. This flux flow occurs if the thermal energy overcomes the pinning energy of the vortices. As the flux lines move across the sample with velocity v , they induce an electric field parallel to I , given by

$$\mathbf{E} = \mathbf{B} \times \frac{\mathbf{v}}{c}, \quad (5.6)$$

which acts like a resistive voltage. In type II superconductors, because the pinning energy is rather low, flux flow resistance is observable even at temperatures significantly below the critical temperature. This effect is of particular importance in high temperature superconductors. In fact, Tinkham (1988) showed how the shape of the resistive transitions in these materials depended on the strength of the pinning energy relative to thermal energy. It is clear that anisotropy in the pinning energy of the vortices will cause an anisotropy in the shapes of the resistive transitions. Such pinning energy anisotropy is likely to be present in single crystals, where dislocation and microcracks are more likely to

form along specific crystal directions. If the shape of the resistive transition changes with the orientation of the field, then the $T_c(B)$ determined by the midpoint of the resistive transitions are likely to reflect the anisotropy of the pinning energy. For this reason, it is preferable to determine $T_c(B)$ as the *onset* of the resistive transition.

The fourth possible explanation for understanding the anisotropic results of Aliev *et al.* is related to the demagnetization factor, and (again) to the fact that the midpoint of the transition was chosen to identify $T_c(B)$. The demagnetization factor, D , is a property of a magnetic sample, depending on the shape of the specimen, and the orientation of the magnetic field relative to it. In what follows, we have to differentiate between the magnetic field strength, H (in A/m), and the magnetic field induction, B (in T), related by $B = \mu H$, where μ is the magnetic permeability of the material. The demagnetization factor can be expressed in terms of the applied field strength, H_0 , the field strength inside the sample (or the field strength that the sample experiences as a whole), H_i , and the magnetization of the sample, M , by the expression

$$H_i = H_0 - D M . \quad (5.7)$$

The magnetization of the sample, M , is related to H_i and B_i (the magnetic induction inside the sample) by the usual relation

$$M = \frac{1}{\mu} B_i - H_i . \quad (5.8)$$

We know that for a superconductor exhibiting a perfect Meissner effect, $B_i \approx 0$, so that Eq. (5.8) becomes

$$H_i = \frac{H_0}{(1-D)} . \quad (5.9)$$

Equation (5.10) indicates that, if the demagnetization factor of a superconducting sample is non-zero ($D = 0$ corresponds to an infinite cylinder in a longitudinal field), then the magnetic field strength that the sample experiences is greater than the applied field strength. Consequently, if one ignores the demagnetization effect while measuring the critical field of a superconductor, one underestimates the true value of $B_{c2}(T)$. Furthermore, since D depends on the orientation of the applied field with respect to the sample, measuring $B_{c2}(T)$ while ignoring the effects of D will yield an anisotropic $B_{c2}(T)$. However, it is important to keep in mind that this effect is present for a sample exhibiting a complete Meissner effect. For a type II superconductor, in fields above B_{c1} , a complete Meissner effect is not fully achieved. In fact, M drops to zero at the onset of the transition, so that the demagnetization factor does not play a role in our measurements, and the field experienced by the sample is equal to the applied field. Again, we see the importance of using the onset of the transition as the criterion for $T_c(B)$. On the other hand, at the midpoint of the transition (used by Aliev *et al.* as their criterion for $T_c(B)$) M is finite, and the demagnetization effect introduces an anisotropy in $B_{c2}(T)$ if it is ignored in the analysis of the data.

This scenario is illustrated in Fig. 5-49 for a fictitious superconductor, and for a sample with $D = 0.2$ for one orientation of the applied field, and $D = 0.3$ for a second orientation of the applied field. This example demonstrates how demagnetization factors can affect the determination of $B_{c2}(T)$. The demagnetization factors of the samples used by Aliev *et al.* were not reported. However, they mentioned that their specimens were cubic in shape. In addition, we estimate for our cube-shaped samples that $D \approx 0.2$ for $\mathbf{B}_{dc} \parallel [100]$ and $D \approx 0.3$ for $\mathbf{B}_{dc} \parallel [110]$, so that our choice of demagnetization factors for our example (Fig. 5-49) is justified. From Fig. 5-49, it is clear that an anisotropic $B_{c2}(T)$ can be measured if the demagnetization factors are ignored, even if the actual $B_{c2}(T)$ is isotropic.

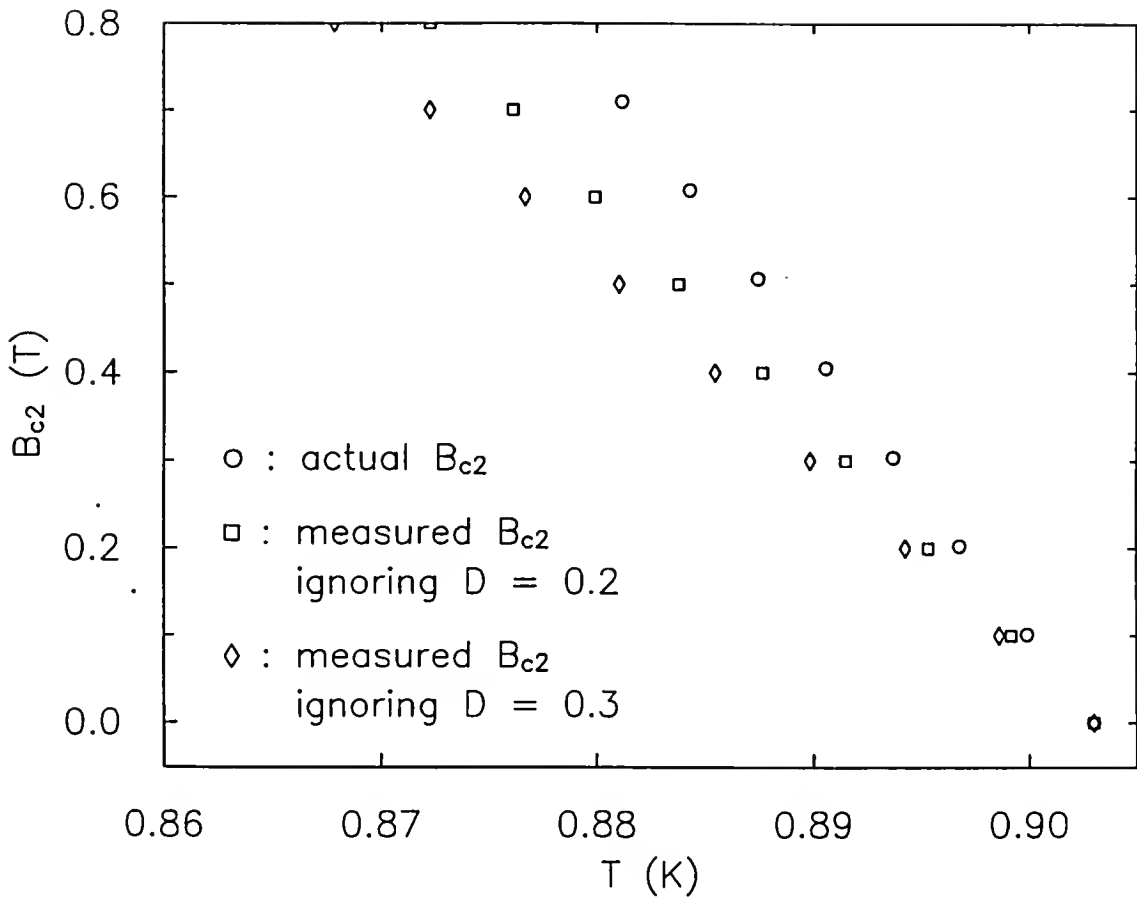


Fig. 5-49. $B_{c2}(T)$ for a fictitious superconductor (\circ). $B_{c2}(T)$ measured while ignoring a demagnetization factor $D = 0.2$ (\square) and assuming a complete Meissner effect. $B_{c2}(T)$ measured while ignoring $D = 0.3$ (\diamond) and assuming a complete Meissner effect. This example demonstrates how ignoring the demagnetization factors can introduce an anisotropy in the determination of $B_{c2}(T)$.

In their publication, Aliev *et al.* do not mention any effort to take into account this demagnetization effect. It is therefore possible that their data reflects the anisotropy of the demagnetization factor of their sample.

The last two arguments, given above to explain the anisotropic results of Aliev *et al.*, could be checked by reanalyzing their data, using the onset of the resistive transitions as the criterion for $T_c(B)$. Unfortunately, this analysis cannot be done from their publication. The motivation for choosing the midpoint of the resistive transition is that one can achieve a greater precision compared to the $T_c(B)$ obtained from the onset of the transition. However, the disadvantage of this method, as was argued above, is the lack of accuracy. To conclude this subsection, we emphasize that, when constructing B-T phase diagrams, one should determine $T_c(B)$ as the onset of the transitions.

5.5.2 Anomaly in Sample No. 3

The phase diagram for sample No. 3 presented in Fig. 5-48 indicates the presence of a second transition line within the superconducting state. This second transition line was constructed by following the dependence of an anomaly in $\chi'(B)$ and $\chi'(T)$ as a function of temperature and field, (Figs. 5-35 through 5-47). In addition, a comparison, of our measurements for fields parallel to the [100] orientation with the data for fields parallel to the [110] orientation, suggests that the anomaly is more pronounced in the latter direction. We now argue that this anomaly is related to a change in the flux line distribution inside the sample, and that it is caused by the large amount of pinning sites present in sample No. 3.

The assertion that flux line pinning plays an important role in sample No. 3 is supported by the fact that this specimen features a reduced transition temperature, along with an enhanced slope of $B_{c2}(T)$ near T_c . This combination is characteristic of type II superconductors possessing numerous pinning sites. The argument is further supported by the SEM pictures of the surface of sample No. 3 (Fig. 5-6), which indicate a large amount

of surface roughness that could provide the pinning cites. More specifically, consider Fig. 5-31, which is a typical sweep of $\chi'(B)$. As the field is slowly increased from zero, the flux lines initially get pinned near the surface, thereby blocking the entrance of additional flux lines inside the bulk of the sample. This initial scenario would explain the much smaller field dependence of $\chi'(B)$, for B_{dc} less than ≈ 5 T, compared to the field dependence observed for samples No. 1 (Fig. 5-33) and No. 2 (Fig. 5-34) in the same field range. As the field is further increased, the flux line density at the surface exceeds $B_{c2}(T)$ locally, and it becomes energetically more favorable for the flux lines to occupy a lattice throughout the bulk of the sample. As the lines unpin, some of them are expelled out of the sample by the Lorentz force, and a dip in $\chi'(B)$ is observed, reflecting the reduced volume occupied by the flux lines. Finally, as the applied field approaches $B_{c2}(T)$, more flux lines penetrate the sample and the transition to the normal state occurs.

Recently, thermal expansion measurements by van Dijk *et al.* (1994) have suggested the presence of a similar flux distribution transition in URu₂Si₂. These authors reported a change in sign of the hysteresis loop occurring below $B_{c2}(T)$. The sign observed at low temperatures and low fields corresponds to flux pinning effects, while the sign for higher field and higher temperature is not clearly understood, although it is most likely related to a change in the flux line distribution. Van Dijk *et al.* also reported some anisotropy associated with their measurements, consistent with our own results which showed that the effect was more pronounced for $\mathbf{B}_{dc} \parallel [110]$ than for $\mathbf{B}_{dc} \parallel [100]$. Within the interpretation given in the previous paragraph, this anisotropy can be understood by the fact that the cross section area of the sample oriented with $\mathbf{B}_{dc} \parallel [110]$ is larger than that for $\mathbf{B}_{dc} \parallel [100]$, so more pinning sites are available and the effect is amplified. Similar changes of sign in the hysteresis loop have also been reported for UBe₁₃ samples by de Visser *et al.* (1992a).

Finally, it is noteworthy to recall that a second transition line within the superconducting state has been reported by Ellman *et al.* (1991) who measured specific

heat on a polycrystalline specimen of UBe_{13} . The phase diagram that they proposed is reproduced in Fig. 5-50, which should be compared to the diagram for sample No. 3 shown in Fig. 5-42. Given our explanation for the additional transition line mapped in Fig. 5-42, we would conclude that it is not related to the one observed by Ellman *et al.*

5.5.3 Temperature Dependence of $\lambda(T)$

Our data of $\chi'(T)$ in zero field (Figs. 5-12, 5-14 and 5-16) suggest that the penetration depth in UBe_{13} follows a power law close to T^3 . Because the exponential temperature dependence predicted from the weak coupling BCS (Eq. 5.5) is very close to a T^3 dependence (see section 4.1, Fig. 4-1), the case for unconventional superconductivity can not be made for UBe_{13} on the basis of these measurements alone. It is interesting to note that our results disagree with previous penetration depth measurements that indicated a T^2 temperature dependence of $\lambda(T)$ (Groß-Alltag *et al.*, 1991). Groß-Alltag *et al.* suggested that their quadratic temperature dependence could be the signature of either a gap having point nodes (axial state) or the presence of impurities in the sample. According to their calculations, a T^3 temperature dependence of $\lambda(T)$ suggests an energy gap with lines of nodes on the Fermi surface. However, within this interpretation, different temperature dependences are expected for different orientations of the magnetic field with respect to the lines of nodes, and, therefore, our T^η , $\eta \approx 3$, results for both $\mathbf{B}_{\text{dc}} \parallel [100]$ and $\mathbf{B}_{\text{dc}} \parallel [110]$ are difficult to explain.

5.6 Conclusions

First, our measurements of the upper critical field indicate that, within our experimental uncertainties of 0.5 mK and 0.5 mT, $B_{\text{c}2}(T)$ is isotropic in the limit $T/T_c \rightarrow 1$. Arguments were given to explain the discrepancy between our results and the ones reported by Aliev *et al.* (1991). In particular, we showed that their criterion of $T_c(B)$ as the midpoint of the resistive transition could introduce some anisotropy in their

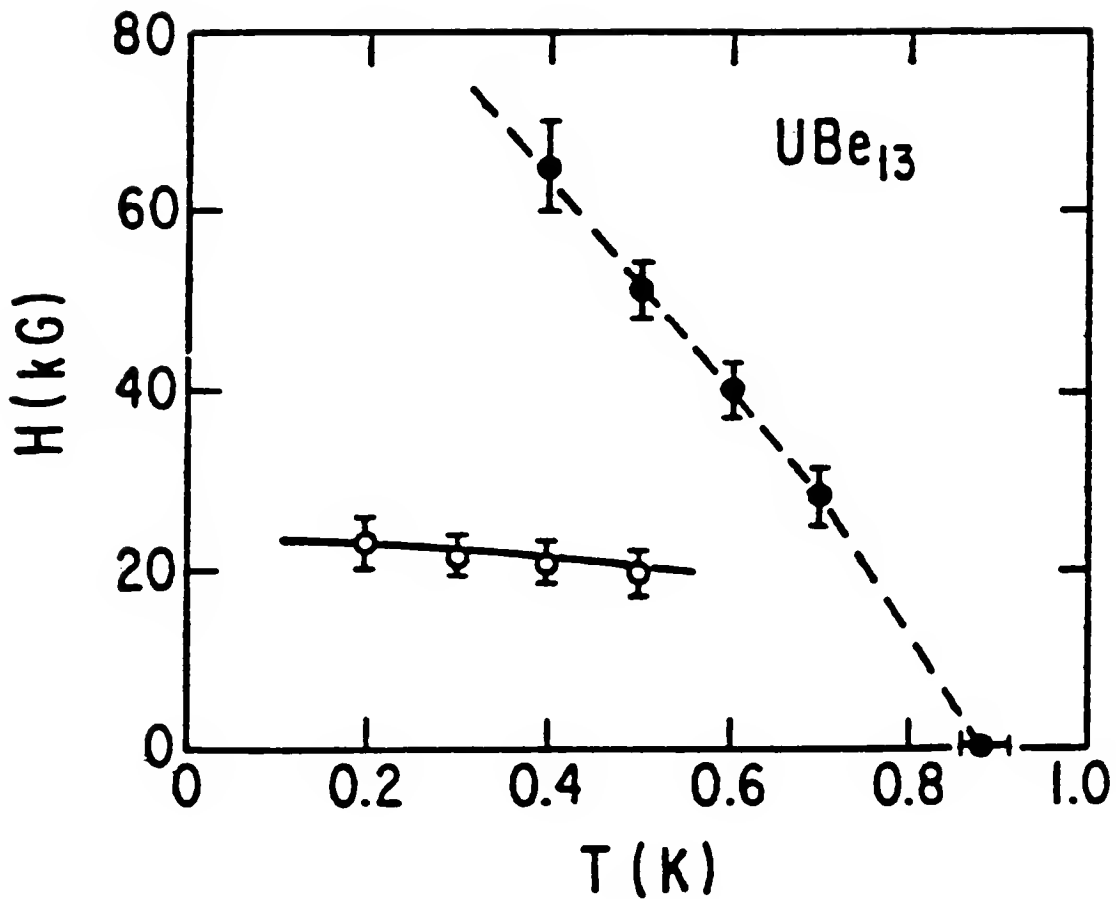


Fig. 5-50. B-T phase diagram proposed by Ellman *et al.* (1991) on a polycrystalline specimen. The closed circles correspond to $B_{\text{c}2}(T)$ as measured from specific heat. The open circles denote the position of the secondary maximum observed in the specific heat. The lines are guides to the eyes.

results, and that using the onset of the transition, as we did, is a better criterion. Consequently, although our results provide constraints on the underlying symmetry of the superconducting order parameter in UBe₁₃, they do not elucidate details about the microscopic picture.

Secondly, we did not observe any signs of second transition within the superconducting state in our highest quality samples (No. 1 and No. 2). Sample No. 3 exhibited an anomaly below $B_{C2}(T)$, and we argued that it was not intrinsic to UBe₁₃ but is related to flux pinning mechanisms, which are expected to play an important role in the mixed state of type II superconductors possessing large numbers of pinning sites.

Finally, the temperature dependence of the penetration depth was found to be close to T^3 for both $\mathbf{B}_{dc} \parallel [110]$ and $\mathbf{B}_{dc} \parallel [100]$. To date, there exists no theoretical work that can explain these results in terms of a superconducting state with an energy gap possessing nodes. On the other hand, because the temperature dependence expected for a BCS superconductor is also close to T^3 for $T/T_c > 0.1$, these measurements alone cannot be taken as evidence for unconventional superconductivity.

CHAPTER 6 CONCLUSIONS

In this chapter, the conclusions drawn from the various experiments described and discussed in Chapters 4 and 5 are reviewed. The first section deals with the work performed on UPt_3 , while the second relates to the UBe_{13} results. In addition, a number of future experimental directions are proposed. These future studies should provide further understanding about the microscopic nature of superconductivity in these two heavy fermion systems.

6.1 UPt₃

Our experimental work on UPt_3 was described in detail in Chapter 4. Earlier experimental work by other groups on this material were reviewed in Section 2.1, while the theoretical aspects of UPt_3 were briefly discussed in subsection 1.2.3.

6.1.1 Conclusions

From our low frequency ac susceptibility measurements, we conclude that the temperature dependence of the penetration depth, $\lambda(T)$, is linear for currents flowing in the a-b plane when $T/T_c \leq 0.5$ (see Figs. 4-11, 4-13, 4-22, 4-23). This result was consistent for all annealed, high quality samples, showing double transitions in the vicinity of T_c . A linear temperature dependence is indicative of a line of nodes in the basal plane of the energy gap structure and is strong evidence for unconventional superconductivity (see section 1.2). Although this result does not, in itself, identify the exact functional form of the order parameter in UPt_3 , it provides an important constraint for the various theoretical models.

A second important conclusion is that the double feature near T_c , observed in our low frequency measurements (Figs. 4-9, 4-11 through 4-14, and 4-21 through 4-23), corresponds to the same double transition observed with bulk measurements such as specific heat, thermal expansion, and sound velocity/attenuation. This assertion is supported, in particular, by the B-T phase diagram constructed from our inductive measurements (Fig. 4-16). This diagram follows the phase diagram constructed by other workers using bulk probes. This conclusion contradicts the statement, often reported, that the double feature observed for UPt_3 in inductive data is an extrinsic property of this material.

The third conclusion is that the temperature dependence of the penetration depth is frequency dependent, even for frequencies two orders of magnitude lower than the energy gap frequency. We believe that this frequency dependence is an intrinsic property of the superconductivity of UPt_3 and reflects its unconventionality.

6.1.2 Future Work

As a continuation of the measurements discussed in this dissertation, one could anneal sample No. 2 (a well characterized, large sample) and remeasure the ac susceptibility, as well as the specific heat. After polishing, one would expect to see a well-defined double feature near T_c for both experiments. More importantly, one might expect to observe a linear temperature dependence of $\lambda(T)$ for $T/T_c \leq 0.5$. In addition, the specific heat data might reveal a change in the upturn already observed in the unannealed sample around 18 mK (Schuberth *et al.*, 1992).

Another extension to our work would be to measure $\lambda(T)$ using probing frequencies between 5 kHz and 5 MHz. This experiment would possibly identify a crossover (or transition) from the low frequency regime probed by our ac susceptibility measurements and the high frequency regime of the tunnel diode oscillator (TDO) data.

In order to probe the gap structure along the c-axis, one could measure $\lambda(T)$ for currents flowing along that axis, i.e. $\lambda_c(T)$. Although Gannon *et al.* (1990) published measurements of $\lambda_c(T)$ from TDO experiments, no low frequency data on $\lambda_c(T)$ has been reported. These measurements would require samples with a long axes parallel to one of the basal plane directions. In order to better understand the origin of the frequency dependence discussed in this work, the $\lambda_c(T)$ measurements should also be performed as a function of the probing frequency.

To measure the energy gap structure of superconductors, a more direct probe, compared to measuring $\lambda(T)$ (or any temperature dependence of thermodynamical properties), is tunnel junction spectroscopy. To date, experiments using this technique have not been reported for UPt₃.

Yip and Sauls (1992) have suggested measurements of the penetration depth as a function of field, $\lambda(B)$. These authors argued that $\lambda(B)$ is strongly dependent on the node structure of the energy gap. For instance, Sauls (1994) considered the E_{2u} state (with a line of nodes in the basal plane, see section 1.2.3) and calculated $\lambda(B)$ for an ellipsoidal Fermi surface. He showed that below a characteristic field, $B_x \approx B_0 (T/T_c)$, where B_0 is the thermodynamical critical field ($B_0 \approx 0.1$ T for UPt₃), $\lambda(B)$ is quadratic, but that above B_x , $\lambda(B)$ is linear up to the lower critical field, B_{c1} (≈ 10 mT for UPt₃). He therefore proposed measurements of $\lambda(B)$ at $T \approx 5$ mK ($T/T_c \approx 0.01$) and suggested that a linear dependence, expected between $B_x \approx 10$ G and B_{c1} , would provide strong evidence for a line of nodes in the basal plane.

In a conventional type II superconductor, the mixed state is characterized by a triangular lattice of flux lines. However, the situation for unconventional superconductors may not be as simple. For example, Tokuyasu *et al.* (1990) investigated vortices in the 2D models (see subsection 1.2.3) for B parallel to the c-axis and found three different possible vortex lattices. For this reason, experiments probing the vortex structure, such as

Scanning Tunneling Microscopy, would provide a strong test for various models of the order parameter.

Finally, more NMR data are needed to unambiguously determine the electron spin susceptibility in the superconducting state. In principle, these experiments should help distinguish between triplet and singlet type pairings (see subsection 2.1.7).

6.2 UBe₁₃

Our experimental work on UBe₁₃ was described in detail in Chapter 5. Earlier experimental work by other groups on this material were reviewed in Section 2.2.

6.2.1 Conclusions

Firstlly, our measurements of the upper critical field indicate that, within our experimental uncertainties of 0.5 mK and 0.5 mT, $B_{c2}(T)$ is isotropic in the limit $T/T_c \rightarrow 1$ (Figs. 5-30 through 5-32). Arguments have been given previously to explain the discrepancy between our results and those reported by Aliev *et al.* (1991). In particular, we showed that their criterion of $T_c(B)$ as the midpoint of the resistive transition could introduce some anisotropy in their results, and that using the onset of the transition, as we did, is a better criterion.

Secondly, we did not observe any sign of a second transition within the superconducting state in our highest quality samples (No. 1 and No. 2). Sample No. 3 exhibited an anomaly below $B_{c2}(T)$, and we argued that it was not intrinsic to UBe₁₃, but related to flux pinning mechanisms, which are expected to play an important role in the mixed state of type II superconductors possessing large numbers of pinning sites.

Finally, the temperature dependence of the penetration depth was found to be close to T^3 for $\mathbf{B}_{ac} \parallel [100]$ and $\mathbf{B}_{ac} \parallel [110]$. Because the temperature dependence expected for a BCS superconductor is also close to T^3 for $T/T_c > 0.1$, these measurements cannot be taken as evidence for unconventional superconductivity.

6.2.2 Future Work

As a direct continuation to our work, one could polish sample No. 3, then measure $\chi'(B)$, for example at $T = 100$ mK (Fig. 5-40), and check if the anomaly below $B_{c2}(T)$ is still observable. If our assertion that this anomaly is related to flux pinning on defects located on the rough surface of this sample (Fig. 5-6) is correct, then the anomaly should disappear after polishing.

Because the BCS exponential behavior of $\lambda(T)$ is especially distinct at the lowest temperatures, experiments of $\lambda(T)$ below $T/T_c < 0.1$ would help distinguish between this conventional behavior and an unconventional power law dependence. Measuring specific heat at lower temperatures ($T/T_c < 0.1$) would also provide a larger temperature range to extract the temperature dependence. To date, the published data for these measurements for UBe₁₃ are limited to $T/T_c \geq 0.1$ and are sample dependent. Systematic specific heat measurement at lower temperatures might also clear up an issue about an additional transition observed below the superconducting one by several groups (see subsection 2.2.2).

As mentioned in subsection 6.1.2 for UPt₃, tunnel junction spectroscopy provides a direct probe for the energy gap structure. To date, experiments using this technique on UBe₁₃ have not given any conclusive results on the gap structure. In addition, the field dependence of the penetration depth, as discussed in subsection 6.1.2 for UPt₃, would also give information about the gap structure in UBe₁₃.

The anisotropy of the upper critical field in the high field region could also be of interest. This experiment would be difficult to analyze because it requires an understanding of Fermi surface anisotropy effects. However, probing the Pauli limiting effects in UBe₁₃ could help distinguish between singlet and triplet pairing.

APPENDIX A CITED MANUFACTURES

Cryogenics Associates, no longer exists, old address (as of 1981) : 6565 Coffman Road, Indianapolis, Indiana 45268.

Dale Electronics Inc., P. O. Box 74, Norfolk, Nebraska 68701. Tel : (402) 371 0080.
Fax : (402) 644 4206.

Du Pont de Nemours & Co., Du Pont Polymers, Pencader Plant, Wilimington, DE 19898.
Fax : (302) 773 3128

Edwards High Vacuum Inc., 3279 Grand Island, N. Y. 14072.

EG & G Brookdeal Electronics Princeton Applied Research, P. O. Box 2565, Princeton, NJ 08540. Tel : (609) 452 2111.

Germanium Power Devices, P.O. Box 3065, 300 Brickstone Square, Shawsheen Village Station, Andover, MA 01180-0865.

Hewlett-Packard Company, 2015 South Park Place, Atlanta, GA 30339. Tel : (404) 955 1500.

LakeShore Cryotronics, Inc., 64 E. Walnut Street, Westerville, OH 43081. Tel : (614) 891 2243. Fax : (614) 891 2243. Fax : (614) 891 1392.

Linear Research Inc., 5231 Cushman Place, Suite 21, San Diego, CA 92110-3910. Tel : (619) 299 0719. Fax : (619) 299 0129.

McMaster-Carr Supply Co., P. O. Box 740100, Atlanta GA 30374-0100. Tel : (404) 346 7000. Fax : (404) 349 9091

Morton Thiokol Inc., 152 Andover St., Danvers, MA 01923.

Newport Research Corp., 18235 Mt. Baldy Circle, Fountain Valley, CA 92708. Tel : (714) 962 7701.

Niomax Superconductors, P. O. Box 704, Witton, Birmingham B6 7UR, Great Britain.

Stanford Research Systems Inc., 1290 D Reamwood Av., Sunnyvale, CA 94089. Tel : (408) 744 9040. Fax : (408) 744 9049.

Tron-Tech, 63 Shark River Rd., Neptune NJ 07753. Tel : (201) 922 8585.

Varian Vacuum Products, 121 Hartwell Av. Lexington, MA 02173-9857. Tel : 1 (800) 882 7426; Fax : (617) 860 5405.

APPENDIX B OUTLINE OF A NUMERICAL CALCULATION OF $\lambda(T)$

The following equations were used in the numerical calculation of the penetration depth, $\lambda(T)$, within the BCS weak coupling-local limit. In this appendix, T stands for the reduced temperature, *i.e.* $T = T(\text{Kelvin})/T_c(\text{Kelvin})$.

$$\lambda(T) = \left(\frac{c}{4\pi} \right)^{1/2} [-K(0,0,T)]^{-1/2}, \quad (\text{B.1})$$

where c is the speed of light and $K(0,0,T)$ is the electromagnetic kernel, $K(\omega, q, T)$, given by the expression (Tinkham, 1976)

$$K(0,0,T) = - \frac{e^2}{mc} 2\pi T \sum_{n=0}^{\infty} \frac{\Delta^2(T)}{\omega_n^2(T) + \Delta^2(T)^{3/2}}, \quad (\text{B.2})$$

where $\Delta(T)$ is the energy gap given by Eq. (4.9), and $\omega_n(T)$ are the Matsubara fermion frequencies given by

$$\omega_n = 2\pi \left(n + \frac{1}{2} \right) T. \quad (\text{B.3})$$

We note that in Eq. (4.9), the weak coupling value for the jump in the specific heat at T_c was used, *i.e.* $(\Delta C/C_n)_{T_c} = 1.43$. Other values may be used to match experimental results for various materials.

With a short computer program, these expressions can be used to calculate $\lambda(T)$ for $0 \leq T \leq 1$. The summation quickly converges so that a low value of n (typically $n < 1000$) gives a good approximation.

REFERENCES

Abrikosov, A. A., Soviet Phys. JETP **5**, 1174 (1957).

Achkir, D., M. Poirier, D. A. Bonn, Ruixing Lang, and W. N. Hardy, Phys. Rev. B **48**, 13184 (1993).

Adenwalla, S., S. W. Lin, Q. Z. Ran, Z. Zhao, J. B. Ketterson, J. A. Sauls, L. Taillefer, D. J. Hinks, M. Levy, and Bimal K. Sarma, Phys. Rev. Lett. **65**, 2298 (1990).

Aeppli, G., D. Bishop, C. Broholm, E. Bucher, K. Siemensmeyer, M. Steiner, and N. Stüsser, Phys. Rev. Lett. **63**, 676 (1989).

Aeppli, G., E. Bucher, C. Broholm, J. K. Kjems, J. Baumann, and J. Hufnagl, Phys. Rev. Lett. **60**, 615 (1988).

Alekseevskii, N. E., V. I. Nizhankovskii, V. N. Narozhnyi, E. P. Khlybov, and A. V. Mitin, J. Low Temp. Phys. **64**, 87 (1986).

Aliev, F. G., V. Kovachik, V. V. Moshchalkov, V. V. Pryadun, N. E. Alekseevskii, A. V. Mitin, N. Agrait, S. Vieira, and R. Villar, J. Low Temp. Phys. **85**, 359 (1991).

Aronson, M. C., R. Clarke, B. G. Demczyk, B. R. Coles, J. S. Smith, A. de Visser, T. Vorenkamp, and J. J. M. Franse, Physica B **186-188**, 788 (1993).

Aronson, M. C., T. Vorenkamp, Z. Koziol, K. Bakker, A. de Visser, and J. J. M. Franse, J. Appl. Phys. **69**, 5487 (1991).

Ashcroft, N. W., and N. D. Mermin, Solid State Physics (Saunders, Philadelphia, 1976).

Baenziger, N. C., and R. E. Rundle, Acta. Cryst. **2**, 258 (1949).

Bakker, K., A. de Visser, and J. J. M. Franse, J. Mag. Mag. Mater. **108**, 65 (1992).

Batlogg, B., D. Bishop, B. Golding, C. M. Varma, Z. Fisk, J. L. Smith, and H. R. Ott, Phys. Rev. Lett. **55**, 1319 (1985).

Behnia K., D. Jaccard, L. Taillefer, J. Flouquet, and K. Maki, J. Magn. Magn. Mater., **108**, 133 (1992).

Behnia, K., L. Taillefer, and J. Flouquet, *J. Appl. Phys.* **67**, 5200 (1990).

Behnia, K., L. Taillerfer, J. Flouquet, D. Jaccard, K. Maki, and Z. Fisk, *J. Low Temp. Phys.* **84**, 261 (1991).

Behroozi, F., M. P. Garfunkel, F. H. Rogan, and G. A. Wilkinson, *Phys. Rev. B* **10**, 2756 (1974).

Bertman, B., and M. Strongin, *Phys. Rev.* **147**, 268 (1966).

Betts, D. S., *Refrigeration and Thermometry below One Kelvin* (Sussex University Press, Sussex, 1976).

Beuers, Z. Fisk, and J. L. Smith, *Z. Phys. B* **64**, 175 (1986).

Bishop, D. J., C. M. Varma, B. Batlogg, E. Bucher, Z. Fisk, and J. L. Smith, *Phys. Rev. Lett.* **53**, 1009 (1984).

Blount, E., C. Varma, and G. E. Aeppli, *Phys. Rev. Lett.* **64**, 3074 (1990).

Blonder, G. E., M. Tinkham, and T. M. Klapwijk, *Phys. Rev. B* **25**, 4515 (1982).

Bogenberger, B., H. v. Löhneysen, T. Trappmann, and L. Taillefer, *Physica B* **186-188**, 248 (1993).

Boukhny, M., G. L. Bullock, and B. S. Shivaram, *Phys. Rev. B* **50**, 8985 (1994).

Brandt, E. H., *Phys. Rev. Lett.* **67**, 2219 (1991).

Brison, J. P., J. Flouquet, and G. Deutscher, *J. Low Temp. Phys.* **76**, 453 (1989).

Brison, J. P., J. C. Lasjaunias, A. Ravex, and J. Flouquet, *Physica C* **153-155**, 437 (1988a).

Brison, J. P., A. Ravex, J. Flouquet, Z. Fisk, and J. L. Smith, *J. Magn. Magn. Mater.* **76-77**, 525 (1988b).

Britton, C. V., Ph.D. Dissertation, University of Florida (1977).

Brodale, G. E., R. A. Fisher, Norman E. Philipps, G. R. Stewart, and A. L. Giorgi, *Phys. Rev. Lett.* **57**, 234 (1986).

Broholm, C., G. Aeppli, R. N. Kleiman, D. R. Harshman, D. J. Bishop, E. Bucher, D. L. Williams, E. J. Ansaldo, and R. H. Heffner, *Phys. Rev. Lett.* **65**, 2062 (1990).

Broholm, C., J. K. Kjems, W. J. L. Buyers, P. Mathews, T. T. M. Palstra, A. A. Menovsky, and J. A. Mydosh, Phys. Rev. Lett. **58**, 1467 (1987).

Brown, S. E., H. Li, M. W. Meisel, J. L. Smith, A. L. Giorgi, and J. D. Thompson, Physica B **165&166**, 377 (1990).

Bruls, G., D. Weber, B. Wolf, P. Thalmeier, B. Lüthi, A. de Visser, and A. Menovsky, Phys. Rev. Lett. **65**, 2294 (1990).

Bucher, E., J. P. Maita, G. W. Hull, R. C. Fulton, and A. S. Cooper, Phys. Rev. B **11**, 440 (1975).

Burlachkov, L. I., Sov. Phys. JETP **62**, 800 (1985).

Butler, W. H., Phys. Rev. Lett. **44**, 1516 (1980).

Chen, D., and A. Garg, Phys. Rev. Lett. **70**, 1689 (1993).

Chen, J. W., S. E. Lambert, M. B. Maple, Z. Fisk, J. L. Smith, G. R. Stewart, and J. O. Willis, Phys. Rev. B **30**, 1583 (1984).

Chen, J. W., S. E. Lambert, M. B. Maple, M. J. Naughton, J. S. Brooks, Z. Fisk, J. L. Smith, and H. R. Ott, J. Appl. Phys. **57**, 3076 (1985).

Choi, C. H., and J. A. Sauls, Phys. Rev. Lett. **66**, 484, (1991).

Chow, W. F., Principles of Tunnel Diode Circuits (J. Wiley & Sons, New York, 1964).

Clayhold, J. A., and H. R. Ott, Bull. Am. Phys. Soc. **38**, 80 (1993).

Clogston, A. M., Phys. Rev. Lett. **9**, 266 (1962).

Decroux, M., and O. Fisher, in Superconductivity in Ternary Compounds II (Springer-Verlag, Berlin Heidelberg, 1982).

de Gennes, P. G., Phys. Kondensierten Materie **3**, 79 (1964).

de Visser, A., J. J. M. Franse, A. Menovsky, and T. T. M. Palstra, Physics B **127**, 442 (1984).

de Visser, A., A. Menovsky, and J. J. M. Franse, J. Magn. Magn. Mater. **63&64**, 365 (1987a).

de Visser, A., A. Menovsky, and J. J. M. Franse, Physica B **147**, 81 (1987b).

de Visser, A., A. A. Menovsky, J. J. M. Franse, K. Hasselbach, A. Lacerda, L. Taillefer, P. Haen, and J. Flouquet, Phys. Rev. B **41**, 7304 (1990).

de Visser, A., N. H. van Dijk, K. Bakker, and J. J. M. Franse, Physica B **186-188**, 212 (1993).

de Visser, A., N. H. van Dijk, K. Bakker, J. J. M. Franse, A. Lacerda, J. Flouquet, Z. Fisk, and J. L. Smith, Phys. Rev. B **45**, 2962 (1992a).

de Visser, A., N. H. van Dijk, J. J. M. Franse, A. Lacerda, J. Flouquet, Z. Fisk, and J. L. Smith, J. Magn. Magn. Mater. **108**, 56 (1992b)

de Wilde Y., J. Heil, A. G. M. Jansen, P. Wyder, R. Deltour, W. Assmus, A. Menovsky, W. Sun, and L. Taillefer, Phys. Rev. Lett. **72**, 2278 (1994).

Einzel, D., P. J. Hirschfeld, F. Gross, B. S. Chandrasekhar, K. Andres, H. R. Ott, J. Beuers, Z. Fisk, and J. L. Smith, Phys. Rev. Lett. **56**, 2513 (1986).

Ellman, B., T. F. Rosenbaum, J. S. Kim, and G. R. Stewart, Phys. Rev. B **44**, 12074 (1991).

Ellman, B., J. Yang, T. F. Rosenbaum, and E. Bucher, Phys. Rev. Lett. **64**, 1569 (1990).

Fetter, L. A., and J. D. Walecka, Quantum Theory of many-Particle Systems (McGraw-Hill, New York) 1980.

Fisher, R. A., S. Kim, B. F. Woodfield, N. E. Phillips, L. Taillefer, K. Hasselbach, J. Flouquet, A. L. Giorgi, and J. L. Smith, Phys. Rev. Lett. **62**, 328 (1989).

Fisher, R. A., B. F. Woodfield, S. Kim, N. E. Phillips, L. Taillefer, A. L. Giorgi, and J. L. Smith, Solid State Commun. **80**, 263 (1991).

Fisk, Z., and G. Aeppli, Science **260**, 38 (1993).

Fisk, Z., D. W. Hess, C. J. Pethick, D. Pines, J. L. Smith, J. D. Thompson, and J. O. Willis, Science **239**, 33 (1988).

Fisk, Z., H. R. Ott, T. M. Rice, and J. L. Smith, Nature **320**, 124 (1986).

Fisk, Z., G. R. Stewart, J. O. Willis, H. R. Ott, and F. Hulliger, Phys. Rev. B **30**, 6360 (1984).

Frings, P. H., and J. J. M. Franse, Phys. Rev. B **31**, 4355 (1985).

Fulde, P., J. Keller, and G. Zwicknagl, Solid State Physics, Vol. 41 (Academic Press, San Diego, 1988), p. 1.

Gannon, J. J., B. S. Shivaram, and D. G. Hinks, *Europhys. Lett.*, **13**, 459 (1990).

Geibel, C., C. Schank, S. Thies, H. Kitazawa, C. D. Bredl, A. Böhm, M. Rau, A. Grauel, R. Caspary, R. Helfrich, U. Ahlheim, G. Weber, and F. Steglich, *Z. Phys. B* **84**, 1 (1991a).

Geibel, C., S. Thies, D. Kaczorowski, A. Mehner, A. Grauel, B. Seidel, U. Ahlheim, R. Helfrich, K. Peterson, C. D. Bredl, and F. Steglich, *Z. Phys. B* **83**, 305 (1991b).

Goll, G., H. v. Löhneysen, I. K. Yanson, and L. Taillefer, *Phys. Rev. Lett.* **70**, 2008 (1993).

Gor'kov, L. P., *Soviet Phys. JETP* **10**, 998 (1960).

Gor'kov, L. P., *Sov. Sci. Rev. A* **9**, 1 (1987).

Gregory, W. D., W. N. Mathews Jr., and E. A. Edelsack, The Science and Technology of Superconductivity (Plenum Press, New York, 1973).

Grewe N., and F. Steglich, Handbook on the Physics and Chemistry of Rare Earths, Vol. 41 (Elsevier Science Publishers, Amsterdam, 1991).

Grimes, C. C., G. Adams, and E. Bucher, *Phys. Rev. B* **44**, 4631 (1991).

Gross, F., B. S. Chandrasekhar, K. Andres, U. Rauchschwalbe, E. Bucher, and B. Lüthi, *Physica C* **153-155**, 439 (1988).

Gross, F., B. S. Chandrasekar, D. Einzel, K. Andres, P. J. Hirschfeld, H. R. Ott, J. Beuers, Z. Fisk, and J. L. Smith, *Z. Phys. B* **64**, 175 (1986).

Groß-Alltag, F., B. S. Chandrasekhar, D. Einzel, P. J. Hirschfeld, and K. Andres, *Z. Phys. B* **82**, 243 (1991).

Gupta, L. C., D. E. MacLaughlin, Cheng Tien, C. Godart, M. A. Edwards, and R. D. Parks, *Phys. Rev. B* **28**, 3673 (1983).

Halperin, W. P., C. N. Archie, F. R. Rasmussen, T. A. Alvesalo, and R. C. Richardson, *Phys. Rev. B* **13**, 2124 (1976).

Hardy, W. N., D. A. Bonn, Ruixing Liang, and Kuan Zhang, *Phys. Rev. Lett.* **70**, 3999 (1993).

Hasselbach, K., A. Lacerda, K. Behnia, L. Taillefer, J. Flouquet, and A. de Visser, *J. Low Temp. Phys.* **81**, 299 (1990).

Hasselbach, K., L. Taillefer, and J. Flouquet, *Phys. Rev. Lett.* **63**, 93 (1989).

Hayden, S. M., L. Taillefer, C. Vettier, and J. Flouquet, *Phys. Rev. B* **46**, 8675 (1992).

Heal, T. J., and G. I. Williams, *Acta Cryst.* **8**, 494 (1955).

Heffner, R. H., D. W. Cooke, Z. Fisk, R. L. Hutson, M. E. Schillaci, J. L. Smith, J. O. Willis, D. E. MacLaughlin, C. Boekema, R. L. Lichti, A. B. Denison, J. Oostens, *Phys. Rev. Lett.* **57**, 1255 (1986).

Heffner, R. H., J. L. Smith, J. O. Willis, P. Birrer, C. Baines, F. N. Gygax, B. Hitti, E. Lippelt, H. R. Ott, A. Schenck, E. A. Knetsch, J. A. Mydosh, and D. E. MacLaughlin, *Phys. Rev. Lett.* **65**, 2816 (1990).

Hein, R. A., *Phys. Rev. B* **33**, 7539 (1986).

Halfand, E., and N. R. Werthamer, *Phys. Rev.* **147**, 288 (1966).

Hirschfeld, P. J., P. Wölfle, and D. Einzel, *Phys. Rev. B* **37**, 83 (1988).

Hirschfeld, P. J., W. O. Putikka, P. Wölfle, and Y. Campbell, *J. Low Temp. Phys.* **88**, 395 (1992).

Hirschfeld, P. J., P. Wölfle, J. A. Sauls, D. Einzel, and W. O. Putikka, *Phys. Rev. B* **40**, 6695 (1989).

Hohenberg, P. C., and N. R. Werthamer, *Phys. Rev.* **153**, 493 (1967).

Hundley, M. F., P. C. Canfield, J. D. Thompson, Z. Fisk, and J. M. Lawrence, *Phys. Rev. B* **42**, 6842 (1990).

Ishida, T., and H. Mazaki, *J. Appl. Phys.* **52**, 6798 (1981).

Itzler, M. A., G. M. Danner, R. Bojko, and P. M. Chaikin, *Phys. Rev. B* **49**, 6815 (1994).

Jaccard, D., J. Sierro, J. P. Brison, and J. Flouquet, *J. Phys. (France)* **49**, C8-741 (1988).

Jin, C., L. Pollack, E. N. Smith, D. M. Lee, J. T. Market, and M. B. Maple, *Bull. Am. Phys. Soc.* **36**, 717 (1991).

Jin, C., D. M. Lee, S.-W. Lin, Bimal K. Sarma, and D. G. Hinks, *J. Low Temp. Phys.* **89**, 557 (1992).

Joynt, R., J. Magn. Magn. Mater. **108**, 31 (1992).

Joynt, R., V. P. Mineev, G. E. Volovik, and M. E. Zhitomirskii, Phys. Rev. B **42**, 2014 (1990).

Joynt, R., T. Maurice Rice, and Kazuo Ueda, Phys. Rev. Lett. **56**, 1412 (1986).

Julian, S. R., F. S. Tautz, G. L. McMullan, and G. G. Lonzarich, Physica B **199&200**, 63 (1994).

Julian, S. R., P. A. A. Teunissen, and S. A. J. Wiegers, Phys. Rev. B **46**, 9821 (1992).

Kanoda, K., K. Akiba, K. Suzuki, T. Takahashi, and G. Saito, Phys. Rev. Lett. **65**, 1271 (1990).

Kim, J. S., Ph. D. Dissertation, University of Florida, Gainesville (May 1992).

Kim, J. S., B. Andraka, and G. R. Stewart, Phys. Rev. B **44**, 6921 (1991).

Kita, H., A. Dönni, Y. Endoh, K. Kakurai, N. Sato, and T. Komatsubara, J. Phys. Soc. Jpn. **63**, 726 (1994).

Khoder, A. F., Phys. Lett. **94A**, 378 (1983).

Kleiman, R. N., D. J. Bishop, H. R. Ott, Z. Fisk, and J. L. Smith, Phys. Rev. Lett. **64**, 1975 (1990).

Klein, O., E. J. Nicol, K. Holczer, and G. Grüner, Phys. Rev. B **50**, 6307 (1994).

Knetsch, E., Ph. D. Dissertation, University of Leiden, The Netherlands (1992).

Knetsch, E. A., J. A. Mydosh, T. Vorenkamp, and A. A. Menovsky, J. Mag. Mag. Mater. **108**, 75 (1992).

Kohori, Y., T. Kohara, H. Shibai, Y. Oda, T. Kaneko, Y. Kitaoka, and K. Asayama, J. Phys. Soc. Jpn. **56**, 2263 (1987).

Koziol, Z., J. J. M. Franse, P. de Châtel, T. Vorenkamp, K. Bakker, A. de Visser, and A. A. Menovsky, Physica C **192**, 284 (1992).

Koziol, Z., Ph.D. Dissertation, University of Amsterdam, Amsterdam, The Netherlands (1994).

Kumar, P., and P. Wölfle, Phys. Rev. Lett. **59**, 1954 (1987).

Landau, L. D., and E. M. Lifshitz, Electrodynamics of Continuous Media (Pergamon Press Ltd., Oxford, 1984).

Langner, A., D. Sahu, and T. F. George, Phys. Rev. B **38**, 9187 (1988).

Lee, Moohee, G. F. Moores, Y.-Q. Song, W. P. Halperin, W. W. Kim, and G. R. Stewart, Phys. Rev. B **48**, 7392 (1993).

Lee, P. A., T. M. Rice, J. W. Serene, L. J. Sham, and J. W. Wilkins, Comments Condens. Matter Phys. **12**, 99 (1986).

Lin, S. W., Ph. D. Dissertation, University of Wisconsin, Milwaukee (August 1993).

Lounasmaa, O. V., Experimental Principles and Methods below 1K (Academic Press, New York, 1974).

Luke, G. M., A. Keren, L. P. Le, W. D. Wu, Y. J. Uemura, D. A. Bonn, L. Taillefer, and J. D. Garrett, Phys. Rev. Lett. **71**, 1466 (1993).

Luke, G. M., L. P. Le, B. J. Sternlieb, Y. J. Uemura, J. H. Brewer, R. Kadono, R. F. Kiefl, S. R. Kreitzman, T. M. Riseman, C. L. Seaman, Y. Dalichaouch, M. B. Maple, and J. D. Garrett, Hyper. Inter. **64**, 517 (1990)

Luke, G. M., L. P. Le, B. J. Sternlieb, W. D. Wu, Y. J. Uemura, J. H. Brewer, R. Kadono, R. F. Kiefl, S. R. Kreitzman, T. M. Riseman, Y. Dalichaouch, B. W. Lee, M. B. Maple, C. L. Seaman, P. E. Armstrong, R. W. Ellis, Z. Fisk, and J. L. Smith, Phys. Lett. **157**, 173 (1991).

Ma, Zhengxiang, R. C. Taber, L. W. Lombardo, A. Kapitulnik, M. R. Beasley, P. Merchant, C. B. Eom, S. Y. Hou, and Julia M. Phillips, Phys. Rev. Lett. **71**, 781 (1993).

Machida, K., and M. Ozaki, Phys. Rev. Lett. **66**, 3293 (1991).

MacLaughlin, D. E., Cheng Tien, W. G. Clark, M. D. Lan, Z. Fisk, J. L. Smith, and H. R. Ott, Phys. Rev. Lett. **53**, 1833 (1984).

Maki, K., Physics **1**, 21 (1964).

Maple, M. B., J. W. Chen, S. E. Lambert, Z. Fisk, J. L. Smith, Z. Fisk, J. L. Smith, H. R. Ott, J. S. Brooks, and M. J. Naughton, Phys. Rev. Lett. **54**, 477 (1985).

Maxwell, E., and M. Strongin, Phys. Rev. Lett. **10**, 212 (1963).

Mayer, H. M., U. Rauchschwalbe, C. D. Bredl, F. Steglich, H. Rietschel, H. Schmidt, H. Wühl, J. Beuers, Phys. Rev. B **33**, 3168 (1986).

Mazaki, H., M. Takano, Y. Ikeda, Y. Bando, R. Kanno, Y. Takeda, and O. Yamamoto, Jpn. J. Appl. Phys. **26**, L1749 (1987).

Mc Lean, W. L., Proc. Phys. Soc. **79**, 572 (1962).

Meisel, M. W., G. R. Stewart, and E. D. Adams, Cryogenics **29** (1989) 1168.

Menovsky, A. A. and J. J. M. Franse, J. Cryst. Growth **65**, 286 (1983).

Midgley, P. A., S. M. Hayden, L. Taillefer, B. Bogenberger, and H. von Löhneysen, Phys. Rev. Lett. **70**, 678 (1993).

Mueller, R. M., G. G. Ilhas, and E. D. Adams, Rev. Sci. Instrum. **53**, 373 (1982).

Mühschlegel, B., Z. Phys., **155**, 313 (1959).

National Bureau of Standards, Table of the Bessel Functions J0(z) and J1(0) for Complex Arguments (Columbia University Press, New York, 1943).

Ott, H. R., in Handbook on the Physics and Chemistry of the Actinides (Elsevier Science Publishers, Amsterdam, 1987).

Ott, H. R., Physica C **162-164C**, 1669 (1989).

Ott, H. R., H. Rudigier, P. Delsing, and Z. Fisk, Phys. Rev. Lett. **52**, 1551 (1984a).

Ott, H. R., H. Rudigier, Z. Fisk, and J. L. Smith, Phys. Rev. B **31**, 1651 (1985).

Ott, H. R., H. Rudigier, Z. Fisk, and J. L. Smith, Phys. Rev. Lett. **50**, 1595 (1983).

Ott, H. R., H. Rudigier, T. M. Rice, K. Ueda, Z. Fisk, and J. L. Smith, Phys. Rev. Lett. **52**, 1915 (1984b).

Palstra, T. T. M., A. A. Menovsky, J. van den Berg, A. J. Dirkmaat, P. H. Kes, G. J. Nieuwenhuys, and J. A. Mydosh, Phys. Rev. Lett. **55**, 2727 (1985).

Pippard, A. B., Proc. R. Soc. London, Ser. A **191**, 399 (1947).

Pobell, F., Matter and Methods at Low Temperatures (Springer-Verlag, Berlin Heidelberg, 1992).

Pollini, A., A. C. Mota, P. Visani, G. Juri, and J. J. M. Franse, *Physica B* **165&166**, 365 (1990).

Pollini, A., A. C. Mota, P. Visani, R. Pittini, G. Juri, T. Teruzzi, and J. J. M. Franse, *Physica C* **185-189**, 2625 (1991).

Proceedings of the International Conference on Magnetism-1991 (Edinburgh), *J. Mag. Mag. Mater.* **108**, (1992).

Putikka, W. O., P. J. Hirschfeld, and P. Wölfle, *Phys. Rev. B* **41**, 7285 (1990).

Putikka, W. O., and R. Joynt, *Phys. Rev. B* **39**, 701 (1989).

Qian, Y. J., M.-F. Xu, A. Schenstrom, H.-P. Baum, J. B. Ketterson, D. Hinks, M. Levy, and B. K. Sarma, *Solid State Commun.* **63**, 599 (1987).

Rainer, D., *Phys. Scrip.* **T23** (1988).

Rauchschwalbe, U., *Physica B* **147**, 1 (1987).

Rauchschwalbe, U., U. Ahlheim, F. Steglich, D. Rainer, and J. J. M. Franse, *Z. Phys. B* **60**, 379 (1985).

Rauchschwalbe, U., C. D. Bredl, F. Steglich, K. Maki, and P. Fulde, *Europhys. Lett.* **3**, 751 (1987).

Raychaudhuri, A. K., C. Egloff, and L. Rinderer, *J. Low Temp. Phys.* **53**, 513 (1983).

Remenyi, G., D. Jaccard, J. Flouquet, A. Briggs, Z. Fisk, J. L. Smith, and H. R. Ott, *J. Phys. (Paris)* **47**, 367 (1986).

Remenyi, G., U. Welp, J. Flouquet, J. J. M. Franse, and A. Menovsky, *J. Mag. Mag. Mater.* **63&64**, 391 (1987).

Roberts, B. W., *J. Phys. Chem. Ref. Data* **5**, 581 (1976).

Rosenblum, E. S., and S. H. Autler, *Rev. Mod. Phys.* **36**, 77 (1964).

Saint-James, D., G. Sarma, and E. J. Thomas, *Type II Superconductivity* (Pergamon Press, Oxford, 1969).

Sarma, B. K., M. Levy, S. Adenwalla, and J. B. Ketterson, in *Ultrasonics of High-Tc and Other Unconventional Superconductors* (Academic Press, Inc., New York, 1992).

Satoh, K., T. Fujita, Y. Maeno, Y. Onuki, and T. Komastubara, *J. Mag. Mag. Mater.* **76&77**, 128 (1988).

Sauls, J. A., *Adv. Phys.* **43**, 113 (1994a).

Sauls, J. A., *J. Low Temp. Phys.* **95**, 153 (1994b).

Schawlow, A. L., and G. E. Devlin, *Phys. Rev.* **113**, 120 (1959).

Schenstrom, A., M-F Xu, Y. Hong, D. Bein, M. Levy, Bimal Sarma, S. Adenwalla, Z. Zhao, T. Tokuyasu, D. W. Hess, J. B. Ketterson, J. A. Sauls, and D. G. Hinks, *Phys. Rev. Lett.* **62**, 332 (1989).

Schmiedeshoff, G. M., Z. Fisk, and J. L. Smith, *Phys. Rev. B* **45**, 10544 (1992).

Schmiedeshoff, G. M., Y. P. Ma, J. S. Brooks, M. B. Maple, Z. Fisk, and J. L. Smith, *Phys. Rev. B* **38**, 2934 (1988).

Schröder, A., J. G. Lussier, B. D. Gaulin, J. D. Garrett, W. J. L. Buyers, L. Rebelsky, and S. M. Shapiro, *Phys. Rev. Lett.* **72**, 136 (1994).

Schuberth, E. A., G. Hofmann, F. Gross, K. Andres, and J. Hufnagl, *Europhys. Lett.* **11**, 249 (1990).

Schuberth, E. A., B. Strickler, and K. Andres, *Phys. Rev. Lett.* **68**, 117 (1992).

Shivaram, B. S., J. J. Gannon, Jr., D. G. Hinks, *Phys. Rev. Lett.* **63**, 1723 (1989).

Shivaram, B. S., Y. H. Jeong, T. F. Rosenbaum, and D. G. Hinks, *Phys. Rev. Lett.* **56**, 1078 (1986a).

Shivaram, B. S., T. F. Rosenbaum, and D. G. Hinks, *Phys. Rev. Lett.* **57**, 1259 (1986b).

Shoemaker, David P., R. E. Marsh, F. J. Ewing, and L. Pauling, *Acta Cryst.* **5**, 637 (1952).

Signore, P. J. C., B. Andraka, G. R. Stewart, and M. W. Meisel, *Physica B* **194-196**, 2029 (1994a).

Signore, P. J. C., J. P. Koster, E. A. Knetsch, C. M. C. M. van Woerkens, M. W. Meisel, S. E. Brown, and Z. Fisk, *Phys. Rev. B* **45**, 10151 (1992).

Signore, P. J. C., M. W. Meisel, S. E. Brown, and Z Fisk, *Physica B* **199&200**, 157 (1994b).

Sigrist, M., and T.M. Rice, Phys. Rev. B **39**, 200 (1989).

Sigrist, M., and K. Ueda, Rev. Mod. Phys. **63**, 239 (1991).

Slichter, C. P., Principles of Magnetic Resonance (Springer-Verlag, Berlin Heidelberg, 1978).

Steglich, F., Physica B **130**, 145 (1985).

Steglich, F., J. Aarts, C. D. Bredl, W. Lieke, D. Meschede, W. Franz, and H. Schäfer, Phys. Rev. Lett. **43**, 1892 (1979).

Steglich, F., U. Ahlheim, C. D. Bredl, C. Geibel, M. Lang, A. Loidl, and G. Sparn, Frontiers in Solid State Sciences (World Scientific, Singapore, 1992).

Stewart, G. R., Rev. Mod. Phys. **56**, 755 (1984).

Stewart, G. R., Z. Fisk, J. L. Smith, J. O. Willis, and M. S. Wire, Phys. Rev. B **30**, 1249 (1984a).

Stewart, G. R., Z. Fisk, J. O. Willis, and J. L. Smith, Phys. Rev. Lett. **52**, 679 (1984b).

Strongin, M., A. Paskin, D. G. Schweitzer, O. F. Kammerer, and P. P. Craig, Phys. Rev. Lett. **12**, 442 (1964).

Sulpice, A., P. Gandit, J. Chaussy, J. Flouquet, D. Jaccard, P. Lejay, and J. L. Tholence, J. Low Temp. Phys. **62**, 93 (1986).

Taillefer, L., Behnia, K. Hasselbach, J. L. Flouquet, S. M. Hayden, and C. Vettier, J. Mag. Mag. Mater. **90&91**, 623 (1990).

Taillefer, L., and G. G. Lonzarich, Phys. Rev. Lett. **60**, 1570 (1988a).

Taillefer, L., F. Piquemal, and J. Flouquet, Physica C **153-155**, 451 (1988b).

Takabatake, T., F. Teshina, H. Fujii, S. Nishigori, T. Suzuki, T. Fujita, Y. Yamagushi, and J. Sakurai, Phys. Rev. B **41**, 9607 (1990).

Tedrow, P. M., G. Faraci, and R. Meservey, Phys. Rev. B **4** 74 (1971).

Tilley, D. R., and J. Tilley, Superfluidity and Superconductivity (IOP Publishing Ltd., New York, 1990)

Tinkham, M., Introduction to Superconductivity (Krieger, Malabar, 1975).

Tinkham, M., Phys. Rev. Lett. **61**, 1658 (1988).

Tokuyasu, T., D. Hess, and J. Sauls, Phys. Rev. B **41**, 8891 (1990).

Trappman, T., H. v. Löhneysen, and L. Taillefer, Phys. Rev. B **43**, 13714 (1991).

Tsuei, C. C., J. R. Kirtley, C. C. Chi, Lock See Yu-Jahnes, A. Gupta, T. Shaw, and B. Ketchen, Phys. Rev. Lett. **73**, 593 (1994).

van de Klundert, L. J. M., E. A. Gijsbertse, and L. C. van der Marel, Physica **69**, 159 (1973).

van der Beek, C. J., and P. H. Kes, Phys. Rev. B **43**, 13032 (1991).

van Dijk, N. H., A. de Visser, J. J. M. Franse, and A. A. Menovsky, Proceedings of the 1994 Conference on Strongly Correlated Electron Systems (Amsterdam, 1994).

van Duzer, T., and C. W. Turner, Principles of Superconductive Devices and Circuits (Elsevier, New York, 1981).

Varmazis, C., J. R. Hook, D. J. Sandiford, and M. Strongin, Phys. Rev. B **11** 3354 (1975).

Varmazis, C., Y. Imry, and M. Strongin, Phys. Rev. B **13**, 2880 (1976).

Varmazis, C., and M. Strongin, Phys. Rev B **10**, 1885 (1974)

Vincent, E., J. Hammann, L. Taillefer, K. Behnia, N. Keller, and J. Flouquet, J. Phys. **3**, 3517 (1991).

Vollhardt, D., and P. Wölfle The Superfluid Phases of Helium 3 (Taylor and Francis, New York, 1990).

Volovik, G. E., and L. P. Gor'kov, Sov. Phys. JETP **61**, 843 (1985).

von Löhneysen, H., Physica B **197**, 551 (1994).

von Löhneysen, H., T. Trappman, and L. Taillefer, J. Magn. Magn. Mater. **108**, 49 (1992).

Vorenkamp, T., M. C. Aronson, Z. Koziol, K. Bakker, J. J. M. Franse, and J. L. Smith, Phys. Rev. B **48**, 6373 (1993a).

Vorenkamp, T., A. de Visser, R. Wester, A. A. Menovsky, J. J. M. Franse, and E. A. Knetsch, Phys. Rev. B **48**, 6385 (1993b).

Vorenkamp, T., Z. Tarnawski, H. P. van der Meulen, K. Kadowaki, V. J. M. Meulenbroek, A. A. Menovsky, and J. J. M. Franse, Physica B **163**, 564 (1990).

Werthamer, N. R., E. Helfand, and P. C. Hohenberg, Phys. Rev. **147**, 295 (1966).

Williamson, S. J., Phys. Rev. B **2**, 3545 (1970).

Wüchner, S., N. Keller, J. L. Tholence, and J. Flouquet, Solid State Commun. **85**, 355 (1993).

Yeshurun, Y., and A. P. Malozemoff, Phys. Rev. Lett. **60**, 2202 (1988).

Yip, S. K., and A. Garg, Phys. Rev. B **48**, 3304 (1993).

Yip, S. K., and J. A. Sauls, Phys. Rev. Lett. **69**, 2264 (1992).

BIOGRAPHICAL SKETCH

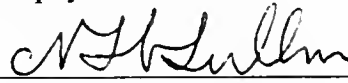
Philippe Jean-Claude Signore was born on October 5, 1967, in Neuilly sur Seine, France. In August 1983, he moved to Titusville, Florida, where he graduated from Astronaut High School in June, 1985. He then entered the University of Tennessee at Chattanooga, where he received, in May 1989, a Bachelor of Science degree, with a major in physics and a minor in mathematics. Since August of that year, he has been working toward the Doctor of Philosophy degree at the University of Florida.

I certify that I have read this study and that in my opinion it conforms to acceptable standards of scholarly presentation and is fully adequate, in scope and quality, as a dissertation for the degree of Doctor of Philosophy.



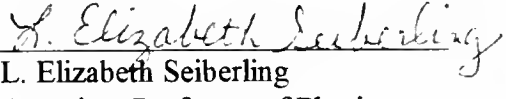
Mark W. Meisel, Chair
Associate Professor of Physics

I certify that I have read this study and that in my opinion it conforms to acceptable standards of scholarly presentation and is fully adequate, in scope and quality, as a dissertation for the degree of Doctor of Philosophy.



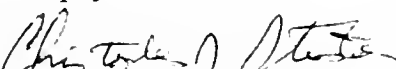
Neil S. Sullivan, Cochair
Professor of Physics

I certify that I have read this study and that in my opinion it conforms to acceptable standards of scholarly presentation and is fully adequate, in scope and quality, as a dissertation for the degree of Doctor of Philosophy.



L. Elizabeth Seiberling
Associate Professor of Physics

I certify that I have read this study and that in my opinion it conforms to acceptable standards of scholarly presentation and is fully adequate, in scope and quality, as a dissertation for the degree of Doctor of Philosophy.



Christopher J. Stanton
Associate Professor of Physics

I certify that I have read this study and that in my opinion it conforms to acceptable standards of scholarly presentation and is fully adequate, in scope and quality, as a dissertation for the degree of Doctor of Philosophy.



Gregory R. Stewart
Professor of Physics

I certify that I have read this study and that in my opinion it conforms to acceptable standards of scholarly presentation and is fully adequate, in scope and quality, as a dissertation for the degree of Doctor of Philosophy.



Gijs Bosman
Professor of Electrical Engineering

This dissertation was submitted to the Graduate Faculty of the Department of Physics in the College of Liberal Arts and Sciences and to the Graduate School and was accepted as partial fulfillment of the requirements for the degree of Doctor of Philosophy.

December, 1994

Dean, Graduate School

LD
3780
4994
S-112

UNIVERSITY OF FLORIDA



3 1262 08557 1122